



Microwave synthesis of inorganic nanocrystals and their evaluation in biological environments

Si-Ming Yu

DOCTORAL THESIS

Doctoral Studies in Material Science

Supervised by Dr. Anna Laromaine Sagué and Dr. Anna Roig Serra

Tutor Dr. José Antonio Ayllón Esteve

Departament de Química, Facultat de Ciències
Universitat Autònoma de Barcelona

2015

Thesis submitted to aspire for the Doctor Degree

Si-Ming Yu

Supervisor's Approval

Dr. Anna Laromaine Sagué

Dr. Anna Roig Serra

Tutor

Dr. José Antonio Ayllón Esteve

Bellaterra (Cerdanyola del Vallès), 09 de juny 2015

Dra. Anna Laromaine Sagué, Investigadora contractada Ramon y Cajal i **Dra. Anna Roig Serra**, Investigadora Científica del CSIC, i el **Dr. José Antonio Ayllón Esteve**, Titular d'Universitat, UAB

CERTIFIQUEN:

Que Si-Ming Yu, amb un Màster en Enginyeria dels Aliments per la “South China University of Technology”, Xina, ha dut a terme aquesta tesis doctoral sota la seva direcció i que porta per títol **“Microwave synthesis of inorganic nanocrystals and their evaluation in biological environments”**, la qual queda recollida en aquesta memòria per optar al grau de Doctor en Ciència en el Programa de Ciència de Materials.

I perquè així consti, signen el present certificat

Dr. Anna Laromaine Sagué

Dr. Anna Roig Serra

Dr. José Antonio Ayllón Esteve

Si-Ming Yu

Bellaterra, 09 de juny 2015

人生就像一场旅行，不必在乎目的地，在乎的是沿途的风景以及看风景的心情。

Life is like a journey, you do not need to care about the destination, just pay attention to the scenery along the way and your mood towards those scenery.

at Institut de Ciència de Materials de Barcelona



Acknowledgements

On Oct. 4th, 2012, I landed in Barcelona for the first time, and I started the new chapter of my PhD research in my life. I did not expect Barcelona to be such a pleasant city, nor did I expect to get a so impressive training and research in the N&N group at ICMAB. I still remember the first day my supervisor, Dr. Anna Laromaine, picked me up from the airport of Barcelona and drove to my new living place. She is always nice and friendly in daily life, careful and strict in research. During the past three years, she taught me the right attitude and the most efficient way to do research, and helped me to improve my skills in writing and presentation. Also, I am very grateful to Dr. Anna Roig for her kind and patient supervision. She is very knowledgeable and responsible, and always teaches me new things. In the last year of my PhD research, I have been working with her side by side, and she is always available when I have some doubts. From my both supervisors, I have learned that the most important thing in doing research is to be patient and to do my best. This is certainly a valuable life-lesson for me to improve and show myself in my future.

Particularly, I would like to acknowledge my collaborators, Dr. Maria Milla and Laura Gonzalez-Moragas (PhD students in NN Group-ICMAB). Thank you Maria for the execution of cell experiments, Laura Gonzalez-Moragas for the evaluation of SPIONs on *in vivo C. elegans* and co-working on the large-scale up synthesis of SPIONs.

I also want to thank all the current and previous members of the NN group, especially Maria, Nerea, Martí, Laura Gonzalez, Laura Asturias, Pengfei, Raluca, Luisa, Muling, Ilargi and Wojtek. Thank you for your kind suggestions during the group meetings, and for your kind help during my stay here. In particular Pengfei, thank you for your nice help in submitting the documents required for the registration to the UAB graduate school.

Thank you for all of the sportsmen in the Badminton-SAF team and Alba-Cerdanyola basketball team. Because of our games in the spare time, I have become fit, healthy and always energetic in my work. Thank you my Spanish teacher and my good friend, Laura Córcoles, you have brought almost too much fun for me, helping me enjoy the life here. I am very surprised by your good level of Chinese, you can even understand the slangs. Thank you my good friend Mateusz Scigaj, I am very impressed in your talent in learning how to cook typical and delicious Chinese food so quickly, even better and more professional than me. Thank you my previous office-mates Mar Tristany, Simo and Blai, I really enjoyed the stays with you.

My appreciation also goes to the technical and the administration staff of the ICMAB, without your kind help, I would have been unable to do the right registration and carry out my work.

Of course, I have to thank my family, my father, my mother and my younger brother. Without their support, I would have been unable to go abroad to pursue my PhD degree.

Last but not least, I have to thank to the China Scholarship Council for the financial support for my studies here (Scholarship reference: SIMING YU-201206150053) and the acceptance of the NN Group as a PhD student.

Foreword and aim of the thesis

From 2009 to 2012, I embarked in my master degree in South China University of Technology (Guangzhou, China). My research focused on the functionalization of nanoparticles with antibodies and explored the potential use of the antibody-nanoparticles complexes in rapid immuno-detection techniques. Since then, I have been intensely interested in the functionalization of nanoparticles and I decided to pursue my PhD thesis in a subject related to this aspect of materials science.

On October 2012, I was accepted in the group of Nanoparticles and Nanocomposites at the Materials Science Institute of Barcelona (ICMAB-CSIC) and I was granted a scholarship by the China Scholarship Council to start my PhD research under the supervision of Dr. Anna Laromaine and Dr. Anna Roig. I chose to join the Group of Nanoparticles and Nanocomposites because of their expertise in the synthesis and functionalization of superparamagnetic iron oxide nanoparticles (SPIONs) for biomedical applications.

Previous to my entrance to the team, the group had already established a facile, fast and green method for the synthesis of superparamagnetic iron oxide nanoparticles (SPIONs) based on microwave heating. Therefore, my work also started with the microwave-assisted synthesis of SPIONs. My first objective was to accomplish the stability of SPIONs in biological media, in particular in cell media. By retrieving recent literature regarding surface functionalization of nanoparticles, I identified serum albumins as good candidates because they are water soluble, biocompatible and easily available. Moreover, in 2005 an albumin-bound nanoparticle of paclitaxel drug (with the commercial name of Abraxane) had been approved by the American Food and Drug Administration to treat breast cancer. This encouraged me to use bovine serum albumin (BSA) for the surface functionalization of SPIONs, and so, the study of the interaction of SPIONs with BSA became an important part of my PhD work. At the same time, I expanded the use of microwave-assisted synthesis method to fabricate gold nanoparticles and Au-SPIONs hybrid nanoparticles. Au-SPIONs hybrid nanoparticles are being evaluated as new candidate materials in several health-related applications such as bio-sensing, imaging and therapeutics. Thus, new simple synthetic methods for those hybrid nanoparticles will certainly be in high demand.

Briefly, this thesis proposes some synthetic pathways to engineer water dispersible, biocompatible nanoparticles and evaluates their interaction with biological entities. To achieve this purpose, I first used a microwave-assisted method to synthesize SPIONs, Au nanoparticles and Au-SPIONs hybrid nanoparticles. I then focused on the surface functionalization of SPIONs with different electrostatic stabilizers and BSA to make them dispersible and stable in cell media. Thereafter, the interaction between SPIONs and BSA was investigated by using several different techniques. Binding behaviors, structural changes and thermodynamics of BSA upon interaction with SPIONs have been elucidated. Finally, working with other group members, we evaluated the influence of the BSA coating on the toxicity, uptake and intracellular localization of SPIONs

on two types of cells. Biological effects of BSA coating on SPIONs were also investigated on an *in vivo* simple model of the *C. elegans*.

This thesis is organized in seven chapters.

- **Chapter 1** introduces: i) basic concepts of nanoscience, nanomedicine and magnetism of iron oxide nanoparticles, ii) general synthetic methods for producing iron oxide and gold nanoparticles, and their biomedical applications, iii) the interaction of nanoparticles with proteins, and the effect of protein coating on the biological responses of nanoparticles.
- **Chapter 2** presents: i) microwave-assisted synthesis of SPIONs and Au nanoparticles, ii) surface functionalization of SPIONs with polyvinyl pyrrolidone, tetramethylammonium hydroxide and trisodium citrate dehydrate and iii) large scale-up synthesis of citrate functionalized SPIONs by using a multi-mode MW apparatus.
- **Chapter 3** further explores the use of microwave assisted method in the synthesis of Au-SPIONs hybrid nanoparticles. A facile, fast and bio-friendly microwave-assisted polyol route was established to synthesize high yield of gold (Au) nanotriangles (NT) decorated with superparamagnetic iron oxide nanoparticles (SPIONs). The yield of AuNTs could be controlled by adjusting synthetic parameters.
- **Chapter 4** contains the surface functionalization of SPIONs by BSA. The stability of the BSA functionalized SPIONs has been investigated in several biologically relevant media. The adsorption mechanism, thermodynamics and structure conformation of BSA upon adsorption on SPIONs were also revealed in detail.
- **Chapter 5** reports the effects of BSA coating on the behavior of SPIONs in biological environments. In particular, degradation of SPIONs with and without BSA coating in citrate buffer (pH 4.6), mimicking the lysosomal acidic environment, was evaluated. We also investigated the cytotoxicity, uptake and localization of SPIONs with and without BSA coating on two types of cells. Furthermore, biological effects of BSA coating were evaluated on the *in vivo* model *C. elegans*.
- **Chapter 6** includes the general conclusions extracted from the PhD work. Some suggestions for future work are also included.
- **Chapter 7** gives the author's CV and the publications that have resulted from the thesis.

PRÓLOGO Y OBJETIVO DE LA TESIS

Entre 2009 y 2012 cursé mi maestría en la Universidad Tecnológica de *South China* (Guangzhou, China). Mi investigación se centró en la funcionalización de nanopartículas con anticuerpos y exploré el uso potencial de los sistemas anticuerpo-nanopartículas para el desarrollo de técnicas rápidas de inmunodetección. A partir de entonces me interesé por la funcionalización de nanopartículas y decidí hacer mi tesis doctoral en un tema relacionado a éste de la ciencia de materiales.

En octubre de 2012 fui aceptado en el Grupo de *Nanoparticles and Nanocomposites* del Instituto de Ciencia de Materiales de Barcelona (ICMAB-CSIC), donde se me concedió una beca de doctorado del *China Scholarship Council* para iniciar mi investigación bajo la supervisión de la Dra. Anna Laromaine y la Dra. Anna Roig. Elegí unirme a este grupo porque sus miembros cuentan con gran experiencia en la síntesis y funcionalización de nanopartículas de óxido de hierro superparamagnéticas (SPIONs) para aplicaciones biomédicas. Anteriormente a mi entrada en el equipo, el grupo había ya establecido un método fácil, rápido y 'verde' para la síntesis de nanopartículas de óxido de hierro superparamagnéticas (SPIONs) utilizando calentamiento por microondas. Así, mi trabajo empezó con la síntesis de SPIONs asistida por microondas. Mi primer objetivo fue lograr la estabilidad de SPIONs en medios biológicos, en particular en los medios de cultivo celular. A partir de una búsqueda bibliográfica sobre la funcionalización superficial de nanopartículas, identifiqué las seroalbúminas como buenas proteínas para usarlas como funcionalización porque son solubles en agua, biocompatibles y de alta disponibilidad. Por otra parte, en el año 2005 una nanopartícula del fármaco *Paclitaxel* funcionalizada con albúmina (comercializada bajo el nombre de *Abraxane*) fue aprobada por la agencia estadounidense *Food and Drug Administration* para el tratamiento del cáncer de mama. Esto me animó a utilizar la albúmina de suero bovino (BSA) para la funcionalización superficial de las SPIONs, y así, el estudio de la interacción de SPIONs con BSA se convirtió en una parte importante de mi trabajo de doctorado. Al mismo tiempo, amplié el uso del método de síntesis asistida por microondas para fabricar nanopartículas de oro (Au-NPs) y Au-SPIONs híbridas. Actualmente las Au-SPIONs híbridas se están evaluando como posibles candidatos para varias aplicaciones relacionadas con la salud, tales como bio-detección, tratamiento de imágenes y en tratamientos terapéuticos. De este modo, el desarrollo de nuevos y sencillos métodos para la síntesis de nanopartículas híbridas generará sin duda una gran demanda.

En resumen, esta tesis propone algunas rutas sintéticas para diseñar nanopartículas dispersables en agua, biocompatibles y evalúa su interacción con entidades biológicas.

Para lograr este propósito, utilicé la síntesis asistida por microondas para obtener SPIONs , nanopartículas de oro y Au – SPIONs híbridas. Posteriormente, me centré en la funcionalización superficial de SPIONs con diferentes estabilizantes electrostáticos y BSA para hacerlas dispersables y estables en los medios de cultivo celular. Así, investigamos la interacción entre SPIONs y BSA mediante el uso de técnicas diferentes. Determinamos constantes de interacción,

cambios estructurales y la termodinámica de la interacción de BSA con SPIONs. Finalmente, trabajando con otros miembros del grupo, analizamos la influencia de la capa de BSA en la toxicidad, la absorción y la localización intracelular de SPIONs en dos tipos de líneas celulares. Los efectos biológicos de recubrimiento BSA en SPIONs también se investigaron en el modelo simple *in vivo* *C. elegans*.

Esta tesis se organiza en siete capítulos:

- **El capítulo 1** introduce: i) los conceptos básicos de la nanociencia, nanomedicina y el magnetismo de las nanopartículas de óxido de hierro, ii) los métodos sintéticos generales para la producción de nanopartículas de óxido de hierro y nanopartículas de oro, y sus aplicaciones biomédicas, iii) la interacción de nanopartículas con proteínas, y el efecto del recubrimiento de proteína en las respuestas biológicas de las nanopartículas.
- **El capítulo 2** presenta: i) la síntesis asistida por microondas de SPIONs y nanopartículas de Au, ii) la funcionalización superficial de SPIONs con polivinil pirrolidona, hidróxido de tetrametilamonio y citrato trisódico hidratado y iii) la síntesis a gran escala de SPIONs funcionalizadas con citrato mediante el uso de un Microondas multi-modo.
- **El capítulo 3** extiende el uso del método de síntesis asistida por microondas de Au-SPIONs híbridas. Se ha establecido una ruta fácil asistida por microondas utilizando polioles de forma rápida y verde para sintetizar nanotriángulos (NT) de oro (Au) decorados con nanopartículas de óxido de hierro superparamagnéticas (SPIONs) con un alto rendimiento. El rendimiento de Au-NTs puede ser controlado ajustando los parámetros de síntesis.
- **El capítulo 4** muestra la funcionalización superficial de SPIONs con BSA. La estabilidad de las BSA-SPIONs funcionalizadas se ha investigado en varias soluciones biológicamente relevantes. El mecanismo de adsorción, la termodinámica y la conformación estructural del BSA sobre los SPIONs se analiza en detalle.
- **El capítulo 5** presenta la modificación del comportamiento de SPIONs en entornos biológicos después de su recubrimiento con BSA. En particular, se evalúa la degradación de SPIONs con y sin recubrimiento de BSA en una solución tampón de citrato (pH 4,6), imitando el ambiente ácido lisosomal. También se investigó la citotoxicidad, la captación y localización de SPIONs con y sin recubrimiento de BSA en dos tipos de células y los efectos biológicos del recubrimiento BSA en el modelo *in vivo* *C. elegans*.
- **El capítulo 6** enumera las principales conclusiones derivadas de esta tesis doctoral y algunas sugerencias para futuros trabajos en el campo.
- **El capítulo 7** recoge información sobre el autor y sus publicaciones durante el período de realización de esta tesis doctoral.

Attributions

I would like to thank all the people who have contributed to my PhD work.

- **Dr. Maria Milla** (NN Group-ICMAB) who performed the cytotoxicity, uptake and intracellular localization of C-SPIONs and BSA-SPIONs with *in vitro* cell lines. She also helped me to do the data analysis.
- **Laura Gonzalez-Moragas** (PhD students in NN Group-ICMAB) with who I collaborated to do the large-scale up synthesis of SPIONs and wrote the paper. She also performed the evaluation of the biological effect of the BSA coating on the *in vivo* platform *C. elegans*.
- **Dr. Caterina Minelli** (National Physical Laboratory, UK) who performed the DCS and XPS measurements and do the data analysis.
- **Dr. Alex Perálvarez-Marín** (UAB) who performed the gel electrophoresis experiments for purification of Au NTs-SPIONs nanocomposites.
- **Dr. Elisa Carenza** (NN Group-ICMAB) who trained me to do the microwave synthesis of iron oxide nanoparticles.
- **Dr. Nerea Murillo-Cremaes** (NN Group-ICMAB) who collaborated with me to do the large-scale up synthesis of SPIONs and gave helpful comments during the writing process.
- **Technical staff of the Nanoquim Platform at ICMAB:** Neus Romà, Enrique Irisarri and Edgar León. Especially, Enrique Irisarri (ICMAB) who trained me in the microwave oven and the fluorescent spectrophotometer.
- **Jose Amable Bernabé** (ICMAB) who trained me to use the dynamic light scattering and zeta potential apparatus.
- **Dr. Judit Oró** (ICMAB) who performed the transmission electron microscopy measurements of my samples.
- **Anna Esther Carrillo** (ICMAB) performed the scanning electron microscopy measurements.
- **Roberta Ceravola** (ICMAB) who performed the isothermal titration calorimetry experiments.
- **Anna Crespi** and **Joan B. Esquiús** (ICMAB) who performed the X-ray Diffraction of my SPIONs samples.
- **People of Servei de Cultius Cel·lulars, Producció d'Anticossos i Citometria** (UAB) who let us use facilities for culturing cells. Especially, Fran Cortes who trained me in culturing cells, and performed some cell experiments in the last period of my PhD.
- **Dr. Silvia Lope Piedrafita** (Servei RMN-UAB) who performed the magnetic resonance imaging of my samples.
- **Bernat Bozzo** (ICMAB) who performed the magnetic measurements of my samples.
- The group of **Romain Quidant** at ICFO-UPC and specially to **Pascal Berto** who performed the photothermal heating experiments of my samples.
- **Pablo Castro Hartmann** (Servei de Microscòpia-UAB) who performed the negative staining transmission electron microscopy and High resolution transmission electron microscopy.
- **Luisa Barrera** (MIT) who helped me in correcting the grammar of my thesis.

List of symbols, abbreviations and acronyms

Au	Gold
ATR-FTIR	Attenuated total reflectance fourier transformed infrared spectra
BA	Benzyl alcohol
BSA	Bovine serum albumin
CB	Citrate buffer
CD	Circular dichroism
DLS	Dynamic light scattering
D_h	Hydrodynamic diameter
DMEM	Dulbecco's Modified Eagle's Medium
DMEM- Na_3Cit	DMEM with 10 mM Na_3Cit
DMEM-FBS	DMEM with 10% FBS
DMEM-FBS- Na_3Cit	DMEM with 10% FBS and 10 mM Na_3Cit
DCS	Differential centrifugal sedimentation
EDTA	Ethylenediaminetetraacetic acid
EPM	electrophoretic mobility
EG	Ethylene glycol
FBS	Fetal bovine serum
FCS	Fluorescence correlation spectroscopy
FTIR	Fourier transformed infrared spectra
H_c	Coercivity
ITC	Isothermal titration calorimetry
LS	Lab scale
M_r	Remanent magnetization
M_s	Saturated magnetization
MRI	Magnetic resonance imaging
MW	Microwave
Na_3Cit	Trisodium citrate dihydrate
NTs	nanotriangles
pI	isoelectric point
PDI	Polydispersity Index
PBS	Phosphate buffered saline
PBS- Na_3Cit	PBS with 10 mM Na_3Cit
PVP	Polyvinyl pyrrolidone
RPMI	Roswell Park Memorial Institute Medium
RPMI- Na_3Cit	RPMI with 10 mM Na_3Cit
RPMI-FBS	RPMI with 10% FBS
RPMI-FBS- Na_3Cit	RPMI with 10% FBS and 10 mM Na_3Cit
SU	Scale up
SPIONs	Superparamagnetic iron oxide nanoparticles
SPR	surface plasmon resonance
SDS-PAGE	Sodium dodecyl sulfate-polyacrylamide gel electrophoresis
TBE	Tris-borate-EDTA
T_B	Blocking temperature
TMAOH	Tetramethylammonium hydroxide
TEM	Transmission electron microscope
τ_1	Longitudinal relaxivity
τ_2	Transversal relaxivity
T_1	Longitudinal relaxation
T_2	Transversal relaxation
τ_N	Neel relaxation time

τ_B	Brown relaxation time
UV-Vis	Ultraviolet-visible spectroscopy
ZFC/FC	Zero-field cooling/field cooling
XPS	X-ray photoelectron spectroscopy
ZFC/FC	Zero-field-cooled/field cooled
ζ	zeta potential

Table of contents	pag.
Acknowledgements	i
Foreword and aim of the thesis	iii
Attributions	vii
List of symbols, abbreviations and acronyms	ix
Index	xi

CHAPTER 1.

INTRODUCTION

1.1 NANOSCIENCE AND NANOMEDICINE: GENERAL CONCEPTS	3
1.2 SYNTHESIS OF IRON OXIDE NANOPARTICLES	4
1.3 MAGNETISM: GENERAL CONCEPTS	10
1.4 APPLICATIONS OF IRON OXIDE NANOPARTICLES IN BIOMEDICINE	13
1.5 SYNTHESIS AND BIOMEDICAL APPLICATIONS OF Au NANOCRYSTALS	15
1.6 PROTEIN-NANOPARTICLE INTERACTION	17
1.6.1 DIFFERENT EFFECTS ON THE PROTEIN-NANOPARTICLE INTERACTION	18
1.6.2 STRUCTURE CHANGE OF PROTEIN UPON INTERACTION WITH NANOPARTICLES	22
1.6.3 APPROACHES FOR STUDYING NANOPARTICLE-PROTEIN INTERACTION	23
1.6.4 EFFECTS OF PROTEIN CORONA ON BIOLOGICAL RESPONSE	25
1.7 CHAPTER REFERENCES	28

CHAPTER 2.

SYNTHESIS AND CHARACTERIZATION OF SPION_s AND Au NANOPARTICLES

2.1 MICROWAVE SYNTHESIS OF SPION_s	39
2.2 SURFACE COATING OF SPION_s	40
2.3 CHARACTERIZATION OF SPION_s	41
2.4 SIZE CONTROL OF SPION_s	43
2.5 MAGNETIC PROPERTIES OF SPION_s	46
2.6 RELAXIVITY MEASUREMENT	48
2.7 SCALE UP SYNTHESIS OF SPION_s	49
2.8 MICROWAVE SYNTHESIS OF Au NANOPARTICLES	55
2.9 CHAPTER CONCLUSIONS	60
2.10 ANNEX OF CHAPTER 2	61
2.11 CHAPTER REFERENCES	67

CHAPTER 3.

MAGNETIC GOLD NANOTRIANGLES BY MICROWAVE POLYOL SYNTHESIS

3.1 BIOMEDICAL APPLICATIONS OF Au-SPION_s HYBRID NANOCOMPOSITES	73
3.2 SYNTHESIS OF Au-SPION_s HYBRID NANOCOMPOSITES: STATE OF THE ART	73
3.3 MICROWAVE POLYOL SYNTHESIS OF Au NANOTRIANGLES-SPION_s HYBRID NANOCOMPOSITES	74
3.4 STRUCTURE AND CHARACTERIZATION OF Au-SPION_s HYBRID NANOCOMPOSITES	77
3.5 EFFECT OF PVP AMOUNT ON THE SHAPE YIELD OF Au NT-SPION_s HYBRID NANOCOMPOSITES	78
3.6 EFFECT OF TEMPERATURE ON THE SHAPE YIELD OF Au NT-SPION_s HYBRID NANOCOMPOSITES	81
3.7 EFFECT OF REACTION TIME ON THE SHAPE YIELD OF Au NT-SPION_s HYBRID NANOCOMPOSITES	82
3.8 MAGNETIC PROPERTIES OF Au-SPION_s HYBRID NANOCOMPOSITES	83
3.9 PROPOSED MECHANISM OF THE FORMATION OF Au NT-SPION_s HYBRID NANOCOMPOSITES	83
3.10 PURIFICATION AND SELF-ASSEMBLY OF Au NT-SPION_s HYBRID NANOCOMPOSITES	85
3.11 CHAPTER CONCLUSIONS	88
3.12 ANNEX OF CHAPTER 3	89
3.13 CHAPTER REFERENCES	91

CHAPTER 4.

STUDY ON THE INTERACTION OF BOVINE SERUM ALBUMIN WITH SUPERPARAMAGNETIC IRON OXIDE NANOPARTICLES

4.1 STABILITY OF SPION_s IN BIOLOGICAL ENVIRONMENTS	95
4.2 STABILIZATION OF SPION_s IN BIOLOGICAL ENVIRONMENTS	98
4.2.1 STABILIZATION OF SPION_s BY ADSORBING BSA	98
4.2.2 STABILIZATION OF SPION_s BY ADDING EXCESS Na₃Cit	104
4.3 CHARACTERIZATION OF BSA LAYER SPIONS	105
4.4 STUDY ON THE INTERACTION MECHANISM OF BSA WITH C-SPION_s	107
4.4.1 ADSORPTION BEHAVIOR OF BSA ON C-SPION _s ' SURFACE	107
4.4.1.1 DLS MEASUREMENTS	107
4.4.1.2 DETERMINATION OF SATURATED AMOUNT OF BSA ADSORBED ON C-SPION _s SURFACE	108
4.4.1.3 DIFFERENTIAL CENTRIFUGAL SEDIMENTATION MEASUREMENTS	109
4.4.1.4 X-RAY PHOTOELECTRON SPECTROSCOPY	110

4.4.1.5 CALCULATION OF THE SATURATED NUMBER OF BSA MOLECULE PER SPION	112
4.4.2 CONFORMATION CHANGE OF BSA UPON INTERACTION WITH C-SPIONs	113
4.4.2.1 UV-Vis MEASUREMENTS	113
4.4.2.2 CIRCULAR DICHROISM	114
4.4.2.3 STEADY-STATE FLUORESCENCE SPECTROSCOPY	115
4.4.2.4 SYNCHRONOUS FLUORESCENCE SPECTROSCOPY	116
4.5 THERMODYNAMICS OF PROTEIN ADSORPTION ON SPIONs	118
4.6 CHAPTER CONCLUSION	119
4.7 ANNEX OF CHAPTER 4	120
4.8. CHAPTER REFERENCES	128

CHAPTER 5.

INTERACTION OF SUPERPARAMAGNETIC IRON OXIDE NANOPARTICLES WITH BIOLOGICAL ENTITIES

5.1 EFFECT OF PROTEIN CORONA ON NANOPARTICLE-CELL INTERACTION	135
5.2 DEGRADATION OF SPIONs AND BSA-SPIONs IN BIOLOGICAL MEDIA	135
5.2.1 DEGRADATION KINETICS	136
5.2.2 SIZE EVOLUTION DURING THE DEGRADATION PROCESS	138
5.3 EFFECT OF PROTEIN CORONA ON NANOPARTICLE-CELL INTERACTION	139
5.3.1 CELL CULTURES	139
5.3.2 CELL VIABILITY: MTT ASSAYS	139
5.3.3 CELLULAR UPTAKE OF SPIONs: DETERMINATION OF IRON CONTENT	141
5.3.4 SPIONs LOCALIZATION WITHIN CELLS AFTER INTERNALIZATION	142
5.4 EVALUATION OF SPIONs ON 3D IN VIVO C-ELEGANS	144
5.5 CHAPTER CONCLUSION	146
5.6 ANNEX OF CHAPTER 5	147
5.7 CHAPTER REFERENCES	149

CHAPTER 6.

CONCLUSIONS AND FUTURE WORK

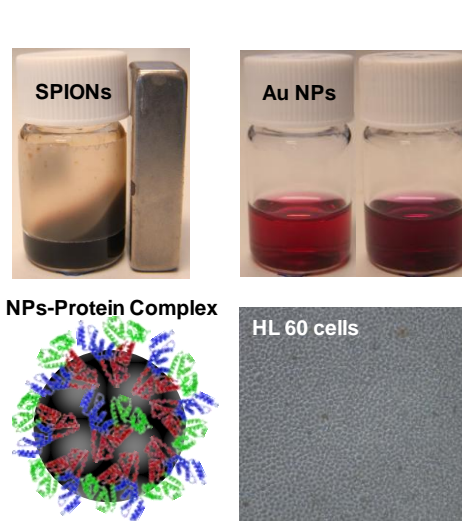
6.1 GENERAL CONCLUSIONS	153
6.2 FUTURE WORK	166

CHAPTER 7.

Curriculum vitae of the author	159
List of publications	163

CHAPTER 1

INTRODUCTION



CHAPTER SUMMARY

This chapter introduces some basic concepts of nanoscience, nanomedicine and magnetism of iron oxide nanoparticles at the nanoscale. General synthetic methods for producing iron oxide nanoparticles and gold nanoparticles, and their applications in nanomedicine are presented. How nanoparticles interact with proteins, what factors affect the nanoparticle-protein interaction and the current methods for characterizing the interaction are also introduced here. Finally, I provide a brief introduction on how does the presence of protein corona influence the cellular responses to nanoparticles.

Chapter Index

	pag.
CHAPTER SUMMARY	1
1.1 NANOSCIENCE AND NANOMEDICINE: GENERAL CONCEPTS	3
1.2 SYNTHESIS OF IRON OXIDE NANOPARTICLES	4
1.3 MAGNETISM: GENERAL CONCEPTS	10
1.4 APPLICATIONS OF IRON OXIDE NANOPARTICLES IN BIOMEDICINE	13
1.5 SYNTHESIS AND BIOMEDICAL APPLICATIONS OF Au NANOCRYSTALS	15
1.6 PROTEIN-NANOPARTICLE INTERACTION	17
1.6.1 DIFFERENT EFFECTS ON THE PROTEIN-NANOPARTICLE INTERACTION	18
1.6.2 STRUCTURE CHANGE OF PROTEIN UPON INTERACTION WITH NANOPARTICLES	22
1.6.3 APPROACHES FOR STUDYING NANOPARTICLE-PROTEIN INTERACTION	23
1.6.4 EFFECTS OF PROTEIN CORONA ON BIOLOGICAL RESPONSE	25
1.7 CHAPTER REFERENCES	28

1.1 NANOSCIENCE AND NANOMEDICINE: GENERAL CONCEPTS

Nanoscience is the study of structures and materials at the nanometer scale. Fig. 1 displays some materials and biological entities at the nanoscale. What makes nanoscience so attractive is the fact that materials at the nanoscale display distinctive properties compared to those of the bulk. In particular, the high surface to volume ratio of the nanomaterials can be a fundamental characteristic in many applications such as in drug delivery or catalysis among many others¹. Moreover, nanomaterials display some unique physical properties that the bulk materials do not have. For instance, owing to quantum-mechanics, nanoparticles with size ranging from 1 nm to 10 nm can display characteristic electronic structures, which greatly depends on their size and shape². In particular, due to quantum effects, Au nanoparticles present a characteristic surface plasmon resonance band that can be observed near 530 nm where the size is in the range of 5-20 nm³. Another example is the quantum dots (a type of semiconductor nanocrystals), the electronic properties of which are reported to be intermediate between those of bulk semiconductors and molecular compounds⁴. The band gap in quantum dots, which determines the frequency range of emitted light, is inversely related to its size, making them widely used as fluorescent dyes⁵. Nowadays, nanoscience is extensively presented in many aspects of our daily life¹, one of the most interesting field of applications of nanoscience-based products is in medicine, so much so that the term "nanomedicine" has been coined.

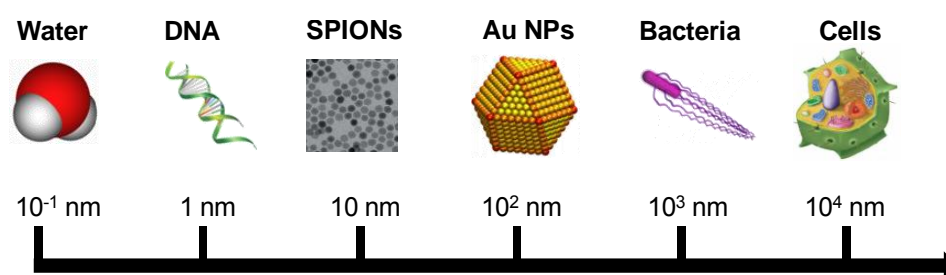


Figure 1. Schematic illustration of material with nanoscale size in the range of 0.1 nm to 10 μ m.

The first use of the term nanomedicine can be traced back to the late 1990s, since then a significant increase in research activity could be witnessed over the past decades. Nanomedicine has been defined as "The application of nanoscience in treatment, diagnosis, monitoring and control of biological systems"⁶. According to this definition, nanomedicine is in fact a large subject covering from *in vivo* imaging, tissue regeneration, drug delivery and therapy to *in vitro* diagnostics⁷. The nanomaterials used for nanomedicine purposes can be inorganic nanoparticles (i.e., iron oxide nanoparticles, gold nanoparticles and semiconductor nanocrystals), polymer nanoparticles and natural nanoparticles (viruses or lipoproteins)⁸. Among the different nanomedical applications, nanoparticle-based drug delivery is one of the most successful examples⁹. For instance, a liposomal formulation of doxorubicin (branded Doxil, a cytotoxic drug used for cancer chemotherapy) was approved by the US Food and Drug Administration (FDA) in 1995 for the treatment of Kaposi's sarcoma and other types of cancer¹⁰. Since then, other types of nanoparticle-based drugs have been also approved for cancer therapy, like liposomal

daunorubicin (DaunoXome, Gilead Sciences) and albumin-bound paclitaxel (Abraxane, Abraxis BioScience)¹¹. Besides drug delivery, nanoparticles have been also used for imaging. Superparamagnetic iron oxide nanoparticles (SPIONs) were also approved for magnetic resonance imaging in the 1990s by the FDA¹². Although nanomedicine is still in its infancy, it displays big promise in the management of cell and tissue screening, diagnostic and therapeutic applications^{13,14}. To achieve these applications, more biocompatible and efficient nanomaterials need to be designed and optimized, since the future of nanomedicine will greatly depend on the judicious and rational design of nanomaterials, as well as the tools and methodologies for the thorough understanding of the interaction of nanomaterials with biological entities¹⁵.

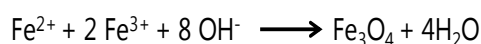
Since the main scope of my thesis is engineering bio-applicable SPIONs, Au nanoparticles and Au-SPIONs hybrid nanocomposites. Therefore, in the following parts I will briefly introduce the state of the art in the synthesis and biological applications of SPIONs and Au nanoparticles, and some basic concepts about magnetism.

1.2 SYNTHESIS OF IRON OXIDE NANOPARTICLES

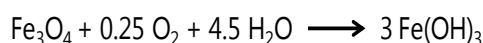
In the last decades, many methods have been developed to synthesize iron oxide nanoparticles. The most commonly used methods are co-precipitation, microemulsion, thermal decomposition, hydrothermal synthesis and microwave-assisted synthesis. I will briefly introduce each method and mention their advantages and disadvantages, and list some representative examples of each synthetic method.

Co-PRECIPIATION

Co-precipitation is a fast method for fabricating iron oxide nanoparticles in aqueous solutions. Co-precipitation of aqueous Fe²⁺/Fe³⁺ salt solutions in basic condition at room temperature results in the synthesis of iron oxide nanoparticles. In particular, when the molar ratio of Fe²⁺/Fe³⁺ is fixed at 1:2, magnetite (Fe₃O₄) is prepared. The reaction can be written as¹⁶:



In the co-precipitation method, through varying the salt used (e.g. chlorides, sulfates, nitrates), the molar ratio of Fe²⁺/Fe³⁺, the pH value and ionic strength of the media, iron oxide nanoparticles with different characteristics (in terms of size, shape and compositions) can be obtained^{17,18}. However, one should pay enough attention to its synthetic environment, a non-oxidizing oxygen-free environment must be ensured to avoid the oxidation of the obtained magnetite to maghemite or even to ferric hydroxide as shown by the following reaction¹⁹:



Biological applications of iron oxide nanoparticles require nanoparticles that are biocompatible, and the pH value of the dispersion should be maintained at the physiological value 7.4. However, the obtained iron oxide nanoparticles dispersion by using co-precipitation is basic. An additional adjustment step is required to change the pH to the physiological value, extra

substances are also introduced to the system which could exert complex effects on the final nanomaterial. A more obvious disadvantage of the co-precipitation method is the resulting polydispersity of the iron oxide nanoparticles obtained (Fig. 2a), which is not desirable when monodisperse nanoparticles are required.

MICROEMULSION

The definition microemulsion given by Bagwe is "a thermodynamically stable isotropic dispersion of two immiscible liquids, since the microdomain of either or both liquids has been stabilized by an interfacial film of surface-active molecules"²⁰. For water-in-oil microemulsion for example, microdroplets (typical size is 1-50 nm) are formed when water is dispersed into the oil phase and the formed microdroplets are stabilized by the surrounding surfactant in the continuous oil phase. Then the stabilized microdroplets can be used as a micro-reactor, where a soluble metal salt can enter and undergoes colliding, coalescing, breaking again and precipitating. Finally, the products can be purified by washing and centrifugation with the aid of adding adequate solvent. By using different molar ratio of water to surfactant, the size of the nanoparticles can be tuned^{21,22}. Munshi *et al.* used the Aerosol OT (AOT)/n-hexane as a reverse micelle to synthesize mono-dispersed SPIONs²³. Woo *et al.* used the oleic acid and benzyl ether as the reverse micelles to synthesize iron oxide nanorods. They showed that not only the phase of the nanorods can be controlled by varying the temperature, atmosphere and hydrous state of the gels during crystallization, but also the diameter and the length of the nanorods can be controlled by adjusting the H₂O/oleic-acid ratio in the gelation process²⁴. Despite the advantages provided by the microemulsion technique, lowering the polydispersity of the obtained nanoparticles remains a big challenge (Fig. 2b). Moreover, large amounts of solvent are needed and the yield of the products is lower compared to other methods like co-precipitation and thermal decomposition, which certainly hinder it to become an efficient method for large scale synthesis of iron oxide nanoparticles²⁵.

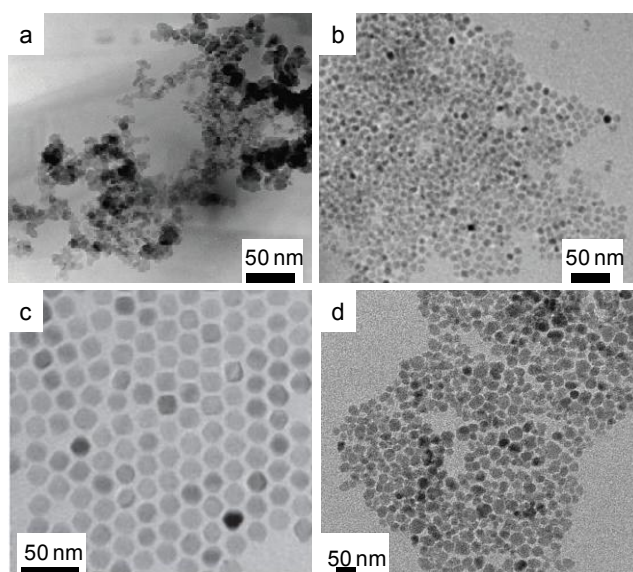


Figure 2. TEM images of SPIONs synthesized using a) co-precipitation, b) microemulsions, c) thermal decomposition and d) microwave assisted method^{26,27}.

THERMAL DECOMPOSITION

Highly monodisperse iron oxide nanoparticles with small size can be synthesized by high-temperature decomposition of an iron precursor in the high-boiling organic solvents in the presence of stabilizers (Fig. 2c). The iron precursors include iron-oleate²⁸, iron fatty acid salts²⁹, iron (III) acetylacetonate³⁰, iron pentacarbonyl³¹, iron choline citrate³², iron carbonate³³ and iron carboxylate³⁴. While the most commonly used high boiling point organic solvents are 1-octadecene³⁵ and 1, 2 hexadecanediol³⁶. Oleic acid³⁰, oleylamine³⁶ and the fatty acids²⁹ are some of the stabilizers used to stabilize the synthesized iron oxide nanoparticles. Many parameters have been reported to affect the size and morphology of iron oxide nanoparticles, among which, iron precursors, solvent and stabilizer are three most important factors during the synthesis. Other factors such as the reaction time, reaction temperature are also crucial for the size and shape control.

For instance, highly disperse maghemite with a size about 13 nm were fabricated by thermal decomposition of iron pentacarbonyl in a mixture of octyl ether and oleic acid at 100 °C, with the aid of adding trimethylamine oxide (CH₃)₃NO as a mild oxidant³⁷. Park *et al.* also showed thermal decomposition of a solution of iron oleate complex could result in highly disperse iron oxide nanoparticles with a size about 12 nm²⁸. By thermal decomposition of metal fatty acid salts in octadecene in the presence of their corresponding fatty acids, monodispersed iron oxide nanoparticles with a controllable size (3-50 nm) and different shapes (dots and cubes) can be synthesized²⁹.

Because the thermal decomposition is normally conducted in organic phases, the produced iron oxide nanoparticles are hydrophobic in nature. Therefore, a post-synthetic step to convert their surface nature to be hydrophilic is necessary for their biological related applications. A commonly used method to change the hydrophobic surface (steric surfactant) to hydrophilic surface (electronic surfactant) is to agitate the hydrophobic iron oxide nanoparticles with an aqueous solution in the presence of the hydrophilic stabilizer. Though mixing and agitating the obtained nanoparticles with an aqueous solution in the presence of the hydrophilic stabilizer, the hydrophobic surface of iron oxide nanoparticles is then replaced by the hydrophilic stabilizer and the resulted iron oxide nanoparticles can be exchanged from the organic phase to the aqueous solution.

Recently, many efforts have been made directing one pot synthesis of water soluble iron oxide nanoparticles by thermal decomposition. Hu *et al.* showed that thermal decomposition of FeCl₃·6H₂O in organic phase of 2-pyrrolidone in the presence of the stabilizer of α, ω -dicarboxyl-terminated poly(ethylene glycol) resulted in the synthesis of water soluble iron oxide nanoparticles³⁸. The synthesis method proposed by Hu *et al.* significantly simplify the synthetic process for fabricating hydrophilic iron oxide nanoparticles.

MICROWAVE ASSISTED SYNTHESIS

This synthesis method is described with more detail because it is the synthetic route we have used to fabricate the nanomaterials described in this thesis.

GENERAL PRINCIPLES OF MICROWAVE CHEMISTRY

Inspired by the pioneering work on the microwave-assisted organic synthesis³⁹, the use of microwave heating in synthesizing inorganic nanoparticles has gained considerable attraction in the past few decades. Compared to conventional heating, microwave heating exhibits many advantages in reducing reaction time, increasing product yields and enhancing nanoparticles properties^{40,41}. Conventional heating, like isomantles, oil baths and hot plates, strongly depends on the convective currents and the thermal conductivity of the solvents in the reaction system, featured in low and inefficient energy transformation to the reaction. In most cases, the temperature of the reaction vessel was observed higher than that of the reaction solution which can result in high polydispersity of the synthesized nanoparticles. In contrast, due to the uniform heating in the whole reaction solvent, microwave heating leads to the synthesis of nanoparticles with narrow size distributions.

In general, microwave heating is based on the efficient heating of a polarizable molecules or ionic solvent. Two mechanisms are responsible for the heat producing processes, namely dipolar polarization and ionic conduction. Dipolar polarization refer to reaction occur in polar solvent, while ionic conduction refer to reactions in ionic solvents. Due to the oscillating field produced by the electromagnetic radiation, the dipoles or ions realign themselves along with the continuous changed electric field, as illustrated in Fig. 3. During the realignment process, heat is produced through molecular friction and dielectric loss⁴², and the amount of heat produced depend on the time scale of the molecules to re-align themselves under the given radiation frequency. No heat could be envisaged if the dipoles realigned too slow (high-frequency irradiation) or too fast (low-frequency irradiation). In the case of ionic conduction, the charged nanoparticles oscillate back and forth in the electric filed, leading to interparticle collision and resulting in heat production. Generally, ionic conduction effect produces heat more efficiently than dipolar polarization effect, in particular for the synthesis in ionic liquids⁴³.

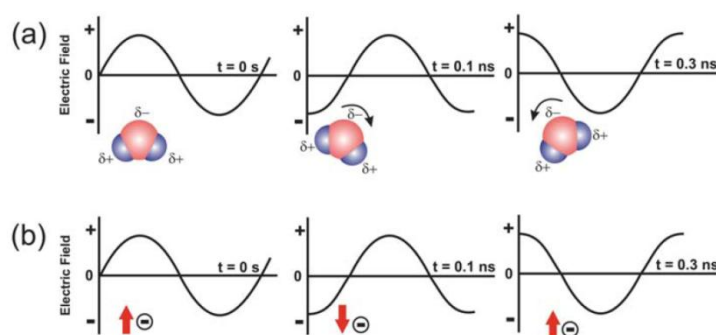


Figure 3. Two main heating mechanisms under microwave irradiation: (a) dipolar polarization; (b) ionic conduction mechanism³.

The efficiency of a solvent in converting electromagnetic energy into heat at given frequency and temperature is determined by its loss factor, known as the dielectric loss tangent $\tan \delta$. $\tan \delta$ is the ratio of the dielectric constant ϵ' and the dielectric loss ϵ'' . ϵ' indicates the ability of a solvent to be polarized in the electric field and ϵ'' is the efficiency of a solvent converting electromagnetic energy to heat⁴⁴. Therefore, for microwave synthesis, a relative high $\tan \delta$ of the solvent is essential. Based on the $\tan \delta$ value, solvents for microwave synthesis can be classified as high- ($\tan \delta > 0.5$), medium- ($\tan \delta \sim 0.1 - 0.5$) and low-adsorbing ($\tan \delta < 0.1$). Table 1. gives some $\tan \delta$ value of solvents for microwave synthesis. From table 1, we can see that benzyl alcohol is a strong microwave adsorbing solvent, which is being widely used in the synthesis of inorganic nanoparticles^{40,45}.

Table 1. Loss tangent ($\tan \delta$) values for different solvents⁴⁶

Solvent	$\tan \delta$
Ethylene glycol	1.35
Ethanol	0.941
2-propanol	0.799
Benzyl alcohol	0.667
Methanol	0.659
1,2-dichlorobenzene	0.28
Water	0.161
Acetone	0.054
Toluene	0.04

MICROWAVE SYNTHETIC MECHANISM OF SPIONS

The mechanism of the formation of SPIONS in benzyl alcohol by microwave heating was proposed by Niederberger and Garnweitner, which is schematically shown in Fig. 4. Formation of SPIONS in benzyl alcohol involves the solvolysis of the acetylacetonate and the subsequent condensation reactions⁴⁷. The proposed mechanism provides useful information for one to control the nucleation and growth of SPIONS during microwave synthesis process.

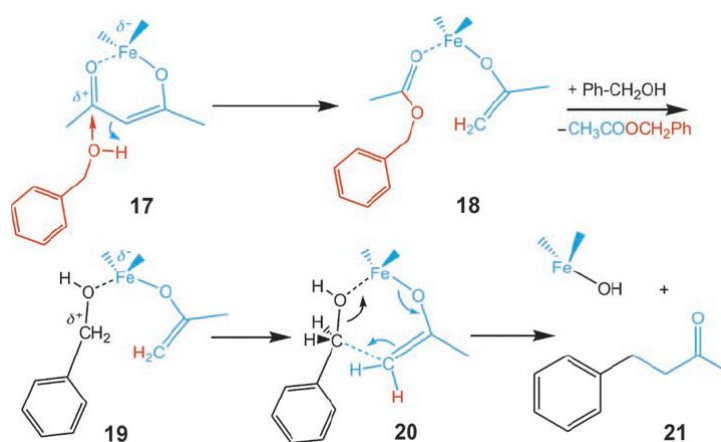


Figure 4. Schematic illustration of the formation of SPIONS in benzyl alcohol under microwave heating⁴⁷.

ADVANTAGES OF MICROWAVE SYNTHESIS

Nowadays, dedicated microwave equipments for chemical laboratory uses can be found which allow precise control of experimental parameters such as the irradiation power, reaction temperature and the pressure and significantly improving the reproducibility of the reaction. Due to the fast heating, microwave assisted synthesis can also improve the yield of nanoparticles. Our previous results show that microwave heating of $\text{Fe}(\text{acac})_3$ in benzyl alcohol for 15 min resulting 6 nm SPIONs, with a yield of about 80%⁴⁰. Moreover, due to the dielectric volumetric heating, the reaction solvent can be heated rapidly and homogeneously (Fig. 2d), making the control over nucleation and growth possible⁴⁸. Therefore, microwave heating provides an ideal way for size and shape control of nanoparticles. Pascu *et al.* revealed that increasing microwave irradiation time and temperature, SPIONs with larger sizes can be produced⁴⁹. By microwave heating of FeCl_3 in water at 220 °C, Li and Wei showed that by adjusting water pH and iron concentration, Fe_2O_3 with different sizes and shapes can be synthesized. In particular, with the addition of phosphate ions, ellipsoidal Fe_2O_3 were produced. By adjusting the initial Fe^{3+} to PO_4^{3-} molar ratio, ellipsoidal Fe_2O_3 with tunable aspect ratio in the range of 1.1 to 6.3 could be engineered (Fig. 5a-f)⁵⁰. Due to the "hot spots" produced during the microwave heating process, Fe_2O_3 nanorings have been also produced (Fig. 5g-h). Replacing the precursor of FeCl_3 with $\text{K}_4[\text{Fe}(\text{CN})_6]$, flower-like Fe_2O_3 nanostructures were reported (Fig. 5i)⁵¹.

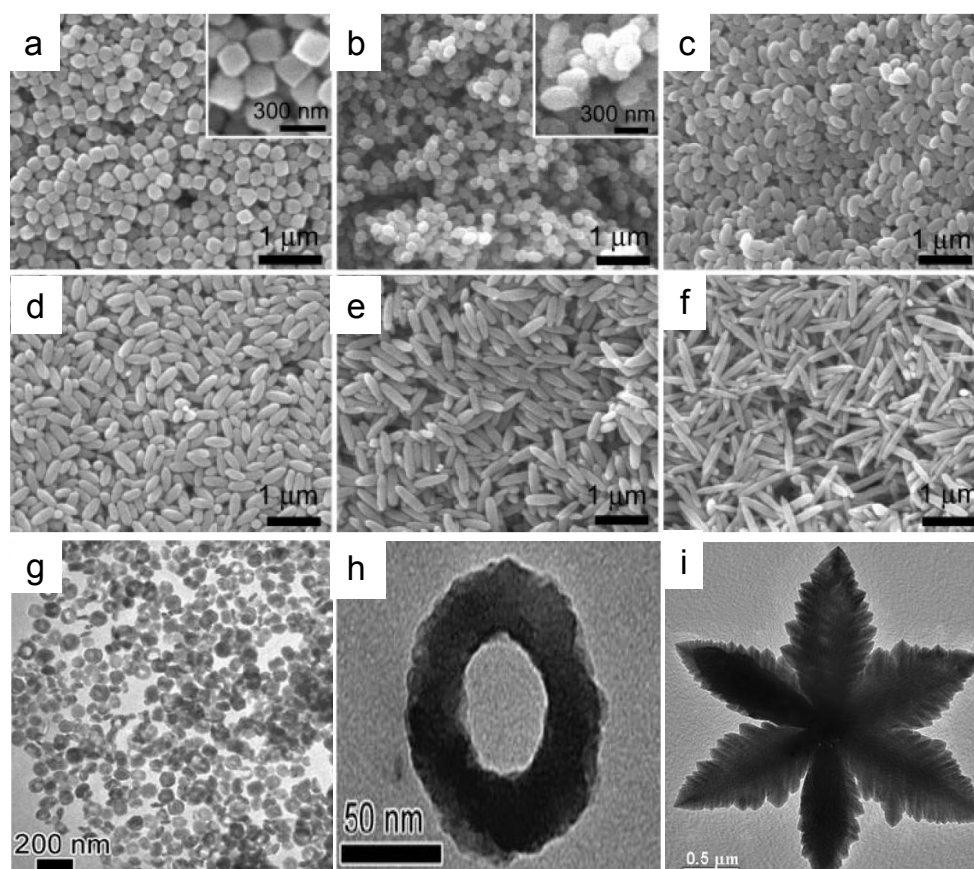


Figure 5. a-f) ellipsoidal Fe_2O_3 with different aspect ratios⁵⁰, g-h) Fe_2O_3 nanorings⁵⁰, i) Flower like Fe_2O_3 nanostructures⁵¹.

DRAWBACKS OF MICROWAVE SYNTHESIS

In addition to those advantages, microwave heating also have some drawbacks. One of the most obvious is the short penetration depth of microwave irradiation, which limits the volume of the microwave reactors, causing problems for large scale synthesis of nanoparticles. Moreover, size control of nanoparticles still shows some limitations, though several works reported that size of nanoparticles can be tuned to some extent⁵². Single iron oxide nanoparticle with size larger than 10 nm synthesized by microwave assisted method have not been reported yet. Moreover, the dedicated microwave reactor is much more expensive than the normal heating plate, which also impedes its broader uses.

1.3 MAGNETISM: GENERAL CONCEPTS

MAGNETISM IN BULK

Magnetism is the unique property of magnetic materials, which is the sum of the magnetic moments of their atoms. Magnetization (M) is the magnetic moment (m) per unit volume, defined as $M = \frac{m}{V}$ (emu/cm³). When a material is exposed to a magnetic field, magnetic induction is produced. Depending on the nature of the material, the magnetic response is different. In general, materials can be classified into diamagnetic, paramagnetic, antiferromagnetic, ferrimagnetic and ferromagnetic.

Diamagnetism: Materials that tend to exclude the external magnetic field are defined as diamagnet, because the induced magnetic moments in those materials are opposite to the applied field. **Paramagnetism:** the magnetic dipole moments of the paramagnet are randomly oriented as shown in Fig. 6a. When an external magnetic field is applied to those materials, only a small fraction of the atomic moments aligns to the field direction. The magnetization of paramagnetic materials as a function of magnetic field is illustrated in Fig. 7a. **Antiferromagnetism:** the response of the antiferromagnetic materials to the external fields at a given temperature is similar to that of paramagnetic materials (Fig. 7a), although the magnetic ordering of moments is completely different. Because those moments are antiparallel to each other with the same absolute value (Fig. 6b), resulting in nearly zero magnetization. **Ferrimagnetism:** ferrimagnets are also recognized as antiferromagnets, but in this case not all the magnetic moments have the same absolute value and a net magnetization resulted (Fig. 6c). **Ferromagnetism:** under the applied magnetic field, all the domains tend to orient parallelly in the same directions, leading to their strong magnetic properties (Fig 6d).

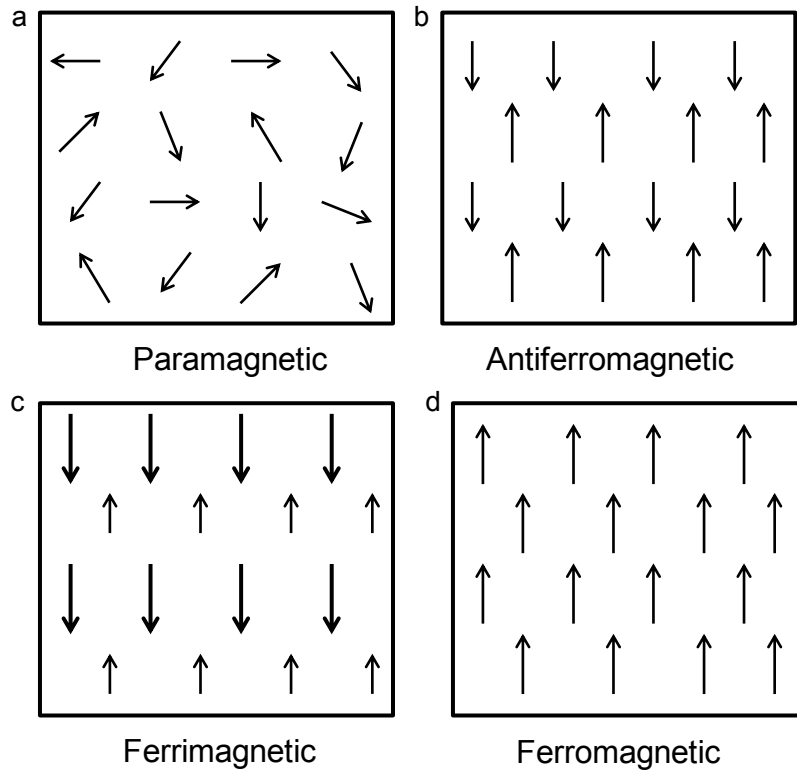


Figure 6. Ordering of magnetic moments in different types of magnetic materials. Graphs are adapted from from Spaldin's book⁵³.

For a magnetic material, the magnetization is not the only parameter determining its magnetic properties, how effectively the material responds to the applied field is also of great importance, which is termed as the susceptibility of the material. Susceptibility is defined as the ratio of M to H following the equation:

$$\chi = \frac{M}{H} \frac{\text{emu}}{\text{g} \cdot \text{Oe}}$$

When plotting M against H , magnetization curves are obtained. Different types of magnetic materials display characteristic magnetization curves, which are schematically shown in Fig. 7. For a diamagnetic material, because applied field results in the production of opposite moment, with its negative susceptibility $\chi < 0$, falling in the range of 10^{-5} to 10^{-6} . For both paramagnetic and antiferromagnetic materials, χ is small and positive, ranging from 10^{-3} to 10^{-5} at room temperature. The observed small χ indicates that to induce some magnetic moments, rather large applied fields are needed. When the applied field is removed, the induced magnetization disappears. In contrast, a large and positive χ is found for both ferrimagnetic and ferromagnetic materials. Applying a small field can induce large magnetization for both materials. To a certain field, a saturation magnetization is obtained, further increasing the field doesn't lead to the increase in the magnetization. Moreover, the applied field is decreased to zero, the magnetization does not reduce to zero and a remanent magnetization (M_r) is still be detected. This phenomenon is defined as hysteresis.

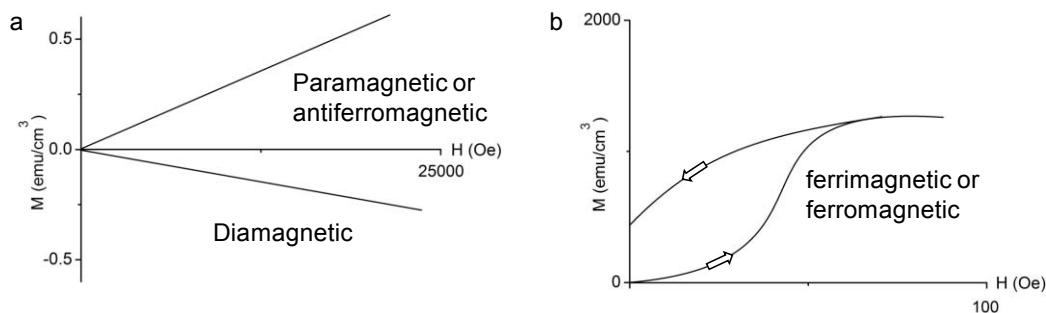


Figure 7. Schematic magnetization curves for different types of magnetic materials. a) Characteristic magnetization curves for diamagnetic, paramagnetic. Graphs are adapted from Spaldin's book⁵³.

MAGNETISM IN NANOSCALE: SUPERPARAMAGNETISM AND BLOCKING TEMPERATURE

One of the most interesting magnetic phenomena for nanoparticles is the "superparamagnetism", which appears, at a given temperature, when the nanoparticles have a small enough size. Magnetic materials consist of regions with uniform magnetic moments separated by the domain walls. The formation of a domain wall is determined by the balance between the magnetostatic energy and the domain-wall energy²⁵. There is a critical size below which a single-domain is formed in each nanoparticle. For those single domain nanoparticles as the size is further reduced, their magnetocrystalline energy becomes comparable to its thermal energy, the balance between which determines its final magnetic property. In particular, when the thermal energy overcomes the magnetocrystalline energy, the magnetization of the single-domain nanoparticle can be reversed from one easy direction to the other spontaneously, even in the absence of an applied field. As a result, no hysteresis can be observed in the magnetization curves, as it was shown in Fig. 8a. Since thermal energy relates to the temperature, hence the temperature plays an important role in determining the superparamagnetic state of a single-domain nanoparticle. The temperature above which the nanoparticles are in the superparamagnetic state is defined as blocking temperature, T_B , which can be determined by the maximum of the zero-field-cooled curve. Fig. 8b shows a typical ZFC/FC curve of a superparamagnetic nanoparticle. As can be seen, below T_B , magnetization increased gradually with the increase in temperature until reaching a maximum point. However, above T_B , thermal energy is strong enough to randomize the magnetic moments leading to a decrease in magnetization.

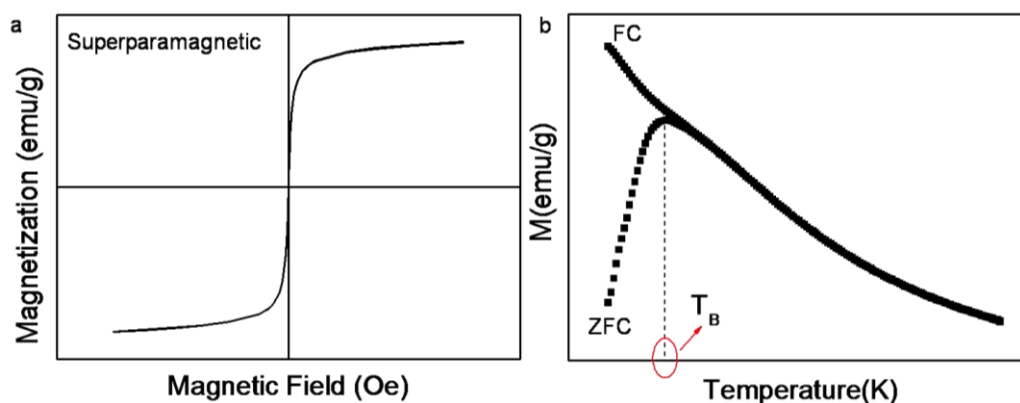


Figure 8. a) Magnetization curve of superparamagnetic material measured at 300k upto 6 Tesla, b) ZFC/FC curves of a material measured at a magnetic field of 50 Oe from 10 k to 300k.

1.4 APPLICATIONS OF IRON OXIDE NANOPARTICLES IN BIOMEDICINE

Due to their unique magnetic property, iron oxide nanoparticles have been widely used in many applications such as catalysis²⁵, data storage⁵⁴, environmental remediation⁵⁵ and biomedicine⁵⁶. Because the aim of the thesis is engineering nanomaterials for safe biological applications, in this section, we only introduce some biomedical applications of iron oxide nanoparticles. As mentioned, key magnetic properties of iron oxide nanoparticles are classified specifically to: saturation magnetization (M_s), coercivity (H_c), blocking temperature (T_B) and relaxation time (τ_N and τ_B , representing Neel and Brown relaxation time, respectively). Depending on which magnetic property is explored, iron oxide nanoparticles can find applications in magnetic resonance imaging (MRI)⁵⁷, drug and gene delivery⁵⁸, hyperthermia⁵⁹ or bioseparation⁶⁰.

MAGNETIC RESONANCE IMAGING (MRI)

In magnetic resonance imaging, exogenous nanoprobe are used to modify the relaxation times of water protons to provide better visualization of the diagnostic area. Because they produced hypointense signals in T_2 and T_2^* -weighted images, SPIONs often work as T_2 negative contrast agents to shorten the T_2 relaxation of protons by generating magnetic field gradients⁶¹. Targeted MRI applications is one of the most promising applications of SPIONs, to realize this, the surface of the SPIONs requires to be functionalized by antibodies or other biomolecules, so they can be directed to several types of receptors⁶². Targeted MRI is also named as magnetic resonance (MR) molecular imaging. An example for MR molecular imaging was reported by Montet *et al.*, in which iron oxide nanoparticels surface were functionalized with bombesin peptides (BN-CLIO-NPs) for targeting bombesin receptors present in the mouse pancreas. The presence of the BN-CLIO-NPs decreased the T_2 of normal tissues, hence better visualization of tumor was obtained by MRI, realizing the efficient imaging of pancreatic ductal adenocarcinoma (PDAC)⁶³. Specific cell labeling and tracking is another successful MRI applications of SPIONs. Due to the high contrast generated by SPIONs, performance and activity of living cells can be monitored *in vivo* for a long time. Recent focus of MRI cell tracking is on stem cells. Carenza *et al.* showed that endothelial progenitor cells (EPCs) can be labeled with SPIONs, the magnetized

cells can be visualized by MRI T₂-weighted images (Fig. 9a). Moreover, enhanced angiogenic performance in terms of increased migration and paracrine secretion of growth factors have been observed after EPCs cells magnetized with SPIONs. The reported approach represents a safe and effective strategy for precise cell guidance into specific brain areas⁶⁴.

DRUG AND GENE DELIVERY

Because the surface of SPIONs can be easily functionalized, SPIONs are now being extensively explored as nanocarriers for drug and gene delivery for therapy. Among those drugs, doxorubicin (DOX) and camptothecin (CPT) are most widely used as potential anti-tumor agents^{65,66}. Recent research show that after DOX and CPT coupling with SPIONs, their inhibition activity have been enhanced comparing to non-encapsulated drugs (Fig. 9b)^{67,68}. This is because SPIONs displayed high water dispersity, which increased the solubility of the hydrophobic loaded drugs. Polyethyleneimine (PEI) and chitosan functionalized SPIONs are two of the most used SPIONs for gene delivery due to their low immunogenicity⁶⁹. However, both stabilizers have obvious drawbacks, PEI has good transfection efficiency but is not biodegradable, while chitosan displays good biodegradability and biocompatibility but with low transfection efficiency. Recent work performed by Wang *et al.* integrated both stabilizers to SPIONs for delivering nucleic acid based therapeutic agents, improving the biodegradability and transfection efficiency⁷⁰.

HYPERTHERMIA

Hyperthermia is defined as "raising the temperature of the local environment of a tumor resulting in changing the physiology of diseased cells finally leading to apoptosis"⁷¹. SPIONs internalized by the tumor cells can adsorb magnetic energy and convert it to thermal energy increasing the temperature and generating the apoptosis of the cells. Generally, surface of SPIONs are functionalized by cancer-specific binding agents for targeting cancer cells. Hence, ideally only the cancer cells will be subjected to the therapeutic heat produced by the targeted SPIONs, while the normal cells will not be affected, increasing the effectiveness of hyperthermia⁷². Moreover, SPIONs show the possibility to cross the blood-brain barrier (BBB) effectively and could be used for treating brain tumors⁷³. At the beginning, hyperthermia only related to the treatment of cancer cells induced by heat. However, very recent studies on hyperthermia have combined the conception of drug delivery as a multifunctional approach for more efficiently treating a number of diseases, known as hyperthermia-based controlled drug delivery. Derfus *et al.* conjugated a 30 bp DNA to dextran-coated iron oxide nanoparticles and linked them with the fluorescent 12, 18 and 24 bp DNA. The conjugates were then trapped in a matrigel as an in vitro model of tumor tissue. Upon using a radiofrequency electromagnetic field (EMF), the fluorescent 12, 18 and 24 bp DNA was released into the surrounding tissue (Fig. 9c)⁷⁴.

BIOSEPARATION

Another important application of SPIONs is for *in vitro* protein or cell separation. In comparison with other separation techniques, magnetic separation shows many advantages. SPIONs can be easily attracted by an external magnetic field and redisperse in media immediately after removal of the magnet⁷⁵. Thus, magnetic separation process can be facile and fast, with all the steps accomplished in one test tube avoiding the use of expensive liquid chromatography systems²⁵. By introducing dopamine (DA) and nitrilotriacetic acid (NTA) to the magnetic surface, Xu's group obtained a Nanoparticle-DA-NTA complex for separating histidine-tagged protein with high specificity, the complex also displayed high stability to heating and high salt concentrations⁷⁶. The same group recently synthesized D-tyrosine phosphate functionalized magnetic nanoparticles (MNP-pY) for selective cancer cell separation from mixed population of cells (Fig. 9d)⁷⁷. The selective separation based on a specific enzymatic reaction, catalytic dephosphorylation, for transforming MNP-pY to MNP-Y (tyrosine coated magnetic nanoparticles). Upon enzymatic transformation, MNP-Ys adhered selectively on the surface of cancer cells, which facilitated the separation of cancer cells from normal cells.

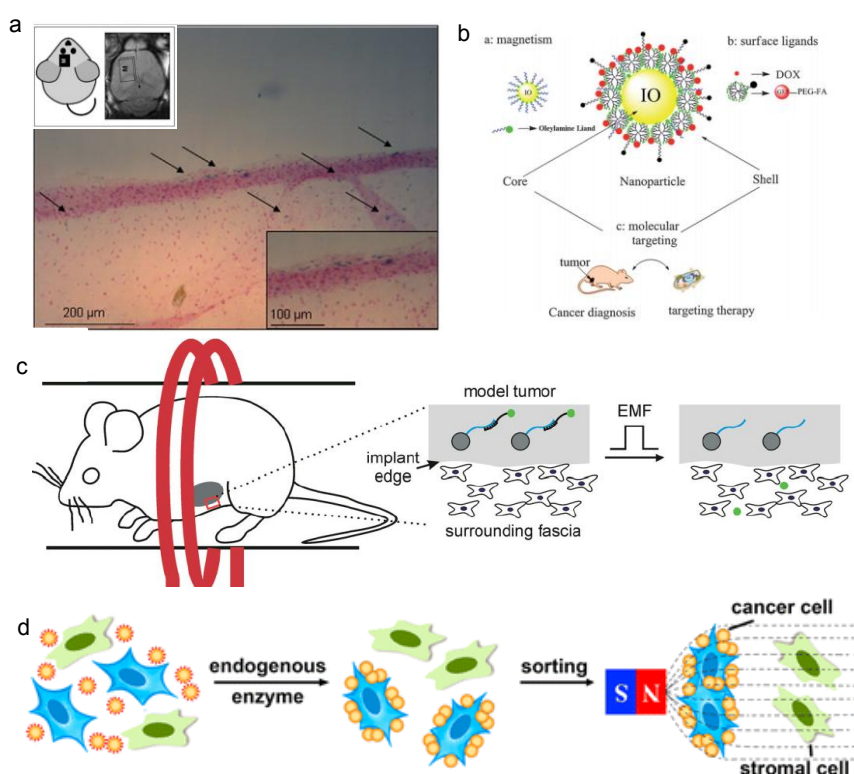


Figure 9. a) SPIONs for cell tracking. The inserts show by putting an external magnet on a mouse brain, Prussian Blue staining identified magnetized EPCs in the brain cortex⁶⁴. b) DOX-conjugated SPIONs for targeting therapy⁶⁵. c) Application of electromagnetic field to implants containing 18 bp tethers resulted in release of model drugs and penetration far into surrounding tissue⁷⁴. d) Enzymatic transformation of magnetic nanoparticles for selectively sorting cancer cells⁷⁷.

1.5 SYNTHESIS AND BIOMEDICAL APPLICATIONS OF Au NANOCRYSTALS

Among the methods used for synthesis of Au nanoparticles, citrate reduction of HAuCl₄ in water to metallic gold, which was first reported by Turkevitch in 1951, is the most widely applied

method to produce Au nanoparticles⁷⁸. The size of the Au nanoparticles obtained by this method is around 20 nm. In 1973, the Turkevitch's method was further improved by Frens to tune the size of Au nanoparticles from 16 nm to 147 nm, through varying the ratio of trisodium citrate to gold precursor⁷⁹. Very recently, Puntès's group further refined the method extending the size of Au nanoparticles to about 200 nm, by performing a kinetically controlled seed-growth⁸⁰. The Au nanoparticles prepared by this method are water soluble and biocompatible due to the citrate coating on their surface and can be readily used for biomedical purposes. Moreover, citrate only loosely attaches to Au nanoparticles surface, which can be easily exchanged by thiolated molecules for further bio-functionalization. Besides Turkevitch's method, Brust-Schiffrin method represents another classical way for fabricating Au nanoparticles⁸¹. In this method, HAuCl₄ are transferred from water to toluene using the phase-transfer reagent of tetraoctylammonium and then reduced to Au nanoparticles in the presence of dodecanethiol. The resulted Au nanoparticles display a size range from 1 nm to 5 nm, with high solubility and stability in non-polar solvents. However, before their safe use in biomedical applications, surface exchange by hydrophilic stabilizers is generally required. For more synthetic approaches for fabricating Au nanoparticles one can refer to Astruc's review³.

Those methods mentioned above exclusively lead to the synthesis of spherical Au nanoparticles. The surface plasmon resonance band of spherical Au nanoparticles falls in the UV-Visible range (500 nm to 600 nm), and the band position are size dependent, which renders the colorimetric property of Au dispersions. The unique plasmonic property of spherical Au nanoparticles makes them widely used in biomedical fields like diagnostics, therapy and imaging. One significant application of Au nanoparticles in diagnostic is the fabrication of sensors for detecting molecules such as gases, ions, proteins and DNA⁸². In a recent study, You *et al.* constructed a Au based fluorescent sensor which was able to identify 52 unknown protein samples with an accuracy of 94.2%⁸². By using oligonucleotide functionalized Au nanoparticles, Conde *et al.* reported the quantification of mutation expression in mRNA of the cancer cells through a easy colorimetric detection⁸³. Due to its high biocompatibility, low cytotoxicity and easy surface functionalization, Au nanoparticles can be used to deliver drug to the disease organelle for therapy. Generally, the surface of the Au nanoparticles is first functionalized by the thiolated ligands because gold surfaces can easily react with thiol (SH) groups forming very strong and stable Au-S bonds³. Then the drug molecules or other therapeutic cargos can be loaded to the Au surfaces through interacting with the thiolated ligand⁸⁴. To realize more accurate drug delivery, targeting ligands are also introduced to Au nanoparticles surface. A complex Au nanoparticles platform composed biotin, anticancer drug paclitaxel and Rhodamine B was constructed by Heo *et al.*, for targeted drug delivery⁸⁵. Biotin was used as targeting ligand to bind with the biotin receptor on cancer cells and Rhodamine B was used to visualize the nanoparticles inside the cells. Au applications in biomedical imaging applications can be sub-classified to X-ray based imaging, fluorescence imaging, surface enhanced Raman spectroscopy

imaging, photoacoustic imaging and optical imaging, depending on which physical property of Au nanoparticles is used⁸⁶.

It is noteworthy that fluorescence imaging and surface enhanced Raman spectroscopy imaging are based on the plasmonic property of Au nanoparticles. In the fluorescence imaging application, the ideal Au nanostructures are those display surface plasmon resonance band in the near-infrared region (NIR), because tissues adsorb weakly in this region, which can enhance the penetration of light to tissues⁸⁷. In Raman spectroscopy imaging, Au nanostructures with sharp edges (like Au triangles and stars) can induce stronger electromagnetic field to enhance the signals of the Raman spectra of the Raman active species bound to the Au nanostructures. Also, surface plasmon resonance band of those Au nanostructures are shifted to the NIR, which avoids adsorption of excitation light by biological samples and limiting the interference for the SERS signals⁸⁸. Based on this, anisotropic Au nanoparticles are also largely demanded for more efficient biomedical uses. In Chapter 3, the synthesis and applications of anisotropic Au nanoparticles is introduced with more details.

1.6 PROTEIN-NANOPARTICLE INTERACTION

In this section, concepts on protein-nanoparticle interaction are reviewed. A large majority of nanomaterials developed for nanomedicine are exposed to biological entities. Hence investigations on the interaction of nanomaterials with different biological entities are necessary. Bio-fluids are most likely the first biological entity to which nanoparticles will be exposed, resulting the adsorption of different types of biomolecules on nanoparticles surfaces. In particular, proteins leads to the formation of what has been defined as protein-corona (Fig. 10a). Studies related to all aspects of the protein corona on nanoparticles surfaces have become a topic of interest in the quest to better understanding of the nano-bio-interfaces. As it has been revealed by many research, structure of the protein corona formed on nanoparticles surface consists of two parts; hard protein corona and soft protein corona. According to the definition provided by the Dawson's group, hard protein corona is the proteins adsorb on nanoparticles surface firmly and irreversible at some certain time, while those loosely bound and exchange rapidly with the surrounding proteins are known as the soft protein corona⁸⁹. Protein corona on nanoparticles modifies the original surface chemistry of nanoparticles, providing a new biological identity to nanoparticles (Fig. 10b). The way proteins adsorb to nanoparticles surface as well as the structure and functionality of the bound proteins are crucial in determining the final fate of nanoparticles in the biological environments.

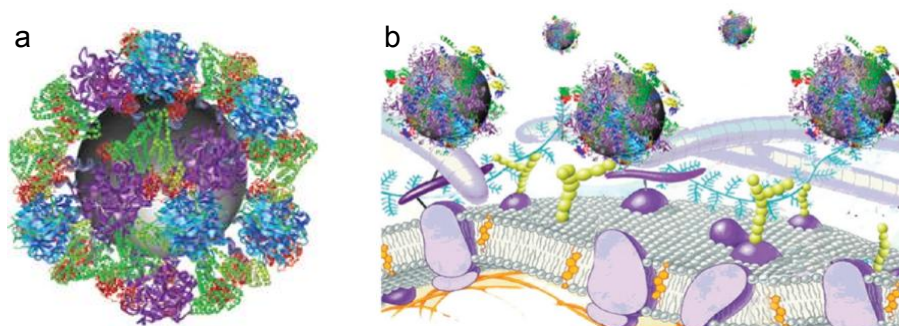


Figure 10. Schematic illustration of nanomaterial-protein corona complex (a) at the bionanointerface at the cellular level (b)^{89,90}.

1.6.1 DIFFERENT EFFECTS ON THE PROTEIN-NANOPARTICLE INTERACTION

Protein adsorption on nanoparticles is a dynamic and multifactorial process, which not only depends on the physicochemical properties of the nanoparticles (surface coating, size, shape and surface charge), but also on the nature of the adsorbed proteins (binding affinity) as well as the nature of the surrounding environment (i.e. cell medium).

EFFECT OF SURFACE COATING

The influence of the surface coating of nanoparticles and their interaction with proteins are subject of intense research. For instance, in one work of Wiogo *et al.*,⁹¹ four commonly used polymers, linear polymethacrylic acid (20kDa), linear and branched polyethylenimine (25kDa), and branched oligoethylenimine (800kDa), were chosen to functionalize magnetite nanoparticles (MNPs). The adsorption capacity of bovine serum albumin (BSA) and fetal bovine albumin (FBS) of those four functionalized MNPs determined by 1-D gel electrophoresis and protein adsorption measurements varied significantly depending on the surface coating. Branched polyethylenimine functionalized MNPs displayed the highest adsorption capacity of both BSA and FBS, about 0.07 mg FBS per mg MNPs and 0.15 mg BSA per mg NPs were found on MNPs surface. In contrast, linear polymethacrylic acid showed the lowest adsorption capacity, the lightest band was found in gel electrophoresis experiments and less than 0.01 mg FBS and BSA per mg MNPs was identified on MNPs surface. Further identification of the adsorbed proteins on MNPs by Liquid Chromatograph–Mass Spectrometer/Mass Spectrometer evidenced different protein profiles of the protein corona. In all cases, albumin and hemoglobin were identified. However, apolipoprotein A-1, apolipoprotein E and complement component 4A, which were observed on linear and branched polyethylenimine functionalized MNPs, were not detected for the others. In another example, Hajdú *et al.* examined the effect of three different carboxylic coating agents, citric acid (CA), poly(acrylic acid) (PAA), and oleic acid double layer (OAOA) on shaping the interaction of superparamagnetic iron oxide nanoparticles (SPIONs) with proteins⁹². By introducing those SPIONs into plasma containing biological media, a similar behavior was observed for CA and PAA SPIONs, while OAOA displayed a different behaviour. Sodium dodecyl sulfate-polyacrylamide gel electrophoresis (SDS-PAGE) experiments showed

protein adsorbed on CA and PAA stabilized SPIONs in a stable manner, where minor changes were observed over time. However, a more dynamic adsorption process was found for OAOA SPIONs. Furthermore, by indentifying the proteins adsorbed on those three SPIONs, different protein profiles were also detected. In 55% plasma medium, complement factor proteins (like C4B-binding protein) and immunoglobulin were the major proteins of the adsorbed protein corona on CA and PAA SPIONs, while lipoproteins (Lipoprotein B100, ApoE and ApoA) consisted of the protein corona formed on OAOA SPIONs surface. Differently, in 10% plasma medium, the major protein components of protein corona observed on CA and PAA SPIONs surface were Apolipoprotein B100 and Fibronectin, while Apolipoprotein A1 was predominant in the compositions of proteins corona on OAOA SPIONs surface.

EFFECT OF SIZE

Differences in size can also shape the interaction of nanoparticles with proteins. Casals *et al.* examined the corona formation on gold nanoparticles of different sizes (4 nm, 10 nm, 13 nm, 16 nm, 24 nm and 40 nm) in complete cellular media, a size-dependent manner of protein corona formation was revealed⁹³. DLS results showed that the amount of the proteins adsorbed on 4 nm Au nanoparticles is the lowest due to their smaller size compared to others. While as expected, the 40 nm Au nanoparticles showed the highest amount of adsorbed proteins. For Au nanoparticles with size in the range of 10 to 20 nm, the speed of the formation of hard protein corona were observed to be the fastest. Tender *et al.* used label-free liquid chromatography mass spectrometry, one and two dimensional gel electrophoresis, and immunoblotting to quantitatively study the protein profile adsorbed on silica nanoparticles with size of 20 nm, 30 nm and 100 nm in human plasma⁹⁴. They observed that 37% of the total identified proteins of the protein corona were significantly affected by the different particle size, even 10 nm difference in size can induce obvious differential binding of gelsolin, clusterin or prothrombin. Smaller proteins of the plasma have the tendency to adsorb onto smaller silica nanoparticles because of their higher surface curvature compared to the largest silica nanoparticles, while larger silica nanoparticles were shown to bind more proteins. Detailed by immunoblot analysis, more lipoprotein clusterin was observed to absorb onto 8 nm silica nanoparticles, prothrombin and the actin regulatory protein gelsolin displayed preference for binding to 100 nm silica nanoparticles. A very recent work conducted by Hu *et al.* also revealed that both the compositions and the abundance of protein corona formed on nanoparticles can be greatly influenced by size differences⁹⁵. By introducing 30 nm, 200 nm and 400 nm Fe₃O₄ nanoparticles into human plasma, 117, 133 and 100 plasma proteins were identified, respectively. Despite the commonly adsorbed serum albumin, apolipoprotein A-I and platelet factor on those three nanoparticles, ceruloplasmin and serum amyloid P-component were observed to bind specifically to 30 nm Fe₃O₄ nanoparticles. While fibronectin, serotransferrin and serum paraoxonase/arylesterase1 were only found on 200 nm Fe₃O₄ nanoparticles and coagulation

factor XIII. A chain and inter-alpha (Globulin) inhibitor H2 were only observed on 400 nm Fe₃O₄ nanoparticles.

EFFECT OF SURFACE CHARGE

Surface charge is also an important factor that can influence the nanoparticle-protein interaction, in particular when the electrostatic force is dominant in the interaction. Hirsch *et al.* evaluated serum proteins adsorption on negative, neutral and positive polyvinyl alcohol (PVA) coated SPIONs, abbreviated for n-PVA-SPIONs, PVA-SPIONs and p-PVA-SPIONs, respectively⁹⁶. After 16 h of incubation, hemopexin was found on both n-PVA-SPIONs and PVA-SPIONs, while complement protein was only observed on p-PVA-SPIONs. However, in 1 h of incubation, angiotensinogen and anti-thrombin III were only detected on both p-PVA-SPIONs and PVA-SPIONs. Similar behavior happened to apolipoprotein A1, which was only observed on PVA-SPIONs after 1 h of incubation. Due to the electrostatic interaction between nanoparticles and proteins, nanoparticles with negative charges have the tendency to adsorb positively charged proteins, and *vice versa*. Based on this principle, it is easy to understand why different surface charged can result in different protein compositions of corona bound to nanoparticles surface. As it was revealed by Gessner *et al.*, proteins with an isoelectric point (pI) greater than 5.5 have the tendency to bind onto nanoparticles with acidic surfaces, while proteins with a pI less than 5.5 prefer to adsorb onto nanoparticles with basic surfaces⁹⁷. However, the principle does not necessarily mean nanoparticles with negative charges or with positive charges can only interact with positive or negative proteins. Wiogo *et al.* demonstrated that negative proteins can also adsorb onto magnetic iron oxide nanoparticles coated with negative surface, this is due to the amphiphilic character of the protein. Although the overall charge of proteins were negative, there are still some positively charged groups on the protein surfaces that can be used as binding sites to the negative surface of the nanoparticles⁹⁸. BSA, for instance, has 60 surface lysine groups which display positive charge, and those positively charged lysine groups can promote BSA binding to negative surface of nanoparticles. Interestingly, Brewer *et al.* reported that BSA displayed a preferential binding to nanoparticles with negatively charged surface⁹⁹. Different surface charge can also result in the similar protein binding behavior. By comparing the binding behavior of human serum albumin (HSA) on positively charged with negatively charged Au nanoparticles, Hühn *et al.* observed a similar adsorption behavior of HSA on both nanoparticles. A slight anti-cooperatative behavior, a monolayer of HSA corona and a similar number of HSA molecules were observed for both Au nanoparticles¹⁰⁰.

EFFECT OF PROTEIN AFFINITY

Aside from the physicochemical properties of nanoparticles, the affinity of the protein towards nanoparticles surface can also affect their interaction with nanoparticles. It has been revealed that when nanoparticles are introduced to serum containing medium, nanoparticles are first occupied by proteins which are the most abundant in serum (such as albumin and fibrinogen),

which are then subsequently displaced by proteins with higher binding affinity but with low concentration in medium. Adsorption rate of human blood proteins, fibrinogen (BFG), immunoglobulin (Ig), albumin, transferrin (Tf) and ferritin to single-wall carbon nanotubes (SWCNTs) was shown to follow the order of BFG > Ig > Tf > BSA > ferritin, which indicates BFG is the most competitive protein among those five proteins. It can be then envisaged that given the same amount of those proteins in biological medium, BFG is the first protein attaches on nanoparticles's surface, which determines the subsequent protein adsorption¹⁰¹.

EFFECT OF CELL MEDIA

Environment to which nanoparticles and proteins are exposed has also to be considered when we study the nanoparticle-protein interaction. Maiorano *et al.* incubated Au nanoparticles in two different cellular media, Dulbecco Modified Eagle's medium (DMEM) and Roswell Park Memorial Institute medium (RPMI), both were supplemented with FBS. He revealed a significant difference in proteins corona formation on Au nanoparticles surface in those two cellular media. Binding kinetics was much faster in RPMI than in DMEM. In the initial 1h of incubation in RPMI, a sharp increase in hydrodynamic diameter was observed and remained stable in the following incubation. While in RPMI, protein corona formation was much slower, the complete adsorption achieved in 50h. Moreover, the amount of proteins bound to Au nanoparticles after 48 h incubation was found to be higher in DMEM than in RPMI¹⁰².

OTHER FACTORS

Besides the factors listed above, there are also many other factors that can influence the interaction of nanoparticles with proteins. A very recent study conducted by Huang *et al.* shows that the orientation of BSA binding on nanoparticles surface can be shaped by different surface structural heterogeneity. Depending on the surface heterogeneity of Au nanoparticles, BSA can bind to Au nanoparticle surface either in a "side-on" manner or in a "end-on" manner¹⁰³. Control of the orientation of protein on nanoparticles surface can be also achieved by modifying the protein surface chemistry. Treuel *et al.* modified human serum albumin (HSA) with succinic anhydride or ethylenediamine to get carboxyl groups dominated surface (HSA_{suc}) or amino groups dominated surface (HSA_{am}) of HSA, and studied the adsorption behaviors of HSA_{suc}, HSA and HSA_{am} on dihydrolipoic acid-coated quantum dots (DHLA-QDs). The thickness of the HSA corona on DHLA-QDs was detected to be 3.3 nm, HSA_{am} corona was slightly higher, with the value of 4.6 nm. However, HSA_{suc} was observed to form a much thicker corona on DHLA-QDs, the thickness is about 8.1 nm. Difference in corona thickness indicates that protein bind onto DHLA-QDs surface in a different orientation. Moreover, the affinity of those three HSA toward DHLA-QDs was found to be distinct. Compared to unmodified HSA, 1000 times increase in affinity was found for HSA_{am}, while 3-fold decrease in binding affinity for was observed for HSA_{suc}¹⁰⁴.

1.6.2 STRUCTURE CHANGE OF PROTEIN UPON INTERACTION WITH NANOPARTICLES

The formation of protein corona on nanoparticle surface can influence the effective size, surface charge and surface chemistry of nanoparticles. However, the curved surfaces of nanoparticles can also modify the conformation and therefore the function of the adsorbed proteins. NP-induced protein structural changes can further affect the subsequent *in vivo* protein-protein interactions, cellular responses and even DNA transcription. Therefore, monitoring the structural change of proteins upon binding to nanoparticles surface is of particular importance. A research conducted by Wang *et al.* showed that 20% of α -helical content of BSA was lost when adsorbed onto nanodiamond nanoparticles¹⁰⁵. α -helical content of BSA was also reported to decrease due to the interaction with doxorubicin loaded superparamagnetic iron oxide nanoparticles, where α -helical content was observed to decrease from 68.62% to 62.76%¹⁰⁶. However, not all nanoparticles can cause the significant change in the secondary structure of protein, the extent of the change is related to the chemical component constituting the nanoparticles. Polyethyleneimine functionalized ZnO nanoparticles was found to have negligible effect on BSA structure¹⁰⁷. Moreover, the surface chemistry and shape nanoparticles also play an important role in determining its effect on proteins conformation changes. Huang *et al.* studied interaction of three types of Au nanoparticles with different surface composition with ubiquitin and fibrinogen at pH 4.0. Structure of both proteins were observed to be significantly perturbed by Au nanoparticles functionalized by 3,7-dimethyl octane 1-thiol and 11-mercapto-1-undecanesulfonate, while the effect of Au nanoparticles with 1-octanethiol surface functional groups was less¹⁰⁸. Chakraborty *et al.* examined the interaction of BSA with two different gold nanostructures, gold nanoparticles (GNP) and gold nanorods (GNR). In which they showed GNP had only slight effect on the secondary change of BSA, while a significant loss in the ellipticity was reported for GNR¹⁰⁹.

The structural change of proteins not only depends on the physicochemical properties of nanoparticles, but the nature of bound proteins also plays an important role. Ge *et al.* studied the interaction of single-wall carbon nanotubes (SWCNTs) with human blood proteins, fibrinogen (BFG), immunoglobulin (Ig), albumin, transferrin (Tf) and ferritin, and the structural changes of proteins on SWCNTs surface were revealed by circular dichroism (CD). It was found that secondary structure of BFG and Ig changed most significantly compared to other proteins, with an obvious decrease and increase in α -helical and β -sheet structure content, respectively¹⁰¹.

Conformation change of proteins can result in protein unfolding, instable and activity loss. The abnormal unfolding of proteins may lead to the exposure of hidden epitopes or the formation of new structural epitopes. Such cryptic epitopes may in turn influence the following cellular signaling. Mortimer *et al.* showed that synthetic layered silicate nanoparticles bound albumin adsorbed strongly and induced its subsequent unfolding, which resulted in exposure of a cryptic

epitope that can be recognized by SR-AI and MARCO. This in turn accelerated the clearance of nanoparticles from the circulation via the mononuclear phagocyte system¹¹⁰. The work done by Deng *et al.* can also well explain the important role of protein unfolding in dictating the cellular responses. They found that upon binding to negatively charged poly (acrylic acid)-conjugated gold nanoparticles surface, fibrinogen undergone unfolding and then activate the particular receptor of THP-1 cells, leading to the release of inflammatory cytokines through the NF-kB pathway¹¹¹.

1.6.3 APPROACHES FOR STUDYING NANOPARTICLE-PROTEIN INTERACTION

Recently, many techniques have been developed for characterizing nanoparticle-protein interactions. Those techniques, in general, were classified by Chan and his co-worker into five aspects with different functions¹¹²: 1) for detecting the thickness of protein layer, 2) for determining the orientation of protein on nanoparticles surface, 3) for monitoring changes in proteins' conformation and 4) for calculating protein affinity and thermodynamics, and 5) for identification and quantitation of the adsorbed proteins.

Adsorption of proteins on nanoparticle surface can lead to the increase in size of nanoparticles in solution. The increase in size, to some extent, reflects the amount and orientation of the adsorbed proteins. Due to its high sensitivity, dynamic light scattering (DLS) is reported as the one of the most commonly used method to detect change in hydrodynamic size of nanoparticles when exposed to protein-rich environments. Our work (Chapter 4) revealed that BSA adsorption on SPIONs cause about 7 nm increase in hydrodynamic size of SPIONs¹¹³. In addition to DLS, differential centrifugal sedimentation (DCS) is also considered as an efficient method to determine the thickness of the adsorbed proteins, as it was shown by Dawson's work¹¹⁴. To get more visualized data about the protein thickness, TEM and AFM are the best choices. However, because of the much less electronic density of proteins under TEM conditions, counter-staining of the samples is necessary for getting a visible image of the protein layer. By negative staining of BSA-SPIONs, TEM images clearly showed a white BSA monolayer surrounding SPIONs surface¹¹³. Different from counter-staining TEM, AFM can give the information of the protein corona thickness by measuring the root-mean-square (RMS) roughness, as what has been reported in Natte's work. By using AFM, they observed a protein layer with thickness less than 2 nm on silica nanoparticles¹¹⁵.

Despite the simple, efficient and visible virtues, the methods mentioned above have their own drawbacks, since they are all performed *ex-situ*. Those measurements necessarily require the isolation and purification of nanoparticle-protein complexes from the excess proteins in solution by repeated centrifugation and washing steps, which can lead to the loss of the weakly bound proteins, this could in turn cause the incorrect interpretation of the thickness of the protein corona¹¹⁶. Therefore, *in situ* characterization of protein thickness in solution is in high demand. G. Ulrich Nienhaus's group is the pioneer in developing fluorescence correlation spectroscopy (FCS) based *in situ* approach to determine the thickness of protein layer on small

fluorescent nanoparticles surface¹¹⁷. Due to the protein adsorption, changes in nanoparticle diffusivity can be monitored by FCS. By using the Stokes-Einstein relation, changes in hydrodynamic radius of nanoparticles before and after protein adsorption can be quantified. Finally, the thickness of the protein layer is obtained. The proposed *in situ* measurement avoids the complex centrifugal and washing steps, reflecting the real and accurate state of the proteins adsorbed on nanoparticles in solution. Now, the *in situ* approach established by G. Ulrich Nienhaus has been adapted and used widely for *in situ* investigation of nanoparticles' interaction with the single purified protein. In particular, for magnetic nanoparticles, F. Gazeau's group took the advantage of the specific magnetic property of magnetic nanoparticles, and proposed a dynamical magnetically-induced birefringence method for *in situ* monitor of magnetic nanoparticles interaction with serum proteins¹¹⁸. This technique measures the optical birefringence of magnetic nanoparticles in solution under the static magnetic field. When the magnetic field is switched off, the birefringence relaxes to zero, then the hydrodynamic size related relaxation time can be obtained. Proteins adsorption on magnetic nanoparticles could affect their characteristic relaxation time, then the increase in hydrodynamic size of magnetic nanoparticles can be determined. Unlike the technique established by Nienhaus's group, the birefringence method is only related to magnetic property of magnetic nanoparticles, this can be used specifically for *in situ* and in real time investigating protein adsorption on magnetic nanoparticles.

Isothermal titration calorimetry (ITC), which can measure directly the binding affinity constant, enthalpy changes and binding stoichiometry between nanoparticles and proteins, is an excellent technique to study the protein affinity and thermodynamics of nanoparticles interaction with proteins. By performing ITC, enthalpically favored interaction between polyethyleneimine functionalized ZnO nanoparticles (PEI-ZnO) and BSA is observed, each PEI-ZnO adsorbed at least three BSA molecules¹⁰⁷. Other techniques like size exclusion chromatography (SEC), surface plasmon resonance (SPR) and tryptophan fluorescence quenching are also being used to detect the protein affinity and thermodynamics¹¹⁹⁻¹²¹.

As mentioned above, nanoparticles can induce conformational changes of the adsorbed proteins. Those conformational changes can be monitored by a combination of several spectroscopic methods as infrared spectroscopy, circular dichroism and fluorescent spectroscopy. Infrared spectroscopy and circular dichroism measurements provide information about the secondary structure of proteins, in terms of the content of α -helix, β -turn or sheet and irregular¹²². Fluorescent spectroscopy provides information about the tertiary structure of proteins, perturbation in micro-environments which amino acids of proteins expose to can be revealed¹²³. Besides, enzyme activity assays can be also used as an indirect way to assess the structural changes of proteins¹²⁴.

Incubation of nanoparticles with blood plasma or serum-rich media results in the complex protein corona which consists of many types of proteins. Identification and quantification of the compositions of the protein corona is of great importance to understand their biological effects.

After complete isolation and elution of proteins from nanoparticles surface, poly(acrylamide) gel electrophoresis (PAGE), combined with mass spectrometry, is extensively used to identify and quantify the compositions of the protein corona^{125,126}. However, this method was recognized as user-bias and lack of sensitivity. A less user bias and more sensitive technique, liquid chromatography tandem mass spectrometry, has been developed very recently. It can identify and quantify the protein corona compositions simultaneously¹²⁷.

1.6.4 EFFECTS OF PROTEIN CORONA ON BIOLOGICAL RESPONSE

It is well known that the protein corona formed on nanoparticles' surface, other than the pristine coating of nanoparticles actually interacts with cells, determining their biological responses. For identical nanoparticles and cells, cellular responses are observed to vary greatly when a protein corona presents on nanoparticles' surface. As it was revealed by Wilhelm *et al.*, cellular uptake of nanoparticles can be recognized as two processes: binding of nanoparticles to the plasma membrane through non-specific adsorption and then the subsequent internalization of nanoparticles by cells¹²⁸. This viewpoint suggests that the affinity of the nanoparticles surface to cells' membrane plays a vital role in determining the overall cellular uptake of nanoparticles. Protein adsorption can modify the surface nature of nanoparticles and change the affinity of nanoparticle to cells. Lesniak *et al.* observed that bare polystyrene nanoparticles, maybe due to their high surface energy, adsorb strongly towards cell membrane, while polystyrene nanoparticles in the presence of serum protein corona showed reduced adhesion trend¹²⁹. In another work, Lesniak *et al.* studied the interaction of silica nanoparticles with A549 lung epithelial cells in media in the presence or the absence of serum¹³⁰. They also observed nanoparticles internalization efficiency was much lower in the case of nanoparticles exposed to cells in media with serum than ones without serum. In serum-free media, more silica nanoparticles were uptaken by cells. Moreover, cellular damage was observed severely when cells exposed to nanoparticles in serum-free media, while no sign of cellular damage was seen in serum media.

The way nanoparticles enter into the cell and their localization within the cells can be also modified by the presence of protein corona. Due to the small size, nanoparticles can enter to different types of cells and access to different cellular organelles depending on their exact size. Nanoparticles with ultra-small size (less than 35 nm) is reported to be even able to cross the blood brain barrier¹³¹. After entering to the cells, nanoparticles can accumulate in different cellular compartments like lysosomes, cytoplasm, vesicle and vacuoles, depending on their interaction with surrounding biological environment¹³². Since the presence of a protein corona can influence the way nanoparticles interacting with cells, the way nanoparticles entering the cells could be modified by the presence of protein corona. This was demonstrated by Lunov *et al.*, who showed that macrophage uptake mechanism of nanoparticles was changed from endocytosis to phagocytosis when nanoparticles exposed to serum containing media¹³³. Moreover, the modified uptake mechanism of nanoparticles could also lead to different

localization of nanoparticles within the cells. In serum-free media, silica nanoparticles were found mainly in vesicles, lysosomes and cytosol. However, nanoparticles were only found in vesicles when nanoparticles exposed to media with serum¹³⁰.

Even more subtle differences in protein composition can affect the way nanoparticles interact with cells. Lesniak *et al.* evaluated the adsorption behavior of polystyrene nanoparticles with different size in heat inactivated and activated serum media, and the effect of different protein corona compositions on cellular uptake was investigated. They revealed that the amount of proteins and the components attached to nanoparticles surface varied significantly in heat inactivated and activated serum media. And more importantly, they observed that lower cellular uptake of nanoparticles are conclusively related to higher amount of protein upload on nanoparticles surfaces. Other works also show the amount of proteins adsorbed on nanoparticles surface is of great importance in determining their cellular uptake efficiency¹³⁴.

Difference in the composition of protein corona can also impart nanoparticles different bio-identity and this in turn can give rise to distinct biological responses. Ge *et al.*, evaluated the cytotoxicity of single-wall carbon nanotubes (SWCNTs) covered by 5 different human blood proteins, namely human blood proteins, fibrinogen (BFG), immunoglobulin (Ig), albumin (BSA), transferrin (Tf) and ferritin, in two different human cell lines, human acute monocytic leukemia cell line (THP-1) and human umbilical vein endothelial cells (HUVECs)¹⁰¹. Even though identical nanomaterial was used, the outcome of the experiments varied significantly. SWCNTs coated by BFG showed nearly no cytotoxicity to both cell lines. Others caused different toxicity on cells depending on the protein composition on SWCNTs surface. By using alveolar macrophages as model cell line, Ruge *et al.* compared the cellular responses of pulmonary surfactant protein A coated magnetic nanoparticles with BSA coated magnetic nanoparticles. They revealed that cellular binding and uptake of magnetic nanoparticles was predominantly enhanced in the presence of surfactant protein A, while an adverse effect was found for BSA coated magnetic nanoparticles¹³⁵.

Finally, there are studies where a particular protein is adsorbed on nanoparticles in order to trigger some biological responses in terms of enhancing nanoparticle uptake by cells or targeting on the specific organs for therapy. Nanoparticles covered by fibrinogen, one of the blood plasma protein, has been proved to cause inflammation as shown by Deng *et al.*¹¹¹. They showed that binding of fibrinogen onto negatively charged poly (acrylic acid)-conjugated gold nanoparticles caused the unfolding of fibrinogen D domain, resulting in the exposure of some cryptic epitope which was identified as the amino acid sequence 377-695 in the terminus of the γ chain. The exposed epitope was then recognized by the integrin receptor Mac-1 and then activated the particular receptor of THP-1 cells, leading to the release of inflammatory cytokines through the NF- κ B pathway. Another example is apolipoproteins, in particular the apo A-I and apo E, which has been demonstrated to be able to cross the blood brain barrier to reach the targeted organs to be treated with¹³⁶. Coating of nanoparticles by apolipoproteins promotes the uptake by blood brain barrier cells in a receptor mediated manner, enhancing the delivery

efficiency of nanoparticles to central nervous system¹³⁶. The nature of the blood brain barrier makes it difficult for drugs to go pass through it to the brain. However, this observation suggests that apolipoproteins coated nanoparticles could be exploited as a novel platform for efficient and accurate drug delivery, many efforts have been directed towards to this aim.

1.7 CHAPTER REFERENCES

- (1) Mansoori, G. A. *Advances in atomic & molecular nanotechnology. Nanotechnology, United Nations Tech Monitor*, **2002**, 53.
- (2) Alivisatos, A. P. *Semiconductor Clusters, Nanocrystals, and Quantum Dots. Science*, **1996**, 271, 933.
- (3) Daniel, M.-C.; Astruc, D. *Gold nanoparticles: assembly, supramolecular chemistry, quantum-size-related properties, and applications toward biology, catalysis, and nanotechnology. Chemical reviews*, **2004**, 104, 293.
- (4) Brus, L. E. *Chemistry and physics of semiconductor nanocrystals. Columbia University*, **2007**.
- (5) Ruedas - Rama, M. J.; Orte, A.; Hall, E. A.; Alvarez - Pez, J. M.; Talavera, E. M. *Effect of surface modification on semiconductor nanocrystal fluorescence lifetime. ChemPhysChem*, **2011**, 12, 919.
- (6) Lobatto, M. E.; Fuster, V.; Fayad, Z. A.; Mulder, W. J. *Perspectives and opportunities for nanomedicine in the management of atherosclerosis. Nature Reviews Drug Discovery*, **2011**, 10, 835.
- (7) Wagner, V.; Dullaart, A.; Bock, A.-K.; Zweck, A. *The emerging nanomedicine landscape. Nature biotechnology*, **2006**, 24, 1211.
- (8) Mulder, W. J.; Strijkers, G. J.; Van Tilborg, G. A.; Cormode, D. P.; Fayad, Z. A.; Nicolay, K. *Nanoparticulate assemblies of amphiphiles and diagnostically active materials for multimodality imaging. Accounts of chemical research*, **2009**, 42, 904.
- (9) Torchilin, V. P. *Recent advances with liposomes as pharmaceutical carriers. Nature reviews Drug discovery*, **2005**, 4, 145.
- (10) Barenholz, Y. C. *Doxil®—the first FDA-approved nano-drug: lessons learned. Journal of controlled release*, **2012**, 160, 117.
- (11) Davis, M. E.; Shin, D. M. *Nanoparticle therapeutics: an emerging treatment modality for cancer. Nature reviews Drug discovery*, **2008**, 7, 771.
- (12) Bulte, J. W.; Kraitchman, D. L. *Iron oxide MR contrast agents for molecular and cellular imaging. NMR in Biomedicine*, **2004**, 17, 484.
- (13) Gao, X.; Cui, Y.; Levenson, R. M.; Chung, L. W.; Nie, S. *In vivo cancer targeting and imaging with semiconductor quantum dots. Nature biotechnology*, **2004**, 22, 969.
- (14) Suh, W. H.; Suh, Y.-H.; Stucky, G. D. *Multifunctional nanosystems at the interface of physical and life sciences. Nano Today*, **2009**, 4, 27.
- (15) Moghimi, S. M.; Hunter, A. C.; Murray, J. C. *Nanomedicine: current status and future prospects. The FASEB Journal*, **2005**, 19, 311.
- (16) Massart, R. *Preparation of aqueous magnetic liquids in alkaline and acidic media. Magnetism, IEEE Transactions on*, **1981**, 17, 1247.
- (17) Hadjipanayis, G. C. *Nonphase Materials: Synthesis, Properties, Applications*, DTIC Document, 1993.
- (18) Sjøgren, C. E.; Briley - Sæbø, K.; Hanson, M.; Johansson, C. *Magnetic characterization of iron oxides for magnetic resonance imaging. Magnetic resonance in medicine*, **1994**, 31, 268.
- (19) Jeong, J.-R.; Shin, S.-C.; Lee, S.-J.; Kim, J.-D. *Magnetic properties of superparamagnetic γ -Fe₂O₃ nanoparticles prepared by coprecipitation technique. Journal of magnetism and magnetic materials*, **2005**, 286, 5.
- (20) Bagwe, R.; Kanicky, J.; Palla, B.; Patanjali, P.; Shah, D. *Improved drug delivery using microemulsions: rationale, recent progress, and new horizons. Critical reviews in therapeutic drug carrier systems*, **2001**, 18, 77.
- (21) Lawrence, M. J. *Surfactant systems: microemulsions and vesicles as vehicles for drug delivery. European journal of drug metabolism and pharmacokinetics*, **1994**, 19, 257.

- (22) Lawrence, M. J.; Rees, G. D. *Microemulsion-based media as novel drug delivery systems. Advanced drug delivery reviews*, **2000**, *45*, 89.
- (23) Gupta, A. K.; Wells, S. *Surface-modified superparamagnetic nanoparticles for drug delivery: preparation, characterization, and cytotoxicity studies. NanoBioscience, IEEE Transactions on*, **2004**, *3*, 66.
- (24) Woo, K.; Lee, H. J.; Ahn, J. P.; Park, Y. S. *Sol–Gel Mediated Synthesis of Fe₂O₃ Nanorods. Advanced Materials*, **2003**, *15*, 1761.
- (25) Lu, A. H.; Salabas, E. e. L.; Schüth, F. *Magnetic nanoparticles: synthesis, protection, functionalization, and application. Angewandte Chemie International Edition*, **2007**, *46*, 1222.
- (26) Yoffe, S.; Leshuk, T.; Everett, P.; Gu, F. *Superparamagnetic iron oxide nanoparticles (SPIONs): synthesis and surface modification techniques for use with MRI and other biomedical applications. Current pharmaceutical design*, **2013**, *19*, 493.
- (27) Yu, S.-M.; Laromaine, A.; Roig, A. *Enhanced stability of superparamagnetic iron oxide nanoparticles in biological media using a pH adjusted-BSA adsorption protocol. J Nanopart Res*, **2014**, *16*, 1.
- (28) Park, J.; An, K.; Hwang, Y.; Park, J.-G.; Noh, H.-J.; Kim, J.-Y.; Park, J.-H.; Hwang, N.-M.; Hyeon, T. *Ultra-large-scale syntheses of monodisperse nanocrystals. Nature materials*, **2004**, *3*, 891.
- (29) Jana, N. R.; Chen, Y.; Peng, X. *Size- and Shape-Controlled Magnetic (Cr, Mn, Fe, Co, Ni) Oxide Nanocrystals via a Simple and General Approach. Chemistry of Materials*, **2004**, *16*, 3931.
- (30) Sun, S.; Zeng, H. *Size-Controlled Synthesis of Magnetite Nanoparticles. Journal of the American Chemical Society*, **2002**, *124*, 8204.
- (31) Lee, Y. T.; Woo, K.; Choi, K.-S. *Preparation of water-dispersible and biocompatible iron oxide nanoparticles for MRI agent. Nanotechnology, IEEE Transactions on*, **2008**, *7*, 111.
- (32) Gržeta, B.; Ristić, M.; Nowik, I.; Musić, S. *Formation of nanocrystalline magnetite by thermal decomposition of iron choline citrate. Journal of alloys and compounds*, **2002**, *334*, 304.
- (33) Narasimhan, B.; Prabhakar, S.; Manohar, P.; Gnanam, F. *Synthesis of gamma ferric oxide by direct thermal decomposition of ferrous carbonate. Materials Letters*, **2002**, *52*, 295.
- (34) William, W. *Synthesis of monodisperse iron oxide nanocrystals by thermal decomposition of iron carboxylate salts. Chemical Communications*, **2004**, 2306.
- (35) Barrera, C.; Herrera, A.; Zayas, Y.; Rinaldi, C. *Surface modification of magnetite nanoparticles for biomedical applications. Journal of Magnetism and Magnetic Materials*, **2009**, *321*, 1397.
- (36) Sun, S.; Zeng, H.; Robinson, D. B.; Raoux, S.; Rice, P. M.; Wang, S. X.; Li, G. *Monodisperse MFe₂O₄ (M= Fe, Co, Mn) nanoparticles. Journal of the American Chemical Society*, **2004**, *126*, 273.
- (37) Hyeon, T.; Lee, S. S.; Park, J.; Chung, Y.; Na, H. B. *Synthesis of Highly Crystalline and Monodisperse Maghemite Nanocrystallites without a Size-Selection Process. Journal of the American Chemical Society*, **2001**, *123*, 12798.
- (38) Dumestre, F.; Chaudret, B.; Amiens, C.; Renaud, P.; Fejes, P. *Superlattices of Iron Nanocubes Synthesized from Fe[N(SiMe₃)₂]₂. Science*, **2004**, *303*, 821.
- (39) Bowman, M. D.; Holcomb, J. L.; Kormos, C. M.; Leadbeater, N. E.; Williams, V. A. *Approaches for scale-up of microwave-promoted reactions. Organic Process Research & Development*, **2007**, *12*, 41.
- (40) Pascu, O.; Carenza, E.; Gich, M.; Estradé, S.; Peiró, F.; Herranz, G.; Roig, A. *Surface Reactivity of Iron Oxide Nanoparticles by Microwave-Assisted Synthesis; Comparison with the Thermal Decomposition Route. The Journal of Physical Chemistry C*, **2012**, *116*, 15108.

- (41) Leadbeater, N. E. *Microwave heating as a tool for sustainable chemistry*; CRC Press, 2010.
- (42) Gabriel, C.; Gabriel, S.; H. Grant, E.; H. Grant, E.; S. J. Halstead, B.; Michael P. Mingos, D. *Dielectric parameters relevant to microwave dielectric heating. Chemical Society Reviews*, **1998**, *27*, 213.
- (43) Kappe, C. O.; Dallinger, D.; Murphree, S. S. *Practical microwave synthesis for organic chemists*; John Wiley & Sons, 2008.
- (44) Mingos, D. M. P.; Baghurst, D. R. *Tilden Lecture. Applications of microwave dielectric heating effects to synthetic problems in chemistry. Chemical Society Reviews*, **1991**, *20*, 1.
- (45) Clavel, G.; Willinger, M. G.; Zitoun, D.; Pinna, N. *Solvent dependent shape and magnetic properties of doped ZnO nanostructures. Advanced Functional Materials*, **2007**, *17*, 3159.
- (46) Baghbanzadeh, M.; Carbone, L.; Cozzoli, P. D.; Kappe, C. O. *Microwave-Assisted Synthesis of Colloidal Inorganic Nanocrystals. Angewandte Chemie International Edition*, **2011**, *50*, 11312.
- (47) Niederberger, M.; Garnweitner, G. *Organic Reaction Pathways in the Nonaqueous Synthesis of Metal Oxide Nanoparticles. Chemistry – A European Journal*, **2006**, *12*, 7282.
- (48) Wang, H.-Q.; Nann, T. *Monodisperse Upconverting Nanocrystals by Microwave-Assisted Synthesis. ACS Nano*, **2009**, *3*, 3804.
- (49) Pascu, O.; Rodríguez Viejo, J. *Synthesis of magnetic nanoparticles and strategies towards magneto-photonic materials. 2012*.
- (50) Hu, X.; Yu, J. C. *Continuous Aspect - Ratio Tuning and Fine Shape Control of Monodisperse α - Fe₂O₃ Nanocrystals by a Programmed Microwave - Hydrothermal Method. Advanced Functional Materials*, **2008**, *18*, 880.
- (51) Polshettiwar, V.; Nadagouda, M. N.; Varma, R. S. *The synthesis and applications of a micro-pine-structured nanocatalyst. Chemical Communications*, **2008**, 6318.
- (52) Bilecka, I.; Elser, P.; Niederberger, M. *Kinetic and Thermodynamic Aspects in the Microwave-Assisted Synthesis of ZnO Nanoparticles in Benzyl Alcohol. ACS Nano*, **2009**, *3*, 467.
- (53) Spaldin, N. A. *Magnetic materials: fundamentals and applications*; Cambridge University Press, 2010.
- (54) Frey, N. A.; Peng, S.; Cheng, K.; Sun, S. *Magnetic nanoparticles: synthesis, functionalization, and applications in bioimaging and magnetic energy storage. Chemical Society Reviews*, **2009**, *38*, 2532.
- (55) Takafuji, M.; Ide, S.; Ihara, H.; Xu, Z. *Preparation of poly (1-vinylimidazole)-grafted magnetic nanoparticles and their application for removal of metal ions. Chemistry of materials*, **2004**, *16*, 1977.
- (56) Gupta, A. K.; Gupta, M. *Synthesis and surface engineering of iron oxide nanoparticles for biomedical applications. Biomaterials*, **2005**, *26*, 3995.
- (57) Maity, D.; Zoppellaro, G.; Sedenkova, V.; Tucek, J.; Safarova, K.; Polakova, K.; Tomankova, K.; Diwok, C.; Stollberger, R.; Machala, L.; Zboril, R. *Surface design of core-shell superparamagnetic iron oxide nanoparticles drives record relaxivity values in functional MRI contrast agents. Chemical Communications*, **2012**, *48*, 11398.
- (58) Dobson, J. *Magnetic nanoparticles for drug delivery. Drug Development Research*, **2006**, *67*, 55.
- (59) Gazeau, F.; Lévy, M.; Wilhelm, C. *Optimizing magnetic nanoparticle design for nanothermotherapy. Nanomedicine*, **2008**, *3*, 831.
- (60) Koh, I.; Josephson, L. *Magnetic nanoparticle sensors. Sensors*, **2009**, *9*, 8130.
- (61) Weinstein, J. S.; Varallyay, C. G.; Dosa, E.; Gahramanov, S.; Hamilton, B.; Rooney, W. D.; Muldoon, L. L.; Neuwelt, E. A. *Superparamagnetic iron oxide nanoparticles:*

diagnostic magnetic resonance imaging and potential therapeutic applications in neurooncology and central nervous system inflammatory pathologies, a review. J Cereb Blood Flow Metab, **2009**, *30*, 15.

(62) Laurent, S.; Forge, D.; Port, M.; Roch, A.; Robic, C.; Vander Elst, L.; Muller, R. N. *Magnetic iron oxide nanoparticles: synthesis, stabilization, vectorization, physicochemical characterizations, and biological applications. Chemical reviews*, **2008**, *108*, 2064.

(63) Montet, X.; Weissleder, R.; Josephson, L. *Imaging pancreatic cancer with a peptide-nanoparticle conjugate targeted to normal pancreas. Bioconjugate Chemistry*, **2006**, *17*, 905.

(64) Carezza, E.; Barceló, V.; Morancho, A.; Levander, L.; Boada, C.; Laromaine, A.; Roig, A.; Montaner, J.; Rosell, A. *In vitro angiogenic performance and in vivo brain targeting of magnetized endothelial progenitor cells for neurorepair therapies. Nanomedicine: Nanotechnology, Biology and Medicine*, **2014**, *10*, 225.

(65) Chang, Y.; Liu, N.; Chen, L.; Meng, X.; Liu, Y.; Li, Y.; Wang, J. *Synthesis and characterization of DOX-conjugated dendrimer-modified magnetic iron oxide conjugates for magnetic resonance imaging, targeting, and drug delivery. Journal of Materials Chemistry*, **2012**, *22*, 9594.

(66) Zhu, A.; Yuan, L.; Jin, W.; Dai, S.; Wang, Q.; Xue, Z.; Qin, A. *Polysaccharide surface modified Fe₃O₄ nanoparticles for camptothecin loading and release. Acta Biomaterialia*, **2009**, *5*, 1489.

(67) Wu, X.; He, X.; Zhong, L.; Lin, S.; Wang, D.; Zhu, X.; Yan, D. *Water-soluble dendritic-linear triblock copolymer-modified magnetic nanoparticles: preparation, characterization and drug release properties. Journal of Materials Chemistry*, **2011**, *21*, 13611.

(68) Cengelli, F.; Grzyb, J. A.; Montoro, A.; Hofmann, H.; Hanessian, S.; Juillerat - Jeanneret, L. *Surface - Functionalized Ultrasmall Superparamagnetic Nanoparticles as Magnetic Delivery Vectors for Camptothecin. ChemMedChem*, **2009**, *4*, 988.

(69) Wang, C.; Ravi, S.; Martinez, G. V.; Chinnasamy, V.; Raulji, P.; Howell, M.; Davis, Y.; Mallela, J.; Seehra, M. S.; Mohapatra, S. *Dual-purpose magnetic micelles for MRI and gene delivery. Journal of Controlled Release*, **2012**, *163*, 82.

(70) Lam, T.; Pouliot, P.; Avti, P. K.; Lesage, F.; Kakkar, A. K. *Superparamagnetic iron oxide based nanoproboscopes for imaging and theranostics. Advances in Colloid and Interface Science*, **2013**, *199–200*, 95.

(71) van Loo, G.; Saelens, X.; Van Gorp, M.; MacFarlane, M.; Martin, S.; Vandenabeele, P. *The role of mitochondrial factors in apoptosis: a Russian roulette with more than one bullet. Cell death and differentiation*, **2002**, *9*, 1031.

(72) Ito, A.; Honda, H.; Kobayashi, T. *Cancer immunotherapy based on intracellular hyperthermia using magnetite nanoparticles: a novel concept of "heat-controlled necrosis" with heat shock protein expression. Cancer Immunol Immunother*, **2006**, *55*, 320.

(73) Cengelli, F.; Maysinger, D.; Tschudi-Monnet, F.; Montet, X.; Corot, C.; Petri-Fink, A.; Hofmann, H.; Juillerat-Jeanneret, L. *Interaction of functionalized superparamagnetic iron oxide nanoparticles with brain structures. Journal of Pharmacology and Experimental Therapeutics*, **2006**, *318*, 108.

(74) Derfus, A. M.; von Maltzahn, G.; Harris, T. J.; Duza, T.; Vecchio, K. S.; Ruoslahti, E.; Bhatia, S. N. *Remotely triggered release from magnetic nanoparticles. Advanced Materials*, **2007**, *19*, 3932.

(75) Safarik, I.; Safarikova, M. *Magnetic techniques for the isolation and purification of proteins and peptides. Biomagnetic Research and Technology*, **2004**, *2*, 7.

(76) Xu, C.; Xu, K.; Gu, H.; Zheng, R.; Liu, H.; Zhang, X.; Guo, Z.; Xu, B. *Dopamine as a robust anchor to immobilize functional molecules on the iron oxide shell of magnetic nanoparticles. Journal of the American Chemical Society*, **2004**, *126*, 9938.

- (77) Du, X.; Zhou, J.; Wu, L.; Sun, S.; Xu, B. *Enzymatic Transformation of Phosphate Decorated Magnetic Nanoparticles for Selectively Sorting and Inhibiting Cancer Cells. Bioconjugate Chemistry*, **2014**, *25*, 2129.
- (78) Schmid, G.; Pfeil, R.; Boese, R.; Bandermann, F.; Meyer, S.; Calis, G. H. M.; van der Velden, J. W. A. *Au₅₅[P(C₆H₅)₃]₁₂Cl₆ — ein Goldcluster ungewöhnlicher Größe. Chemische Berichte*, **1981**, *114*, 3634.
- (79) Giersig, M.; Mulvaney, P. *Preparation of ordered colloid monolayers by electrophoretic deposition. Langmuir*, **1993**, *9*, 3408.
- (80) Bastús, N. G.; Comenge, J.; Puentes, V. *Kinetically controlled seeded growth synthesis of citrate-stabilized gold nanoparticles of up to 200 nm: size focusing versus Ostwald ripening. Langmuir*, **2011**, *27*, 11098.
- (81) Cooper-Stevenson, P. *A study of the nucleation and growth processes in the synthesis of colloidal gold. Discussions of the Faraday Society*, **1951**, *11*, 55.
- (82) Huo, Q.; Litherland, S. A.; Sullivan, S.; Hallquist, H.; Decker, D. A.; Rivera-Ramirez, I. *Developing a nanoparticle test for prostate cancer scoring. J Transl Med*, **2012**, *10*, 44.
- (83) Conde, J.; de la Fuente, J. M.; Baptista, P. V. *RNA quantification using gold nanoprobe-application to cancer diagnostics. J Nanobiotechnology*, **2010**, *8*.
- (84) Hostetler, M. J.; Green, S. J.; Stokes, J. J.; Murray, R. W. *Monolayers in three dimensions: synthesis and electrochemistry of ω -functionalized alkanethiolate-stabilized gold cluster compounds. Journal of the American Chemical Society*, **1996**, *118*, 4212.
- (85) Heo, D. N.; Yang, D. H.; Moon, H.-J.; Lee, J. B.; Bae, M. S.; Lee, S. C.; Lee, W. J.; Sun, I.-C.; Kwon, I. K. *Gold nanoparticles surface-functionalized with paclitaxel drug and biotin receptor as theranostic agents for cancer therapy. Biomaterials*, **2012**, *33*, 856.
- (86) Mieszawska, A. J.; Mulder, W. J. M.; Fayad, Z. A.; Cormode, D. P. *Multifunctional Gold Nanoparticles for Diagnosis and Therapy of Disease. Molecular Pharmaceutics*, **2013**, *10*, 831.
- (87) Durr, N. J.; Larson, T.; Smith, D. K.; Korgel, B. A.; Sokolov, K.; Ben-Yakar, A. *Two-photon luminescence imaging of cancer cells using molecularly targeted gold nanorods. Nano letters*, **2007**, *7*, 941.
- (88) Küstner, B.; Gellner, M.; Schütz, M.; Schöppler, F.; Marx, A.; Ströbel, P.; Adam, P.; Schmuck, C.; Schlücker, S. *SERS Labels for Red Laser Excitation: Silica-Encapsulated SAMs on Tunable Gold/Silver Nanoshells. Angewandte Chemie International Edition*, **2009**, *48*, 1950.
- (89) Walczyk, D.; Bombelli, F. B.; Monopoli, M. P.; Lynch, I.; Dawson, K. A. *What the Cell "Sees" in Bionanoscience. Journal of the American Chemical Society*, **2010**, *132*, 5761.
- (90) Gaspar, R. *Nanoparticles: Pushed off target with proteins. Nat Nano*, **2013**, *8*, 79.
- (91) Wiogo, H. T.; Lim, M.; Bulmus, V.; Gutiérrez, L. a.; Woodward, R. C.; Amal, R. *Insight into serum protein interactions with functionalized magnetic nanoparticles in biological media. Langmuir*, **2012**, *28*, 4346.
- (92) Jedlovsky-Hajdú, A. I.; Bombelli, F. B.; Monopoli, M. P.; Tombácz, E.; Dawson, K. A. *Surface coatings shape the protein corona of SPIONs with relevance to their application in vivo. Langmuir*, **2012**, *28*, 14983.
- (93) Casals, E.; Pfaller, T.; Duschl, A.; Oostingh, G. J.; Puentes, V. *Time Evolution of the Nanoparticle Protein Corona. ACS Nano*, **2010**, *4*, 3623.
- (94) Tenzer, S.; Docter, D.; Rosfa, S.; Wlodarski, A.; Kuharev, J.; Reikik, A.; Knauer, S. K.; Bantz, C.; Nawroth, T.; Bier, C.; Sirirattanapan, J.; Mann, W.; Treuel, L.; Zellner, R.; Maskos, M.; Schild, H.; Stauber, R. H. *Nanoparticle Size Is a Critical Physicochemical Determinant of the Human Blood Plasma Corona: A Comprehensive Quantitative Proteomic Analysis. ACS Nano*, **2011**, *5*, 7155.

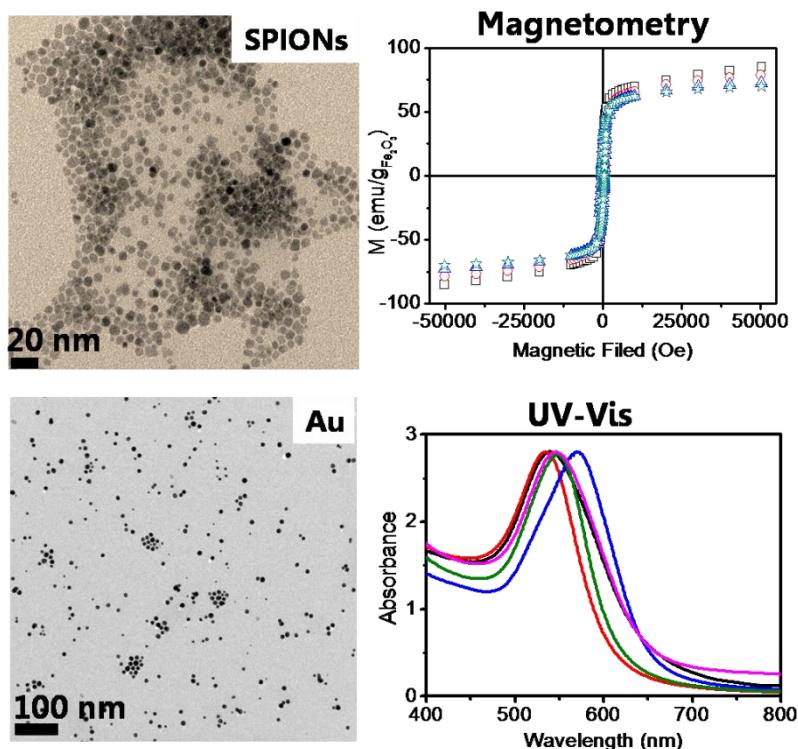
- (95) Hu, Z.; Zhang, H.; Zhang, Y.; Wu, R. a.; Zou, H. *Nanoparticle size matters in the formation of plasma protein coronas on Fe₃O₄ nanoparticles. Colloids and Surfaces B: Biointerfaces*, **2014**, *121*, 354.
- (96) Hirsch, V.; Kinnear, C.; Moniatte, M.; Rothen-Rutishauser, B.; Clift, M. J. D.; Fink, A. *Surface charge of polymer coated SPIONs influences the serum protein adsorption, colloidal stability and subsequent cell interaction in vitro. Nanoscale*, **2013**, *5*, 3723.
- (97) Gessner, A.; Lieske, A.; Paulke, B.-R.; Müller, R. H. *Functional groups on polystyrene model nanoparticles: Influence on protein adsorption. Journal of Biomedical Materials Research Part A*, **2003**, *65A*, 319.
- (98) Wiogo, H. T. R.; Lim, M.; Bulmus, V.; Gutiérrez, L.; Woodward, R. C.; Amal, R. *Insight into Serum Protein Interactions with Functionalized Magnetic Nanoparticles in Biological Media. Langmuir*, **2012**, *28*, 4346.
- (99) Brewer, S. H.; Glomm, W. R.; Johnson, M. C.; Knag, M. K.; Franzen, S. *Probing BSA Binding to Citrate-Coated Gold Nanoparticles and Surfaces. Langmuir*, **2005**, *21*, 9303.
- (100) Hühn, D.; Kantner, K.; Geidel, C.; Brandholt, S.; De Cock, I.; Soenen, S. J.; Rivera_Gil, P.; Montenegro, J.-M.; Braeckmans, K.; Mullen, K. *Polymer-coated nanoparticles interacting with proteins and cells: focusing on the sign of the net charge. ACS nano*, **2013**, *7*, 3253.
- (101) Ge, C.; Du, J.; Zhao, L.; Wang, L.; Liu, Y.; Li, D.; Yang, Y.; Zhou, R.; Zhao, Y.; Chai, Z. *Binding of blood proteins to carbon nanotubes reduces cytotoxicity. Proceedings of the National Academy of Sciences*, **2011**, *108*, 16968.
- (102) Maiorano, G.; Sabella, S.; Sorce, B.; Brunetti, V.; Malvindi, M. A.; Cingolani, R.; Pompa, P. P. *Effects of Cell Culture Media on the Dynamic Formation of Protein–Nanoparticle Complexes and Influence on the Cellular Response. ACS Nano*, **2010**, *4*, 7481.
- (103) Huang, R.; Carney, R. P.; Ikuma, K.; Stellacci, F.; Lau, B. L. T. *Effects of Surface Compositional and Structural Heterogeneity on Nanoparticle–Protein Interactions: Different Protein Configurations. ACS Nano*, **2014**, *8*, 5402.
- (104) Treuel, L.; Brandholt, S.; Maffre, P.; Wiegele, S.; Shang, L.; Nienhaus, G. U. *Impact of Protein Modification on the Protein Corona on Nanoparticles and Nanoparticle–Cell Interactions. ACS nano*, **2014**, *8*, 503.
- (105) Wang, H.-D.; Niu, C. H.; Yang, Q.; Badea, I. *Study on protein conformation and adsorption behaviors in nanodiamond particle–protein complexes. Nanotechnology*, **2011**, *22*, 145703.
- (106) Liu, Y.; Ji, F.; Liu, R. *The interaction of bovine serum albumin with doxorubicin-loaded superparamagnetic iron oxide nanoparticles: spectroscopy and molecular modelling identification. Nanotoxicology*, **2013**, *7*, 97.
- (107) Chakraborti, S.; Joshi, P.; Chakravarty, D.; Shanker, V.; Ansari, Z.; Singh, S. P.; Chakrabarti, P. *Interaction of polyethyleneimine-functionalized ZnO nanoparticles with bovine serum albumin. Langmuir*, **2012**, *28*, 11142.
- (108) Huang, R.; Carney, R. P.; Stellacci, F.; Lau, B. L. *Protein–nanoparticle interactions: the effects of surface compositional and structural heterogeneity are scale dependent. Nanoscale*, **2013**, *5*, 6928.
- (109) Chakraborty, S.; Joshi, P.; Shanker, V.; Ansari, Z. A.; Singh, S. P.; Chakrabarti, P. *Contrasting Effect of Gold Nanoparticles and Nanorods with Different Surface Modifications on the Structure and Activity of Bovine Serum Albumin. Langmuir*, **2011**, *27*, 7722.
- (110) Mortimer, G. M.; Butcher, N. J.; Musumeci, A. W.; Deng, Z. J.; Martin, D. J.; Minchin, R. F. *Cryptic epitopes of albumin determine mononuclear phagocyte system clearance of nanomaterials. ACS nano*, **2014**, *8*, 3357.
- (111) Deng, Z. J.; Liang, M.; Monteiro, M.; Toth, I.; Minchin, R. F. *Nanoparticle-induced unfolding of fibrinogen promotes Mac-1 receptor activation and inflammation. Nature nanotechnology*, **2011**, *6*, 39.

- (112) Walkey, C. D.; Chan, W. C. *Understanding and controlling the interaction of nanomaterials with proteins in a physiological environment. Chemical Society Reviews*, **2012**, *41*, 2780.
- (113) Yu, S.-M.; Laromaine, A.; Roig, A. *Enhanced stability of superparamagnetic iron oxide nanoparticles in biological media using a pH adjusted-BSA adsorption protocol. Journal of Nanoparticle Research*, **2014**, *16*.
- (114) Monopoli, M. P.; Walczyk, D.; Campbell, A.; Elia, G.; Lynch, I.; Baldelli Bombelli, F.; Dawson, K. A. *Physical– chemical aspects of protein corona: relevance to in vitro and in vivo biological impacts of nanoparticles. Journal of the American Chemical Society*, **2011**, *133*, 2525.
- (115) Natte, K.; Friedrich, J. F.; Wohlrab, S.; Lutzki, J.; von Klitzing, R.; Österle, W.; Orts-Gil, G. *Impact of polymer shell on the formation and time evolution of nanoparticle–protein corona. Colloids and Surfaces B: Biointerfaces*, **2013**, *104*, 213.
- (116) Dominguez-Medina, S.; McDonough, S.; Swanglap, P.; Landes, C. F.; Link, S. *In Situ Measurement of Bovine Serum Albumin Interaction with Gold Nanospheres. Langmuir*, **2012**, *28*, 9131.
- (117) Nienhaus, G. U.; Maffre, P.; Nienhaus, K. *Studying the protein corona on nanoparticles by FCS. Fluorescence Fluctuation Spectroscopy (FFS)*, **2012**, 115.
- (118) Lartigue, L. n.; Wilhelm, C.; Servais, J.; Factor, C. c.; Dencausse, A.; Bacri, J.-C.; Luciani, N.; Gazeau, F. *Nanomagnetic sensing of blood plasma protein interactions with iron oxide nanoparticles: impact on macrophage uptake. Acs Nano*, **2012**, *6*, 2665.
- (119) Klein, J. *Probing the interactions of proteins and nanoparticles. Proceedings of the National Academy of Sciences*, **2007**, *104*, 2029.
- (120) Zeng, Z.; Patel, J.; Lee, S.-H.; McCallum, M.; Tyagi, A.; Yan, M.; Shea, K. J. *Synthetic polymer nanoparticle–polysaccharide interactions: a systematic study. Journal of the American Chemical Society*, **2012**, *134*, 2681.
- (121) Kim, J. A.; Åberg, C.; Salvati, A.; Dawson, K. A. *Role of cell cycle on the cellular uptake and dilution of nanoparticles in a cell population. Nature nanotechnology*, **2012**, *7*, 62.
- (122) Chithrani, B. D.; Ghazani, A. A.; Chan, W. C. *Determining the size and shape dependence of gold nanoparticle uptake into mammalian cells. Nano letters*, **2006**, *6*, 662.
- (123) Paul, B. K.; Bhattacharjee, K.; Bose, S.; Guchhait, N. *A spectroscopic investigation on the interaction of a magnetic ferrofluid with a model plasma protein: effect on the conformation and activity of the protein. Physical Chemistry Chemical Physics*, **2012**, *14*, 15482.
- (124) Gagner, J. E.; Lopez, M. D.; Dordick, J. S.; Siegel, R. W. *Effect of gold nanoparticle morphology on adsorbed protein structure and function. Biomaterials*, **2011**, *32*, 7241.
- (125) Göppert, T. M.; Müller, R. H. *Adsorption kinetics of plasma proteins on solid lipid nanoparticles for drug targeting. International Journal of Pharmaceutics*, **2005**, *302*, 172.
- (126) Cedervall, T.; Lynch, I.; Foy, M.; Berggård, T.; Donnelly, S. C.; Cagney, G.; Linse, S.; Dawson, K. A. *Detailed Identification of Plasma Proteins Adsorbed on Copolymer Nanoparticles. Angewandte Chemie International Edition*, **2007**, *46*, 5754.
- (127) Capriotti, A.; Caracciolo, G.; Caruso, G.; Cavaliere, C.; Pozzi, D.; Samperi, R.; Laganà, A. *Analysis of plasma protein adsorption onto DC-Chol-DOPE cationic liposomes by HPLC-CHIP coupled to a Q-TOF mass spectrometer. Anal Bioanal Chem*, **2010**, *398*, 2895.
- (128) Wilhelm, C.; Gazeau, F.; Roger, J.; Pons, J.; Bacri, J.-C. *Interaction of anionic superparamagnetic nanoparticles with cells: kinetic analyses of membrane adsorption and subsequent internalization. Langmuir*, **2002**, *18*, 8148.
- (129) Lesniak, A.; Salvati, A.; Santos-Martinez, M. J.; Radomski, M. W.; Dawson, K. A.; Åberg, C. *Nanoparticle adhesion to the cell membrane and its effect on nanoparticle uptake efficiency. Journal of the American Chemical Society*, **2013**, *135*, 1438.

- (130) Lesniak, A.; Fenaroli, F.; Monopoli, M. P.; Åberg, C.; Dawson, K. A.; Salvati, A. *Effects of the presence or absence of a protein corona on silica nanoparticle uptake and impact on cells. ACS nano*, **2012**, *6*, 5845.
- (131) Dawson, K. A.; Salvati, A.; Lynch, I. *Nanotoxicology: nanoparticles reconstruct lipids. Nature nanotechnology*, **2009**, *4*, 84.
- (132) Saptarshi, S. R.; Duschl, A.; Lopata, A. L. *Interaction of nanoparticles with proteins: relation to bio-reactivity of the nanoparticle. J Nanobiotechnol*, **2013**, *11*.
- (133) Lunov, O.; Syrovets, T.; Loos, C.; Beil, J.; Delacher, M.; Tron, K.; Nienhaus, G. U.; Musyanovych, A.; Mailander, V.; Landfester, K. *Differential uptake of functionalized polystyrene nanoparticles by human macrophages and a monocytic cell line. Acs Nano*, **2011**, *5*, 1657.
- (134) Lesniak, A.; Campbell, A.; Monopoli, M. P.; Lynch, I.; Salvati, A.; Dawson, K. A. *Serum heat inactivation affects protein corona composition and nanoparticle uptake. Biomaterials*, **2010**, *31*, 9511.
- (135) Ruge, C. A.; Kirch, J.; Cañadas, O.; Schneider, M.; Perez-Gil, J.; Schaefer, U. F.; Casals, C.; Lehr, C.-M. *Uptake of nanoparticles by alveolar macrophages is triggered by surfactant protein A. Nanomedicine: Nanotechnology, Biology and Medicine*, **2011**, *7*, 690.
- (136) Kreuter, J. *Mechanism of polymeric nanoparticle-based drug transport across the blood-brain barrier (BBB). Journal of microencapsulation*, **2013**, *30*, 49.

CHAPTER 2

SYNTHESIS AND CHARACTERIZATION OF SPIONs AND Au NANOPARTICLES.



CHAPTER SUMMARY

In this chapter, microwave (MW) assisted method was selected to synthesize SPIONs. By using stabilizers such as polyvinyl pyrrolidone (PVP), tetramethylammonium hydroxide (TMAOH) and trisodium citrate dihydrate (Na_3Cit), water soluble SPIONs with different surface coating have been prepared. The size of the SPIONs core has been modulated to some extent by increasing the reaction temperature and time, magnetic properties of SPIONs of different sizes have been measured as well.

Due to the small capacity of single mode MW apparatus commonly used in the lab, only milligram (around 20 mg) of SPIONs can be prepared in each batch. Therefore, we also scaled up the synthesis of SPIONs by using a multi-mode MW apparatus to obtain $\sim 3g$ /batch, the as prepared SPIONs maintained the spherical shape, the monodispersity and the superparamagnetic properties of the SPIONs obtained in the lab-scale.

Finally, small Au nanoparticles with narrow size distribution and high water solubility were also synthesized by an one step MW assisted method in 10 min. The size and optical properties of the Au nanoparticles can be easily tuned by simply changing the amount of PVP used.

Chapter Index

	pag.
CHAPTER SUMMARY	37
2.1 MICROWAVE SYNTHESIS OF SPIONs	39
2.2 SURFACE COATING OF SPIONs	40
2.3 CHARACTERIZATION OF SPIONs	41
2.4 SIZE CONTROL OF SPIONs	43
2.5 MAGNETIC PROPERTIES OF SPIONs	46
2.6 RELAXIVITY MEASUREMENT	48
2.7 SCALE UP SYNTHESIS OF SPIONs	49
2.8 MICROWAVE SYNTHESIS OF Au NANOPARTICLES	55
2.9 CHAPTER CONCLUSIONS	60
2.10 ANNEX OF CHAPTER 2	61
2.11 CHAPTER REFERENCES	67

2.1 MICROWAVE SYNTHESIS OF SPIONs

To date, many methods have been developed to synthesize SPIONs, including co-precipitation¹, thermal decomposition², microemulsion³, and microwave assisted synthesis⁴. Each of those methods displays advantages, as well as some drawbacks. Microwave-assisted synthesis of SPIONs has attracted considerable interest due to their rather simple and short synthetic process. Recently, we established a facile and fast microwave-assisted synthetic route to obtain monodisperse SPIONs with good magnetic properties under moderate temperature. Moreover, we showed that microwave synthesis reduced by a factor of 10 the energy consumption associated to the materials fabrication, and decreased by 40% the overall cost compared with high temperature thermal decomposition route⁵. Therefore, in the whole thesis, MW assisted method was chosen to synthesize nanoparticles.

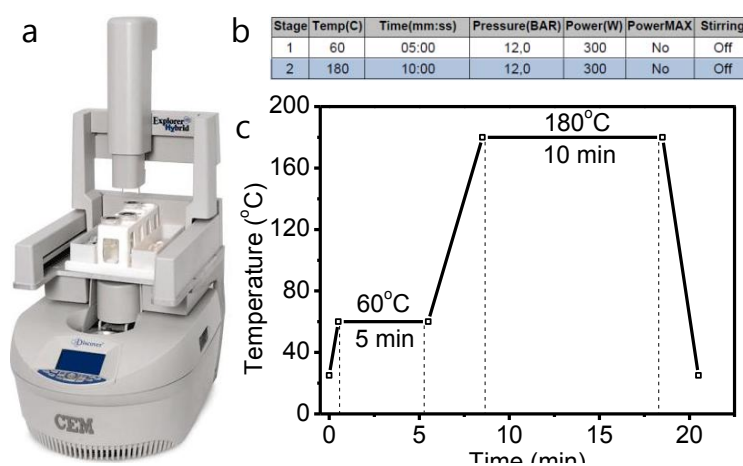


Figure 1. a, Digital photograph of the MW heater used in this thesis. b, The parameters used in a typical MW synthesis of SPIONs, including the setting of the MW heating ramp. c, a schematic graph of the real heating process during the MW heating.

In a typical MW synthesis of SPIONs, 123.6 mg (0.35) mmol iron precursor $\text{Fe}(\text{acac})_3$ were mixed gently with 4.5 mL benzyl alcohol in a glass tube to form a homogenous solution. The initial color of the mixture was reddish. The glass tube with the precursor solution was then transferred to the MW oven (Fig. 1a), followed by a two step heating ramp as shown in Fig. 1b, 60 °C for 5 min and 180 °C for 10 min. The heating ramp is schematically included in Fig. 1c, indicating that in 20 min, one batch of SPIONs can be synthesized. It is noteworthy that the first heating step at 60 °C for 5 min was designed to dissolve $\text{Fe}(\text{acac})_3$ completely in benzyl alcohol. As temperature increased further to 180 °C, $\text{Fe}(\text{acac})_3$ started to decompose to iron oxide nucleates. The initially formed nuclei then assembled together to form SPIONs seeds and continued to grow into small SPIONs in 10 min. After the MW heating, a dark black color of the solution was obtained, indicating the synthesis of SPIONs.

Fig. 2a shows a representative image of the as-synthesized SPIONs by MW heating. Spherical SPIONs with regular shape were observed. After counting about 300 individual particles, size

distribution histogram was plotted, the size of the SPIONs was determined to be $6.1 \pm 1 \text{ nm}$. Moreover, the narrow size distribution found in histogram indicated the high monodispersity of the SPIONs prepared by MW heating. Select area electron diffraction was performed to reveal the crystallinity of the SPIONs, Fig. 2c showed clear diffraction patterns. The electron diffraction rings correspond to (220), (311), (400), (422), (511) and (440) planes, indicating the inverse spinel structure (magnetite, maghemite).

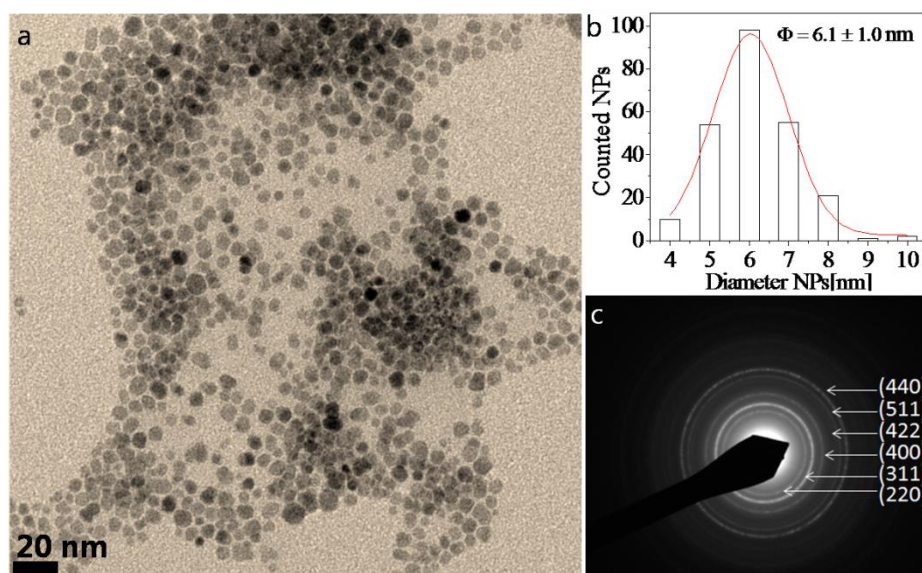


Figure 2. a) TEM image of the SPIONs obtained by using the typical MW synthesis with a heating ramp of 60 °C, 5 min and 180 °C, 10 min. b) Size distribution histogram of SPIONs shown in Figure 2a. c) select area electron diffraction of SPIONs shown in Figure 2a.

2.2 SURFACE COATING OF SPIONs

Since the aim of our work is to produce nano-bio-particles, hence water dispersity of SPIONs is a prerequisite for their potential use in the biological applications, especially for *in vivo* applications⁶. To address this issue, providing a hydrophilic surface to the synthesized SPIONs is necessary. Among methods used, the ligand-exchange strategy is the one of the commonly used ways to confer the SPIONs hydrophilic surface and water dispersity. The method involves mixing and stirring of the hydrophobic SPIONs dispersions with the aqueous solution in the presence of hydrophilic ligand. The hydrophobic surfactant is then removed by the hydrophilic ligands, making SPIONs dispersible in water. However, not only the ligand-exchange strategy is complicated, but also the stability of the resulted SPIONs dispersions has not been effectively improved⁷. Here, more straightforward methods, *in situ* coating and post-synthesis functionalization, were used to synthesize SPIONs with high water dispersity. On this purpose, polyvinyl pyrrolidone (PVP), tetramethylammonium hydroxide (TMAOH) and trisodium citrate dihydrate (Na_3Cit) were chosen as our stabilizers. PVP has been used in producing stable Au and Ag nanocrystals with different structures, due to its preferential affinity to the Au and Ag surfaces^{8,9}. PVP has also been used for stabilizing metal oxide like Fe_3O_4 ¹⁰. Moreover, PVP has been proved to have low toxicity on biological entities⁹. It is noteworthy that TMAOH was

chosen because our previous work^{5,11} showed that it is an efficient electrostatic stabilizer to make the SPIONs water dispersible and stable in water. Na₃Cit, one of the widely used additives in food and drug industry, with excellent biocompatibility, is now widely used to stabilize NPs in aqueous solution¹². For *in situ* coating, PVP was added to the reaction system during the MW synthetic process, while TMAOH and Na₃Cit, were added to SPIONs surface during the cleaning steps after the MW synthesis of SPIONs, detailed information about the coating protocols can be referred to the annex part of this chapter. SPIONs stabilized by PVP, TMAOH and Na₃Cit were abbreviated as PVP-SPIONs, T-SPIONs and C-SPIONs, respectively (Corresponding schematic structures are given in Fig. 3).

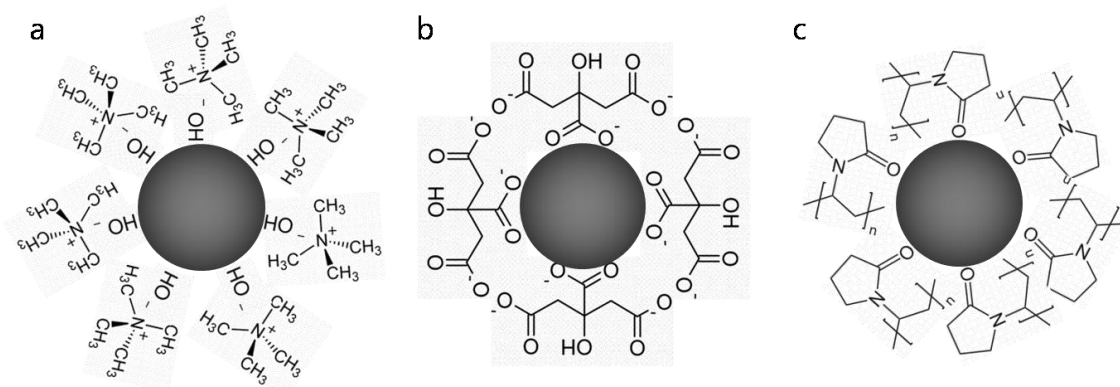


Figure 3. Schematic structure of the as obtained T-SPIONs (a), C-SPIONs (b) and PVP-SPIONs (c).

2.3 CHARACTERIZATION OF SPIONs

The obtained PVP-SPIONs were characterized by TEM and electron diffraction, results are shown in Fig. 4. PVP-SPIONs display a spherical shape (Fig. 4a) and a mean size of 5.6 ± 1 nm (Fig. 4b). Select area electron diffraction also indicates the inverse spinel structure (magnetite, maghemite) of the PVP-SPIONs (Fig. 4c). Because T-SPIONs and C-SPIONs were prepared using a post-synthesis functionalization method, they have an identical mean size of 6.1 ± 1 nm (Fig. 2). Mean size of PVP-SPIONs was observed 1 nm smaller than those of T-SPIONs and C-SPIONs, this may be due to the presence of PVP during the microwave synthetic process. In the presence of PVP, the generated nuclei were simultaneously stabilized by PVP. The presence of PVP on the nuclei surface lowered the growth rate of SPIONs seeds, resulting in smaller PVP-SPIONs.

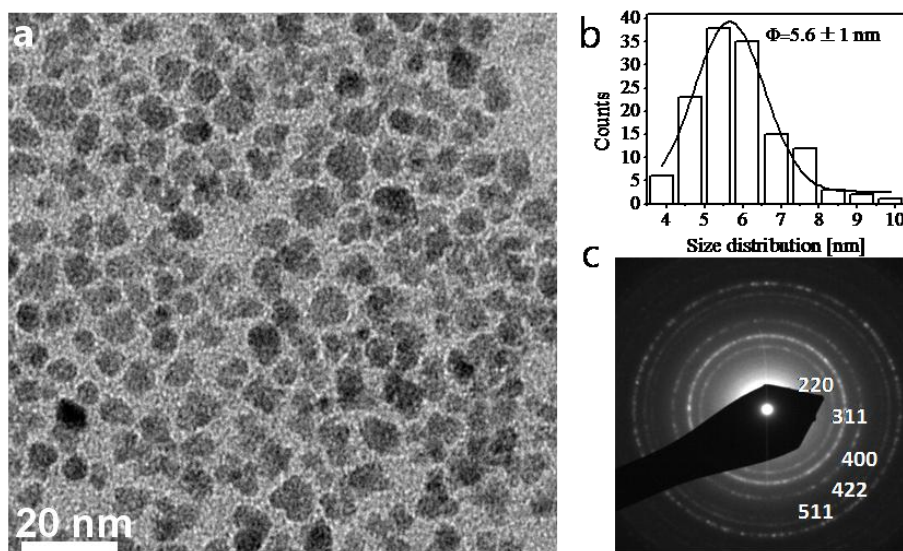


Figure 4. a, TEM image of the PVP-SPIONs. b, Size distribution histogram of PVP-SPIONs. c, select area electron diffraction of PVP-SPIONs.

The water solubility and hydrodynamic size distribution of the obtained three SPIONs were monitored by dynamic light scattering (DLS), and their surface charges were determined by zeta potential measurements. DLS volume-weighted size distributions indicated T-SPIONs, C-SPIONs and PVP-SPIONs are highly dispersible in water, as evidenced by the narrow size distribution observed Fig. 5a. Due to the hydrophilic nature of the three stabilizers, the obtained SPIONs could maintain their stability in water for 6 months, no aggregations were observed. PVP-SPIONs and C-SPIONs display the similar hydrodynamic diameter (D_h), about 14 nm, while T-SPIONs show a larger D_h size at around 19 nm, which is about 5 nm larger than the other two samples. It is noteworthy DLS measures the fluctuations of the scattered lights caused by the random Brownian motion of nanoparticles dispersed in solution, hydrodynamic radius is calculated based on the detected fluctuations using Stokes-Einstein equation. In fact, D_h measured by DLS is the "Stokes" size, which does not reflect the real size of the nanoparticle core. Moreover, different coatings on NPs surface can cause the Brownian motion of nanoparticles in solution differently. As a result, different D_h values were measured. Surface charges on SPIONs surface with different coating were also determined by zeta potential measurements. Zeta potential values for T-SPIONs, C-SPIONs and PVP-SPIONs are -54 mV, -36 mV and -32 mV respectively, indicating all the three SPIONs are highly negatively charged.

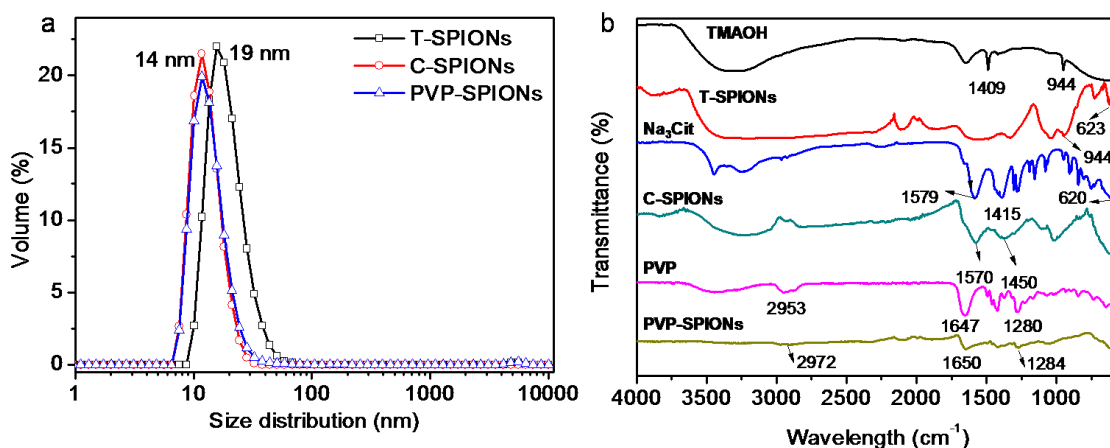


Figure 5. a), DLS volume-weighted size distribution of T-SPIONs, C-SPIONs and PVP-SPIONs dispersed in H₂O. b), FTIR spectra of TMAOH, Na₃Cit, PVP, T-SPIONs, C-SPIONs and PVP-SPIONs.

Surface coating of the obtained SPIONs were also investigated by FTIR measurements, results are shown in Fig. 5b. FTIR spectrum of T-SPIONs, C-SPIONs and PVP-SPIONs present adsorption bands at around 620 cm⁻¹, these bands are attributed to the Fe-O stretching vibration, evidencing the existence of magnetite¹³. Typical band for TMAOH at 944 cm⁻¹, characteristic of the asymmetric methyl deformation mode of C-N on TMAOH¹⁴, was found to shift to 975 cm⁻¹, indicating the existence of TMAOH on T-SPIONs. Peaks at 1570 cm⁻¹ and 1450 cm⁻¹ are characteristic of the RCO₂ symmetric and asymmetric stretches¹⁵, though both peaks show a slight shift from 1579 cm⁻¹ and 1415 cm⁻¹, respectively, suggesting citrate ligand is present on the SPIONs surface. FTIR of PVP-SPIONs shows two clear peaks at 1650 cm⁻¹ and 1284 cm⁻¹, which are characteristic adsorption bands from the C=O and C-N stretching vibrations of PVP, respectively¹⁰. Peak at 1420 cm⁻¹ is assigned to the vibration of CH₂ groups of PVP. A small peak at 2972 cm⁻¹ is also observed, which corresponds to the asymmetric stretching vibration of CH₂ groups of PVP¹⁶. Compared to the FTIR spectra of pure PVP, a small red shift in all the characteristic peaks are observed for PVP on SPIONs surface, indicating the mild interaction between PVP and SPIONs.

2.4 SIZE CONTROL OF SPIONs

Applications of nanoparticles greatly depend on their physical and chemical properties, and some of the properties are strongly related to their crystal size and shape. Hence, producing nanoparticles of different size or shapes can broaden their applications. For SPIONs, their magnetic properties like saturation magnetization and blocking temperature are strongly size dependent. Therefore, to providing SPIONs with different magnetic properties, control over their size is necessary. According to La Mer's theory¹⁷, separation of nucleation and growth is the basic rule to control the size of nanoparticles,. Inhomogenous heating causes thermal gradients in the reaction solution, which could affect the homogenous generation of nuclei and subsequently cause the final product rather polydispersed. MW heating, due to its dielectric volumetric heating, is able to heat the solution homogenous and eliminate thermal gradient

produced by normal heating. The fast and homogenous heating can also realize the separation of the nucleation and growth, hence facilitate the control over nanoparticle size. Many factors can affect the size of nanoparticles in the MW synthesis process, including the classical synthetic parameters like precursor concentration¹⁸ and other microwave-specific parameters, such as temperature, reaction time, microwave frequency¹⁸⁻²⁰. Here, we focus on size control by changing microwave-specific parameters.

Size control by varying MW irradiation time is considered as a general and the simplest way. By prolonging the irradiation time from 5 min to 35 min, Bilecka observed that, the size of ZnO NPs can be tuned from 3.5 nm to 7 nm. The authors proposed that MW synthesis of ZnO NPs followed the single growth regime, dominated by a constantly ongoing Ostwald ripening¹⁸. Hence, increasing the irradiation time significantly resulted in the larger size of the synthesized ZnO NPs. In addition to MW irradiation time, MW reaction temperature also plays an important role in determining the size of the final product. In the same work mentioned above, reaction temperature was proved to have a more profound effect in controlling the NPs size compared to irradiation time. Size of ZnO NPs was observed to be tuned from 5.8 nm to 12.2 nm when temperature increased from 393K to 453K¹⁸. The authors ascribed this to the faster crystal growth rate of ZnO NPs at higher temperatures.

In our work, we also investigated the effect of reaction temperature and time on the size of SPIONs. We first prolonged the reaction time (180 °C, 20 min) but kept the other settings constant. TEM image of the obtained SPIONs are shown in Fig. 6a. Similar to SPIONs obtained in 10 min, SPIONs prepared in 20 min show a spherical shape, select area electron diffraction patterns shown in the inset also indicated the components of the obtained SPIONs were magnetite or maghemite. Differently, an increase in size was observed, the average size is observed at 7.5 nm (Fig. 6c). Then we evaluated the effect of the reaction temperature on the size of SPIONs, where the temperature was elevated to 210 °C. A larger increase in size was observed, reaching a value at about 8 nm (Fig. 6d).

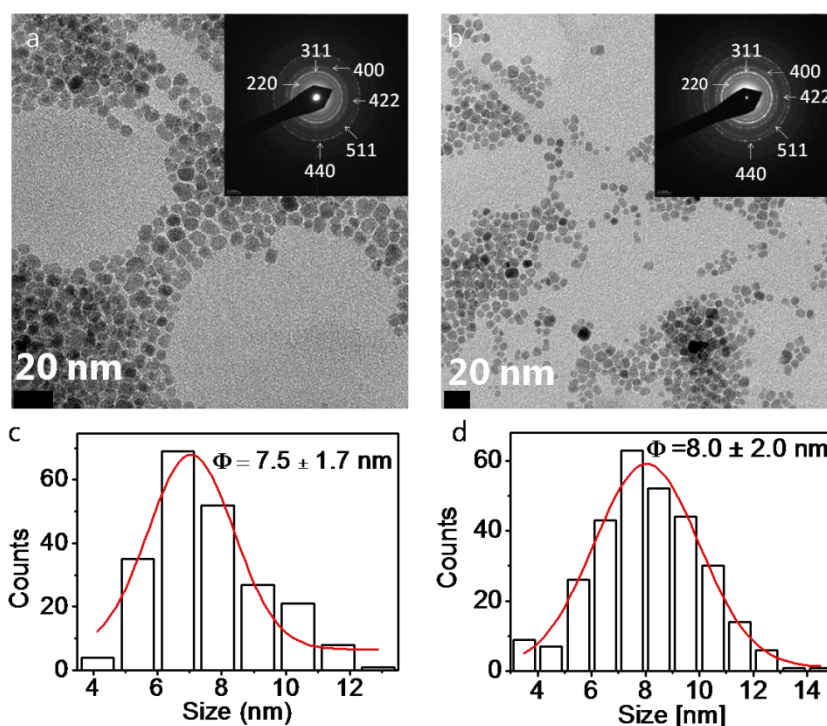


Figure 6. TEM image of the SPIONs obtained by using the MW synthesis with a heating ramp of a, 60 °C, 5 min and 180 °C, 20 min; b, 60 °C, 5 min and 210 °C, 10 min. Inset in both cases show the select area electron diffraction patterns. c and d correspond to size distribution histogram of SPIONs shown in Figure a and b, respectively.

Comparison of the size of the SPIONs synthesized under different conditions is given in Table 1. It is noteworthy that for each conditions, at least two independent experiments were performed. In particular, for SPIONs obtained under the typical MW condition, 10 individual experiments were performed, and the size was always determined to be around 6 nm. Therefore, we conclude that prolong the irradiation time and elevate reaction temperature can lead to a moderate increase in SPIONs size.

Table 1. Size comparison of SPIONs synthesized under different MW conditions (n is the replication).

	MW Heating Ramp					
	60°C	5 min	60°C	5 min	60°C	5 min
	180°C	10 min	180°C	20 min	210°C	10 min
Size (nm)	6.1 ± 1.0 nm		7.4 ± 1.5 nm		8.0 ± 2.0 nm	
n	10		2		2	

The increase in size of PVP-SPIONs was also investigated by increasing the reaction temperature to 210 °C. The morphology of the as prepared PVP-SPIONs is shown in Fig. 7a, similar to those obtained at temperature of 180 °C, spherical SPIONs core were observed. As expected, the mean size of PVP-SPIONs increased from about 5 nm to 7.3 ± 1.6 nm (Fig. 7b). The size increase

was also confirmed by DLS measurements, D_h of PVP-SPIONs obtained at temperature of 210 °C were found to be about 16.3 nm (Fig. 7c), about 2 nm larger than those synthesized at 180 °C (Fig. 5a).

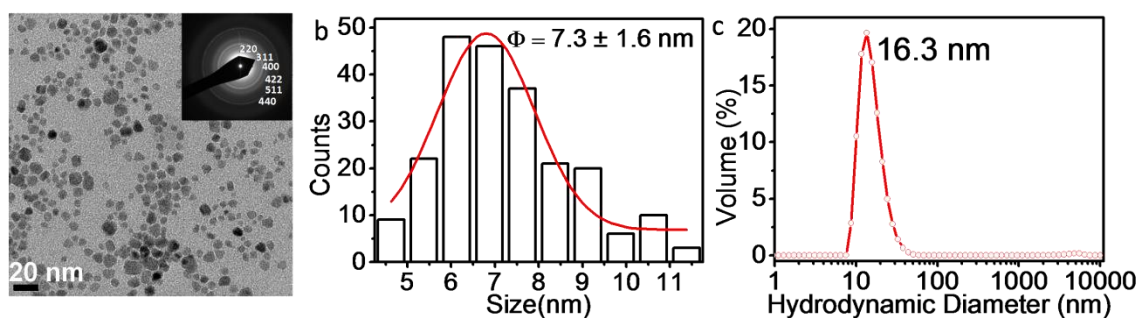


Figure 7. a, TEM image of PVP-SPIONs obtained at 210 °C, inset is the select area electron diffraction. b, size distribution histogram of PVP-SPIONs determined by TEM. c, D_h size distribution of PVP-SPIONs in MQ H₂O determined by DLS.

2.5 MAGNETIC PROPERTIES OF SPIONs

We further investigated the magnetic properties of SPIONs obtained under different microwave conditions. In particular, we select the SPIONs prepared at temperature of 180 °C and 210 °C, the resulted SPIONs were labeled as SPIONs-180 °C and SPIONs-210 °C. Also, PVP-SPIONs synthesized by the *in situ* coating process at two different temperature of 180 °C and 210 °C were chosen, corresponding to PVP-SPIONs-180 °C and PVP-SPIONs-210 °C, respectively. Magnetic properties were recorded using a SQUID magnetometer, by which magnetization curve and zero-field-cooling and field cooling magnetization curves (ZFC/FC) were obtained. Magnetization was recorded as a function the applied magnetic field up to 5 Tesla at 5K. Magnetization curves are shown in Fig. 8a. SPIONs-180 °C, with a core size at about 6 nm, display a high saturation magnetization (M_s) of approximate 85.18 emu/g_{Fe₂O₃}, indicating the high magnetic response of SPIONs-180 °C to the external magnet. In fact, the high magnetic response of SPIONs-180 °C can be clearly seen from the inset image of Fig. 8, where SPIONs dispersions response strongly to the magnet in the vicinity. Though size of SPIONs-210 °C determined by TEM shows 2 nm larger than those of SPIONs-180 °C, lower M_s value was observed, about 78.6 emu/g_{Fe₂O₃}. M_s is expected to be proportional to the size of magnetic materials, the larger the size of SPIONs, the higher the M_s value are expected. However, M_s observed for SPIONs-180 °C and SPIONs-210 °C display the opposite trend. This can be explained by the uneven size distribution of SPIONs shown in the size histogram. Though mean size of SPIONs-210 °C was determined to be 8.0 nm, however, as shown by its size distribution histogram, a fraction of SPIONs fall in the small size region, which may lower the M_s value of the whole sample. In contrast, a fraction of SPIONs with larger size is found in the size histogram of SPIONs-180 °C, which may result in the larger M_s value. The similar trend is also observed for PVP-SPIONs obtained at temperature of 180 °C or 210 °C, where M_s value of PVP-SPIONs-180 °C was found slightly higher than those of PVP-SPIONs-210 °C.

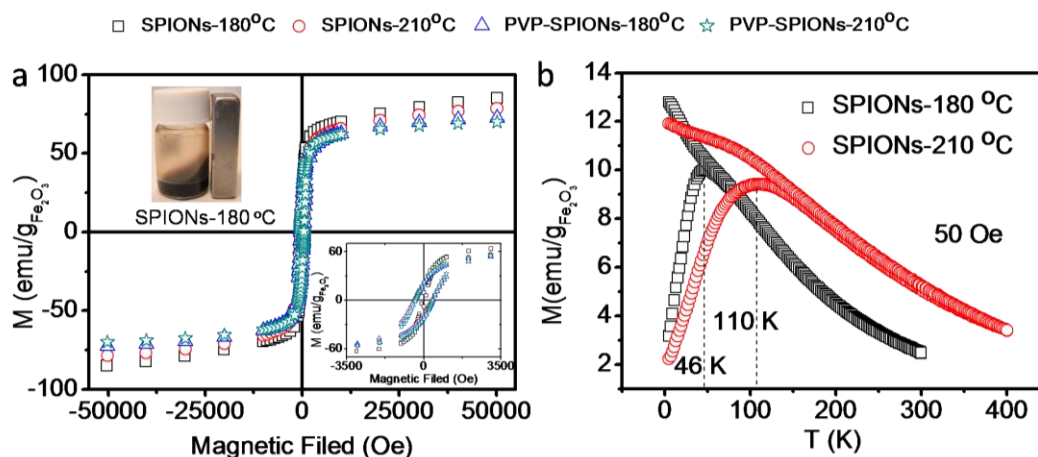


Figure 8. a, Magnetization curves of SPIONs-180 °C, SPIONs-210 °C, PVP-SPIONs-180 °C and PVP-SPIONs-210 °C were recorded as a function the applied magnetic field under 5 Tesla at 5K. Inset is the hysteresis loops at lower magnetic field. b, ZFC-FC curves of SPIONs-180 °C and SPIONs-210 °C were plotted as a function of temperature in a fixed magnetic field of 50 Oe.

Inset in Fig. 8a shows the magnetization curves (hysteresis loop) at lower magnetic field, from where other magnetic properties, remanent magnetization (M_r) and coercivity can be determined. Results are summarized in Table 2. M_r value for SPIONs-180 °C is found at about 9.25 emu/g_{Fe₂O₃}, which is much lower than that of SPIONs-210 °C, with a value of 20.5 emu/g_{Fe₂O₃}. PVP-SPIONs-180 °C and PVP-SPIONs-210 °C showed a similar M_r value at around 22 emu/g_{Fe₂O₃}. Similar to M_r value, coercivity of SPIONs-210 °C was also observed much larger than that of SPIONs-180 °C, indicating its stronger magnetic response than PVP-SPIONs-180 °C. No difference in coercivity was observed for PVP-SPIONs-180 °C and PVP-SPIONs-210 °C. ZFC/FC curves were recorded for SPIONs-180 °C and SPIONs-210 °C. Blocking temperature (T_B) of SPIONs-180 °C were found to be 46 K, while SPIONs-210 °C showed a much higher value at 110 K (Fig. 8b). Since T_B is proportional to the size of the magnetic core, higher T_B observed for SPIONs-210 °C than SPIONs-180 °C indicating the larger mean size of SPIONs-210 °C. Moreover, the obtained T_B in both cases indicate their superparamagnetic property.

Furthermore, we evaluated the effect of the temperature on the yields of the obtained SPIONs, results were given in Table 2. It was observed that, higher temperature lead to the high yields of SPIONs. The yield of SPIONs-180 °C was found only at 50% at a temperature of 180 °C, when reaction temperature increased to 210 °C, yields reached at 80%. PVP-SPIONs showed the similar trend, yields improved from 60 % to 70 % as the reaction temperature increased correspondingly.

Table 2. Summary of the characterization of SPIONs obtained under different reaction conditions

Sample	d (TEM) ^a (nm)	d (DLS) ^b	M _s (emu/g) ^c	M _r (emu/g) ^d	Coercivity (Oe) ^e	T _B (K) ^f	yield (%) ^g
SPIONs-180°C	6.1 ± 1	14	85.18	9.25	100.78	46	50
SPIONs-210°C	8.0 ± 2.0	15.6	78.6	20.5	381	110	78
PVP-SPIONs-180 °C	5 ± 1.1	14	73	21.19	401.58	-	60
PVP-SPIONs-210 °C	7.3 ± 1.6	16	70	22.24	401.56	-	70

^a Mean size of SPIONs determined by TEM measurements. ^b Hydrodynamic diameter of SPIONs in MQ H₂O detected by dynamic light scattering. ^c Saturation magnetization (M_s) determined from magnetization curve. ^d Remanent magnetization (M_r) determined from magnetization curve at lower magnetic force. ^e Coercivity determined from magnetization curve at lower magnetic force. ^f Blocking temperature (T_B) determined from ZFC/FC curve. ^g Yields calculated by flame atomic adsorption spectrometry.

In summary, size of SPIONs in our case, can be modified to some extent by changing microwave-specific parameters as temperatures and reaction time, the magnetic properties of the as obtained SPIONs can be modified as well. Temperature displayed more efficiency in increasing the size of SPIONs, because larger size of SPIONs were found than those obtained from the elongated time. Moreover, by simply increasing reaction temperature, the yield of the obtained SPIONs can be improved.

2.6 RELAXIVITY MEASUREMENT

Relaxivity measurements were carried out in the PVP-SPIONs-180 °C to assess their performance as MRI contrast agents. T₁ and T₂ relaxation times were measured on a 7 Tesla magnet (BioSpec 70/30 USR, BrukerBioSpin, Ettlingen, Germany) in the UAB RMN service center. Fig. 10a shows the transversal relaxations (T₂) weighted MR images at different Fe concentrations, displaying that higher concentrations of PVP-SPIONs impart darker T₂ weighted MR images (Fig. 9a). The *r*₂ relaxivity was calculated at 54.2 mM⁻¹ s⁻¹ (Fig. 9b). The longitudinal relaxivity (*r*₁) was also calculated from the longitudinal relaxations (T₁), which is given in Table 3, as well as the *r*₂ /*r*₁ ratio. In general, SPIONs are used as T₂ negative contrast agent because they can shorten the T₂ relaxation of water²¹. The obtained PVP-SPIONs *r*₂ relaxivity and the *r*₂ /*r*₁ ratio are lower compared with those of commercially available SPIONs in the same magnetic field (7T)²². We assign this is due to the small size and the good dispersity of PVP-SPIONs in water. Moreover, the *r*₁ relaxivity is also observed smaller than gadolinium tetraazacyclododecanetetraacetic acid in the same magnetic field (7 T), which is commercially available as a good T₁ contrast agent²³. However, *r*₂ and *r*₁ relaxivities are strongly magnetic field dependent²¹. We argue that PVP-SPIONs could be suitable for use as T₁ contrast agent under lower magnetic field like 1.5 T.

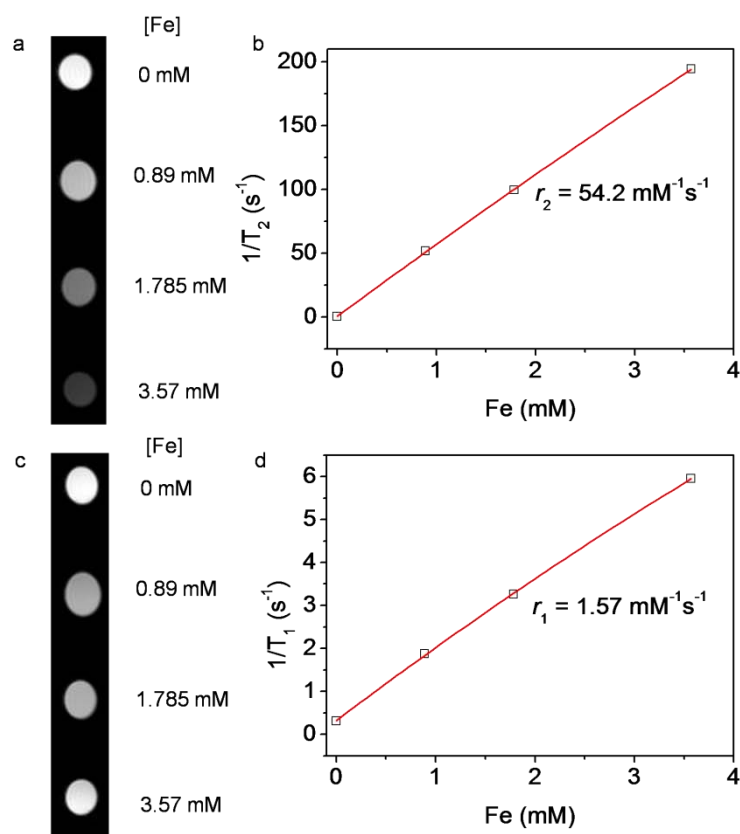


Figure 9. a) and c) T_2 and T_1 weighted MR images of PVP-SPIONs-180 °C, respectively. b) and d) Plot of $1/T_2$ and $1/T_1$ over Fe concentration of PVP-SPIONs-180 °C, respectively.

Table 3. Relaxation properties of the PVP-SPIONs-180 °C

Sample	r_1 ($\text{mM}^{-1}\text{s}^{-1}$)	r_2 ($\text{mM}^{-1}\text{s}^{-1}$)	r_2/r_1
PVP-SPIONs-180 °C	1.57	54.23	34.56

2.7 SCALE UP SYNTHESIS OF SPIONS

As the number of applications of SPIONs for nanomedicine increases, larger amounts of SPIONs at reasonable cost will be in high demand. Microwave-assisted synthesis results in high quality SPIONs, however the typical reaction volume ranges from 1 to 5 mL leading to yields less than 20 mg of SPIONs (in terms of the Fe content)⁵. As an example, FDA-approved iron oxide based MRI contrast agent Gastromark® required 52.5 mg Fe per a single adult dose. Therefore, efforts to turn a laboratory milligram-scale synthesis of SPIONs into gram-scale production are of great value.

Attempts to demonstrate large-scale synthesis of SPIONs have already been published. Co-precipitation was used by Kolen'ko *et al.* to scale up the synthesis of SPIONs using $\text{FeCl}_3 \cdot 4\text{H}_2\text{O}$ and $\text{FeCl}_3 \cdot 6\text{H}_2\text{O}$ as iron precursors.²⁴ However, the yield was relatively low (68%) and the

resulting SPIONs had poor monodispersity (polydispersity was 46%). Ibarra-Sánchez *et al.* evaluated the high temperature decomposition of $\text{Fe}(\text{acac})_3$ in a large scale and found the reaction was sensitive to the stirring rate, the stirring periods and the reaction temperature.²⁵ Unfortunately, SPIONs obtained by thermal decomposition are hydrophobic, and required of a ligand exchange before can be used for *in vivo* use. Based on the potential biomedical applications of SPIONs, the synthetic methods to scale up should not only be simple, safe, energy and cost efficient, but also affording water soluble, biocompatible and high saturation magnetization nanoparticles. All these requirements could be achieved by scaling up a microwave assisted reaction.

Previous research on scale-up of microwave-assisted organic reactions indicated that two scale-up main approaches: the flow approach and the batch-type approach (Main features of the different approaches have been summarized in Table 1 in the annex of this chapter). In our work, we aimed to study the feasibility of the microwave scale-up of SPIONs by using a batch-type approach, in particular, a multi-mode unit was chosen to achieve multigram-scale synthesis. On this purpose, we evaluate the impact of different microwave-specific factors (equipment, reaction time, temperature, power) on the reaction product, and focus on the reproducibility between the lab-scale synthesis and the scaled-up synthesis.

We started the scale-up synthesis transferring a 50 ml reaction mixture in a 100-ml Teflon vessel in the multi-mode platform Milestone ETHOS ONE, corresponding to a ~ 10 -fold scale-up of the synthesis performed in the lab-scale using single-mode CEM Discovery unit. Morphological and structural characterizations of the scaled-up batches (henceforth, referred as SU) were performed using transmission electron microscopy, selected area electron diffraction and X-ray diffraction. Dynamic light scattering was used to monitor the hydrodynamic size and the stability of the SPIONs dispersion in H_2O . The magnetic properties were recorded in a SQUID magnetometer. The yields of the reactions were determined by flame absorption spectroscopy.

To scale up the previously optimized reaction for lab-scale synthesis of C-SPIONs (referred as LS), a major issue is the direct scalability of the method.²⁶ We used the same reaction temperature and irradiation time (heating ramp: 60 °C, 5 min and 180 °C, 10 min) as in the lab-scale synthesis to investigate whether the optimized reaction conditions could be applied directly for the large-scale synthesis of SPIONs. Differently, smaller spherical SPIONs (referred as SU-1) with a mean size of 3.8 ± 0.8 nm were obtained (Fig. 10a and 10c), while hydrodynamic diameter displayed a similar value (Fig. 12a), this may due to the formation of small SPIONs aggregates as confirmed by the TEM images (Fig. 10a).

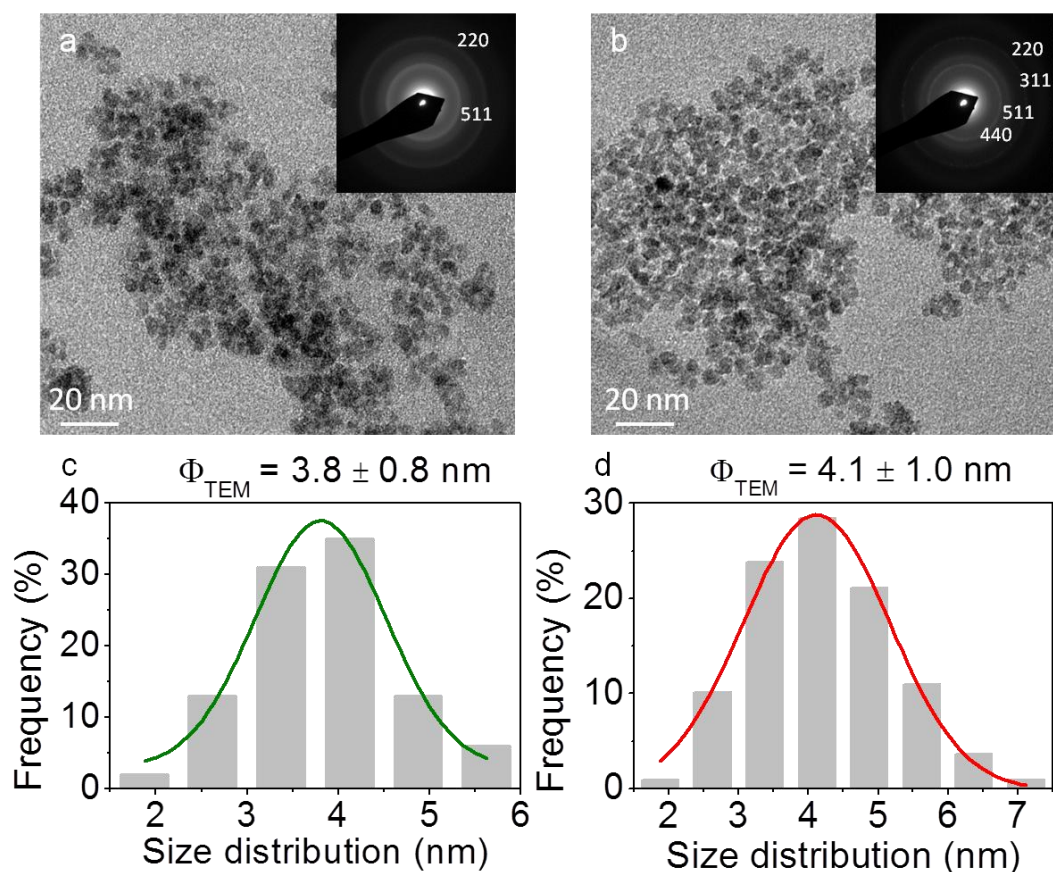


Figure 10. Characterisation of the scale-up batches by TEM. Panels a and b show TEM images of: a) SU-1 and b) SU-2. Panels c and d show the size distribution histogram of the scale-up batches: c) SU-1 and d) SU-2.

As mentioned above, microwave-specific parameters, temperature and reaction time can control the size of SPIONs moderately. Following the similar strategy, we doubled the reaction time in the scale up synthesis, while kept other reaction parameters unchanged. Extended reaction time (sample referred as SU-2) resulted in a 0.3 nm increase in SPIONs diameter, which had a mean core size of $4.1 \pm 1.0 \text{ nm}$ (Fig. 10b, 10d), and similar hydrodynamic size (Fig. 12a). Due to the larger volume of the reaction mixture, a 10-min prolongation in the reaction time didn't seem enough for complete growth of the synthesized SPIONs, and SPION size increased only slightly. In addition to MW irradiation time, effect of increase in reaction temperature of the scale up synthesis was also investigated. Interestingly, by increasing temperature to $210 \text{ }^\circ\text{C}$, we obtained SPIONs (sample referred as SU-3) with very similar TEM size and polydispersity ($5.9 \pm 1.4 \text{ nm}$) and polydispersity (24%) as the LS sample, but in a reaction volume more than 10 times larger (Fig. 11a and 11c). Similar results were found for the hydrodynamic size too (Fig. 12a and Table 5). We ascribed this size increase of $\sim 2 \text{ nm}$ to the faster crystal growth rate of SPIONs observed at higher temperatures. Although the morphological shape is slightly irregular, the obtained SPIONs were crystalline (Fig. 11b) and showed good monodispersity. The XRD patterns of SU-3 (Fig. 11d) were coincident with those of maghemite iron oxide phase and confirmed a good degree of crystallinity

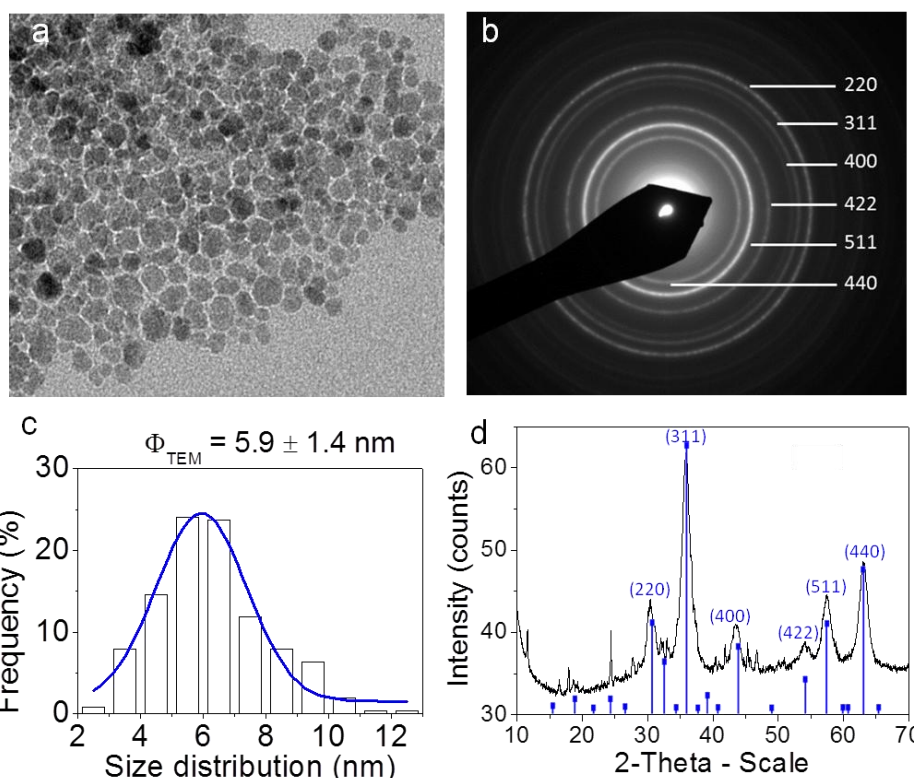


Figure 11. Characterisation of the SU-3 batch: a) TEM image, b) SAED pattern indexed to maghemite iron oxide phase, c) Size distribution histogram and mean size value, d) XRD diffractogram indexed for maghemite iron oxide phase.

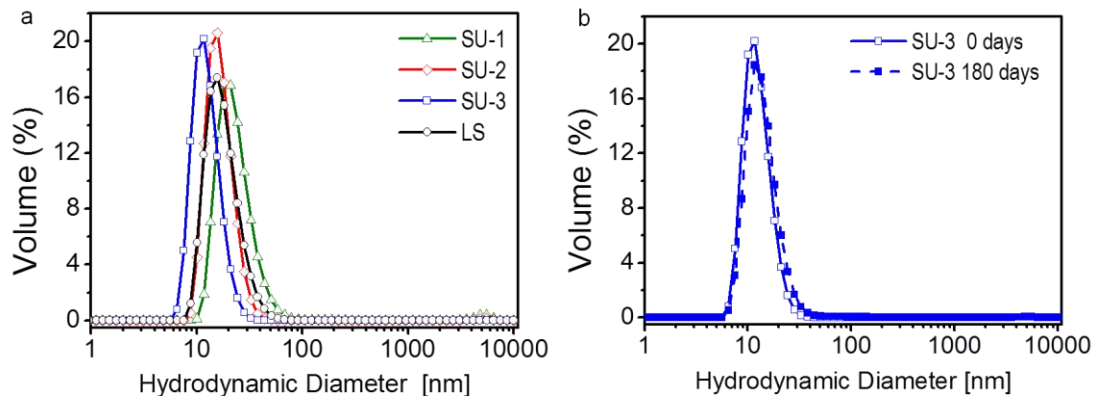


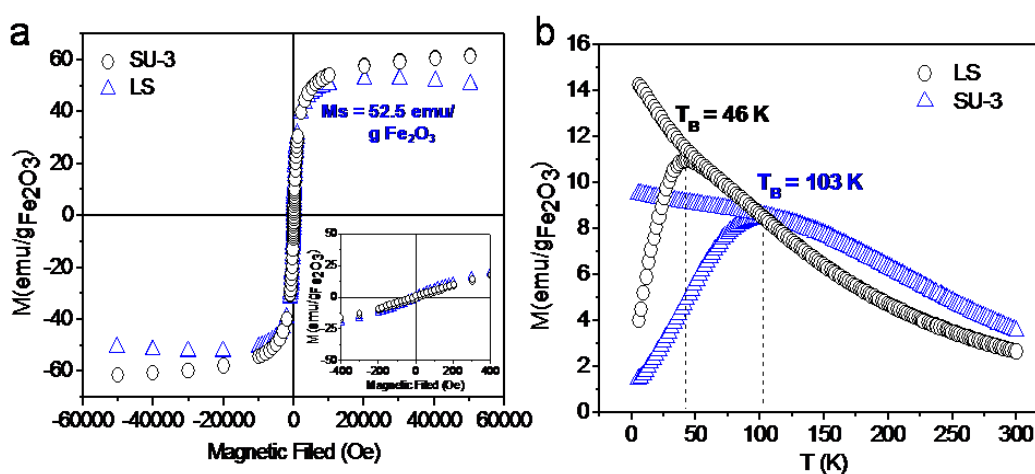
Figure 12. DLS measurements. a) Volume-weighted size distribution of the as-synthesized scale-up and laboratory batches in MQ H₂O. b) Volume-weighted size distribution of SU-3 in MQ H₂O six months after synthesis.

These results indicate a good reproducibility between the lab-scale reaction and the large-scale process after reaction parameter re-optimization, in terms of size and colloidal stability. The colloidal stability of SU-3 was re-measured 6 months after its fabrication. Fig. 12b shows that the scale-up SPIONs stored at room temperature remained stable in water, no size increase was observed. This is an extremely interesting information when considering the 'shelf-time' of those nanoparticles. A summary of the reaction parameters used is provided in Table 4. In all the cases, sodium citrate was added to both LS and SU batches to confer water dispersability to the as-synthesized SPIONs, due to the interparticle electrostatic repulsion.

Table 4. Reaction conditions of all synthesis.

	Vessel material	Vessel volume	Starting materials		Time to 60 °C	Time at 60 °C	Max. Temp	Time to max. T	Time at Max. T	Max power
			Fe(acac) ₃	Benzyl alcohol						
LS	Closed, glass	10 ml	123.6 mg (78 mM)	4.5 ml	N.C.	5 min	180 °C	N.C.	10 min	300 W
SU-1	Sealed, Teflon	100 ml	1.373 g (78 mM)	50 ml	3 min	5 min	180 °C	5 min	10 min	500 W
SU-2	Sealed, Teflon	100 ml	1.373 g (78 mM)	50 ml	3 min	5 min	180 °C	5 min	20 min	500 W
SU-3	Sealed, Teflon	100 ml	1.373 g (78 mM)	50 ml	3 min	5 min	210 °C	5 min	20 min	500 W

We further characterised the properties of the as synthesized SPIONs with respect to magnetic behaviour (Fig. 13), results are summarized in Table 5. Neither remnant magnetization nor coercivity were observed at room temperature (Fig. 13a), which corresponds to typical magnetization loops of superparamagnetic materials. A saturation magnetization of 53 emu/g Fe₂O₃ was determined at 300 K (Table 5), which was slightly lower than our value of the LS sample (62 emu/g Fe₂O₃), this could indicate a slightly less crystalline structure. Even though, the high value of the saturation magnetization for the SU-3 system at room temperature is a strong indication of the crystallinity of the material since poorly crystalline samples would show a much lower value. Superparamagnetism of SPIONs for all batches was confirmed by the ZFC-FC measurements. The blocking temperature correlates very well with the mean size of the nanoparticle determined by TEM and DLS with the lowest T_B for the smallest particles (SU-1) (Fig. 13c). The blocking temperature (T_B) of the scaled batch was significantly higher than those from the small-scale batch (103 and 49 K, respectively) (Fig. 13b and c), which can be attributed to the slightly larger size and size distribution of SU-3 SPIONs. Still, this increase on T_B do not compromise the superparamagnetic behaviour of the final material as it is far below room temperature. Thus, SU-3 nanoparticles are superparamagnetic at room temperature. These results indicate that the SPIONs prepared in the lab-scale and large-scale are comparable regarding the magnetic properties of the final products.



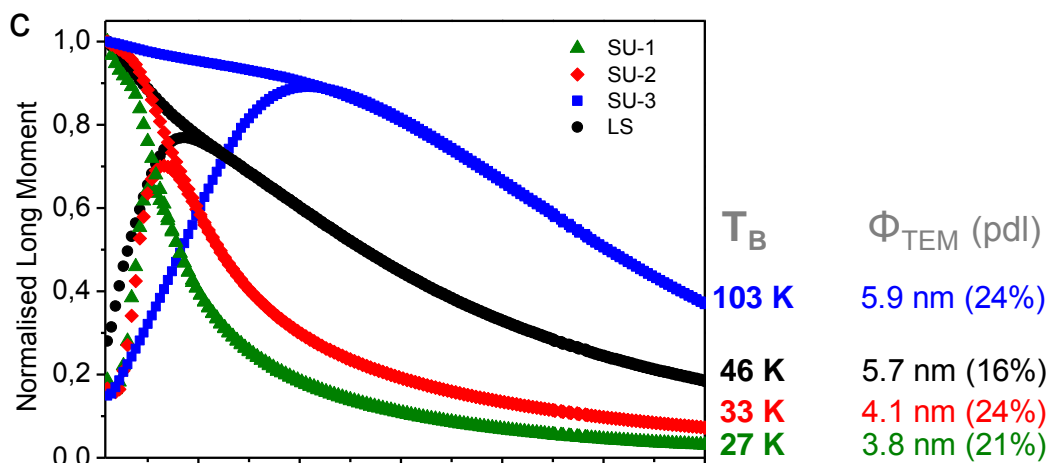


Figure 13. Magnetization curves (a) and Zero-Field-Cooling Field-Cooling (ZFC-FC) curves of LS and SU-3. Magnetization curves were measured at 300 K, ZFC-FC curves were measured at a 50 Oe applied field. c) Zero-Field-Cooling Field-Cooling (ZFC-FC) measurements of LS and SU batches at a 50 Oe applied field.

Table 5. Physicochemical characterization of the laboratory-scale (LS) and the scale-up (SU) batches.

	Lab-Scale (LS)	Scale-up (SU)
TEM size (nm)	5.7 ± 0.9	5.9 ± 1.4
Hydrodynamic size (nm)	17	16
Saturation magnetisation at 300 K (emu/g Fe₂O₃)	62	53
Blocking temperature at 50 Oe (K)	49	103
Yield (% Fe)	50-78%	84%
Mass of NPs per vessel (mg Fe₂O₃)	22	261

Finally, we computed the yield of the scale-up process through the iron concentration measured by flame absorption spectroscopy (Table 5). Under the optimal conditions of the scale-up experiments, a yield of 84 % was obtained, which is higher than lab-scale synthesis in the single-mode equipment (ranges from 50% to 78% as shown in Table 2). Interestingly, Panzarella *et al.* found that the rate of nucleation was more rapid in a multi-mode oven than in a single-mode unit with a more uniform field²⁷, which could account for the higher yield observed. Upon microwave irradiating of one single vessel, we synthesized 261 mg Fe₂O₃ nanoparticles (Table 5), corresponding to more than 10 times the amount obtained in the laboratory scale synthesis (22 mg). Using the optimized reaction conditions, our synthesis could be further scaled-up 10 times using the parallel synthesis approach by integrating a multivessel rotor system in the multimode instrument. These would allow us to produce ~3 grams of nanoparticles in half an hour with a very low energy consumption (<1 kW). Using the single-mode equipment, the same amount of production would require 32 hours of MW irradiation, with its associated high energy consumption (~10 kW) and cost. Table 6 compares the cost associated with the production of

10 g Fe₂O₃ NPs in the lab-scale and after the scale-up equipment. Hence, the reported scale-up notably shortens the synthesis times and reduces the energy consumption compared to the lab-scale process without significantly altering the physicochemical properties of our final material consisting on high quality water soluble SPIONs.

Table 6. Cost estimate to produce 10 g of SPIONs by microwave-assisted reaction.

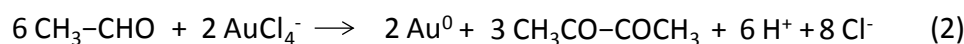
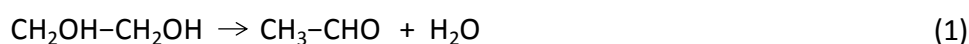
	Lab-Scale (LS)	Scale-up (SU)
Time ^a (hours)	136	2
Energy consumption (KWh)	40.9	1.1
Energy cost ^b (€)	3.75	0.10
Reagents price ^c (€)	86.36	80.61
Labour cost ^d (€)	3.231.82	49.94
Total cost (€)	3.321.93	130.65

^aCalculated by considering the necessary time used in one batch and adding the required batches to yield 10 g of material. ^bA 0.0917 €/kWh energy price was assumed according to Eurostat (<http://ec.europa.eu/eurostat>). ^cFor the reagents, supplier prices from 2014 were used. ^dA 23.7 €/hour labour cost was assumed according to Eurostat (<http://ec.europa.eu/eurostat>).

2.8 MICROWAVE SYNTHESIS OF Au NANOPARTICLES.

Gold nanoparticles have been widely studied motivated by their interesting optical properties. The characteristic localized surface plasmon resonance (LSPR) make gold nanoparticles useful in many biomedical applications such as imaging²⁸, sensing²⁹, drug and gene delivery³⁰ and photothermal therapies³¹. Various approaches have been developed for synthesizing gold nanoparticles, as introduced in Chapter 1. Among them, PVP-mediated polyol process has been revealed to be a facile, fast and efficient way. By performing the PVP-mediated polyol synthesis, not only the size of Au crystals can be easily controlled³², but also their shape can be tuned accordingly^{33,34}. In the PVP-mediated polyol process, liquid polyol serves as both the solvent and the mild reducing reagent³⁵, while PVP was used as the capping reagents for stabilizing the formed Au nanocrystals⁸. In this work, ethylene glycol (EG) and benzyl alcohol (BA) were selected as our reaction solvent to synthesize Au nanocrystals. EG was chosen because it is one of the most commonly used solvent in the polyol synthesis of Au nanocrystals with well-defined nanostructures⁸. Since our synthesis of SPIONs was performed in BA, we also performed Au nanocrystals synthesis experiments in BA. Briefly, synthesis of Au nanoparticles involved mixing 10⁻⁶ mol HAuCl₄ in 2 ml EG or BA with the addition of appropriate amount of PVP, the mixture was then heated to 120 °C in the normal heating plate and maintained for 10 min. During the synthesis process, molar ratio of PVP to HAuCl₄ at 2:1 and 10:1 were chosen to evaluate the effect of PVP on the final size of Au nanocrystals. After the synthesis, Au nanoparticles were purified by two times washing/precipitation with acetone, and finally dispersed in MQ H₂O for further characterization. The synthetic mechanisms of Au in EG and BA are given in Fig. 14^{8,36}.

Au synthesized in EG



Au synthesized in BA

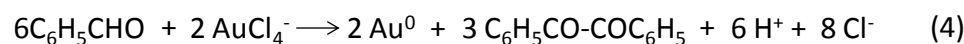
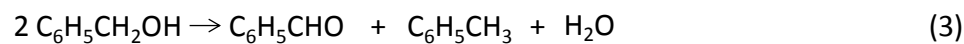


Figure 14. Synthetic mechanism of Au nanoparticles in EG and BA

Due to the surface plasmon oscillation of Au nanoparticles, Au nanoparticles dispersions display characteristic colors, which are size and shape dependent³⁷. In other words, color of the Au nanoparticles dispersions provides visible information about the size and shape Au nanocrystals. The color of the Au dispersion changes as size or shape of the Au crystals changes. In general, ultra-small Au nanospheres (in the range of several nanometers) show a characteristic ruby red color, increase in Au size can change its red color to blue (several ten nanometers)³⁸. The digital images of Au nanoparticles synthesized under different conditions were shown in the inset of Fig. 15. For Au nanoparticles synthesized in EG and BA, different molar ratio of PVP to HAuCl₄ resulted in different colors, suggesting Au nanoparticles with different size were synthesized. For Au NPs synthesized in EG, red-purple dispersion was obtained when molar ratio of PVP to HAuCl₄ was kept at 2:1, Au dispersion color changed to ruby red when mole ratio of PVP to HAuCl₄ increased to 10:1. In the case of Au NPs synthesized in BA, similar phenomenon were observed. Purple Au dispersion were prepared at a molar ratio of PVP to HAuCl₄ of 2:1, Au dispersion obtained at molar ratio of PVP to HAuCl₄ of 10:1 displays a red-purple color. To compare the size of Au nanoparticles synthesized in different conditions, DLS measurements were performed. We observed that the hydrodynamic size of Au nanoparticles synthesized in EG is always smaller than those synthesized in BA, when same amount of PVP was used. Size of Au nanoparticles prepared in EG decreased from 19 nm to 9 nm when molar ratio of PVP to HAuCl₄ increased from 2:1 to 10:1. Hydrodynamic size of Au nanoparticles prepared in BA at a molar ratio of PVP to HAuCl₄ of 10:1 was determined to be 32 nm, which is 24 nm larger than those obtained in EG using the same amount of PVP. This must due to the weak reducing ability of BA comparing to EG, since only one hydroxide group is found in each BA molecule. As shown in Fig. 14, to prepare the same amount of Au nanoparticles, it requires double amount of BA than EG, indicating more efficiency of EG in reducing Au precursor to Au nanoparticles than BA. Therefore, in the same reaction conditions, fewer Au nuclei were likely to be synthesized in BA, which resulted in the larger size of the final Au nanoparticles in BA than those obtained in EG.

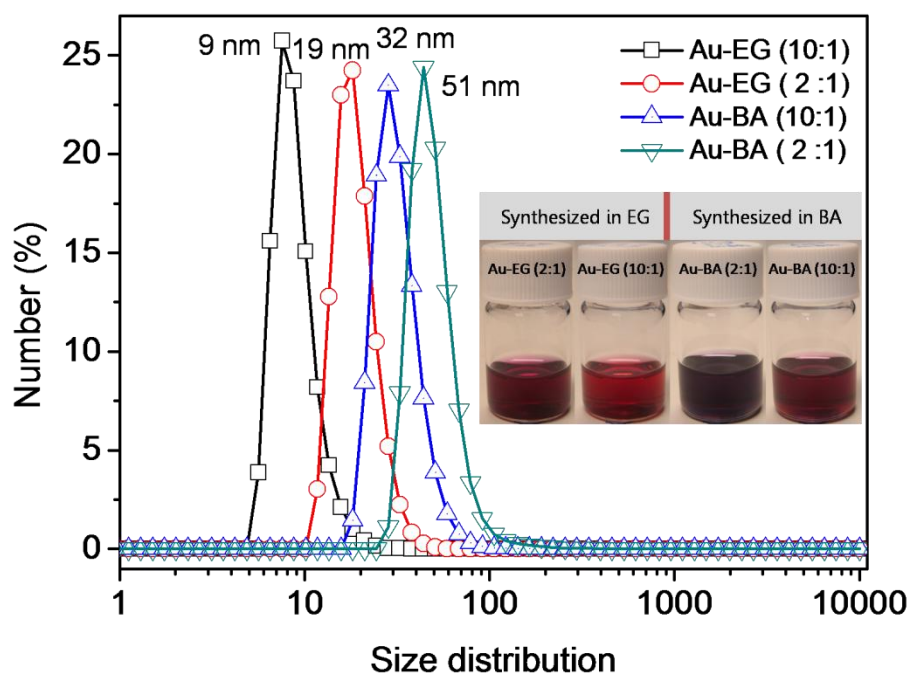


Figure 15. Number-weighted hydrodynamic size distribution of the obtained Au nanoparticles dispersed in H₂O monitored by dynamic light scattering. Inset are the digital images of the corresponding Au samples.

It is well known that Au nanoparticles display characteristic surface plasmon resonance, which has been revealed to depend on the shape, size and dielectric constants of the metal and the surrounding material³⁷. Changes in Au nanoparticles size could change their surface geometry, which in turn could cause the shift of their typical surface plasmon resonance (SPR) band. Generally, increase in Au nanoparticles size lead to a red shift of their surface plasmon resonance band, while a blue shift means a decrease in size. The surface plasmon resonance of Au nanoparticles prepared under different conditions were characterized by UV-Vis spectrometry, results were shown in Fig. 16. In both cases (in EG and in BA), increasing the amount of PVP caused a blue shift of the band, indicating smaller Au nanoparticle was synthesized in the presence of more PVP, which is consistent with the DLS measurements. For Au nanoparticles synthesized in EG, two narrow adsorption bands can be observed at around 540 nm and 535 nm, corresponding to Au nanoparticles synthesized at molar ratio of PVP to HAuCl₄ of 2:1 and 10:1, respectively. Au nanoparticles synthesized in BA at a molar ratio of PVP to HAuCl₄ of 2:1 display a SPR band at around 580 nm, 20 nm blue shift is found when increasing the amount of PVP.

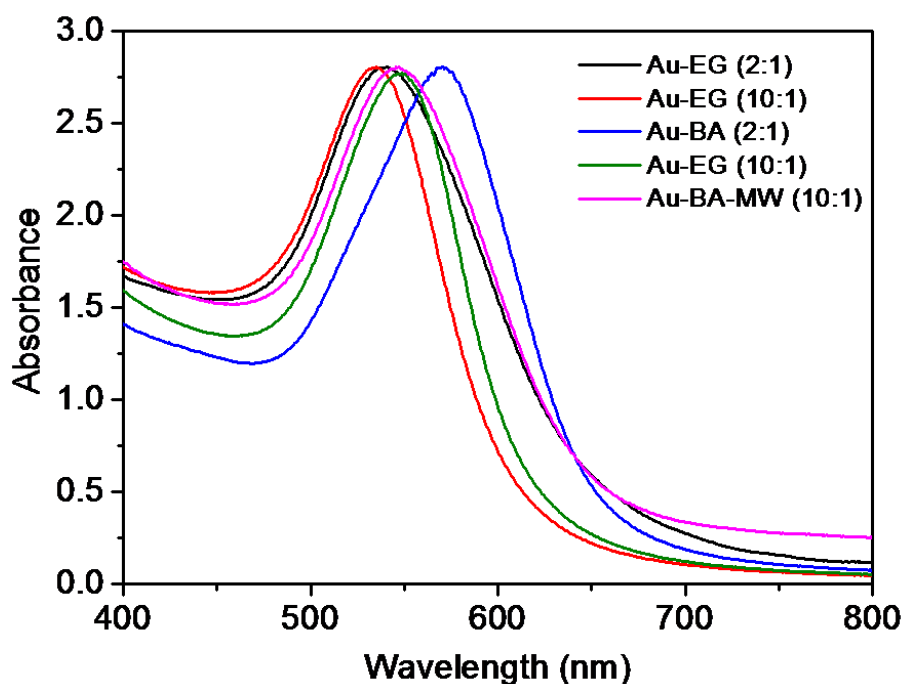


Figure 16. UV-Vis spectra of Au nanoparticles obtained under different conditions. Au-EG abbreviated for Au NPs synthesized in EG using normal heating method, Au-BA abbreviated for Au NPs synthesized in BA using normal heating method, Au-BA-MW abbreviated for Au NPs synthesized in BA using microwave heating method.

Finally, microwave synthesis of Au nanoparticles was also performed, where BA was chosen as the reaction solvent, a molar ratio of PVP to HAuCl_4 of 10: 1 was used. The resulted Au nanoparticles showed a band position at around 545 nm, a slight blue shift is observed compared to those obtained by the normal heating method using the same molar ratio of PVP to HAuCl_4 in BA (Fig. 16). The as obtained Au nanoparticles by microwave heating were further characterized by TEM, electron diffraction and DLS, as shown in Fig. 17. TEM image displays small, regular and spherical Au nanocrystals (Fig. 17a), with a mean size about 10 ± 1.8 nm (Fig. 17b). Electron diffraction patterns indicate single crystal of Au nanoparticles have been obtained. Narrow size distribution, with a mean size centering at 21 nm was observed by DLS measurements (Fig. 17c), indicating the monodispersity of the obtained Au nanocrystals. In comparison with Au nanoparticles obtained by the normal heating method in BA using the same amount of PVP, a 10 nm decrease was observed in their hydrodynamic size, though a slight blue shift in the UV-Vis spectra. In fact, for small Au nanospheres, some changes in their size only cause slight change in their surface plasmon resonance³⁷. The smaller size of Au nanoparticles obtained by microwave method may due to the faster heating rate conferred by microwave radiation. Faster nucleation and growth of Au nuclei in BA leading to the formation of smaller Au nanoparticles.

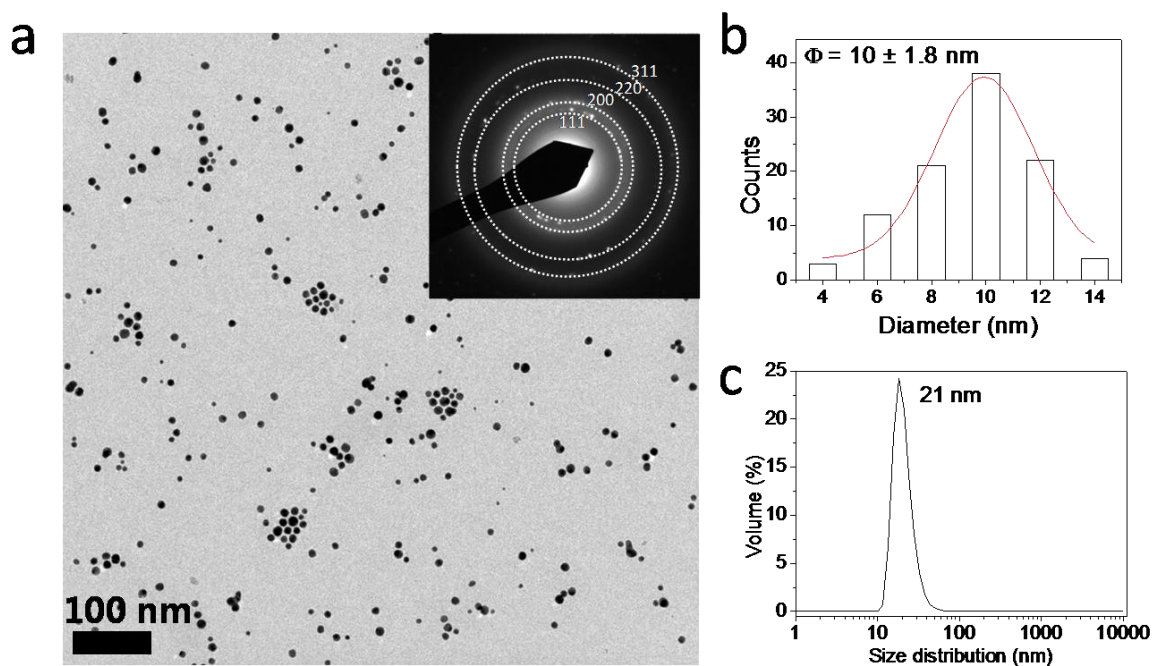


Figure 17. a, TEM image of Au nanoparticles obtained by microwave heating in BA at a mole ratio of PVP to HAuCl_4 of 10: 1, inset is the select area electron diffraction. b, Size distribution histogram of Au nanoparticles determined by TEM measurements. c, Number-weighted hydrodynamic size distribution of the obtained Au nanoparticles dispersed in H_2O monitored by dynamic light scattering.

2.9 CHAPTER CONCLUSIONS

We used MW method to synthesize spherical SPIONs with the size about 6.1 ± 1 . Both *in situ* coating and post-synthetic coating method were used to functionalize the SPIONs surface. PVP, TMAOH and Na₃Cit were chosen as the stabilizers, leading to the synthesis of PVP-SPIONs, T-SPIONs and C-SPIONs, respectively. All these three SPIONs displayed good dispersity and stability in H₂O. By simply increasing the MW irradiation time and reaction temperature, a moderate increase in size was observed for SPIONs. We revealed that increase in irradiation time and reaction temperature affected the final SPIONs size differently. Longer irradiation time prolonged the Ostwald ripening time of SPIONs, while higher temperature promoted a faster crystal growth rate for SPIONs. Magnetometry experiments showed the superparamagnetic behavior of our synthesized SPIONs, different magnetic properties in terms of saturation magnetization, remanent magnetization, coercivity and blocking temperature were found for SPIONs with different coating and size. Moreover, we observed that increasing reaction temperature could also improve the yields of the SPIONs.

Moreover, we tested the feasibility of large scale up synthesis of SPIONs by using a multi-mode MW apparatus. We revealed that larger scale-up synthesis of SPIONs by directly using previously optimized reactions at the laboratory-scale is a big challenge, which involves defining a new process setup able to achieve good reproducibility with the lab-scale product. By carefully optimizing microwave-specific parameters (reaction temperature, time, and power), SPIONs with very similar size, colloidal stability and magnetic properties as those produced in the lab-scale synthesis can be obtained. Our large-scale set up allows the synthesis of up to 3 grams SPIONs per reaction by means of implementing a multivessel rotor system in less than 1 hour. These results are of value from an industrial viewpoint, as multi-mode equipments overcome the bottleneck in productivity associated with single-mode microwave systems, where reactions must be processed sequentially, and make feasible multigram production of SPIONs by MW-assisted synthesis.

Finally, we also synthesized small Au nanoparticles by a polyol synthetic process by either normal plate heating or microwave heating, in the presence of PVP. EG showed a stronger reducing ability than benzyl alcohol, as smaller size of Au nanoparticles were always observed in the EG synthetic process. By simply changing the molar ratio of PVP to Au added in the reaction system, the size and the optical property of Au nanostrystals can be tuned moderately. In addition, we transferred the polyol synthesis of Au nanostrystals from the normal plate heating to microwave heating. In 10 min, small Au nanoparticles with the mean size around 10 nm were obtained. The Au nanostrystals are monodispersed in water.

2.10 ANNEX OF CHAPTER 2

In this part, detailed information about the MW synthesis process of SPIONs, MW scale-up synthesis of SPIONs, synthesis of Au nanoparticles and characterization of SPIONs are described.

2.10.1. MW SYNTHESIS OF SPIONs

MW-assisted method was used to synthesize pristine SPIONs in a CEM Discover reactor (Explorer 12-Hybrid) at a frequency of 2.45 GHz and 300 W. Briefly, 0.35 mmol $\text{Fe}(\text{acac})_3$ were dissolved completely in 4.5 mL anhydrous benzyl alcohol in a special MW-tube and vortexed for 30 seconds. Reaction tubes were transferred to the microwave reactor, the heating ramp was 5 min at 60 °C and 10 min reaction at 180 °C, and further cooled down to 50 °C in 3 min using compressed nitrogen.

2.10.1.1. MW SYNTHESIS OF T-SPIONs

20 μL 25 wt. % TMAOH was added to each MW-tube and sonicated for 1min. Then the solution of SPIONs is divided into 2 equal parts in 50 ml centrifugal tubes. Each tube was filled with acetone and centrifuged at 6000 rpm for 30 min. After removing the supernatant, 20 μL 25 wt. % TMAOH was added to each tube and sonicated for 1min, SPIONs were then washed and centrifuged three times. Collected SPIONs pellets were dried completely in a 60 °C oven overnight, and redispersed in 2 ml MQ H_2O containing 10 μL 25 wt. % TMAOH; pH of the obtained T- SPIONs colloidal dispersion was about 11.

2.10.1.2 MW SYNTHESIS OF C-SPIONs

150 μL 10 wt.% Na_3Cit was added to each reaction MW-tube and sonicated for 1min. Then, the solution of SPIONs is divided into 2 equal parts in separate 50 ml centrifugal tubes. Each centrifugal tube was filled up to 50 ml with acetone to wash the SPIONs and the tubes were then subjected to centrifugation at 6000 rpm for 30 min. After removing the supernatant, 150 μL 10 wt.% Na_3Cit was added to each centrifugal tube and sonicated for 1min. SPIONs were washed and centrifuged again under the same conditions. Collected SPIONs pellets were dried completely in a 60 °C oven overnight, and redispersed in 2 ml MQ H_2O ; pH of the obtained C-SPIONs colloidal dispersion was about 8.3.

2.10.2. MW SYNTHESIS OF PVP-SPIONs

Similarly, CEM Discover reactor (Explorer 12-Hybrid) at a frequency of 2.45 GHz and 300 W. Briefly, 0.035 mmol $\text{Fe}(\text{acac})_3$ and 680 mg PVP were dissolved completely in 4 mL anhydrous benzyl alcohol in a special MW-tube and vortexed for 30 seconds. Reaction tubes were transferred to the microwave reactor, the heating ramp was 5 min at 60 °C and 10 min reaction at 180 °C, and further cooled down to 50 °C in 3 min using compressed nitrogen. The obtained black solution was divided into 2 equal parts in separate 50 ml centrifugal tubes. Each centrifugal tube was filled up to 50 ml with acetone to wash the SPIONs and the tubes were

then subjected to centrifugation at 6000 rpm for 30 min. Washing steps repeated twice before redispersed in 2 ml MQ H₂O.

2.10.3. SCALE-UP SYNTHESIS OF SPIONS IN A MULTIMODE MW APPARATUS

Scaled-up synthesis of SPIONS was performed in a multi mode Milestone ETHOS One unit at a frequency of 2.45 GHz and 500 W. Briefly, 1.373 g Fe(acac)₃ were dissolved completely in 50 mL anhydrous benzyl alcohol in a 100 ml Teflon tube and vortexed for 30 seconds. The reaction tube was placed into a protective sleeve, sealed with a screw-top, and transferred to the microwave reactor. The heating ramp was 3 min from RT to 60 °C, 5 min at 60 °C, 5 min to the maximum temperature (either 180 °C or 210 °C), and 10 to 20 min reaction at maximum temperature (as indicated in Table 3). The reaction tube was cooled down to 85 °C within 15 min by means of a high airflow over the vessels, and then cooled to RT in an ice bath (~10 min). Direct temperature monitoring and control was achieved via a fiber-optic probe inserted into the reaction vessel. 1.7 mL 10 wt.% Na₃Cit was added to the reaction tube and sonicated for 5 min. Then an aliquote of the as synthesized SPIONS was washed twice with acetone following the same way as described for single-mode. Collected SPIONS pellets were dried and redispersed in MQ H₂O.

2.10.4. BRIEF DESCRIPTION OF MICROWAVE EQUIPMENT

The introduction of dedicated scientific microwave equipment has been critical to allow reproducible protocol development and scale-up. Today's available instrumentation allow for careful control of the reaction parameters, including direct temperature measurement of the reaction mixture with the aid of fibre-optic probes or infrared sensors, and software that allows on-line temperature/pressure control by regulation of the microwave power. There are two main types of scientific microwave apparatus: single-mode and multi-mode. Lab-scale syntheses are performed using single-mode reactors, which generate a single, highly homogeneous energy field of high power density. These systems couple efficiently with small samples and the maximum power output is in most cases limited to 300 W. Multimode units have a larger microwave cavity, allowing the use of bigger reaction vessels or the use of multivessel rotors which will be simultaneously irradiated. Here, the microwaves that enter the cavity are reflected by the walls and the load over the large cavity. Hence, field homogeneity is a key parameter determining the final properties of the as synthesized material in multi-mode systems.^{26,39,40}

For our experiments, all equipment used is commercially available. Lab-scale reactions using a single-mode microwave unit were performed in a CEM Discover microwave unit. Scale-up reactions using sealed-vessel synthesis were performed in a multimode Milestone ETHOS One unit.

CEM Discover: The instrument, consisted of a focused microwave system with selectable power output from 0 to 300 W. The temperature was monitored using an IR sensor located underneath the reaction vessel. Temperature, pressure and power profiles were monitored using

commercially available software provided by the microwave manufacturer. The cooling option, using compressed nitrogen, was used to cool vials in few minutes.

Milestone ETHOS One. The instrument, equipped with two magnetrons, has a combined output power from 0 to 1500 W. One Teflon vessel of 100 ml capacity was employed in our experiments. The reagents were placed into the vessel, and it was in turn placed into a protective sleeve and sealed with a screw-top. Direct temperature monitoring and control was achieved via a fiber-optic probe inserted into the reaction vessel. While there was no direct pressure measurement, the spring mechanism in the Teflon vessel cover ensures a pressure point of 20 bar is not exceeded. In the case of overpressure, the system automatically releases the pressure and the vessel then reseals. Reaction parameters (temperature, power and time) were programmed into a controller unit. The software utilized the fiber optic sensor to adjust the power required at each time point to reach the programmed temperature.

2.10.5 SYNTHESIS OF GOLD NANOCRYSTALS

Gold nanocrystals were produced by a modified polyol process, in our case ethylene glycol (EG) and benzyl alcohol (BA) were chosen as the solvent. Briefly, different amount of PVP (50 or 100 mg) and 1 μL HAuCl_4 (250 mM in EG) were added to the solvent, the mixture was sonicated and vortexed for about 5 min to form a homogeneous solution. For conventional heating method, the mixture was put on a normal heating plate and the temperature was increased up gradually to 120 $^\circ\text{C}$ and kept for 10 min. For microwave heating, the mixture was transferred into a CEM Discover reactor (Explorer 12-Hybrid) at a frequency of 2.45 GHz and 300 W, then following a heating ramp of 120 $^\circ\text{C}$, 10 min. The obtained Au dispersions were then washed twice by adding sufficient acetone and centrifuged at 6000 rpm for 30 min to remove the excess PVP. Finally, the collected Au precipitates were dispersed in H_2O for further characterization.

2.10.6. CHARACTERIZATION

2.10.6.1. DLS MEASUREMENTS.

DLS measurements were performed to monitor the changes of SPIONs in the hydrodynamic diameter (D_h), polydispersity Index (PDI) and diffusion coefficient, which are all relative to the stability of SPIONs dispersions over time.

D_h of the C-SPIONs and T-SPIONs were determined by using a Zetasizer Nano ZS (Malvern) device with a He/Ne 633 nm laser at 25 $^\circ\text{C}$ and at a SPIONs concentration of 50 $\mu\text{g}/\text{mL}$. For each sample, 3 independent measurements were performed with 15 scans for each measurement.

DLS measures the fluctuations of the intensity of the scattered lights caused by the random Brownian motion of NPs in solution. This fluctuation can be quantified through the autocorrelation function (ACF), $G(\tau)$ given by Eq. (1), where τ is the time difference between 2 measured signals. For monodisperse NPs, the correlation function can be expressed as Eq. (2), where A is the baseline of the correlation function, B is the intercept of the correlation function, Γ is the decay rate (the inverse of the correlation time). The relationship between Γ and

translational diffusion coefficient D is shown by Eq. (3). q is determined by Eq. (4), where n is the refractive index of dispersant, λ_0 is the wavelength of the laser, θ is the scattering angle. From Eq. (3), translational diffusion coefficient D can be calculated. Once D is known, the hydrodynamic radius can be obtained through Stokes-Einstein equation, given by Eq. (5), where R_h is the hydrodynamic diameter, k is Boltzmann's constant, T is absolute temperature and η is viscosity of solvent.

The decay rate obtained by correlation function is related to a characteristic relaxation time, which provides information regarding to the dispersing state of NPs in solution. The characteristic relaxation time of well dispersed NPs is significantly faster than that of the aggregates. Since diffusion coefficient D is proportional to the reciprocal of the decay rate, it also could be used to describe changes in the dispersing state of NPs in solution along with time. Any detected decrease in diffusion coefficient D is related to the decreased stability of NPs dispersion, which can be also confirmed by the increasing Z-average sizes calculated through Stokes-Einstein equation

$$G(\tau) = \langle I(t) \cdot I(t+\tau) \rangle \quad (1)$$

$$G(\tau) = A[1 + B \exp(-2\Gamma\tau)] \quad (2)$$

$$\Gamma = \tau^{-1} = Dq^2 \quad (3)$$

$$q = (4 \pi n / \lambda_0) \sin (\theta/2) \quad (4)$$

$$R_h = KT/6\pi\eta D \quad (5)$$

2.10.6.2. ZETA POTENTIAL MEASUREMENTS.

Zeta potential was carried out to determine the changes of SPIONs in electrophoretic mobility (EPM) and zeta potential (ζ) on a Zetasizer Nano ZS (Malvern) apparatus with a zeta potential analyzer software. SPIONs solutions were placed in a disposable plastic cuvette, followed by collecting experimental data automatically. For each measurement, 20 cycles were collected, and at least 3 independent measurements were performed for each sample.

2.10.6.3. ATTENUATED TOTAL REFLECTANCE FOURIER TRANSFORMED INFRARED SPECTRA MEASUREMENTS (ATR-FTIR).

ATR-FTIR was performed on a Spectrum RX1 FTIR Spectrometer (Perkin Elmer, USA), in the frequency range $4000-400 \text{ cm}^{-1}$ with a resolution of 4 cm^{-1} . All SPIONs samples were isolated from the solution by centrifugation, dried completely in the oven and placed on the crystal surface of the ATR-FTIR machine for measurements.

2.10.6.4. TRANSMISSION ELECTRON MICROSCOPE (TEM).

Size distribution, morphology and diffraction patterns of C-SPIONs and T-SPIONs were collected in JEOL JEM-1210 electron microscope at an operating voltage of 120 KV. TEM samples were prepared by placing one drop of the corresponding SPIONs dispersion on the copper grid for few seconds, blotting the copper grid with a filter paper and evaporate it

completely at room temperature. Typically, about 200 to 300 different SPIONs were counted to depict the size distribution and the mean size of SPIONs.

2.10.6.5. IRON CONTENT DETERMINATION

To determine the iron concentration, samples were sonicated for 10 min in an ultrasound bath. An aliquot of the sample was diluted with HCl (1%), and the iron content of the resulting solution was determined by flame absorption spectroscopy (air-acetylene) with a Perkin-Elmer 2100 spectrometer in triplicate. The yield of the reactions was determined based on the iron concentration of the SPIONs dispersions.

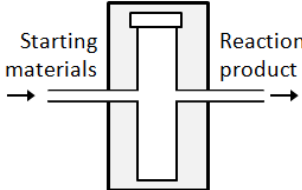
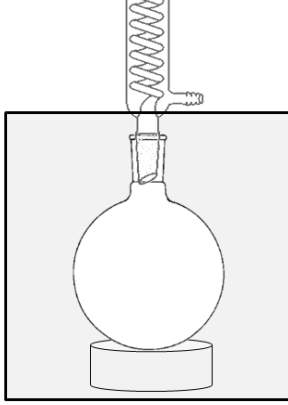
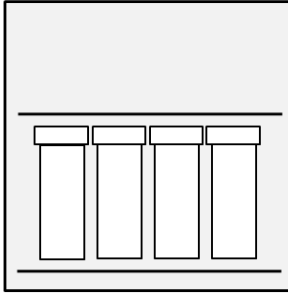
2.10.6.6. SUPERCONDUCTIVE QUANTUM INTERFERENCE DEVICE (SQUID)

The magnetic characterization was performed with a Quantum Design MPMS5XL Magnetometer. 150 μ L of SPIONs of known concentration were first dried in a polycarbonate capsule at 60 °C overnight, and then transferred to the SQUID sample holder. Magnetization curves of SPIONs at 300 K were recorded as a function of applied magnetic field up to 5 Tesla. Zero-field-cooling and field cooling magnetization (ZFC-FC) as a function of temperature in a fixed magnetic field of 50 Oe was also recorded.

2.10.6.7. UV-VIS SPECTROSCOPY

The Ultraviolet-visible infrared (UV-Vis) spectra were collected on a Varian Cary-5000 UV-Vis spectrophotometer using a quartz cuvette with an optical path of 1 cm.

Table 1. Main features of the different well-established microwave scale-up approaches.

	FLOW APPROACH	BATCH-TYPE APPROACH	
		Large batch synthesis	Parallel synthesis
Scheme	<p>(MW-irradiated area in grey)</p> 		
Conditions	Continuous-flow or Stop-flow	Open vessel	Sealed vessel
Automatisation	Yes	No	No
Microwave Equipment	Single-mode or Multi-mode	Multi-mode	Multi-mode
Vessel type	Typically Teflon or glass vessels	Standard glassware	Thick-walled vessels
Batch size	High throughput	Limited (≤ 5 L)	Limited (0.5~1 L)
Temperature and Pressure	Moderate/High	Moderate	High
Reaction parameter reoptimization	Minimal	May be required	Generally required
Heterogenous mixtures	Not supported	Not recommended	Supported
Safety issue	Less concern	Higher concern	Higher concern

2.11 CHAPTER REFERENCES

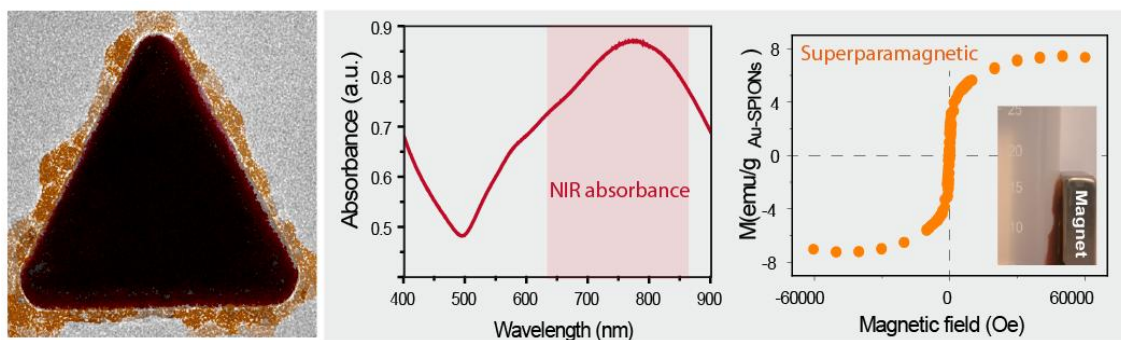
- (1) Wei, X.; Wei, Z.; Zhang, L.; Liu, Y.; He, D. *Highly water-soluble nanocrystal powders of magnetite and maghemite coated with gluconic acid: Preparation, structure characterization, and surface coordination. J Colloid Interf Sci*, **2011**, 354, 76.
- (2) Sun, S.; Zeng, H. *Size-Controlled Synthesis of Magnetite Nanoparticles. J Am Chem Soc*, **2002**, 124, 8204.
- (3) Deng, Y.; Wang, L.; Yang, W.; Fu, S.; Elaïssari, A. *Preparation of magnetic polymeric particles via inverse microemulsion polymerization process. J Magn Magn Mater*, **2003**, 257, 69.
- (4) Baghbanzadeh, M.; Carbone, L.; Cozzoli, P. D.; Kappe, C. O. *Microwave-Assisted Synthesis of Colloidal Inorganic Nanocrystals. Angew Chem Int Edit*, **2011**, 50, 11312.
- (5) Pascu, O.; Carenza, E.; Gich, M.; Estradé, S.; Peiró, F.; Herranz, G.; Roig, A. *Surface Reactivity of Iron Oxide Nanoparticles by Microwave-Assisted Synthesis; Comparison with the Thermal Decomposition Route. J Phys Chem C*, **2012**, 116, 15108.
- (6) Kim, B. H.; Lee, N.; Kim, H.; An, K.; Park, Y. I.; Choi, Y.; Shin, K.; Lee, Y.; Kwon, S. G.; Na, H. B.; Park, J.-G.; Ahn, T.-Y.; Kim, Y.-W.; Moon, W. K.; Choi, S. H.; Hyeon, T. *Large-Scale Synthesis of Uniform and Extremely Small-Sized Iron Oxide Nanoparticles for High-Resolution T1 Magnetic Resonance Imaging Contrast Agents. J Am Chem Soc*, **2011**, 133, 12624.
- (7) De Palma, R.; Peeters, S.; Van Bael, M. J.; Van den Rul, H.; Bonroy, K.; Laureyn, W.; Mullens, J.; Borghs, G.; Maes, G. *Silane Ligand Exchange to Make Hydrophobic Superparamagnetic Nanoparticles Water-Dispersible. Chemistry of Materials*, **2007**, 19, 1821.
- (8) Xu, J.; Li, S.; Weng, J.; Wang, X.; Zhou, Z.; Yang, K.; Liu, M.; Chen, X.; Cui, Q.; Cao, M.; Zhang, Q. *Hydrothermal Syntheses of Gold Nanocrystals: From Icosahedral to Its Truncated Form. Advanced Functional Materials*, **2008**, 18, 277.
- (9) Yilma, A. N.; Singh, S. R.; Dixit, S.; Dennis, V. A. *Anti-inflammatory effects of silver-polyvinyl pyrrolidone (Ag-PVP) nanoparticles in mouse macrophages infected with live Chlamydia trachomatis. International Journal of Nanomedicine*, **2013**, 8, 2421.
- (10) Sun, H.; Jiao, X.; Han, Y.; Jiang, Z.; Chen, D. *Synthesis of Fe₃O₄-Au Nanocomposites with Enhanced Peroxidase-Like Activity. European Journal of Inorganic Chemistry*, **2013**, 2013, 109.
- (11) Carenza, E.; Barceló, V.; Morancho, A.; Levander, L.; Boada, C.; Laromaine, A.; Roig, A.; Montaner, J.; Rosell, A. *In vitro angiogenic performance and in vivo brain targeting of magnetized endothelial progenitor cells for neurorepair therapies. Nanomed-Nanotechnol*, **2014**, 10, 225.
- (12) Euliss, L. E.; Grancharov, S. G.; O'Brien, S.; Deming, T. J.; Stucky, G. D.; Murray, C. B.; Held, G. A. *Cooperative Assembly of Magnetic Nanoparticles and Block Copolypeptides in Aqueous Media. Nano Lett*, **2003**, 3, 1489.
- (13) Namduri, H.; Nasrazadani, S. *Quantitative analysis of iron oxides using Fourier transform infrared spectrophotometry. Corrosion Science*, **2008**, 50, 2493.
- (14) Ouasri, A.; Rhandour, A.; Dhamelincourt, M. C.; Dhamelincourt, P.; Mazzah, A. *Vibrational study of (CH₃)₄NSbCl₆ and [(CH₃)₄N]₂SiF₆. Spectrochimica Acta Part A: Molecular and Biomolecular Spectroscopy*, **2002**, 58, 2779.
- (15) Sasidharan, S.; Jayasree, A.; Fazal, S.; Koyakutty, M.; Nair, S. V.; Menon, D. *Ambient temperature synthesis of citrate stabilized and biofunctionalized, fluorescent calcium fluoride nanocrystals for targeted labeling of cancer cells. Biomaterials Science*, **2013**, 1, 294.
- (16) Song, Y.; Wang, R.; Rong, R.; Ding, J.; Liu, J.; Li, R.; Liu, Z.; Li, H.; Wang, X.; Zhang, J.; Fang, J. *Synthesis of Well-Dispersed Aqueous-Phase Magnetite Nanoparticles and Their Metabolism as an MRI Contrast Agent for the Reticuloendothelial System. European Journal of Inorganic Chemistry*, **2011**, 2011, 3303.

- (17) LaMer, V. K.; Dinegar, R. H. *Theory, Production and Mechanism of Formation of Monodispersed Hydrosols*. *J Am Chem Soc*, **1950**, *72*, 4847.
- (18) Bilecka, I.; Elser, P.; Niederberger, M. *Kinetic and Thermodynamic Aspects in the Microwave-Assisted Synthesis of ZnO Nanoparticles in Benzyl Alcohol*. *ACS Nano*, **2009**, *3*, 467.
- (19) Hu, X.; Yu, J. C.; Gong, J.; Li, Q.; Li, G. *α -Fe₂O₃ Nanorings Prepared by a Microwave-Assisted Hydrothermal Process and Their Sensing Properties*. *Advanced Materials*, **2007**, *19*, 2324.
- (20) Nyutu, E. K.; Chen, C.-H.; Dutta, P. K.; Suib, S. L. *Effect of Microwave Frequency on Hydrothermal Synthesis of Nanocrystalline Tetragonal Barium Titanate*. *J Phys Chem C*, **2008**, *112*, 9659.
- (21) Leung, K. C.-F.; Xuan, S.; Zhu, X.; Wang, D.; Chak, C.-P.; Lee, S.-F.; Ho, W. K.-W.; Chung, B. C.-T. *Gold and iron oxide hybrid nanocomposite materials*. *Chemical Society Reviews*, **2012**, *41*, 1911.
- (22) Basly, B.; Felder-Flesch, D.; Perriat, P.; Billotey, C.; Taleb, J.; Pourroy, G.; Begin-Colin, S. *Dendronized iron oxide nanoparticles as contrast agents for MRI*. *Chemical Communications*, **2010**, 46, 985.
- (23) Shen, Y.; Goerner, F. L.; Snyder, C.; Morelli, J. N.; Hao, D.; Hu, D.; Li, X.; Runge, V. M. *T₁ Relaxivities of Gadolinium-Based Magnetic Resonance Contrast Agents in Human Whole Blood at 1.5, 3, and 7 T*. *Investigative Radiology*, **2015**, *50*, 330.
- (24) Kolen'ko, Y. V.; Bañobre-López, M.; Rodríguez-Abreu, C.; Carbó-Argibay, E.; Sailsman, A.; Piñeiro-Redondo, Y.; Cerqueira, M. F.; Petrovykh, D. Y.; Kovnir, K.; Lebedev, O. I.; Rivas, J. *Large-Scale Synthesis of Colloidal Fe₃O₄ Nanoparticles Exhibiting High Heating Efficiency in Magnetic Hyperthermia*. *The Journal of Physical Chemistry C*, **2014**, *118*, 8691.
- (25) Ibarra-Sánchez, J. J.; Fuentes-Ramírez, R.; Roca, A. G.; del Puerto Morales, M.; Cabrera-Lara, L. I. *Key Parameters for Scaling up the Synthesis of Magnetite Nanoparticles in Organic Media: Stirring Rate and Growth Kinetic*. *Industrial & Engineering Chemistry Research*, **2013**, *52*, 17841.
- (26) Kremsner, J. M.; Stadler, A.; Kappe, C. O. *The Scale-Up of Microwave-Assisted Organic Synthesis*. **2006**, 266, 233.
- (27) Bilecka, I.; Djerdj, I.; Niederberger, M. *One-minute synthesis of crystalline binary and ternary metal oxide nanoparticles*. *Chemical communications*, **2008**, 886.
- (28) Luke, G.; Yeager, D.; Emelianov, S. *Biomedical Applications of Photoacoustic Imaging with Exogenous Contrast Agents*. *Ann Biomed Eng*, **2012**, *40*, 422.
- (29) Xu, L.; Kuang, H.; Xu, C.; Ma, W.; Wang, L.; Kotov, N. A. *Regiospecific Plasmonic Assemblies for in Situ Raman Spectroscopy in Live Cells*. *Journal of the American Chemical Society*, **2011**, *134*, 1699.
- (30) Duncan, B.; Kim, C.; Rotello, V. M. *Gold nanoparticle platforms as drug and biomacromolecule delivery systems*. *Journal of Controlled Release*, **2010**, *148*, 122.
- (31) Hirsch, L. R.; Stafford, R. J.; Bankson, J. A.; Sershen, S. R.; Rivera, B.; Price, R. E.; Hazle, J. D.; Halas, N. J.; West, J. L. *Nanoshell-mediated near-infrared thermal therapy of tumors under magnetic resonance guidance*. *Proceedings of the National Academy of Sciences*, **2003**, *100*, 13549.
- (32) Wang, Y.; Zheng, Y.; Huang, C. Z.; Xia, Y. *Synthesis of Ag Nanocubes 18–32 nm in Edge Length: The Effects of Polyol on Reduction Kinetics, Size Control, and Reproducibility*. *J Am Chem Soc*, **2013**, *135*, 1941.
- (33) Sun, Y.; Xia, Y. *Shape-Controlled Synthesis of Gold and Silver Nanoparticles*. *Science*, **2002**, *298*, 2176.
- (34) Xiong, Y.; Washio, I.; Chen, J.; Sadilek, M.; Xia, Y. *Trimeric Clusters of Silver in Aqueous AgNO₃ Solutions and Their Role as Nuclei in Forming Triangular Nanoplates of Silver*. *Angew Chem Int Edit*, **2007**, *46*, 4917.

- (35) Zhang, Y.; Ding, H.; Liu, Y.; Pan, S.; Luo, Y.; Li, G. *Facile one-step synthesis of plasmonic/magnetic core/shell nanostructures and their multifunctionality*. *Journal of Materials Chemistry*, **2012**, *22*, 10779.
- (36) Matsura, V. A.; Potekhin, V. V.; Ukraintsev, V. B. *Kinetics of Hydrogenation and Oxidation of Benzyl Alcohol in the Presence of Colloid Palladium in situ*. *Russian Journal of General Chemistry*, **2002**, *72*, 105.
- (37) Eustis, S.; El-Sayed, M. A. *Why gold nanoparticles are more precious than pretty gold: Noble metal surface plasmon resonance and its enhancement of the radiative and nonradiative properties of nanocrystals of different shapes*. *Chemical Society Reviews*, **2006**, *35*, 209.
- (38) Srivastava, S.; Frankamp, B. L.; Rotello, V. M. *Controlled Plasmon Resonance of Gold Nanoparticles Self-Assembled with PAMAM Dendrimers*. *Chemistry of Materials*, **2005**, *17*, 487.
- (39) Ángel, D.-O.; Antonio, d. I. H.; Jesús, A.; R., C. J.; Antonia, H. M.; M., M. J. d.; Pilar, P.; de, C. A. *Reproducibility and Scalability of Microwave-Assisted Reactions*, 2011.
- (40) Bowman, M. D.; Holcomb, J. L.; Kormos, C. M.; Leadbeater, N. E.; Williams, V. A. *Approaches for Scale-Up of Microwave-Promoted Reactions*. *Organic Process Research & Development*, **2007**, *12*, 41.

CHAPTER 3

MAGNETIC GOLD NANOTRIANGLES BY MICROWAVE POLYOL SYNTHESIS



CHAPTER SUMMARY

The combination of magnetic and optical properties in a single nanomaterial offers enormous potential in bio-sensing, imaging and therapeutical applications. However, uncomplicated approaches to synthesize hybrid magneto-plasmonic nanoparticles avoiding cytotoxic reactants to target biomedical uses remain a huge challenge. This is particularly the case for nanoparticles with anisotropic plasmonic shapes. In this chapter, we report a facile, fast and bio-friendly microwave-assisted polyol route to synthesize high yield of gold (Au) nanotriangles (NT) surface decorated with superparamagnetic iron oxide nanoparticles (SPIONs). We obtained hybrid nanoparticles (Au NT-SPIONs) readily dispersible in water, superparamagnetic at room temperature and interestingly display the local surface plasmon resonance (LSPR) maximum in the near infrared (NIR) region.

Chapter Index

	pag.
CHAPTER SUMMARY	71
3.1 BIOMEDICAL APPLICATIONS OF Au-SPIONs NANOCOMPOSITES	73
3.2 SYNTHESIS OF Au-SPIONs NANOCOMPOSITES: STATE OF THE ART	73
3.3 MICROWAVE POLYOL SYNTHESIS OF Au NANOTRIANGLES-SPIONs NANOCOMPOSITES	74
3.4 STRUCTURE AND CHARACTERIZATION OF Au-SPIONs NANOCOMPOSITES	77
3.5 EFFECT OF PVP AMOUNT ON THE SHAPE YIELD OF Au NT-SPIONs NANOCOMPOSITES	78
3.6 EFFECT OF TEMPERATURE ON THE SHAPE YIELD OF Au NT-SPIONs NANOCOMPOSITES	81
3.7 EFFECT OF REACTION TIME ON THE SHAPE YIELD OF Au NT-SPIONs NANOCOMPOSITES	82
3.8 MAGNETIC PROPERTIES OF Au-SPIONs NANOCOMPOSITES	83
3.9 MECHANISM OF THE FORMATION OF Au NT-SPIONs NANOCOMPOSITES	84
3.10 PURIFICATION AND SELF-ASSEMBLY OF Au NT-SPIONs NANOCOMPOSITES	85
3.11 CHAPTER CONCLUSIONS	88
3.12 ANNEX OF CHAPTER 3	90
3.13 CHAPTER REFERENCES	92

3.1 BIOMEDICAL APPLICATIONS OF Au-SPIONS NANOCOMPOSITES

Recently, nanocomposites have attracted increasing interest in biomedical applications due to the integrated properties from individual nanoparticles. In particular, combination of Au nanoparticles and SPIONs into a single composite nanoparticles (Au-SPIONs) could allow us to use simultaneously the combined plasmonic property from Au nanoparticles and magnetic property from SPIONs, which show great potential use in biomedical imaging¹, drug delivery¹, cell sorting and bio-separation², hyperthermia³ and biosensing⁴⁻⁶. Moreover, the combination of two individual nanoparticles can modify some properties depending on the structure of the Au-SPIONs nanocomposites⁷. Au-Fe₃O₄ flowers for example, their magnetic properties have been reported to be enhanced due to the increase number of magnetic domains within the nanocomposites⁸, higher transverse relaxivity (r_2) value was observed than that of the dumbbell nanocomposites⁹. While Fe₃O₄@Au core/shell nanocomposites display the lowest r_2 value among the reported Au-SPIONs hybrid nanostructures¹⁰. Fe₃O₄@Au core/shell nanocomposites were revealed to be able to produce more heat than single Fe₃O₄ nanoparticles due to the higher magnetic anisotropy of the superparamagnetic fraction, which significantly enhance their efficiency in hyperthermia³. Fe₃O₄@Au core/shell nanocomposites or Au-SPIONs dumbbell nanocomposites, due to the presence of the outer Au component, their surface can be easily further functionalized through the Au-S bound chemistry. When fluorescent probes are conjugated to the surface, a multi-modal of MRI-FOI (magnetic resonance imaging-fluorescent optical imaging) contrast agent can be prepared¹. When anticancer drug cisplatin attached to the surface, those nanocomposites are then served as a drug nanocarrier¹. Moreover, their surface can be functionalized with DNA strands, different kinds of antibody or enzymes for sensitive biosensing and bioseparation^{2,4-6}.

In summary, Au-SPIONs nanocomposites can not only provide physicochemical properties originated from individual Au nanoparticle and SPION, but also some enhanced properties due to the combination. Those enhanced properties make nanocomposites promising for new biomedical applications.

3.2 SYNTHESIS OF Au-SPIONS NANOCOMPOSITES: STATE OF THE ART

Nowadays, enormous efforts have been dedicated to the synthesis of Au-SPIONs nanocomposites. Among the methods available, one pot synthesis, seed mediated synthesis and a "bottom-up" approach (chemically bonding the two types of particles) are the three most widely used methods. In the one pot synthetic strategy, gold and iron precursors mixed in the same vessel decompose to form Au-SPIONs heterostructures; benefiting from the different nucleation temperatures of Au and SPIONs. First, Au nucleates and grow, followed by the deposition of SPIONs onto Au nanoparticles, basically resulting in core-shell heterostructures^{11,12}. The seed mediated synthesis requires first the synthesis of Au or iron oxide nanoparticles in a previous step, and then, these nanoparticles serve as the nucleation site for

the other component to grow upon. The seed mediated synthetic process is versatile and the most widely used strategy for engineering different heterostructures, such as dumbbells^{13,14}, core-shell¹⁵, nanoflowers¹⁶, star-shape¹⁷ and clusters¹⁸. The third strategy involves the separate synthesis of Au and iron oxide nanoparticles, which are then assembled together to form the Au-SPIONs heterostructures by choosing an appropriate third component. In general, this method leads to the formation of core-satellite or other type of aggregated heterostructures^{19,20}. The above mentioned routes described mainly produce spherical Au nanoparticles displaying an LSPR spectral band in the UV-Vis range. In contrast, the work of Truby *et al.* reported a ligand mediated self-assembly of carboxyl functionalized Au nanorods conjugated to SPIONs with a well-defined LSPR band at 900 nm²⁰. Unfortunately, this method uses cetyltrimethylammonium bromide (CTAB) or cetyltrimethylammonium chloride (CTAC) for the formation of the gold nanorods and entails poor control on the SPIONs mass fraction on the Au surfaces. Additionally, Quaresma *et al.* reported the direct formation of gold seeds on magnetite nanoparticles followed by a seed growth to form a star-shape gold outer layer resulting in a broad peak in the plasmonic signal at the NIR region¹⁷.

Au nanotriangles are excellent nanoheaters in photothermal therapy²¹ and an effective nanomaterial for biosensing²². The majority of synthetic methods for Au NT are based on a multi-step seed-mediated approach, involving the use of the highly toxic cationic surfactant CTAB^{23,24} resulting in a poorly biocompatible time-consuming method. Even though, the achievement of monodisperse gold nanotriangles by seed mediated growth and improved purification in over 90% shape-yield as recently reported by the group of Liz-Marzan²² is highly remarkable. Furthermore, a polyol process based on metal reduction at high temperature by ethylene glycol in the presence of PVP is the other most used approach to generate nanoparticles with controllable shapes including Ag cubes and nanotriangles. Relevant seminal contributions in this synthesis mechanism have been reported by the Y. Xia's group²⁵⁻²⁷.

3.3 MICROWAVE POLYOL SYNTHESIS OF Au NANOTRIANGLES-SPIONs NANOCOMPOSITES

In this chapter, a facile, fast and non-toxic microwave polyol route was developed to synthesize Au-SPIONs nanocomposites with high yield of nanotriangles. The experimental procedure for the synthesis involves two main steps: i) preparation of PVP coated SPIONs in benzyl alcohol and ii) the growth of gold crystals in ethylene glycol in the presence of both PVP-SPIONs and PVP. The whole procedure is schematically illustrated in Fig. 1.

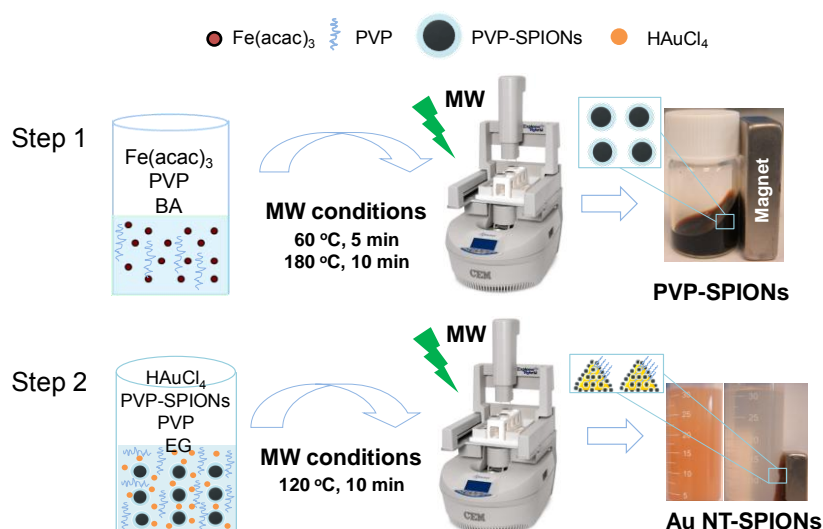






Figure 1. Schematic illustration of the microwave polyol synthesis of Au NTs-SPIONs nanocomposites.

In the previous chapter, synthesis and characterization of PVP-SPIONs have been detailed. We showed that by increasing the maximum reaction temperature from 180 °C to 210 °C, the size of PVP-SPIONs can be tuned from 5.6 nm to about 7.5 nm. The both obtained PVP-SPIONs were stable in water, essentially with high saturated magnetization and superparamagnetic property at room temperature. After the microwave (MW) synthesis, the obtained PVP-SPIONs were dispersed in ethylene glycol (EG). Then 40 μL 100 mM HAuCl_4 and various amounts of PVP (0, 25 mg, 50 mg, 100 mg and 150 mg) were added to the PVP-SPIONs EG solution and mixed by vortex to form a homogenous solution. In order to determine the influence of PVP on the shape yields of the hybrid nanostructures, molar ratio of PVP to HAuCl_4 of 0, 0.625:1, 1.25:1, 2.5:1 and 3.75:1 were evaluated, corresponding to 25 mg, 50 mg, 100 mg and 150 mg PVP. The effect of MW temperature and time, $T = 80, 100$ and 120 °C and $t = 5, 10, 20$ and 40 min, on the resulting hybrid structures were also investigated. The as-obtained hybrid Au-SPIONs nanoparticles were washed twice with acetone to remove the free PVP, collected by centrifugation at 6000 rpm for 2 min and redispersed in 2 mL MQ H_2O for further characterization. To ensure reproducibility of the results each synthetic condition was repeated three times. Table 1 summarizes the reaction conditions used and the characteristics of the obtained materials reporting the mean values of the independent experiments performed.

Table 1. Reaction conditions and characteristics of the obtained materials using in all cases 4mL EG.

Sample	PVP-SPIONs (mmol)	HAuCl ₄ (mmol)	Free PVP (mg)	molar ratio of free PVP to HAuCl ₄	EG (mL)	T ^a (°C)	t ^b (min)	LSPR band max (nm)	Shape-yield (%)				Hydrodynamic Diameter (nm)
													
1	-	0,004	-	0	4	120	10	-	Au aggregates				> 1000
2	-	0,004	100	2.5 : 1	4	120	10	540	-	-	-	100 ^c	10
3	0,035	0,004	100	2.5 : 1	4	80	10	649	30	17	28	25	122
4	0,035	0,004	100	2.5 : 1	4	100	10	677	38	20	24	18	147
5	0,035	0,004	100	2.5 : 1	4	120	10	709	31	30	27	12	169
6	0,035	0,004	100	2.5 : 1	4	120	5	678	39	24	26	11	175
8	0,035	0,004	100	2.5 : 1	4	120	20	722	32	29	27	12	155
9	0,035	0,004	100	2.5 : 1	4	120	40	739	41	24	29	6	153
10	0,035	0,004	25	0.625 : 1	4	120	10	800	60	16	22	2	204
11	0,035	0,004	50	1.25 : 1	4	120	10	725	52	9	31	8	169
13	0,035	0,004	150	3.75 : 1	4	120	10	535	-	-	-	100 ^d	9
14	0,035	0,004	-	-	4	120	10	573	-	-	-	100 ^e	100

^a Reaction temperature, ^b Reaction time, ^c Small spherical Au NPs with a mean size of 9 nm, ^d Small spherical Au NPs with similar size to PVP-SPIONs, ^e Big roughly spherical Au NPs with size larger than 50 nm.

This synthetic approach offers a facile and fast route, avoiding the use of toxic reactants as the CTAB or CTAC to synthesize hybrid Au NT-SPIONs nanoparticles. Without any purification, a remarkable 60 % yield of hybrid Au NT-SPIONs nanoparticles was obtained with the following conditions, mixing the PVP-SPIONs with HAuCl₄·3H₂O and 25 mg of PVP (PVP:HAuCl₄ molar ratio=0.625:1) homogeneously in ethylene glycol by sonication. Reactants were heated to 120 °C for 10 min inside the microwave reactor. After MW synthesis, the black color of the PVP-SPIONs dispersion in EG (Fig. 2a) changed to orange (Fig. 2b) pointing to the successful synthesis of Au nanoparticles. Using an external magnet we separated easily and completely the orange product (Fig. 2c) indicating that all the Au nanoparticles contained SPIONs. Besides Au NT-SPIONs hybrid nanostructures, a mixture of hexagons, platonic structures (icosahedrons and cubes) and smaller rounded nanoparticles were also observed. If we consider hexagons as a planar form of completely truncated triangles, then the resulting yield of triangles and hexagons is over 75%.

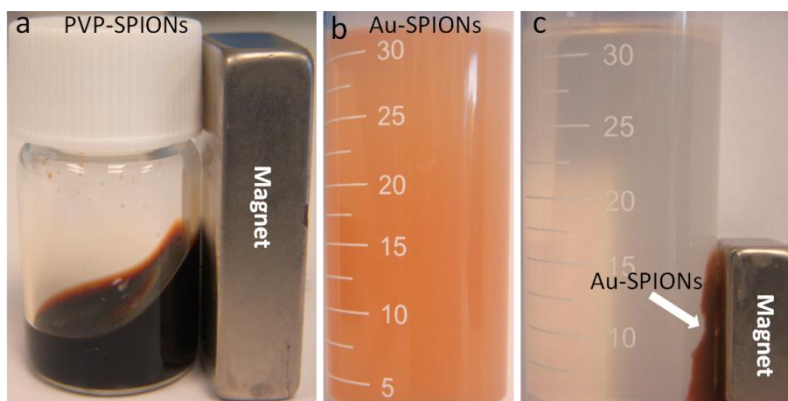


Figure 2. Digital images a) PVP-SPIONs aqueous solution showing a black color and strong magnetic response. b) hybrid Au-SPIONs nanoparticles dispersed in water displaying an orange color and c) strong magnetic response of the hybrid Au-SPIONs nanoparticles to the external magnet.

3.4 STRUCTURE AND CHARACTERIZATION OF Au-SPIONs NANOCOMPOSITES

Fig. 3a displays a representative SEM image of hybrid gold particles resulting from the reaction conditions mentioned above where the highest portion of nanotriangles can be recognized. Different Au morphologies can be seen more clearly in Fig. 3b. Fig. 3c indicates that the shape yield of Au nanotriangles account for about 60% of the whole product. High resolution TEM images are included as Fig. 3d and 3e, confirming that the structure of the nanocomposites is composed of a single Au NT core with well-defined equilateral shape, a mean size of 284 ± 43 nm and its surface decorated by a monolayer of SPIONs. Fig. 3e further reveals the homogeneity of the SPIONs coating along the Au NT surface.

The UV-Vis-NIR spectra in Fig. 3f clearly showed a major NIR LSPR band at 800 nm, which is characteristic of anisotropic Au structures (e.g. Au nanorods or nanotriangles), suggesting high yields of anisotropic Au NPs. The LSPR band at 800 nm is however rather broad and we argue it can be related to the presence of other anisotropic Au structures and their size dispersion or to the surface roughness that SPIONs endow to the Au nanoparticles. Although this latter assumption was previously shown to have little effect on the absorption spectral band²⁰. Besides the NIR LSPR band found at 800 nm, a small shoulder of LSPR band can be observed in the UV-Vis region, around 570 nm assigned to the small fraction of spherical Au-SPIONs NPs. It is noteworthy that in previous synthetic approaches reported for Au NT, spherical Au NPs are a common by-product^{21,28} whereas in our case spherical Au NPs account only for 2% of the final product, which is a relatively low amount.

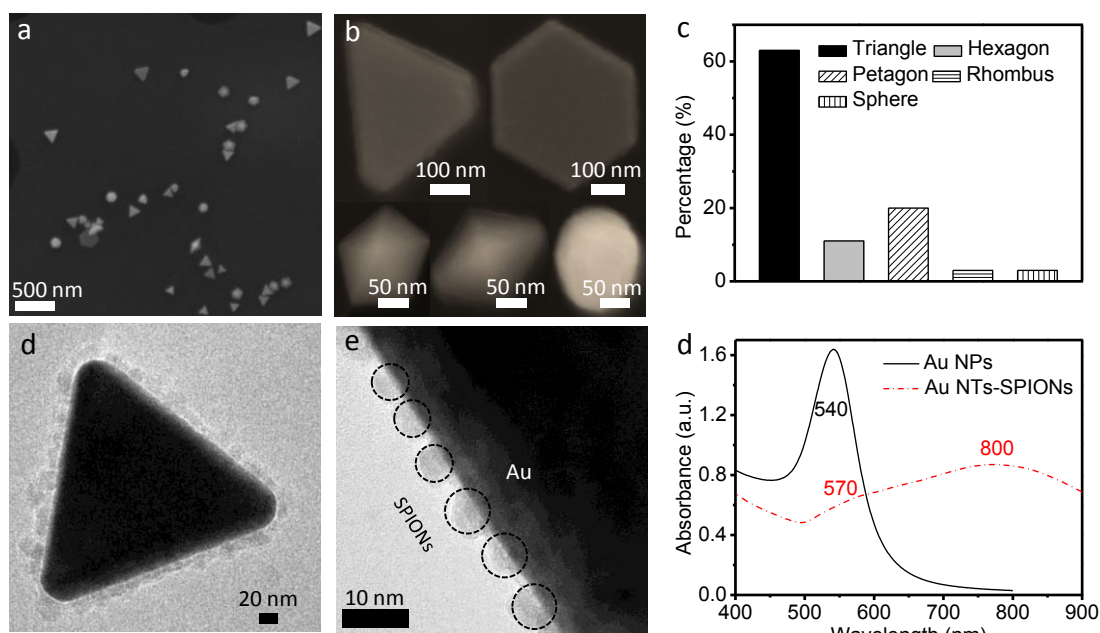


Figure 3. a) Representative SEM image of hybrid Au NTs-SPIONs nanoparticles. b) Different Au morphologies mentioned in the text (different scale bars for each morphology) c) The percentage of shape yield of different Au structures. d) HR-TEM image of a single Au NTs-SPIONs nanoparticle. e) high magnification of the selected square from Fig. 1b and f) UV-Vis-NIR spectra of Au nanospheres and hybrid Au-SPIONs nanoparticles.

Previous reports from Xia's group indicated the important role of PVP in the formation of Ag anisotropic structures with high yields in EG and in water^{27,29}. We have also identified the PVP:HAuCl₄ molar ratio as a key parameter to control the yield of Au NTs. We believe that PVP serves as the capping agent for both of SPIONs and Au nanoparticles, and stabilizes the Au nanoparticles. Even though, a deep mechanistic understanding of the growth mechanism is beyond the scope of this work, we interrogated how the amount of free PVP, reaction temperature and time affect the hybrid nanocrystals synthesis.

3.5 EFFECT OF PVP AMOUNT ON THE SHAPE YIELD OF Au NT-SPIONs NANOCOMPOSITES

The following reactions were performed at 120 °C for 10 min. MW heating of HAuCl₄ in EG in the absence of PVP and PVP-SPIONs resulted in aggregates and no individual Au NPs could be observed (Fig. 4a). MW heating of HAuCl₄ in EG in the presence of PVP without PVP-SPIONs resulted in spherical Au NPs, with a mean size of 9 nm (Fig. 4b and 4c). These findings indicated that in our system both free PVP and PVP-SPIONs play crucial roles in the formation of anisotropic Au-SPIONs hybrids.

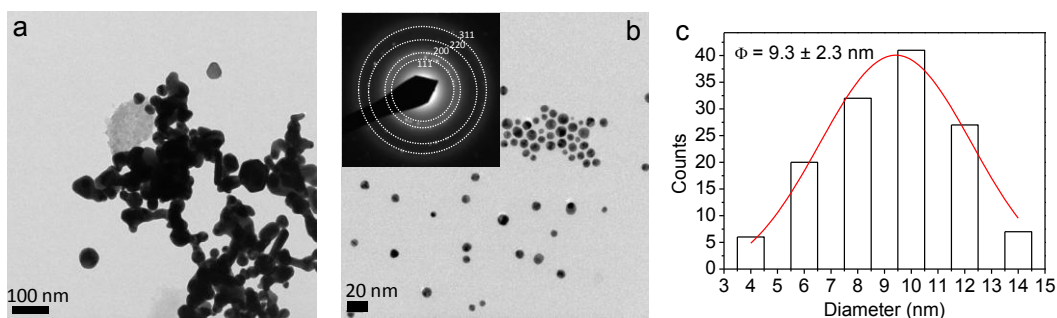


Figure 4. a) TEM image of Au aggregates obtained by MW heating of HAuCl_4 in EG in the absence of PVP and PVP-SPIONs. b) TEM image of small Au NPs synthesized by MW heating of HAuCl_4 in EG in the presence of 100 mg PVP, without PVP-SPIONs. Inset is the select area electron diffraction, indicating the cubic structure of the obtained Au NPs. c) size distribution histogram of the Au NPs determined from TEM images, indicating a mean size = 9.3 ± 2.3 nm.

Later, different amounts of PVP, 0, 25, 50, 100 and 150 mg corresponding to PVP/ HAuCl_4 molar ratios equal to 0, 0.625:1, 1.25:1, 2.5:1, 3.5:1 were used. The yield of Au NTs-SPIONs hybrid nanoparticles significantly increases by gradually decreasing the amount of PVP in the reaction, reaching a maximum of 60% when 25 mg PVP was added. Additionally, the number of Au spheres and hexagons decrease while the percentage of platonic structures was almost not affected. TEM images of the nanocomposites obtained at different PVP amounts (Fig. 5c) and the shape histogram compiled from several TEM images confirmed these observations (Fig. 5a). If we compile the histogram considering planar structures (triangles and hexagons), platonic structures and spheres, it indicates that planar shapes increase at the expense of spheres at lower PVP molar ratios.

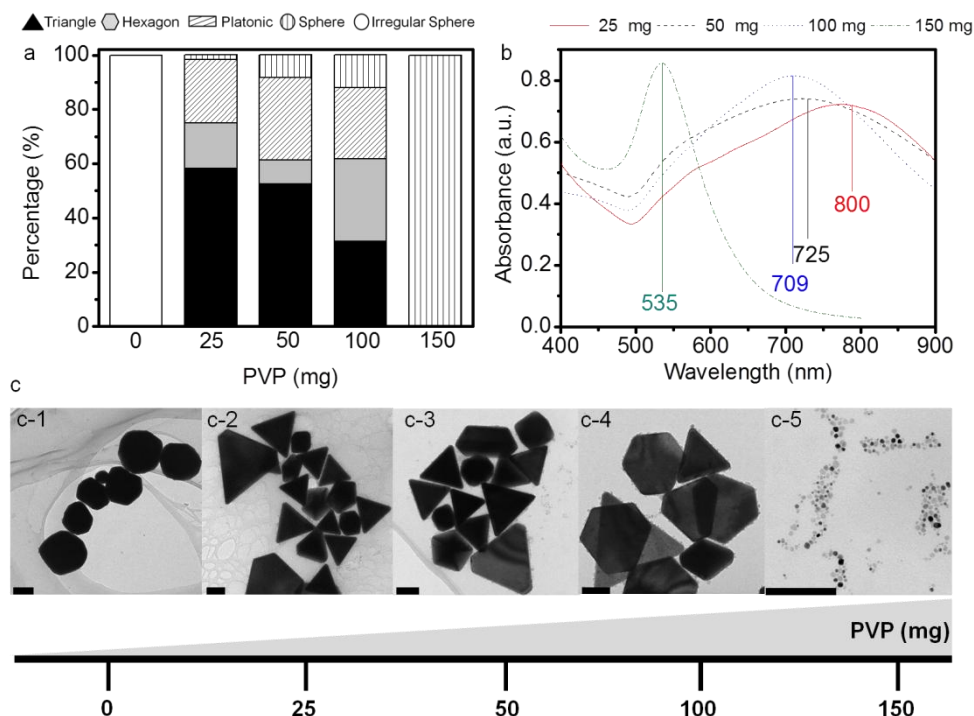


Figure 5. a) Shape-yields of Au-SPIONs nanocomposites at a free PVP amount of 0 mg, 25mg, 50mg, 100 mg and 150 mg. b) UV-Vis-NIR spectra of Au-SPIONs nanocomposites at a free PVP amount of 25mg, 50mg, 100 mg and 150 mg. c) Representative TEM images of Au-SPIONs nanocomposites (scale bar represents 100 nm), c-1 to c-5 correspond to free PVP amount of 25mg, 50mg, 100 mg and 150 mg, respectively.

UV-Vis-NIR spectra of the Au-SPIONs hybrids obtained using different PVP amounts are displayed in Fig. 5b. LSPR peak red shifted when decreasing the amount of PVP, with a maximum LSPR peak at 800 nm observed when 25 mg PVP was used. Indeed, larger size of Au NTs for the lowest amount of PVP was confirmed by TEM. In particular, the edge length of the Au NTs obtained with 100 mg of PVP was 150 nm while increased to 280 nm when 25 mg of PVP were used (Fig. 6a and 6b). Hydrodynamic diameter (D_h) of Au NP-SPIONs nanocrystals confirmed those findings (Fig. 6c). Therefore, we ascribe the red shift of the NIR LSPR peak to the increase edge length and the improved purity of the Au NT. Additionally PVP-SPIONs offers a protective role to the gold nanoparticles since the absorption spectra recorded for the as-obtained materials and for materials kept during 3 months were identical indicating that no major reshaping of the Au particles occurs (Fig. 6d).

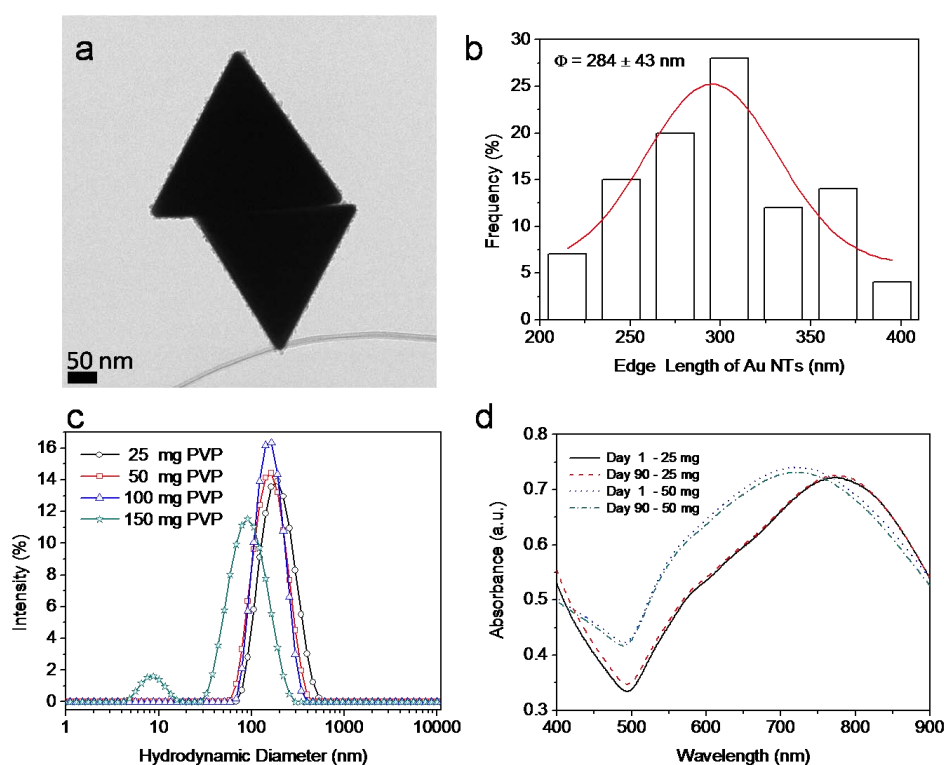


Figure 6. a) The representative image of Au NTs-SPIONs hybrid nanostructures. b) The edge length histogram of Au NTs-SPIONs hybrid nanostructures determined from TEM images (25 mg PVP). c) DLS of Au-SPIONs nanocomposites obtained at different amounts of PVP. d) UV-Vis-NIR spectra taken after the synthesis and after 90 days, indicating that major reshaping does not occur to our SPIONs coated Au nanostructures.

Differently, when the amount of PVP is further increased to 150 mg, only individual and small round shape Au and SPIONs were observed (Fig. 5c-5). Fig. 5b also displays a narrow absorption peak in the UV-Vis region (535 nm) from the small spherical Au-SPIONs obtained using 150 mg of PVP. HR-TEM images reveal that Au NPs and SPIONs bound to each other form pairs or trimers (Fig. 7a). When no extra free PVP was added and the PVP supply was solely from the one attached to the SPIONs surface, the hybrids formed were also spherical with a testimonial presence of some hexagons and with the LSPR band maximum at 573 nm (Fig. 7b and 7c). This observation indicates the need of free PVP as structuring agent for the nanotriangles to

nucleate and further grow. Interestingly independent of the shape of Au NPs, a monolayer of SPIONs was always visible on the Au surface (Fig. 8).

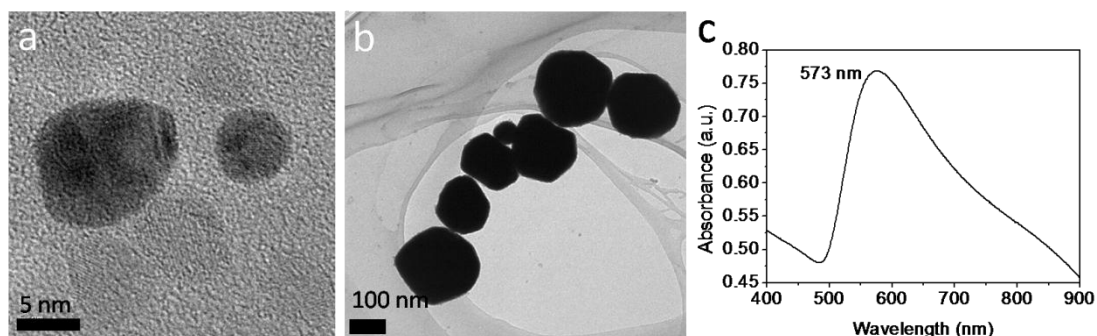


Figure 7. a) HR-TEM of Au NPs-SPIONs (dimers and trimers) formed using 150 mg of PVP. b) TEM image of the Au-SPIONs composites resulted when performing the MW synthesis of HAuCl_4 and PVP-SPIONs in EG with no free PVP added. Majority of them are roughly spherical. b) UV-VIS-NIR absorbance spectrum of those composites

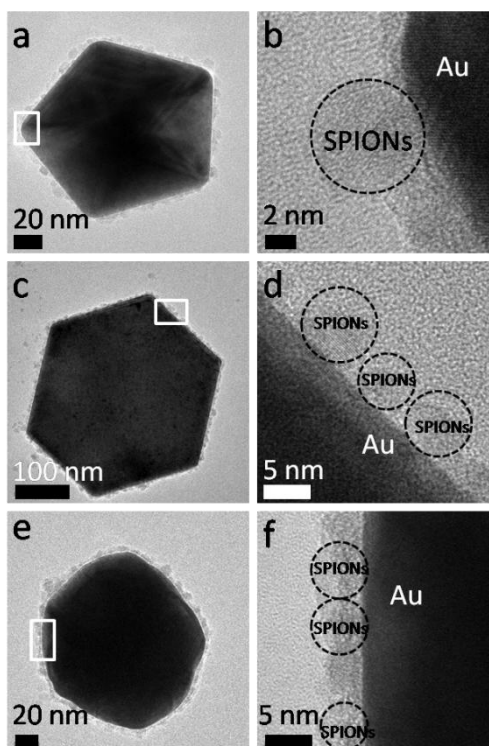


Figure 8. HR-TEM images. Au icosahedron-SPIONs at low (a) and high magnification (b). planar Au hexagon-SPIONs at low (c) and high magnification (d). Au pseudosphere-SPIONs at low (e) and high magnification (f).

3.6 EFFECT OF TEMPERATURE ON THE SHAPE YIELD OF Au NT-SPIONs NANOCOMPOSITES

Effect of the temperature on the shape-yield was investigated by using 100 mg PVP, 10 min reaction time and synthesis' temperatures of 80, 100 and 120 °C, results are shown in Fig. 9a. Notice that those are rather low temperatures in comparison to the 160 °C used in the polyol synthesis of Ag nanotriangles. Upon increasing the temperature, the most significant observation was the gradual decrease in the percentage of Au spheres and the gradual increase in the number of Au planar structures. The percentage of the Au NTs-SPIONs nanocomposites is

around 32% for the three temperatures. LSPR peak of the Au-SPIONs nanocomposites displayed a gradual red shift while increasing temperature (Fig. 9b). Main LSPR peak centered at around 649 nm for hybrids at 80 °C, while shifted to 709 nm when temperature increased to 120 °C. The observed red shift is likely related to the increased number of anisotropic Au nanostructures since Au spheres accounted for nearly 25% of the total at 80 °C and only 12% at 120 °C. Moreover, DLS measurements showed that the hydrodynamic size (D_h) gradually increases with the increasing temperature (Fig. 9c). A mean size of 122 nm was observed at 80 °C that increased to 169 nm when the synthesis was performed at 120 °C.

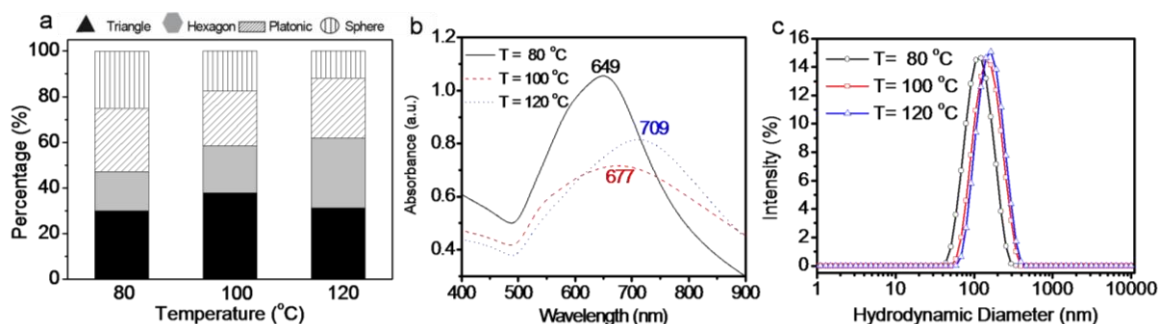


Figure 9. a) Shape-yields of Au-SPIONs nanocomposites obtained at different temperatures. b) UV-Vis-NIR spectra of those nanocomposites. c) DLS measurements of those nanocomposites obtained at different temperature.

3.7 EFFECT OF REACTION TIME ON THE SHAPE YIELD OF Au NT-SPIONs NANOCOMPOSITES

Reaction time on the shape-yield of different Au-SPIONs nanostructures seems to have little influence aside for a slight decrease of the number of spheres as the reaction time is extended. (Fig. 10a). LSPR band shows a blue shift when reaction extended (Fig. 10b), which is in contrast to the results obtained from the other synthetic methods as the reaction evolves²⁶. However, our observation agrees with the results reported by de la Fuente's group²¹ that assigns this slight blue shift to the evolution from the well-defined triangles to the tip-truncated ones. Indeed, formation of truncated Au triangles can be inferred from the small decreasing D_h size of Au-SPIONs hybrid nanostructures obtained at longer reaction time (Fig. 10c).

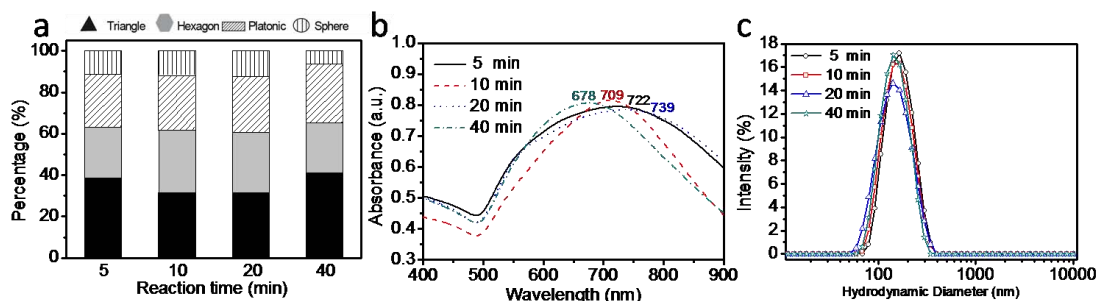


Figure 10. a) shape-yields of the different Au-SPIONs nanoparticles obtained at different reaction times. b) their UV-Vis-NIR spectra of Au-SPIONs c) DLS measurements.

3.8 MAGNETIC PROPERTIES OF Au-SPIONs NANOCOMPOSITES

SPIONs endow magnetic functionality to the hybrids constructs¹³ and their magnetic properties recorded in a superconducting quantum interference device (SQUID) magnetometer; the magnetization curve (M-H loop) and zero-field-cooling curve are depicted in Fig. 11. Compared to PVP-SPIONs a significant decrease in the saturated magnetization value was observed assigning it to the diamagnetic nature of the gold (7.3 emu/g) (Fig. 11a).

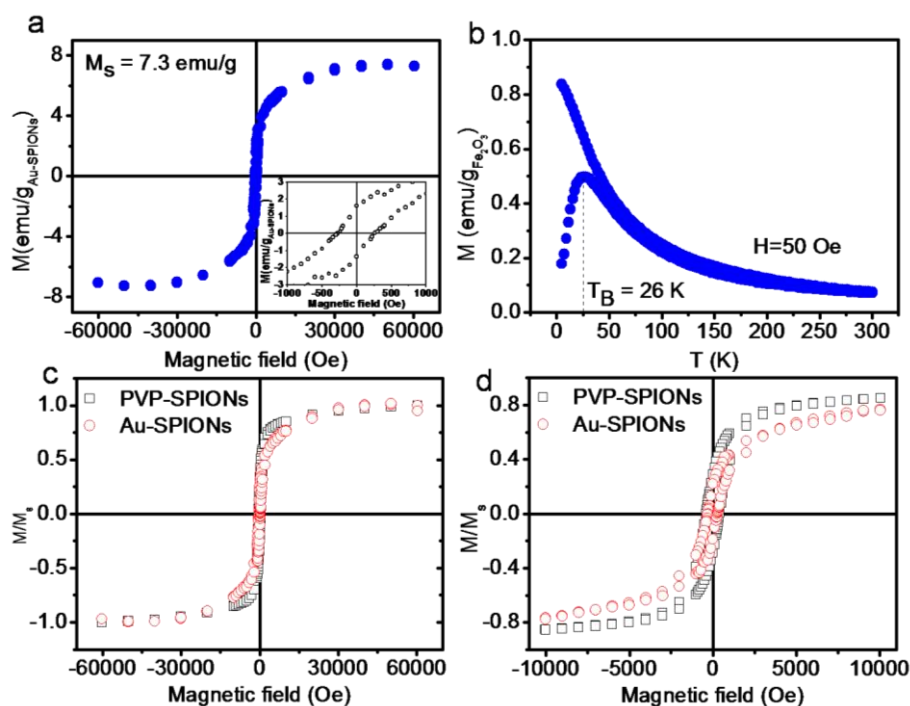


Figure 11. a) Magnetization curve of Au-SPIONs hybrid nanoparticles at 5K. b) ZFC-FC curve of Au-SPIONs hybrid nanoparticles at 50 Oe. c) normalized hysteresis loops of PVP-SPIONs and hybrid Au NT-SPIONs at 5k. d) blow up at lower fields.

From the saturated magnetization of Au NT-SPIONs and of PVP-SPIONs, we can determine that an approximate 10% mass ratio of SPIONs decorate the Au surface. Besides, when plotting the normalized hysteresis loops of both materials the curves are almost superimposing confirming that the gold is not affecting greatly the magnetic behavior of the SPIONs (Fig. 11c and 11d). ZFC/FC curves of Au-SPIONs hybrid nanoparticles were also performed at an applied magnetic field of 50 Oe. Curves indicate PVP-SPIONs in the hybrids maintained their superparamagnetic character with a blocking temperature of 27 °C (Fig. 11b).

3.9 PROPOSED MECHANISM OF THE FORMATION OF Au NT-SPIONs NANOCOMPOSITES

As mentioned in Chapter 1 and Chapter 2, microwave heating represents an attractive non-conventional energy source for chemical synthesis due to the high acceleration and yield of the chemical reaction obtained³⁰. In comparison to conventional heating methods, microwave radiation avoids production of temperature gradients within the vessel, which would increase the probability of asynchronic nucleation and heterogeneous nanocrystal growth. In addition,

microwave heat polar substances rapidly and intensely, allowing us to selectively heat at desired sites. Based on the heating selectivity and the increase of the molecular motion, complex nanostructured materials can be fabricated. In the case of gold, where surface energies of the major facets are quite similar, there is not a generalized mechanism explaining nucleation and growth of anisotropic nanoparticles. Fig. 12 schematizes a simplified mechanism proposed for the triangular shape nanoparticles although at this point we can't provide an explanation of the initial symmetry breaking to avoid spherical growth. Notice that, microwave heating of HAuCl_4 in EG in the presence of PVP leads to the reduction of Au (III) to Au (0), where both EG and PVP served as reducing reagents¹¹. When Au (0) nucleates, free PVP adsorbs to all golds surfaces, due to the strong affinity of Au surface to the nitrogen of the PVP, resulting in small spherical Au NPs. However, when introducing PVP-SPIONs to the same system, Au anisotropic nanostructures with their surfaces decorated with SPIONs were produced. It is known that the shape of the initial nuclei is of great importance in determining the structure of the final products²⁹. PVP-SPIONs are negatively charged ($Z_{\text{potential}} = -30 \text{ mV}$) exposing the OH^- group of the PVP. The polar OH^- rich zone on the SPIONs surface can be served as preferential sites to nucleate the gold in a similar manner as we have previously reported for the *in-situ* synthesis of nanoparticles on hydroxyl rich substrates^{31,32}. Those initially formed gold seeds of triangular shape serve as the nucleation site for the later reduced Au atoms to grow on. During crystal grow, free PVP will preferentially adsorb to the facets with the lowest energy. Selectively adsorbing on the {111} facets (top and bottom facets of Au nanocrystals) while {100} facets (three side facets) continued growing at a faster rate. Finally, depending on the ratio of {111} to {100} facets on the side faces, either triangular or tip-truncated Au nanostructures can be obtained²⁹. Moreover, decreasing the amount of PVP could lead to the slower generation of Au nuclei, which in turn resulted in the larger edge length of the anisotropic Au nanostructures like triangles. The elongated edge length of the Au NTs can be evidenced from the larger D_h size determined by DLS measurements (Fig. 6c) and the red shift of LSPR peak observed in the NIR region (Fig. 5b). Besides, we also observed that increasing the PVP amount higher than 100 mg resulted in the formation of Au-SPIONs pairs instead of anisotropic Au-SPIONs hybrid nanostructures. Thus, excess of PVP suppresses the formation of the initial triangular SPIONs-Au clusters and leads to the formation of small individual Au NPs partially attached to SPIONs. At the PVP concentrations, temperatures and synthesis times scanned here we have observed that a constant fraction (around 25%) of hybrid nanoparticles self-nucleate into nucleus of different forms, octahedron or icosahedrons. These shapes are thermodynamically favorable as reported for the silver structures²⁹.

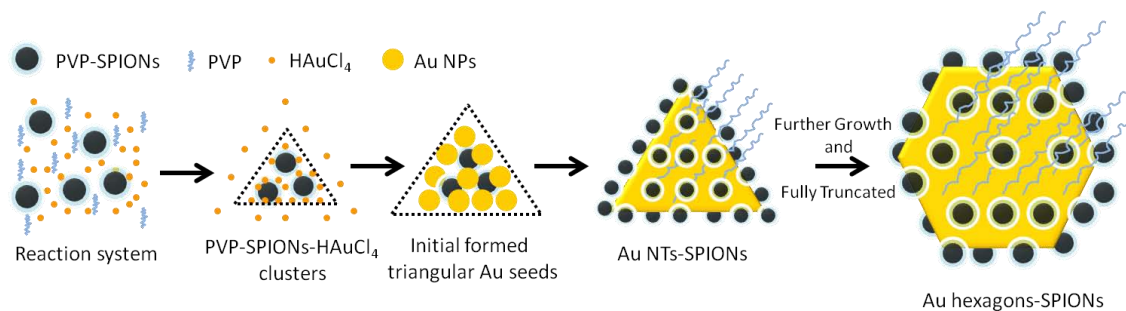


Figure 12. Schematic illustration of the formation of anisotropic Au-SPIONs hybrid nanomaterials. A proposed mechanism for the formation of Au NTs-SPIONs, truncated Au NTs-SPIONs and Au hexagons-SPIONs.

3.10 PURIFICATION AND SELF-ASSEMBLY OF Au NT-SPIONs NANOCOMPOSITES

3.10.1 GEL ELECTROPHORESIS

Previous work indicated that gel electrophoresis is an efficient way for purification of Au NTs, hence in our work, gel electrophoresis experiments were also performed to purify our Au NTs-SPIONs nanostructures. Protocols for the gel electrophoresis experiments followed what has been reported by de la Fuente's group²¹. Briefly, samples were loaded inside the wells of agarose gel (0.6 ×) immersed in an electrophoresis cuvette filled with TBE ×1. Electrophoresis separation was run at 100 V for 1 to 3 h. Due to the different shapes and sizes of the Au-SPIONs nanocomposites, more than one band is supposed to appear after gel separation. At the same time, PVP-SPIONs and Au spherical nanoparticles with a size about 200 nm were loaded inside the wells as references. After gel separation, each band was cut and dissolved completely in appropriate amount of GEX buffer heated at 60 °C. Then the solution was centrifuged at 14500 rpm for 20 min to pellet the nanoparticles. The collected nanoparticles were redispersed in MQ water and used for further characterization.

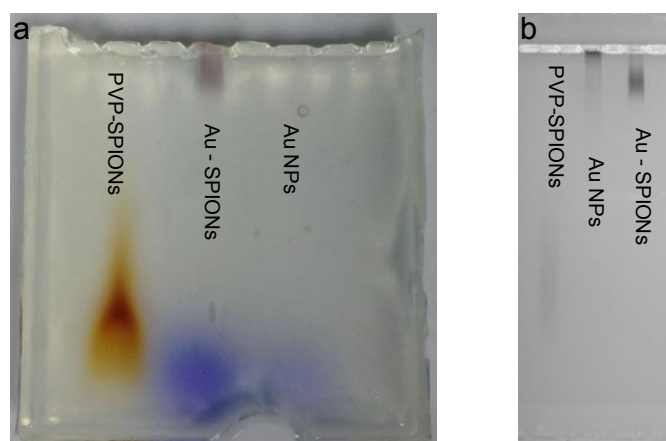


Figure 13. a) Digital image of the gel with bands after running 1 h, b) Digital image of the gel with bands after running 3 h.

First experiment was performed in a small gel run at 100 V for 1h, Fig. 13a shows bands after running. A clear but broad band was observed for PVP-SPIONs, Au-SPIONs band only moved

slightly with no clear band identified, while no band was found for Au NPs due to its low concentration. To improve the band separation, we repeated the experiments in a bigger gel running longer time (3h) and higher concentration of Au NPs, results were shown in Fig. 13b. Similarly, a clear band of PVP-SPIONs was found. Though more concentrated Au NPs were used, no clear band was found. This may due to the large size of Au NPs, and also it is noteworthy that Au NPs have the tendency to aggregate in solution, the formed large aggregates could lower their mobility in the gel electrophoresis. However, for Au-SPIONs, a clear band was observed, some Au-SPIONs were also found in the initial gel wells as well. Then, the band was cut and the Au-SPIONs were recovered for TEM characterization (Fig. 14). Au-SPIONs recovered from the bottom of the gel were labeled as Au-SPIONs-Bottom, the Au-SPIONs recovered from the top of the gel were labeled as Au-SPIONs-Top. TEM image of Au-SPIONs-Bottom shows a mixture of different Au structures (Fig. 14a and inset), while TEM image of Au-SPIONs-Top shows lots of crystals with snow-flower like structures, we assigned them to the salts from the TBE buffer. Due to the high content of salts in the sample, Au-SPIONs were difficult to be focused by TEM. Therefore, gel electrophoresis showed limitation in efficiently purifying our Au NTs-SPIONs nanocomposites, which may be due to their specific chemophysical properties which are different from pure Au NTs.

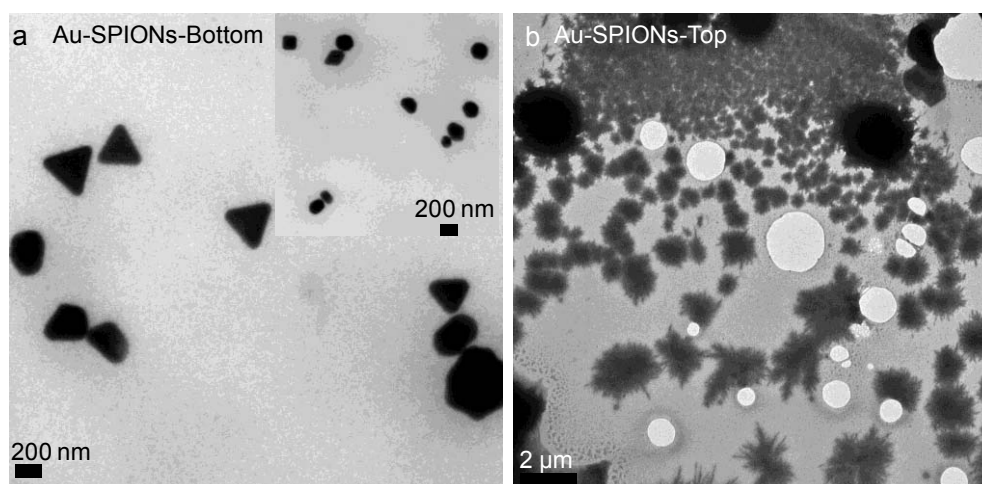


Figure 14. a) TEM image of Au-SPIONs-Bottom (inset is another area) and b) TEM image of Au-SPIONs-Top.

3.10.2 SELF-ASSEMBLY

Self assemble experiments of Au NTs-SPIONs followed what described in the reference²². Briefly, Au-SPIONs were concentrated and redispersed in ethanol-hexane at a 2:3 volume ratio. The Au-SPIONs dispersion in ethanol-hexane was then placed gently on the top of pure water surface. Due to the different polarity of the water and organic phase, Au-SPIONs were assembled in its interface. After evaporation of the organic solvents, assembled Au-SPIONs layer was able to be seen. For further characterization of the Au-SPIONs layer by TEM, a "horizontal lifting" technique was performed. TEM grid was gently moved to touch the Au-SPIONs layer parallel to the surface, due to the water-air interface, monolayer of Au-SPIONs was transferred to TEM grid.

Fig. 15a gives the image of Au-SPIONs after self assembly experiments, where a layer at the water-organic interface can be clearly seen. Under the illuminated microscope, gold-like color of the Au-SPIONs layer can be observed. Moreover, when putting an external magnet close to the well, the layer moved slowly towards the magnet, indicating the Au layer with magnetic properties due to the SPIONs decoration. The assembled Au-SPIONs were further characterized by TEM, results were shown in Fig. 15c and 15d. As expected, some Au NTs-SPIONs were do assembled together linking to each other regularly through each side, as indicated in Fig. 15c and Fig. 15d. Some other structures of Au-SPIONs were also found under the TEM observation as shown in Fig. 15d. This is because Au NTs-SPIONs nanostructure is not pure, accounts for 60% of the total structures, other Au structures presenting in the Au-SPIONs nanocomposites were assembled as well during the process. Therefore, more experiments need to be performed in order to get a better assemble of Au NTs-SPIONs hybrid nanostructures.

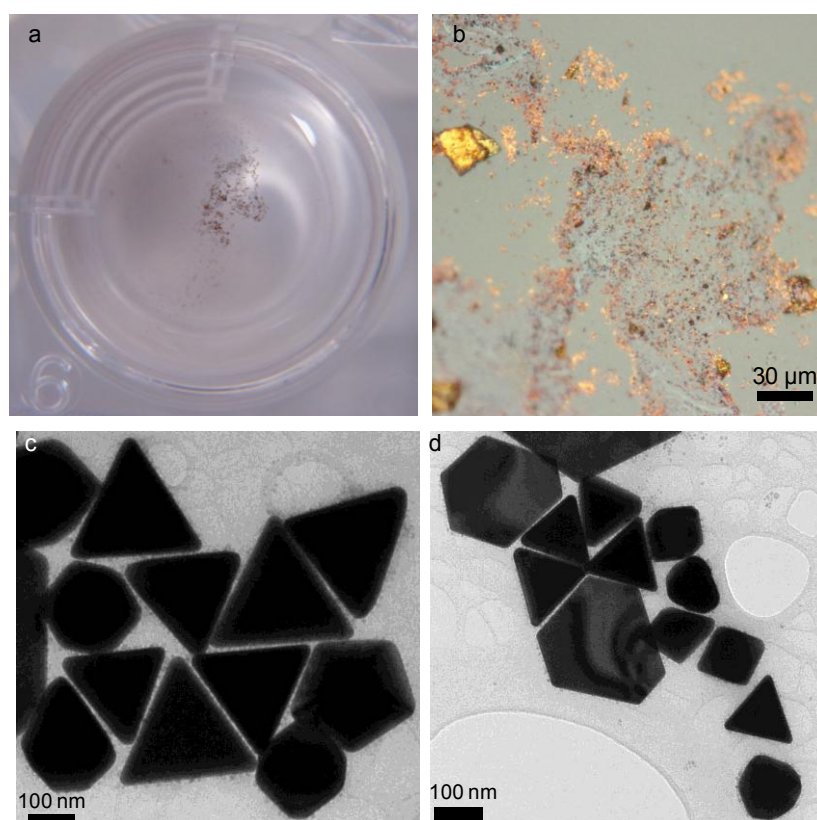


Figure 15. a) Au-SPIONs layer at the water-air interface after self assembly, b) image of the Au-SPIONs layer taken under illuminated microscope, c) and d) TEM images of the assembled Au-SPIONs layer.

In conclusion, gel electrophoresis is not a ideal method for purifying our Au NTs-SPIONs. Au NTs-SPIONs can be self assembled at the water-air interface, forming a monolayer of Au NTs-SPIONs nanostructures. Further experiments are necessary to improve the results.

3.11 CHAPTER CONCLUSIONS

A facile, fast and bio-friendly method was performed to synthesize Au-SPIONs hybrid nanoparticles readily dispersible in water. The microwave-assisted polyol route avoids the use of any toxic surfactant and it takes place at moderate temperature (80 °C - 120 °C). Remarkably, 60% shape-yield of Au triangles with their surfaces homogeneously decorated with a monolayer of SPIONs prior to any purification was achieved. We hypothesized that hydroxyls on the PVP-SPIONs form preferential hot spots that served as nucleation sites determining the shape of the initially Au seeds. The obtained hybrid Au NTs-SPIONs nanoparticles not only display strong magnetic response, but also show a characteristic LSPR band in the NIR region, which is important for applications requiring both magnetic and plasmonic properties. In addition, our method allows a certain degree of control of the anisotropic Au-SPIONs nanocomposites with tunable optical properties by simply changing the parameters used during the synthesis, in our case PVP amount, reaction temperature and reaction time. Moreover, the method could be used as a general strategy applicable to fabricate other hybrid nanocomposites.

Due to the specific chemico-physical properties of Au-SPIONs nanocomposites, gel electrophoresis shows difficulty in purifying Au NTs-SPIONs nanostructures. Due to the PVP coating, Au NTs-SPIONs can assemble at the water air interface forming as a monolayer.

3.12 ANNEX OF CHAPTER 3

In this part, detailed information about the MW synthesis process of SPIONs, MW scale-up synthesis of SPIONs, synthesis of Au nanoparticles and characterization of SPIONs are described.

3.12.1 SYNTHESIS OF Au-SPIONs NANOCOMPOSITES

Various amounts of PVP (25 mg, 50 mg, 100 mg and 150 mg) were added to the as obtained PVP-SPIONs dispersions in EG (4 mL) and sonicated to obtain homogenous mixtures. Then, 40 μ L 100 mM HAuCl₄ was added to the mixture. The molar ratio of free PVP to HAuCl₄ were 0.625:1, 1.25:1, 2.5:1 and 3.75:1, corresponding to 25 mg, 50 mg, 100 mg and 150 mg PVP respectively. The effect of MW temperature (T= 80, 100 and 120 °C) and time (t = 5, 10, 20 and 40 min) on the resulting hybrid structures were also investigated. In this synthesis, PVP is used as the capping agent (of both the SPIONs and the gold), to shape and stabilize the Au nanoparticles and as a mild reducing agent whilst EG is acting as solvent and reducing agent. As-obtained hybrid Au-SPIONs nanoparticles were washed twice with acetone to remove free PVP, collected by centrifugation at 6000 rpm for 2 min and redispersed in 2 mL MQ H₂O for further characterization. To ensure reproducibility of the results each synthetic condition was repeated three times. Table S1, in the supplementary information, summarizes the reaction conditions used and the characteristics of the obtained materials reporting the mean values of the independent experiments performed.

3.12.2 MATERIALS CHARACTERIZATION

Hydrodynamic diameter and zeta potential of PVP-SPIONs and Au-SPIONs were determined with a Zetasizer Nano ZS (Malvern) with a He/Ne 633 nm laser at 25 °C. For each sample, 3 independent measurements were performed with 15 scans for each measurement. Attenuated total reflectance Fourier transformed infrared spectra (ATR-FTIR) was performed on a Spectrum RX1 FTIR Spectrometer (Perkin Elmer, USA) in the frequency range 4000-400 cm⁻¹ with a resolution of 4 cm⁻¹. Samples were isolated from the solution by centrifugation, dried in the oven and placed on the crystal surface of the ATR-FTIR equipment. Size distribution, morphology and diffraction patterns of PVP-SPIONs and Au-SPIONs were collected in a JEOL JEM-1210 electron microscope at an operating voltage of 120 KV. High-resolution transmission electron microscopy (HRTEM) was performed on a JEOL 2010F HRTEM. TEM samples were prepared by placing several drops of the samples on the copper grid, blotting the copper grid with a filter paper and let the water to completely evaporate at room temperature. Typically, at least 300 different nanoparticles were counted with ImageJ to depict the size histogram distribution and the mean particle size. Scanning electron microscopy (SEM) analysis of Au-SPIONs hybrid nanostructures were performed on a QUANTA FEI 200 FEG-ESEM. A self-assembled gold monolayer was obtained using a hexane:ethanol (2:3) and water mixture, similarly as it has been previously described¹⁸. The assembled Au NTs-SPIONs monolayer was then transferred to a TEM grid for further characterization. Ultraviolet-visible-near infrared (UV-Vis-NIR) spectra were collected on a Cary-5000 UV-Vis-NIR spectrophotometer. To determine

the iron concentration, samples were sonicated for 10 min in an ultrasound bath. An aliquot of the sample was diluted with HCl (1%) and the iron content of the resulting solution was determined by flame absorption spectroscopy (air-acetylene) with a Perkin-Elmer 2100 spectrometer in a triplicate assay. Superconductive Quantum Interference Device (SQUID) measurements were recorded on a magnetometer (Quantum Design MPMS5XL) to determine the magnetization of the PVP-SPIONs and the Au-SPIONs. Typically, 150 μ L of an aqueous solution with known Fe concentration was placed and dried in the polycarbonate capsule to be inserted in the SQUID magnetometer sample holder. Magnetization curves, of the PVP-SPIONs and the hybrid Au-SPIONs, were recorded at 5K as a function of applied magnetic field up to 6 Tesla. Zero-field-cooling and field cooling magnetization values (ZFC-FC) as a function of temperature in a magnetic field of 50 Oe were also recorded.

3.13 CHAPTER REFERENCES

- (1) Xu, C.; Wang, B.; Sun, S. *Dumbbell-like Au–Fe₃O₄ Nanoparticles for Target-Specific Platin Delivery*. *Journal of the American Chemical Society*, **2009**, *131*, 4216.
- (2) Yu, C.-J.; Lin, C.-Y.; Liu, C.-H.; Cheng, T.-L.; Tseng, W.-L. *Synthesis of poly(diallyldimethylammonium chloride)-coated Fe₃O₄ nanoparticles for colorimetric sensing of glucose and selective extraction of thiol*. *Biosensors and Bioelectronics*, **2010**, *26*, 913.
- (3) Mohammad, F.; Balaji, G.; Weber, A.; Uppu, R. M.; Kumar, C. S. S. R. *Influence of Gold Nanoshell on Hyperthermia of Superparamagnetic Iron Oxide Nanoparticles*. *The Journal of Physical Chemistry C*, **2010**, *114*, 19194.
- (4) Stoeva, S. I.; Huo, F.; Lee, J.-S.; Mirkin, C. A. *Three-Layer Composite Magnetic Nanoparticle Probes for DNA*. *Journal of the American Chemical Society*, **2005**, *127*, 15362.
- (5) García, I.; Gallo, J.; Genicio, N.; Padro, D.; Penadés, S. *Magnetic Glyconanoparticles as a Versatile Platform for Selective Immunolabeling and Imaging of Cells*. *Bioconjugate Chemistry*, **2011**, *22*, 264.
- (6) Xie, J.; Zhang, F.; Aronova, M.; Zhu, L.; Lin, X.; Quan, Q.; Liu, G.; Zhang, G.; Choi, K.-Y.; Kim, K.; Sun, X.; Lee, S.; Sun, S.; Leapman, R.; Chen, X. *Manipulating the Power of an Additional Phase: A Flower-like Au–Fe₃O₄ Optical Nanosensor for Imaging Protease Expressions In vivo*. *ACS Nano*, **2011**, *5*, 3043.
- (7) Lim, Y. T.; Cho, M. Y.; Kim, J. K.; Hwangbo, S.; Chung, B. H. *Plasmonic Magnetic Nanostructure for Bimodal Imaging and Photonic-Based Therapy of Cancer Cells*. *ChemBioChem*, **2007**, *8*, 2204.
- (8) Dongkyu, K.; Mi Kyung, Y.; Tae Sup, L.; Jae Jun, P.; Yong Yeon, J.; Sangyong, J. *Amphiphilic polymer-coated hybrid nanoparticles as CT/MRI dual contrast agents*. *Nanotechnology*, **2011**, *22*, 155101.
- (9) Lee, J.; Yang, J.; Ko, H.; Oh, S.; Kang, J.; Son, J.; Lee, K.; Lee, S. W.; Yoon, H. G.; Suh, J. S.; Huh, Y. M.; Haam, S. *Multifunctional Magnetic Gold Nanocomposites: Human Epithelial Cancer Detection via Magnetic Resonance Imaging and Localized Synchronous Therapy*. *Advanced Functional Materials*, **2008**, *18*, 258.
- (10) Bardhan, R.; Chen, W.; Perez-Torres, C.; Bartels, M.; Huschka, R. M.; Zhao, L. L.; Morosan, E.; Pautler, R. G.; Joshi, A.; Halas, N. J. *Nanoshells with Targeted Simultaneous Enhancement of Magnetic and Optical Imaging and Photothermal Therapeutic Response*. *Advanced Functional Materials*, **2009**, *19*, 3901.
- (11) Zhang, Y.; Ding, H.; Liu, Y.; Pan, S.; Luo, Y.; Li, G. *Facile one-step synthesis of plasmonic/magnetic core/shell nanostructures and their multifunctionality*. *Journal of Materials Chemistry*, **2012**, *22*, 10779.
- (12) Mezni, A.; Balti, I.; Mlayah, A.; Jouini, N.; Smiri, L. S. *Hybrid Au–Fe₃O₄ Nanoparticles: Plasmonic, Surface Enhanced Raman Scattering, and Phase Transition Properties*. *The Journal of Physical Chemistry C*, **2013**, *117*, 16166.
- (13) Yu, H.; Chen, M.; Rice, P. M.; Wang, S. X.; White, R. L.; Sun, S. *Dumbbell-like Bifunctional Au–Fe₃O₄ Nanoparticles*. *Nano Letters*, **2005**, *5*, 379.
- (14) George, C.; Dorfs, D.; Bertoni, G.; Falqui, A.; Genovese, A.; Pellegrino, T.; Roig, A.; Quarta, A.; Comparelli, R.; Curri, M. L.; Cingolani, R.; Manna, L. *A Cast-Mold Approach to Iron Oxide and Pt/Iron Oxide Nanocontainers and Nanoparticles with a Reactive Concave Surface*. *Journal of the American Chemical Society*, **2011**, *133*, 2205.
- (15) Shi, W.; Zeng, H.; Sahoo, Y.; Ohulchanskyy, T. Y.; Ding, Y.; Wang, Z. L.; Swihart, M.; Prasad, P. N. *A General Approach to Binary and Ternary Hybrid Nanocrystals*. *Nano Letters*, **2006**, *6*, 875.
- (16) Wei, Y.; Klajn, R.; Pinchuk, A. O.; Grzybowski, B. A. *Synthesis, Shape Control, and Optical Properties of Hybrid Au/Fe₃O₄ “Nanoflowers”*. *Small*, **2008**, *4*, 1635.
- (17) Quaresma, P.; Osorio, I.; Doria, G.; Carvalho, P. A.; Pereira, A.; Langer, J.; Araujo, J. P.; Pastoriza-Santos, I.; Liz-Marzan, L. M.; Franco, R.; Baptista, P. V.; Pereira, E. *Star-shaped*

magnetite@gold nanoparticles for protein magnetic separation and SERS detection. RSC Advances, **2014**, *4*, 3659.

(18) Ma, L. L.; Feldman, M. D.; Tam, J. M.; Paranjape, A. S.; Cheruku, K. K.; Larson, T. A.; Tam, J. O.; Ingram, D. R.; Paramita, V.; Villard, J. W.; Jenkins, J. T.; Wang, T.; Clarke, G. D.; Asmis, R.; Sokolov, K.; Chandrasekar, B.; Milner, T. E.; Johnston, K. P. *Small Multifunctional Nanoclusters (Nanoroses) for Targeted Cellular Imaging and Therapy. ACS Nano*, **2009**, *3*, 2686.

(19) Schmidtke, C.; Kloust, H.; Bastus, N. G.; Merkl, J.-P.; Tran, H.; Flessau, S.; Feld, A.; Schotten, T.; Weller, H. *A general route towards well-defined magneto- or fluorescent-plasmonic nanohybrids. Nanoscale*, **2013**, *5*, 11783.

(20) Truby, R. L.; Emelianov, S. Y.; Homan, K. A. *Ligand-Mediated Self-Assembly of Hybrid Plasmonic and Superparamagnetic Nanostructures. Langmuir*, **2013**, *29*, 2465.

(21) Pelaz, B.; Grazu, V.; Ibarra, A.; Magen, C.; del Pino, P.; de la Fuente, J. M. *Tailoring the Synthesis and Heating Ability of Gold Nanoprisms for Bioapplications. Langmuir*, **2012**, *28*, 8965.

(22) Scarabelli, L.; Coronado-Puchau, M.; Giner-Casares, J. J.; Langer, J.; Liz-Marzán, L. M. *Monodisperse Gold Nanotriangles: Size Control, Large-Scale Self-Assembly, and Performance in Surface-Enhanced Raman Scattering. ACS Nano*, **2014**, *8*, 5833.

(23) Sau, T. K.; Murphy, C. J. *Room Temperature, High-Yield Synthesis of Multiple Shapes of Gold Nanoparticles in Aqueous Solution. Journal of the American Chemical Society*, **2004**, *126*, 8648.

(24) Millstone, J. E.; Métraux, G. S.; Mirkin, C. A. *Controlling the Edge Length of Gold Nanoprisms via a Seed-Mediated Approach. Advanced Functional Materials*, **2006**, *16*, 1209.

(25) Wiley, B.; Sun, Y.; Mayers, B.; Xia, Y. *Shape-Controlled Synthesis of Metal Nanostructures: The Case of Silver. Chemistry – A European Journal*, **2005**, *11*, 454.

(26) Washio, I.; Xiong, Y.; Yin, Y.; Xia, Y. *Reduction by the End Groups of Poly(vinyl pyrrolidone): A New and Versatile Route to the Kinetically Controlled Synthesis of Ag Triangular Nanoplates. Advanced Materials*, **2006**, *18*, 1745.

(27) Sun, Y.; Xia, Y. *Shape-Controlled Synthesis of Gold and Silver Nanoparticles. Science*, **2002**, *298*, 2176.

(28) Malikova, N.; Pastoriza-Santos, I.; Schierhorn, M.; Kotov, N. A.; Liz-Marzán, L. M. *Layer-by-Layer Assembled Mixed Spherical and Planar Gold Nanoparticles: Control of Interparticle Interactions. Langmuir*, **2002**, *18*, 3694.

(29) Xiong, Y.; Washio, I.; Chen, J.; Sadilek, M.; Xia, Y. *Trimeric Clusters of Silver in Aqueous AgNO₃ Solutions and Their Role as Nuclei in Forming Triangular Nanoplates of Silver. Angewandte Chemie International Edition*, **2007**, *46*, 4917.

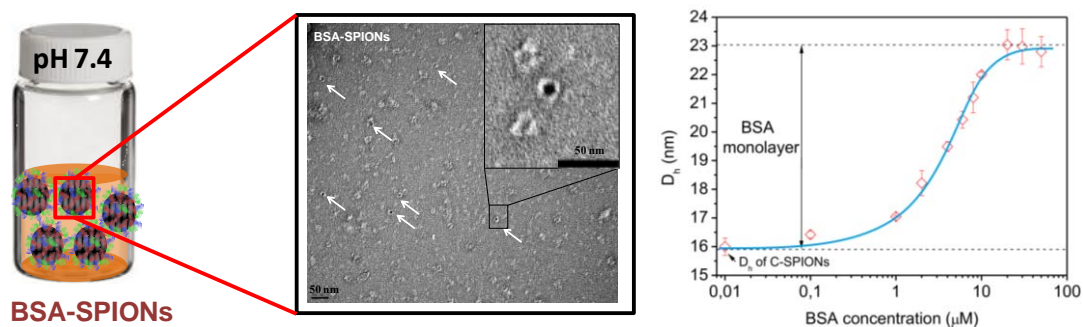
(30) Baghbanzadeh, M.; Carbone, L.; Cozzoli, P. D.; Kappe, C. O. *Microwave-Assisted Synthesis of Colloidal Inorganic Nanocrystals. Angewandte Chemie International Edition*, **2011**, *50*, 11312.

(31) Pascu, O.; Caicedo, J. M.; Lopez-Garcia, M.; Canalejas, V.; Blanco, A.; Lopez, C.; Arbiol, J.; Fontcuberta, J.; Roig, A.; Herranz, G. *Ultrathin conformal coating for complex magneto-photonic structures. Nanoscale*, **2011**, *3*, 4811.

(32) Zeng, M.; Laromaine, A.; Feng, W.; Levkin, P. A.; Roig, A. *Origami magnetic cellulose: controlled magnetic fraction and patterning of flexible bacterial cellulose. Journal of Materials Chemistry C*, **2014**, *2*, 6312.

CHAPTER 4

STUDY ON THE INTERACTION OF BOVINE SERUM ALBUMIN WITH SUPERPARAMAGNETIC IRON OXIDE NANOPARTICLES



CHAPTER SUMMARY

In this chapter, an adsorption protocol was used to adsorb BSA on the surface of both T-SPIONs and C-SPIONs. The resulting BSA-SPIONs remained monodisperse in a wide range of biologically relevant media after 24h incubation.

The adsorption behavior of BSA on C-SPIONs surface was studied in detail by several analytical methods, indicating a "side on" binding of BSA on the nanoparticles and the formation of a BSA monolayer with a thickness of about 3.5 nm. Next, spectroscopic investigations suggest only a slight unfolding of BSA structure upon adsorption on C-SPIONs surface. Finally, isothermal titration calorimetry analysis (ITC) was used to measure the binding constant of BSA on the C-SPIONs surface, which was much larger than the one measured for the other proteins present in FBS.

Chapter Index

	pag.
CHAPTER SUMMARY	93
4.1 STABILITY OF SPION _s IN BIOLOGICAL ENVIRONMENTS	95
4.2 STABILIZATION OF SPION _s IN BIOLOGICAL ENVIRONMENTS	98
4.2.1 STABILIZATION OF SPION _s BY ADSORBING BSA	98
4.2.2 STABILIZATION OF SPION _s BY ADDING EXCESS Na ₃ Cit	104
4.3 CHARACTERIZATION OF BSA LAYER SPIONS	105
4.4 STUDY ON THE INTERACTION MECHANISM OF BSA WITH C-SPION _s	107
4.4.1 ADSORPTION BEHAVIOR OF BSA ON C-SPION _s ' SURFACE	107
4.4.1.1 DLS MEASUREMENTS	107
4.4.1.2 DETERMINATION OF SATURATED AMOUNT OF BSA ADSORBED ON C-SPION _s SURFACE	108
4.4.1.3 DIFFERENTIAL CENTRIFUGAL SEDIMENTATION MEASUREMENTS	109
4.4.1.4 X-RAY PHOTOELECTRON SPECTROSCOPY	110
4.4.1.5 CALCULATION OF THE SATURATED NUMBER OF BSA MOLECULE PER SPION	112
4.4.2 CONFORMATION CHANGE OF BSA UPON INTERACTION WITH C-SPION _s	113
4.4.2.1 UV-Vis MEASUREMENTS	113
4.4.2.2 CIRCULAR DICHROISM	114
4.4.2.3 STEADY-STATE FLUORESCENCE SPECTROSCOPY	115
4.4.2.4 SYNCHRONOUS FLUORESCENCE SPECTROSCOPY	113
4.5 THERMODYNAMICS OF PROTEIN ADSORPTION ON SPION _s	118
4.6 CHAPTER CONCLUSION	120
4.7 ANNEX OF CHAPTER 4	121
4.8. CHAPTER REFERENCES	128

4.1 STABILITY OF SPIONS IN BIOLOGICAL ENVIRONMENTS

Biomedical applications of SPIONs, or NPs in general, involve inevitably the contact with biological fluids, which are media with high ionic strength and often also contain several biomolecules. A main issue that materials science researchers face is to ensure the stability of the engineered NPs in those complex biological media. Due to the interaction with the biological entities in the media, NPs tend to destabilize and sediment after undergoing an aggregation process, leading to the significant increase in their hydrodynamic size, as well as changes in NPs surface properties in terms of shape, surface area and charge¹⁻⁵. Recent studies also evidence that some biological responses greatly depend on the behavior of NPs in the biological media, the change in NPs hydrodynamic size can influence their final bio-distribution and trigger desirable or deleterious biological effects⁵⁻¹⁰. Moreover, this aggregation and sedimentation in biological conditions could possibly affect the *in vitro* and *in vivo* toxicity assessments of NPs, and introduce problems of reproducibility, difficulty in the interpretation of the toxicity results, inaccurate determination of the dose for potential treatments and the reduced diagnostic efficiency^{7,8}. For these reasons, stability of the synthesized SPIONs in biological environments is imperative before accurate and reliable *in vitro* and *in vivo* assays are to be performed.

In this chapter, stability of T-SPIONs and C-SPIONs were assessed in biologically relevant media: phosphate buffer saline (PBS), RPMI and DMEM at a SPIONs concentration of 50 $\mu\text{g}/\text{mL}$. PBS is a buffer solution commonly used in biological research. It contains sodium chloride, sodium phosphate, and (in some formulations) potassium chloride and potassium phosphate. The buffer helps to maintain a constant pH. RPMI and DMEM are cell media which are extensively used in *in vitro* toxicity and stability assays of nanoparticles. The three media differ significantly in their ionic strength and salt content, like Ca^{2+} and Mg^{2+} . The salt content in terms of Ca^{2+} concentration, for example, follows the order of $\text{PBS} < \text{RPMI} < \text{DMEM}$, with a value of 0, 0.4 and 1.8 mM, respectively¹¹.

Fig. 1 shows the D_h evolution of T-SPIONs and C-SPIONs in H_2O and the biological media as a function of time. Both SPIONs show good stability in H_2O since D_h doesn't change up to 3 months, this is attributed to the highly negative charged surface of both SPIONs. However, when incubated in biological media, T-SPIONs destabilized and precipitated rapidly (Fig. 1a). In all the cases, a similar behavior is observed; D_h of T-SPIONs in RPMI, for instance, goes up sharply from 25 nm to about 2800 nm in 2 min, and subsequently precipitated. Moreover, the addition of 10% FBS to RPMI and DMEM media did not prevent the sedimentation of T-SPIONs, as D_h of T-SPIONs in RPMI-FBS and DMEM-FBS show a sharp increase within 10 min.

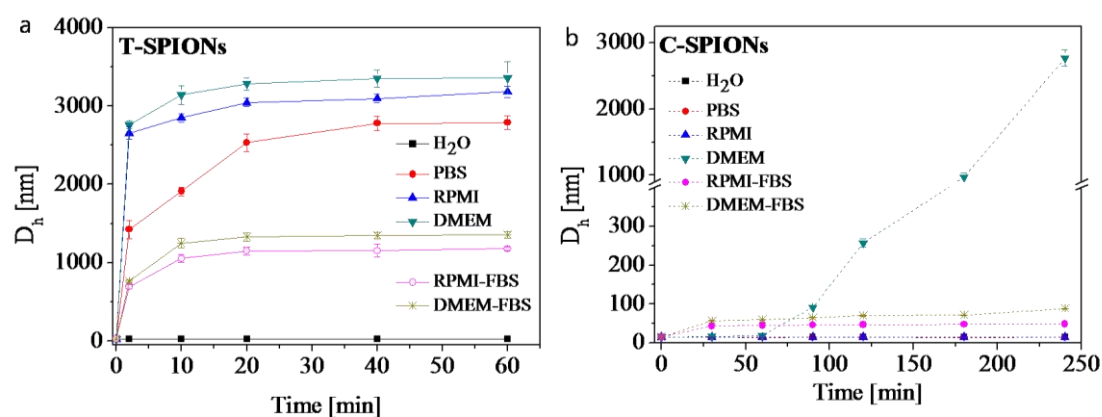


Figure 1. Stability of (a) T-SPIONs and (b) C-SPIONs in H₂O, PBS, RPMI-FBS and DMEM-FBS monitored by measuring D_h as a function of time. Consistent with the dramatic increase in D_h, significant decrease in diffusion coefficient, obvious increase in zeta potential (ζ) and electrophoretic mobility (EPM) were also detected (Table 1), confirming the destabilization of T-SPIONs in these media.

Table 1. Hydrodynamic Diameter (D_h), Polydispersity Index (PDI), Diffusion Coefficient, Zeta potential (ζ) and Electrophoretic Mobility (EPM) data extracted from DLS and Zeta potential measurements of T-SPIONs (50 μ g/mL) in various media at an incubation time of 20 min.

Dispersion Media	DLS			Zeta potential	
	D _h (nm)	PDI	Diffusion Coefficient ($\mu\text{m}^2/\text{s}$)	ζ (mV)	EPM ($\mu\text{mcm}/\text{Vs}$)
H ₂ O	25 \pm 0.2	0.196	21.4	-54	-4.231
PBS	1910 \pm 109	0.347	0.303	-21.6	-2.336
RPMI	2847 \pm 55	0.335	0.173	-18.8	-1.47
DMEM	3281 \pm 80	0.418	0.148	-11.9	-0.93
RPMI-FBS	1177 \pm 25	0.325	0.658	-9.41	-0.74
DMEM-FBS	1335 \pm 41	0.362	0.379	-9.94	-0.78

On the other hand, C-SPIONs displayed a different aggregation behavior in the same media. C-SPIONs show excellent stability in PBS and RPMI, as D_h remains unchanged up to 24h (Fig. 1b). C-SPIONs in DMEM, show an intermediate stability. D_h remained unchanged in the first 1h, although it increased rapidly to about 250 nm in the following 1h, and reached 2800 nm in 4h. In RPMI-FBS and DMEM-FBS, D_h of C-SPIONs show a slight increase in the initial 30 min and remains flat in the later time, also suggesting the good stability of C-SPIONs in the serum containing media, the slight increase in both cases could be interpreted as the adsorption of serum proteins on the surface of C-SPIONs. Changes in diffusion coefficient, zeta potential (ζ) and EPM (Table 2) further confirm these findings.

Table 2. D_h , PDI, Diffusion Coefficient, ζ and EPM data extracted from DLS and Zeta potential measurements of C-SPIONs (50 $\mu\text{g}/\text{mL}$) in various media at an incubation time of 240 min.

Dispersion Medium	DLS			Zeta potential	
	D_h (nm)	PDI	Diffusion Coefficient ($\mu\text{m}^2/\text{s}$)	ζ (mV)	EPM ($\mu\text{mcm}/\text{Vs}$)
H ₂ O	16 \pm 1	0.103	32	-36	-4.65
PBS	15 \pm 1	0.121	31	-30.3	-3.954
RPMI	15 \pm 1	0.11	31	-30.9	-3.875
DMEM	2766 \pm 123	0.172	0.429	-20	-1.563
RPMI-FBS	49 \pm 1	0.312	10	-10.15	-0.79
DMEM-FBS	88 \pm 1	0.231	5.56	-10.16	-0.79

From the above results, we can see clearly that C-SPIONs show better stability than T-SPIONs in biological media, indicating that surface coating greatly influences the stability of SPIONs in these media. Although both T-SPIONs and C-SPIONs show negative charged surface, the adsorption mechanism of TMAOH and citrate ligands on SPIONs surface are different. For T-SPIONs, TMAOH cations adsorb onto SPIONs surface through electrostatic interaction and this results in an electrostatic double layer which provide stability to SPIONs in aqueous solution¹². However, this electrostatic double layer can be easily disassembled by the species presenting in biological media like salts and biomolecules¹². As for C-SPIONs, the three carboxylate groups of citrate ligand have strong coordination affinity to Fe(III) ions, some of the carboxylate groups strongly coordinate to SPIONs surface, the rest of carboxylate groups extend into the water, providing a more robust coating and higher stability to SPIONs in H₂O and in some complex media like PBS and RPMI¹³.

Moreover, the stability and aggregation behavior of SPIONs in biological media was reported to be not only dependent on the SPIONs surface coating, but also on the nature of the surrounding media^{7,14}. Some previous studies reported that NPs aggregate and settle down immediately when exposed to biological media¹⁵⁻¹⁷, where high ionic strength was considered an important factor to cause the NPs aggregation. When NPs are in contact with these media, surface charges on their surface were suppressed by the high ionic strength of salts presented in these media, decreasing the electrostatic repulsion and subsequently precipitating the NPs^{18,19}. In particular, Safi M. and co-workers found that the divalent calcium and magnesium cations present in the cell media significantly reduce the stability of the C-SPIONs through the complex reaction with the citrate ligands⁶. Similar significant aggregation phenomenon happened to our synthesized T-SPIONs in biological media and C-SPIONs in DMEM, despite the highly negatively charged surface of both T-SPIONs and C-SPIONs. This suggests that the surface coating of C-SPIONs and T-SPIONs are not enough to maintain their stability when exposed to biologically relevant media with high salts content, which could in turn limit their biological applications.

Thus, improvement of the stability of SPIONs in biologically relevant media is of significant importance.

4.2 STABILIZATION OF T-SPIONs AND C-SPIONs IN BIOLOGICAL ENVIRONMENTS

In the last decade, many efforts were made to ensure stable NPs dispersions for *in vitro* or *in vivo* applications. A common used strategy to stabilize them is to functionalize their surface using polymers. Polyethylenimine (PEI) is a well-known polymer that stabilizes efficiently NPs^{20,21}, as well as polyethylene glycol (PEG), chitosan, dextran, citrate are other examples^{6,22-24}. The choice of polymers undoubtedly needs to be carefully evaluated to avoid any potential toxicity to cells and interference in the interpretation of NPs' cytotoxicity.^{3,25} Moreover, in many cases, functionalization of NPs with polymers is not sufficient for their biological application purposes since resulting NPs are stable in biological relevant media only for few hours. Wiogo *et al.*¹⁹ showed that although the surface of SPIONs were modified by polymethacrylic acid, polyethylenimine, and branched oligoethylenimine, they aggregated and precipitated in biological media, despite the positive or negative charged surface of the SPIONs.

Bovine serum albumin (BSA) is the most abundant protein in serum and one of the most important components in biological culture media. It has been reported as an efficient stabilizing agent to keep the dispersing state of several types of NPs, including gold NPs^{26,27}, carbon nanotubes²⁸, and titanium dioxide³. Recently, a pH adjustment protocol was proposed by Guiot. *et al.*²⁹ to stabilize TiO₂-NPs with different surface coatings in biological media, where the pH of TiO₂-NPs was first adjusted before adsorption of BSA. As a result, the protocol showed robust ability in stabilizing TiO₂-NPs in LB media (Lysogeny broth media, which is primarily used for the growth of bacteria). Meanwhile, other works demonstrated that addition of excess trisodium citrate (Na₃Cit) could also stabilize SPIONs dispersions^{12,30}. These findings provide novel ways for further enhancing the dispersion stability of SPIONs in complex biological media.

4.2.1 STABILIZATION OF SPIONs BY ADSORBING BSA

A pH ADJUSTED AND BSA ADSORPTION PROTOCOL

To further improve the stability of T-SPIONs in biological media and C-SPIONs in DMEM, we adsorbed BSA to those SPIONs. We believe that the adsorption of BSA on NPs surface could offer higher stability and biocompatibility in comparison with strategies use poly (methyl methacrylate) (PMMA), PEI or other organic layers^{27,31}. In particular, I have used a modified pH adjusted and BSA adsorption protocol based on that proposed by Guiot²⁹ (Fig. 2).

The protocol presented by Guiot *et al.*²⁹ is based on the colloidal stability theory, in particular the DLVO theory, which indicates that the electrostatic repulsion force, rather than Van der Waals attraction force is responsible for the colloidal stability of NPs dispersions. In other words, once the electrostatic repulsion increase, the stability of the NPs dispersions improved. Following Guiot's approach, we first adjusted the pH of our colloidal dispersion at 11 where

SPIONs and BSA exhibit a net charge of identical sign, and then we added BSA to the SPIONs dispersion. BSA with a negative net charge at pH 11 can still be attached to the negative charge NPs due to the intrinsic amphiphilic character of the protein.^{19,26} The addition of enough BSA in the SPIONs solutions, allows the coverage of the SPIONs while maintaining its stability. The BSA coverage avoids the aggregation of the SPIONs solutions once we change the solutions to physiological pH.²⁷



Figure 2. A schematic illustration of the pH adjusted and BSA adsorption protocol.

The pH of the synthesized C-SPIONs was first adjusted to 11 by adding 0.1 M NaOH (pH of synthesized T-SPIONs was already 11). At pH 11, the zeta potential measurement of BSA and C-SPIONs decreased from -22 mV (pH 7.4) to -28 mV and -36 mV (pH 8.3) to -42 mV respectively. Then, SPIONs dispersions were incubated with BSA solution for 1 h, and then pH of the mixture was adjusted to the physiological value of 7.4. The resulting SPIONs after BSA adsorption are referred to as BSA-T-SPIONs and BSA-C-SPIONs, respectively. BSA-T-SPIONs and BSA-C-SPIONs dispersions prepared are extremely stable due to the electrostatic repulsion among them and the BSA coverage on their surface.

STABILIZATION OF BSA-T-SPIONs AND BSA-C-SPIONs IN WATER

50 μ L of the obtained BSA-T-SPIONs and BSA-C-SPIONs (1 mg/mL) were diluted 20 times in water to a final concentration of 50 μ g SPIONs/mL and their stability was monitored by DLS over 24 h. DLS intensity-weighted size distributions (Fig. 3a), D_n , diffusion coefficient and diffusion time remain unchanged over 24 h (Table 1 and Table 2 in the annex part), implying high stability of the prepared BSA-T-SPIONs and BSA-C-SPIONs dispersions over time. Some previous studies suggested the existence of two layers contributing to the stabilization of NPs with proteins: the hard protein corona, strongly interacting with the NPs' surface and the soft protein corona, proteins loosely bounded to the NPs surface.¹⁸ Therefore the dilution of our samples and the excess of the BSA could contribute to the stabilization of the NPs.

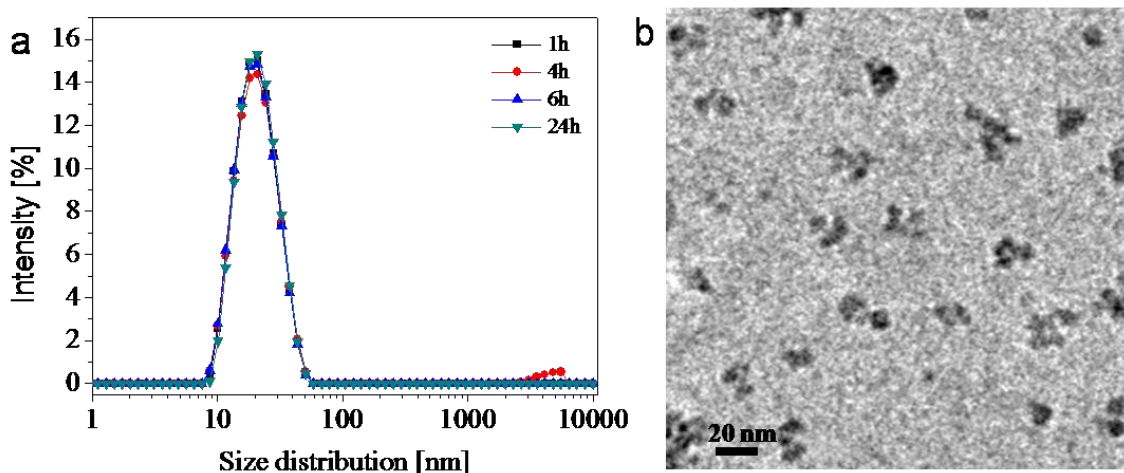


Figure 3. a, DLS intensity-weighted size distributions of C-SPIONs (control) and the prepared BSA-C-SPIONs at an evaluated time of 1h, 4h, 6h, and 24h in water; (b) Cryo-TEM image of the prepared BSA-C-SPIONs after 24h preparation in water.

Cryo-TEM is an useful technique that provides a representative view of the real dispersing state of NPs in solution, therefore, Cryo-TEM analysis was also performed to reveal the stability of the obtained BSA-C-SPIONs, as it is shown in Fig. 3b. BSA-C-SPIONs exist in the solution as small clusters but well separated from each other, suggesting the well dispersing state of BSA-C-SPIONs in solution even after 24h incubation. This possibly is due to the electrostatic repulsion provided by their negative charged surfaces, as well as the effect of steric stabilization.

STABILIZATION OF BSA-T-SPIONs AND BSA-C-SPIONs IN BIOLOGICAL MEDIA

To test the practical effect of our protocol, we evaluated the stability of BSA-T-SPIONs and BSA-C-SPIONs in PBS, RPMI and DMEM. Firstly, they were diluted 20 times to a final BSA-SPIONs concentration at 50 μg SPIONs/mL with the appropriate media and we monitored their aggregation evolution upon incubation after 24h. Digital images of BSA-T-SPIONs and BSA-C-SPIONs in PBS after 24h showed clear dispersions in both cases, no aggregates or precipitates were observed (Fig. 4), indicating both prepared SPIONs remained stable in PBS after 24h incubation.

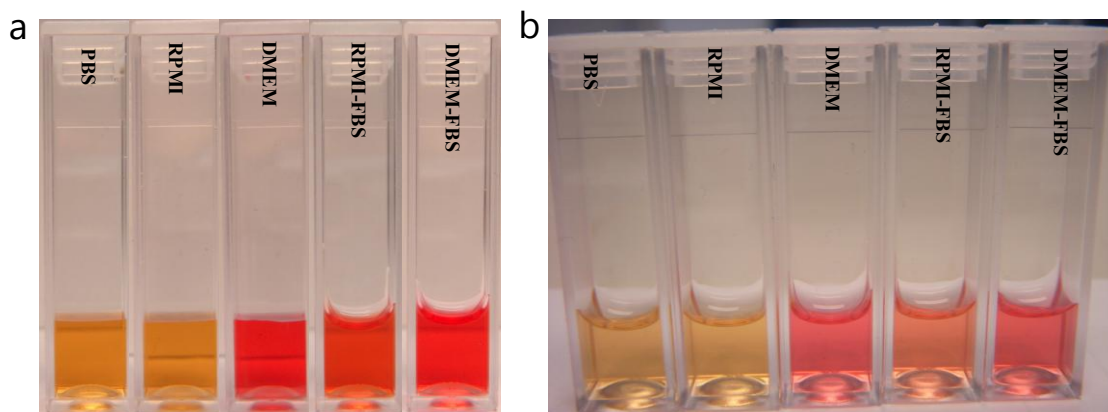


Figure 4. Digital images of BSA-T-SPIONs (a) and BSA-C-SPIONs (b) in PBS, RPMI, DMEM, RPMI-FBS and DMEM-FBS after 24h incubation.

Stability of BSA-T-SPIONs and BSA-C-SPIONs upon incubation with PBS after 24h were also monitored by DLS measurements. Fig. 5a and Fig. 6b show a slight increase in D_h , diffusion coefficients and diffusion times for both BSA-T-SPIONs and BSA-C-SPIONs over the tested period (Table 3 and 4 in the annex part), indicating the stable behavior of BSA-T-SPIONs and BSA-C-SPIONs in PBS.

Figure 5. DLS intensity-weighted size distributions of T-SPIONs (control) and (a) the prepared BSA-T-SPIONs and (b) BSA-T-SPIONs in PBS, (c) in RPMI, (d) in DMEM, (e) in RPMI-FBS and (f) in DMEM-FBS at an evaluated time of 1h, 4h, 6h, and 24h.

Stability of 50 μ g/mL BSA-T-SPIONs and BSA-C-SPIONs solutions in RPMI and DMEM, which have higher salt content compared to PBS, was tested. Intensity-weighted size distributions of BSA-T-SPIONs in RPMI and DMEM show a gradual shift toward larger size as incubation time increased, D_h increases from 24 nm to 100 nm in RPMI over 24h and to 220 nm in DMEM (Fig. 5c and 5d). The increase in D_h is also confirmed by the decrease diffusion coefficient and the increased diffusion time (Table 5 and 6). Although BSA-T-SPIONs increased in size in RPMI and

DMEM, the present size is still desirable for *in vitro* toxicity studies when compared to the rapid and significant aggregation behavior of the synthesized T-SPIONs in the same media. Moreover, no sedimentation appeared in 24h for BSA-T-SPIONs in both media (Fig. 4a).

Figure 6. DLS intensity-weighted size distributions of C-SPIONs (control) and BSA-C-SPIONs in (a) PBS; (b) RPMI; (c) DMEM; (d) RPMI-FBS and (e) DMEM-FBS at an evaluated time of 1h, 4h, 6h, and 24h.

As expected, BSA-C-SPIONs remain extremely stable in RPMI and DMEM even after 24h incubation, no aggregates or precipitates could be identified in the dispersions (Fig. 4b, Fig. 6b and c). Intensity-weighted size distributions of BSA-C-SPIONs in RPMI as a function of time superimposed to each other (Fig. 6b), diffusion coefficient and diffusion time also did not change (Table 7 in the annex part), indicating the identical distribution of the BSA-C-SPIONs in 24h. D_h of BSA-C-SPIONs in DMEM only increased few nanometers (Fig. 6c), whereas synthesized C-SPIONs show dramatic aggregation, implying the robustness of the pH adjusted

and BSA adsorption protocol. Slight changes in diffusion coefficient and diffusion time are found for BSA-C-SPIONs in DMEM, confirming their excellent stability (Table 8 in the annex part).

Media for cell culture are always supplemented with serum proteins, therefore we further tested the stability of BSA-T-SPIONs and BSA-C-SPIONs under serum conditions, RPMI-FBS and DMEM-FBS respectively. In all these cases, DLS intensity-weighted size distributions as a function of time exhibit minor shifts in D_{hr} , as well as slight changes in diffusion coefficient and diffusion time, which clearly precludes the possibility of aggregation or sedimentation of BSA-T-SPIONs and BSA-C-SPIONs in these media (Fig. 5e and 5f, Fig. 4d and 4e, Table 9, 10, 11 and 12 in the annex part).

DETERMINATION OF THE NECESSARY BSA CONCENTRATION

In the present investigation, we also found that to endow SPIONs dispersions with sufficient stability in the biological media, the concentration of BSA needed during the preparation varied significantly (Table 3) depending on the media. For both SPIONs, the necessary concentration of BSA follows the order of in DMEM > RPMI > PBS > RPMI-FBS and DMEM-FBS. We attribute this to the different compositions of these media. As mentioned before, the salt content in terms of Ca^{2+} and Mg^{2+} concentration follows the order of PBS < RPMI < DMEM and it is reported that the divalent calcium and magnesium cations are those mainly cause the SPIONs aggregation through interaction with the surface coating of SPIONs. BSA adsorption on SPIONs's surface could complex with these divalent cations, protecting the SPIONs surface by screening these divalent cations from interacting directly with the SPIONs surface, thus keeping the SPIONs stable in the tested media. Hence, in biological media with higher concentration of divalent cations, it is expected that the amount of BSA needed should also be higher. For this reason, the amount of BSA needed is the highest in DMEM, followed by RPMI and PBS. Furthermore, Ji *et al.*³ found that proteins in FBS, like globulin and transferrin, exhibit a synergistic effect on stabilizing the NPs dispersions with BSA. Therefore, in RPMI-FBS and DMEM-FBS, FBS itself served as the additional stabilization reagent in addition to BSA, thus the amount of BSA needed to stabilize T-SPIONs and C-SPIONs in those media is lower compared to those media without FBS. The presence of FBS is clearly detected in the DLS intensity-weighted size distributions in Fig. 6d and Fig.6e.

Table 3. The necessary concentration of BSA needed for T-SPIONs and C-SPIONs in different media by using the pH adjusted and BSA adsorption protocol.

SPIONs	Concentration of BSA needed (w/v %)				
	PBS	RPMI	DMEM	RPMI-FBS	DMEM-FBS
T-SPIONs	2	10	15	1	1
C-SPIONs	1	2	5	0.5	0.5

Moreover, we observed that in all the tested media, the necessary concentration of BSA needed for C-SPIONs is always lower than that for T-SPIONs. We relate this to the different surface

coating of C-SPIONs and T-SPIONs. As it was concluded before, citrate ligands exhibit stronger resistance to high salt and high ionic strength than TMAOH. Previous studies also revealed that nonspecific binding of BSA to self-assembled monolayers following the order of hydrophobic > COO^- > NH_3^+ > OH^- > ethylene glycol^{32,33}, which indicates BSA has a preference and a higher affinity for binding to SPIONs surface with citrate ligands (with three COO^- groups per molecule) than those with TMAOH coating (with one OH^- per molecule). As a result, BSA is envisaged to bind more effectively on C-SPIONs than on T-SPIONs under the same BSA concentration. For those reasons, using less BSA and we could get the same or even better stability of C-SPIONs in biological media than T-SPIONs.

4.2.2 STABILIZATION OF SPIONs BY ADDING EXCESS Na_3Cit

For comparative purpose, I also investigated the addition of excess Na_3Cit to enhance the stability of the T-SPIONs and C-SPIONs in biological media as previously reported^{12,30}. Briefly, a solution of 50 $\mu\text{g}/\text{mL}$ SPIONs in biological media and with a 10 mM Na_3Cit were prepared and their stability was monitored by DLS over 24h. Results show that adding 10 mM excess Na_3Cit could not prevent the aggregation of T-SPIONs in all of the tested media, T-SPIONs destabilized and precipitated in 1h (Fig. 7a). While stability of C-SPIONs was maintained in 24h by adding 10 mM excess Na_3Cit in DMEM as well as in the other media (Fig. 7b). D_h doesn't increase in PBS- Na_3Cit within 24h, only a slight increase in RPMI- Na_3Cit and DMEM- Na_3Cit was found. In RPMI-FBS- Na_3Cit and DMEM-FBS- Na_3Cit , D_h increase to about 35 nm in the initial 1h, and kept unchanged in the following 24h. The increase in D_h during the first 1h could be due to the formation of protein corona on C-SPIONs surface, as it was demonstrated by Walczyk³⁴ who described that protein corona on NPs surface formed in a relatively stable manner over a period of one hour.

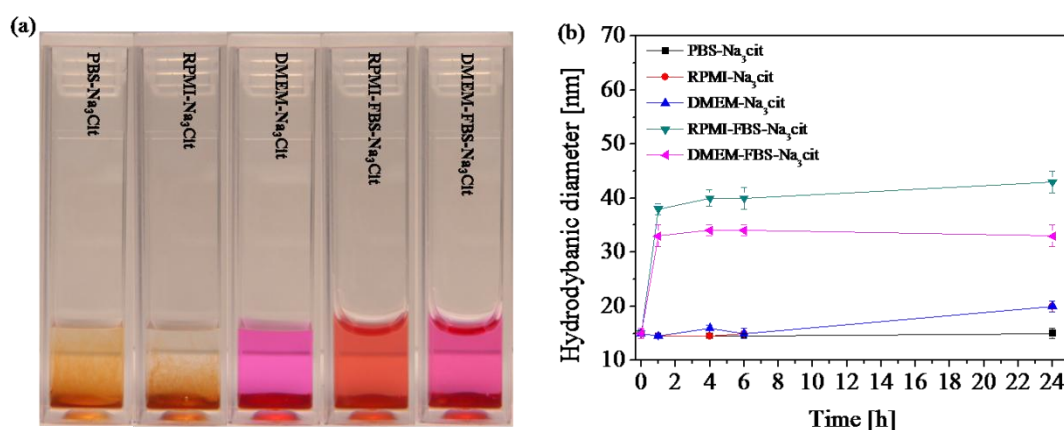


Figure 7. (a) Digital images of T-SPIONs in PBS- Na_3Cit , RPMI- Na_3Cit , DMEM- Na_3Cit , RPMI-FBS- Na_3Cit and DMEM-FBS- Na_3Cit after 1h incubation, (b) Graph showing the changes in hydrodynamic size of C-SPIONs in PBS- Na_3Cit , RPMI- Na_3Cit , DMEM- Na_3Cit , RPMI-FBS- Na_3Cit and DMEM-FBS- Na_3Cit at an evaluated time of 24h.

In summary, the reported BSA adsorption protocol shows excellent prospect in preparing extremely stable SPIONs dispersions in several biologically relevant media, which are desirable

for reliable *in vitro* and *in vivo* nanoparticle assessments. Although, the addition of excess Na_3Cit could prevent C-SPIONs from aggregation in DMEM and other media, the stabilization effect is not working for T-SPIONs. Moreover, high concentration of Na_3Cit in biological media is reported to produce risky effects to the growth of the cells^{35,36}. Therefore, the modified BSA adsorption and pH adjusted protocol seems a general and more suitable method to improve the stability of SPIONs in biological media.

4.3 CHARACTERIZATION OF BSA ADSORPTION ON SPIONs

We further characterized the BSA layer on T-SPIONs and C-SPIONs surface by commonly used physicochemical characterization methods.

Fig. 8a shows the changes in D_h of T-SPIONs and C-SPIONs before and after performing the BSA adsorption protocol. Diluted BSA-T-SPIONs shows 5 nm increase in D_h and 6 nm for diluted BSA-C-SPIONs. The dimension of BSA is reported to be (8 × 8 × 8 × 3.4 nm) as a triangular equilateral prism³⁷, the increase of D_h for both SPIONs corresponds to the shorter dimension of BSA, therefore, we conclude that a BSA monolayer was formed on both SPIONs surface. The result obtained here is in agreement with previous findings using BSA as a model protein and Au NPs as model NPs^{27,38}. To provide clearer evidence of the formed BSA monolayer on SPIONs surface, we present negative staining TEM data for the purified BSA-T-SPIONs and BSA-C-SPIONs in water. Representative negative staining TEM images (Fig. 8c and 8d) show clear evidence of this BSA monolayer, which completely covers the both SPIONs surface. Moreover, after measuring the thickness of these images, an increase in diameter of 6 ± 1 nm was computed, which is consistent with the data obtained by DLS, suggesting a BSA monolayer with thickness about 3nm was formed on T-SPIONs and C-SPIONs surface.

The formation of protein corona on SPIONs surface will likely change their zeta potential and the isoelectric point (IEP)³⁹, thus the change in zeta potential of C-SPIONs and T-SPIONs before and after the BSA adsorption on their surface. The zeta potential value of T-SPIONs and C-SPIONs (-54 mV and -42mV, respectively) increased to -24 mV and -22 mV for BSA-T-SPIONs and BSA-C-SPIONs respectively (Fig. 8b). Both zeta potential values were close to that of BSA under the same condition, indicating the coverage of both SPIONs' surface by BSA.

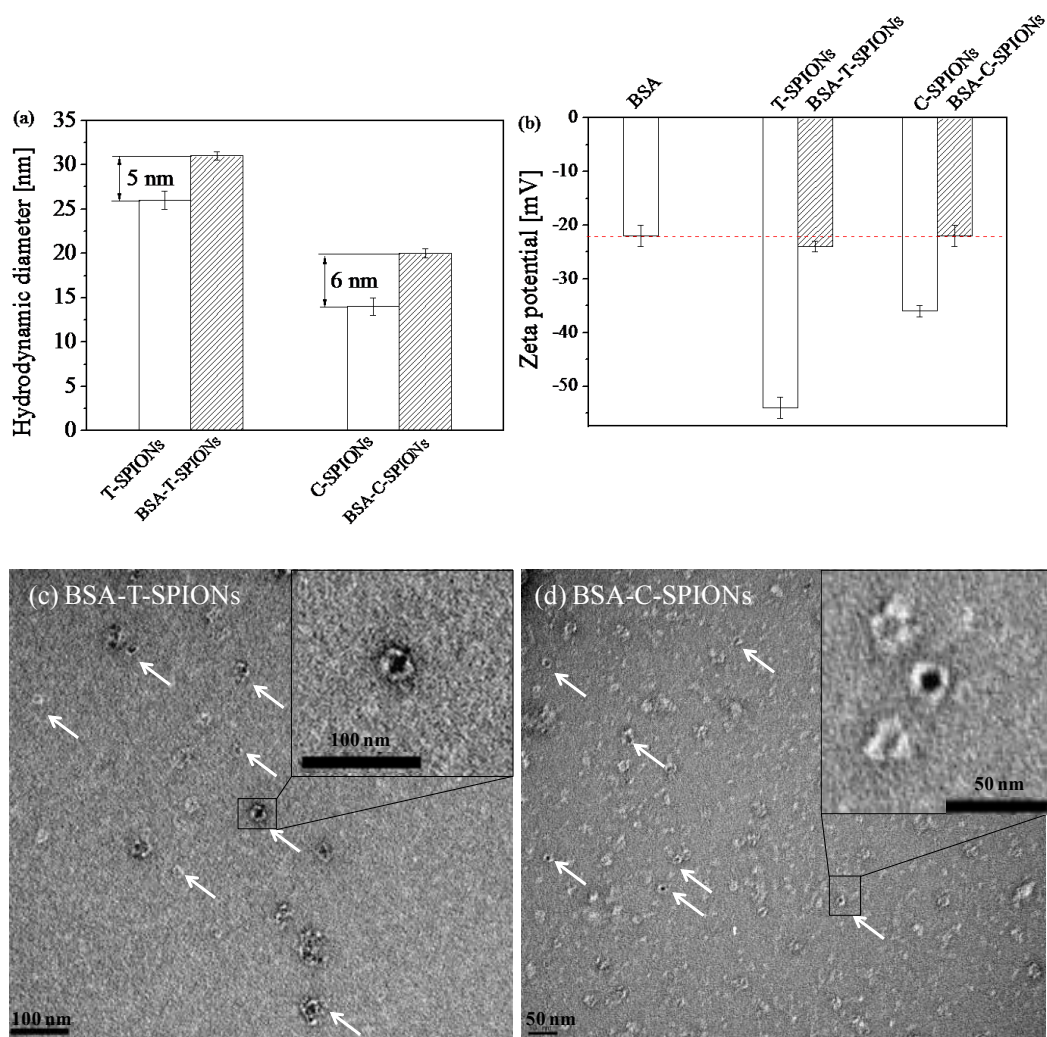


Figure 8. (a) Hydrodynamic size and (b) zeta potential of T-SPIONs, BSA-T-SPIONs, C-SPIONs and BSA-C-SPIONs. Negative staining TEM images of (c) BSA-T-SPIONs and (d) BSA-C-SPIONs.

Recent studies on the interaction of Au NPs and BSA pointed to two possible binding mechanisms: 1) strong binding of BSA to Au NPs due to the electrostatic attraction between positive residues of BSA and negative charged surface coating on Au NPs surface⁴⁰ and 2) the surface coating on Au NPs is removed by BSA upon absorption, amino acids on BSA, in particular cysteine, bind directly to the Au NPs surface²⁶. To the best of our knowledge, the interaction mechanism of BSA and SPIONs is still poorly investigated. FTIR confirmed the BSA binding on T-SPIONs and C-SPIONs surfaces and their interaction. BSA-T-SPIONs and BSA-C-SPIONs were separated from the excess BSA solution by centrifugation at 10000 rcf for 3h (under which condition excess BSA have been proved not to be centrifuged down¹⁸), dried completely and then FTIR spectra were collected. Spectra of BSA-T-SPIONs and BSA-C-SPIONs show clearly two adsorption bands at wavelength around 1635 cm^{-1} and 1515 cm^{-1} (Fig. 9), which are characteristic of amide I and amide II bonds of proteins, further confirming the formation of BSA layer on the surface of BSA-T-SPIONs and BSA-C-SPIONs. FTIR spectrum of BSA-T-SPIONs (Fig. 9) shows an adsorption band at 975 cm^{-1} , this band is assigned to the asymmetric methyl deformation mode C-N on TMAOH⁴¹, though with 30 nm shift from 944 cm^{-1} .

Another band also appears at 1394 cm^{-1} (Fig. 9), characteristic of the asymmetric methyl deformation mode of $-(\text{CH}_3)$ on TMAOH^{42} . These results indicate that TMAOH ligands still exist on BSA-T-SPIONs, implying that the binding of BSA to T-SPIONs surface is through interactions with the TMAOH layer, instead of replacing it. The FTIR spectrum of BSA-C-SPIONs present an absorption band at 1450 cm^{-1} (shifts from 1415 cm^{-1} Fig. 9), characteristic of asymmetric stretches of RCO_2 of $\text{Na}_3\text{Cit}^{43}$, suggesting the existence of citrate ligands on BSA-C-SPIONs. The disappearance of absorption bands at 1579 cm^{-1} of Na_3Cit and band shift from 1415 cm^{-1} to 1450 cm^{-1} imply strong interaction of citrate group with BSA.

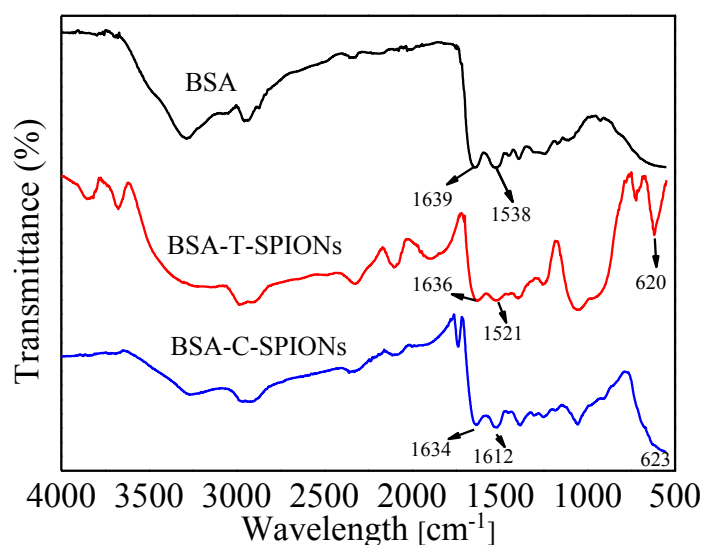


Figure 9. FTIR spectrum of BSA, BSA-T-SPIONs and BSA-C-SPIONs

4.4 STUDY ON THE INTERACTION MECHANISM OF BSA WITH C-SPIONs

We show above the adsorption of BSA on both C-SPIONs and T-SPIONs surface, using a pH-adjusted and BSA adsorption protocol. In this section, we focus on the understanding of the complex interaction mechanism of BSA with C-SPIONs. Specifically, the adsorption behavior, conformation change and thermodynamics of BSA upon interaction with C-SPIONs were elucidated.

4.4.1 ADSORPTION BEHAVIOR OF BSA ON C-SPIONs' SURFACE

4.4.1.1 DLS MEASUREMENTS

The D_h of C-SPIONs was monitored by DLS upon incubation with different concentrations of BSA ranging from $0.1\text{ }\mu\text{M}$ to $100\text{ }\mu\text{M}$ at room temperature for 1 h. As shown in Fig. 10a, only slight increase in D_h was detected at low BSA concentrations, less than 1 nm for $0.1\text{ }\mu\text{M}$ BSA and about 1.5nm at $1\text{ }\mu\text{M}$ BSA. Further increase in BSA concentration ($1\text{ }\mu\text{M}$ to $30\text{ }\mu\text{M}$) leads to the rapid increase in D_h of BSA-SPIONs, reaching a plateau of 23 nm for a BSA concentration of 30

μM . This D_h plateau indicates the saturated adsorption of BSA on C-SPIONs surfaces, which can be also evidenced by the appearance of a small peak at about of 8 nm at high BSA concentration (Fig. 10b). We assigned this small peak to the unattached free BSA in the solution. On the basis of the BSA dimensions ($8 \times 8 \times 3.5$ nm) and the increase in D_h of BSA-SPIONs when saturated amount of BSA adsorbed (7 nm in D_h , 3.5 nm in radius), we could assume that BSA adheres to C-SPIONs surface with the triangle base ("side on" adsorption). This result was also confirmed by the above negative staining TEM, where we could see clearly a protein shell with a thickness of about 3 nm surrounding the SPIONs core (inset of Fig. 8d).

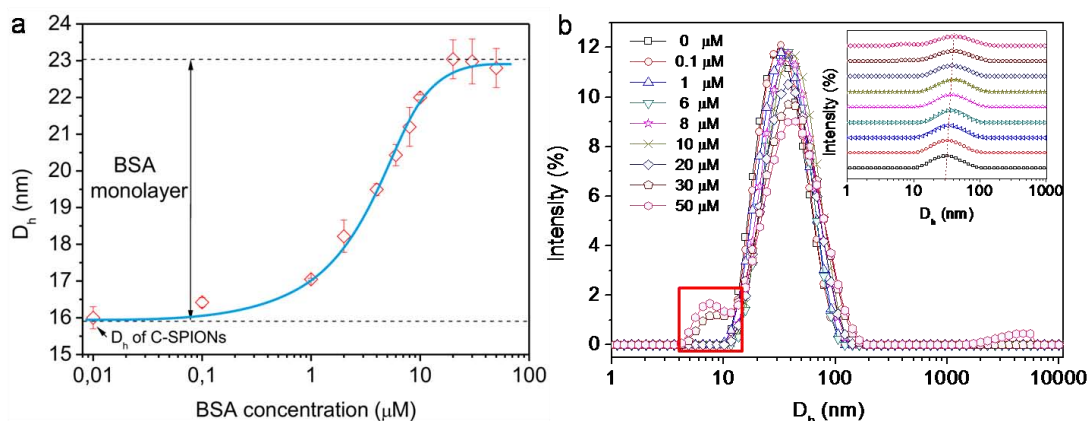


Figure 10. a) Hydrodynamic diameter (D_h) evolution of BSA-SPIONs prepared under different BSA concentration. b) Intensity-weighted D_h distribution curves of BSA-SPIONs prepared under different BSA concentration. The peaks circled by red rectangle indicate the presence of excess BSA in solution. Inset is the separated D_h distribution curves of BSA-SPIONs.

4.4.1.2 DETERMINATION OF SATURATED AMOUNT OF BSA ADSORBED ON C-SPIONs SURFACE

To further quantify the saturated amount of BSA adsorbed on C-SPIONs surface, UV-Vis experiments were performed. First, UV-Vis adsorption spectra of BSA solutions with a series of concentrations of 0.25, 0.5, 1.0, 1.5 and 2 mg/mL were measured. When we plotted the BSA concentration against its corresponding absorption value at 280 nm, a calibration curve with a linear relation was obtained (R^2 of 0.995) (Fig 11a).

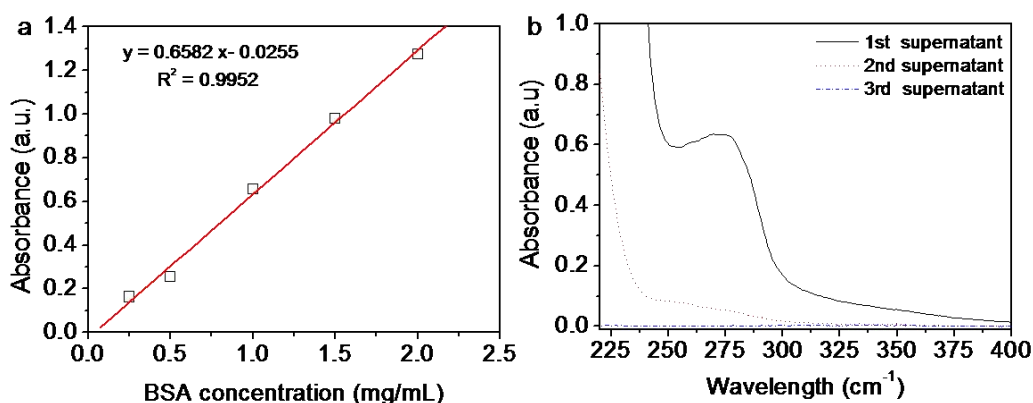


Figure 11. a) The calibration curve of BSA solution measured under different BSA concentration. b) The UV-Vis adsorption spectra of collected supernatant after each washing step.

BSA-SPIONs were prepared using the described protocol. After incubation of C-SPIONs with BSA (BSA concentration is 2.5 mg/mL, 37 μ M) for 1h, dispersions were transferred to a centrifugal filter unit (Amicon, 100 000 MW, Millipore), centrifuged at 6000 rpm for 25 min to remove unbound BSA. The removed supernatant was collected, UV-Vis spectra was recorded and the concentration of BSA in the supernatant was determined by using the above calibration curve. The concentrated BSA-SPIONs were then redispersed in MQ water and filtered again under the same conditions. The filtration and centrifugation steps were repeated several times until the supernatant shows no UV-Vis absorption at 280 nm. Finally, the saturated amount of BSA adsorbed on C-SPIONs was determined by subtracting the initial amount of BSA with the unbound BSA detected in the supernatant. In our case, after 3 times washing steps, UV-Vis spectra of the isolated solution did not show any absorption at 280 nm (Fig. 11b), indicating the complete isolation of free BSA from the BSA-SPIONs complexes. We calculated that the saturated BSA adsorption value on C-SPIONs' surface is about 1.8 mg BSA per mg SPIONs, corresponding to approximate 10 BSA molecules per one C-SPION. The calculated 10 BSA molecules on each C-SPIONs' surface were considered as the hard BSA corona, since those loosely bound BSA have been removed in during the repeat filtration and centrifugation steps. The value obtained here is comparable with the recent finding reported by Venerando *et al.*,⁴⁴ where about 6 ± 2 BSA molecules were observed on each iron oxide NPs' surface.

4.4.1.3 DIFFERENTIAL CENTRIFUGAL SEDIMENTATION MEASUREMENTS

Differential centrifugal sedimentation (DCS) measures high-resolution particle size distributions and can be used to assess the potential aggregation of a sample. As shown in Fig. 12a, DCS number-weighted size distribution of C-SPIONs displays only one narrow peak with an average size of 7.5 ± 0.5 nm, which is consistent with the previous TEM results (6 ± 1 nm). Note that DCS measures the Stokes' diameter of C-SPIONs, which in fact includes also all the entities that surrounding the NPs (such as citrate and solvent molecules) that move with it. A shift in peak position was observed for BSA-SPIONs, the average size of the BSA-SPIONs shows about 1 nm smaller than that of the C-SPIONs. It is noteworthy that for simplicity, all the size distributions in Fig. 12a are plotted assuming an average NPs density equal to that of SPIONs. This assumption is clearly untrue due to the presence of the protein shell around C-SPIONs, which contributes to decreasing their density, while increasing their size. The net effect is an increase in the sedimentation time of the NPs, which resulted in the size distributions of BSA-SPIONs appearing at lower sizes with respect to C-SPIONs. Notably, a larger mode shift was measured for the NPs in presence of excess BSA, indicating that these NPs have a thicker shell with respect to the NPs that underwent washing cycles. The difference in shell thickness may be due to the removal of the soft BSA corona from the surface of the NPs during the washing cycles³⁴.

If we model the BSA-SPIONs as spherical core/shell particles, where the core is represented by the C-SPION and the shell is made of BSA molecules^{34,45}, the thickness of the BSA shell can be calculated by modeling the NPs as spherical core/shell particles. Fig. 12b shows the measured

average thickness as a function of a range of possible densities. For example, when BSA density of 1.22 g/cm^3 was used⁴⁶, shell thickness of $\sim 3.3 \text{ nm}$ and $\sim 1.9 \text{ nm}$ were obtained for BSA-SPIONs before and after removal of excess BSA, respectively. The thickness of the BSA layer measured here is consistent with that determined by DLS.

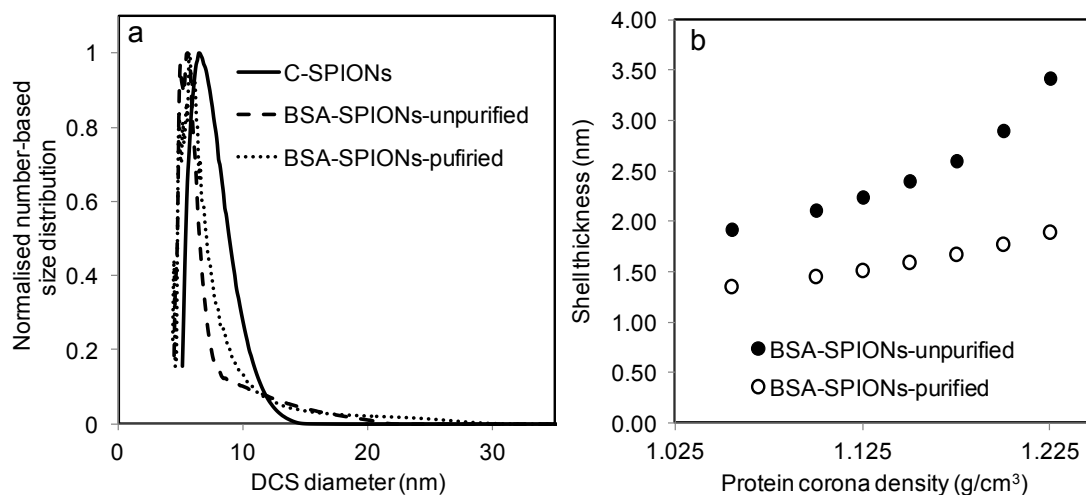


Figure 12. (a) Normalized light extinction number-weighted DCS size distribution of C-SPIONs (continuous line), BSA-SPIONs with excess protein in suspension (dashed line) and BSA-SPIONs after removal of excess proteins (dotted line). (b) BSA shell thickness as a function of the protein shell density for BSA-SPION before (black circles) and after (white circles) excess protein removal. The thickness was calculated by assuming a spherical core/shell particle model for the BSA coated NPs.

4.4.1.4 X-RAY PHOTOELECTRON SPECTROSCOPY

X-ray photoelectron spectroscopy (XPS) allows us to analyze the surface of C-SPIONs before and after BSA adsorption (Fig. 13). It is noteworthy that the BSA-SPIONs sample measured here has been purified with the removal of excess BSA. The presence of BSA on C-SPIONs is clearly indicated by the detection of nitrogen on the particles' surface, which is absent in C-SPIONs sample. Additionally, the complex structure of the C 1s high resolution spectrum exhibits peaks indicative of C-N bonds and resembles the typical spectrum expected for BSA⁴⁷. We also observed an increase in the characteristic signal for sulphur, further confirming the BSA adsorption on C-SPIONs surface.

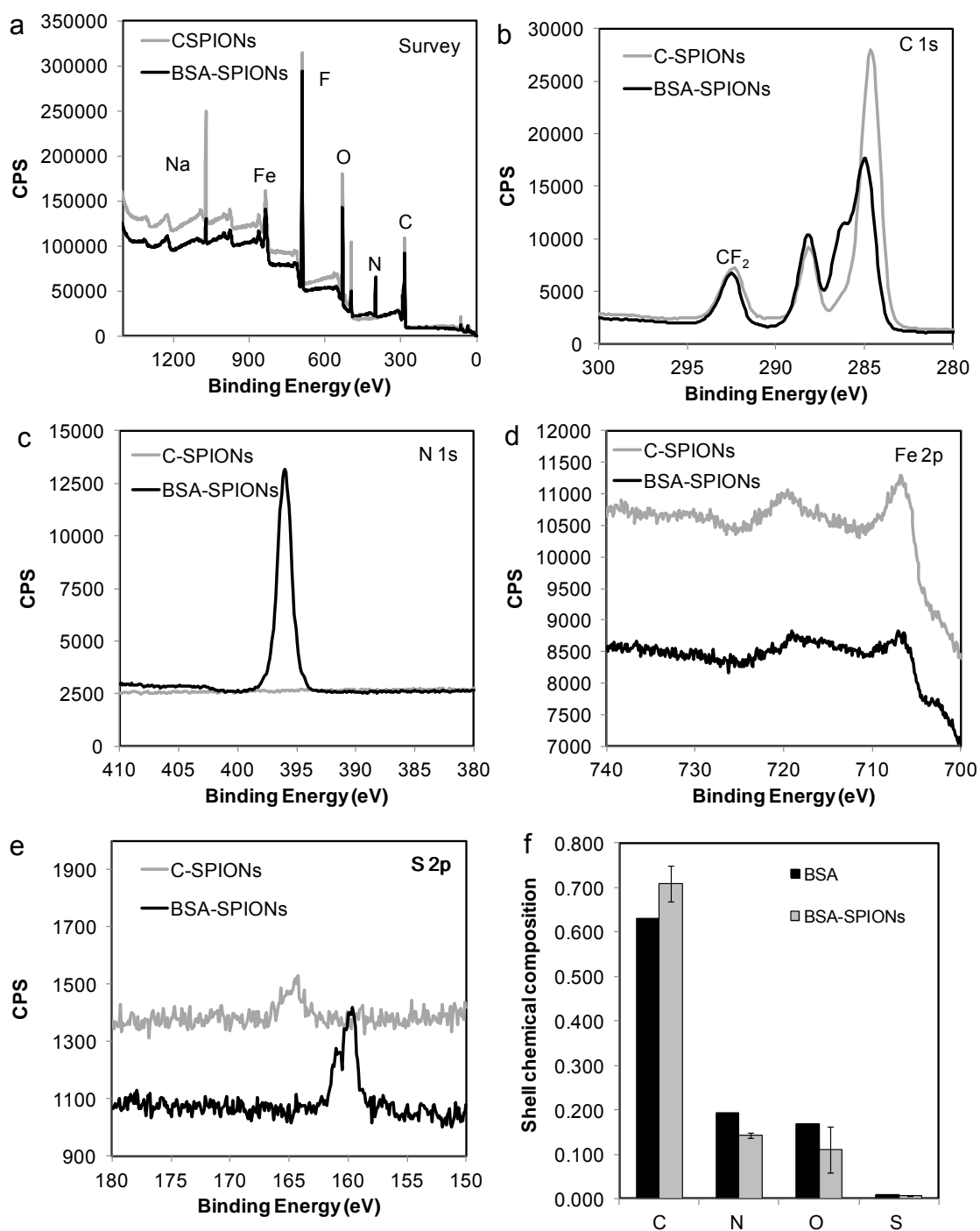


Figure 13. XPS study (a) and high resolution C 1s (b), N 1s (c), Fe 2p (d), S 2p (e) and spectra of C-SPIONs and BSA-SPIONs. (f) Elemental composition of the BSA monolayer surrounding the C-SPION (grey) and, for comparison, the expected composition for pure BSA (black).

The XPS measurements were also utilized to produce an approximated measurement of the chemical composition of the protein shell. The approximation is due to the fact that we are ignoring the geometry of the NPs and treating the sample as a flat surface^{48,47}. The measured chemical composition of the shell is shown in Fig. 13f, where the elemental composition expected for pure BSA is also shown for comparison. The measured higher level of carbon and lower level of nitrogen with respect to the expected values indicates that other adsorbate (in our

case is sodium citrate) except BSA also presented at the surface of the NPs. The detected sodium citrate on SPIONs further confirms the above finding by FT-IR, which indicated that BSA adsorb on SPIONs surface though interacting with the coated citrate ligand other than replacing them. Comparison of the ratio between the measured and expected amount of nitrogen in the NPs coating provides an estimation of the percentage of BSA layer in the shell, which resulted 74%.

4.4.1.5 CALCULATION OF THE SATURATED NUMBER OF BSA MOLECULE PER SPION

To calculate the theoretical saturated number of BSA molecule on each SPION's surface, a core-shell model was used (Fig. 14a). Assuming that each SPION's surface is fully covered by BSA forming a complete and continuous BSA layer, BSA adsorbs on SPION's surface with a "side-on" manner and the adsorbed BSA maintains its original equilateral triangular prism after its adsorption. The 3D triangular prism structure of BSA is schematically given in Fig. 14b and 14c, with a dimension of $8 \times 8 \times 3.5 \text{ nm}^{49}$. Then the saturated number of BSA molecule per SPION is calculated using the following equation:

$$N = \frac{\frac{4}{3} \pi (r_{SPION + BSA \text{ shell}}^3 - r_{SPION}^3)}{V_{BSA}}$$

Where V_{BSA} is the volume of each BSA molecule, about 83 nm^3 provided in the reference⁵⁰, $r_{SPION + BSA \text{ shell}}$ is the radius of the BSA-SPION core shell NPs (here $r_{SPION + BSA} = r_{SPION} + r_{BSA \text{ shell}}$), r_{SPION} is the measured radius of the SPIONs, $r_{BSA \text{ shell}}$ is 3.5 nm and N is the saturated number of BSA molecule per SPION. Specifically, r_{SPION} measured by DLS is 7.5 nm, 3.5 nm by DCS and 3.0 nm by TEM.

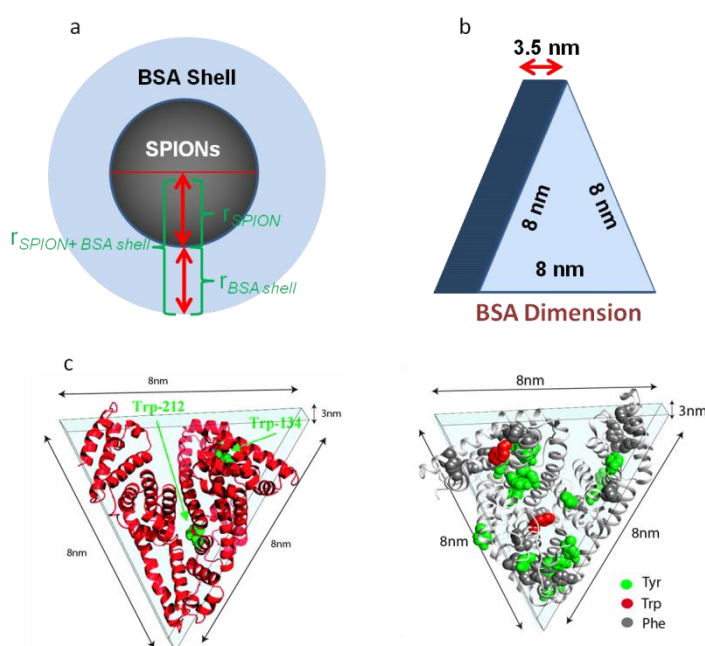


Figure 14. a) Core shell model of the BSA-SPION NPs for calculation, b) Schematically illustrated dimension of the BSA equilateral triangle prism, c) Schematic drawings indicate the positions of Trp and Tyr residues inside the BSA molecule.

The thickness of the BSA monolayer and the saturated number of BSA molecule per SPION were obtained by using different analytical methods as summarized in Table 4. All the methods indicate the formation of a BSA monolayer on C-SPIONs' surface with a thickness of 3 - 3.5 nm. The saturated number of BSA molecule per SPION calculated for each method are comparable (around 10 BSA per SPION), with an exception for DLS. As mentioned previously, the size of C-SPIONs measured by DLS is actually the Stokes size (hydrodynamic diameter), including the citrate layer and the water layer surrounding the SPIONs core. Therefore, the radius of SPION given by DLS is larger than the real size it should be, which resulted the calculation of higher saturated value of BSA molecule per SPION.

Table 4. Comparison of the thickness of the BSA monolayer and the saturation number of BSA molecule per SPION determined by different analytical methods.

Methods	Thickness of the BSA monolayer(nm)	Saturation number of BSA molecule per SPION
DLS	3.5	37 ^c
DCS	3.3	13 ^d
TEM ^a	3 ^b	10 ^e
UV-Vis	-	10

^a BSA-SPIONs was negatively stained by uranyl acetate before TEM measurement, for a better visual image of the BSA shell. ^b Thickness determined in a dry state. ^{c,d,e} Number determined according to the model described above.

Adsorption of proteins on NPs surface is a complex process, depending on the physicochemical properties of the surface coating⁵¹, the characteristics of the adsorbed proteins⁵², as well as the nature of the medium exposed⁵³. Differences in those factors could resulted the amounts or orientation of protein bound on nanoparticles' surfaces^{54,55}. From the biomedical point of view, orientation of proteins upon adsorption on NPs surface is of great importance, since some bioactive sites of proteins could be screened if the orientation of proteins is not desirable. Our collective data show that upon exposure to SPIONs, 10 BSA molecules was quantitatively detected on each SPION surface with a side on adsorption manner, forming a BSA monolayer with the thickness about 3 nm. This probably determined by their special electrostatic interaction. The positive patches (lysine and arginine amino acids) of BSA can facilitate its binding with negatively charged C-SPIONs^{19,26}. In order to bind completely and strongly on C-SPIONs surface, BSA has to adjust its orientation to achieve maximal attraction force with C-SPIONs. Therefore, BSA adsorbs on C-SPIONs surface on its triangle base (side on), by which more positive patches are exposed to the negatively charged C-SPIONs surface.

4.4.2 CONFORMATION CHANGE OF BSA UPON INTERACTION WITH C-SPIONs

4.4.2.1 UV-Vis MEASUREMENTS

Upon adsorption on NPs, proteins could undergo structure changes. Typically, UV-Vis spectra of BSA displays two characteristic adsorption peaks, one at about 220 nm and another one around at 280 nm. The strong adsorption peak at around 220 nm is assigned to the transition of $\pi-\pi^*$ of the polypeptide backbone structure C=O of BSA⁵⁶. While, the adsorption peak at about 280

nm is mainly due to the aromatic amino acid residues like tryptophan (Trp), tyrosine(Tyr) and phenylalanine⁵⁷. To better elucidate the interaction of BSA with C-SPIONs, a series of samples were prepared, where the amount of protein maintained constant (4 μM) while increasing the concentration of C-SPIONs. In all the concentrations chosen, SPIONs surface have a full coverage with BSA.

Generally, interaction of protein with NPs causes changes in UV-Vis spectra of proteins in terms of intensity or adsorption wavelength of the characteristic peak⁵⁸. Fig. 15a clearly shows that the adsorption intensity of both peaks at 220 nm and 280 nm of BSA increase gradually along with the increasing concentration of C-SPIONs. In addition, both peaks show a shift in their adsorption wavelength. Peak at 220 nm undergoes a red shift, while peak at 280 nm shows a blue shift. As revealed previously, increase in adsorption intensity or red shift in wavelength at 220 nm relates to the unfolding of BSA, leading to the exposure of more hydrophobic residues to the surrounding aqueous medium⁵⁹. The blue shift and the observed increase in intensity at 280 nm indicate aromatic residues buried inside BSA exposed to an microenvironment with high polarity⁵⁸. Taking together, UV-Vis results show interaction of C-SPIONs with BSA induced the slight unfolding of BSA.

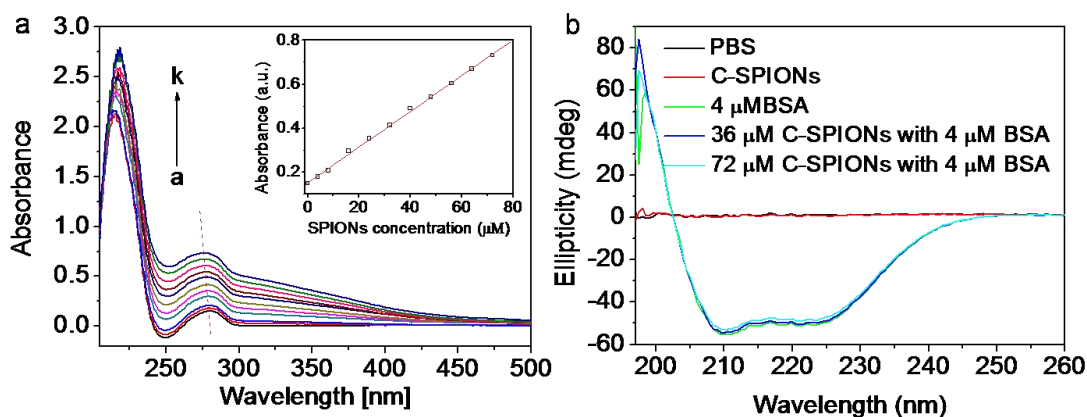


Figure 15. a) The UV-Vis spectra of 4×10^{-6} M BSA with the increasing concentration of C-SPIONs at pH 7.4. C-SPIONs concentration is from 0 μM to 72 μM (curves a to k correspond to 0, 1, 4, 8, 16, 24, 32, 40, 48, 56, 64 and 72 μM of C-SPIONs). Inset is the UV-Vis adsorption value of BSA at around 280 nm under different C-SPIONs concentration. b) The CD spectra of 4×10^{-6} M BSA under two concentrations of C-SPIONs at pH 7.4.

4.4.2.2 CIRCULAR DICHROISM

Circular dichroism spectroscopy (CD) was performed to further reveal the conformational changes of BSA upon interaction with C-SPIONs. Negative adsorption peaks at both 208 nm and 222 nm indicate the α -helix content of a protein⁶⁰. Decrease in their intensity means the decrease in α -helix content⁶¹. The results of CD measurements were presented in Fig. 15b. As can be seen, slight changes in both the intensity and wavelength of two characteristic peaks at both 208 nm and 222 nm were observed, in comparison with that of pure BSA. Considering that those slight changes might be caused by the adsorption of C-SPIONs, CD spectra of C-SPIONs was also recorded in the same buffer as a control. Result show that in the investigated UV

region, C-SPIONs does not display any adsorption, indicating that the slight perturbation observed in the CD spectra is originated from the interaction of BSA with C-SPIONs. To quantify the slight change in terms of α -helix content of BSA, a specific protein secondary structure algorithm was performed, only 3% decrease in α -helix content was determined in comparison with that of pure BSA. This slight decrease in α -helix change implies C-SPIONs induced slight unfolding of BSA.

4.4.2.3 STEADY-STATE FLUORESCENCE SPECTROSCOPY

To further investigate the structural changes of BSA upon interaction with C-SPIONs, fluorescence spectroscopy was also performed in our work. Due to its high sensitivity to the conformational changes of proteins, fluorescence spectroscopy is widely used to reveal the interaction mechanism between protein and NPs^{54,58}. Trp, Tyr and phenylalanine are three intrinsic fluorophores imparting fluorescence property to proteins. Among these three, Trp is reported to be the most sensitive to the surrounding environments⁶². BSA has two Trp residues in different regions, which are classified to Trp212 and Trp134. Trp212 is situated within the hydrophobic loop, while Trp134 is located in the hydrophilic region (as shown in Fig. 14c)^{54,63}. If structural changes of BSA occur in regions close to those Trp residues, perturbation in fluorescence parameters like intensity and peak position can be monitored.^{54,63}

Herein, to avoid the confusing fluorescence from either Tyr or phenylalanine residues, excitation wavelength of 295 nm instead of 280 nm was chosen to exclusively excite the Trp residues of BSA. Fig. 16a displays the fluorescence emission spectra of BSA in the absence or presence of C-SPIONs at pH 7.4. A gradual decrease in the intensity of the maximum emission band and a small red shift in the maximum emission wavelength were observed when increasing the concentration of SPIONs. The small red shift of the maximum emission wavelength detected here suggests the exposure of buried Trp residues to the surrounding environment, resulted in the decrease in the hydrophobicity and increase in the polarity of the Trp residues⁵⁸.

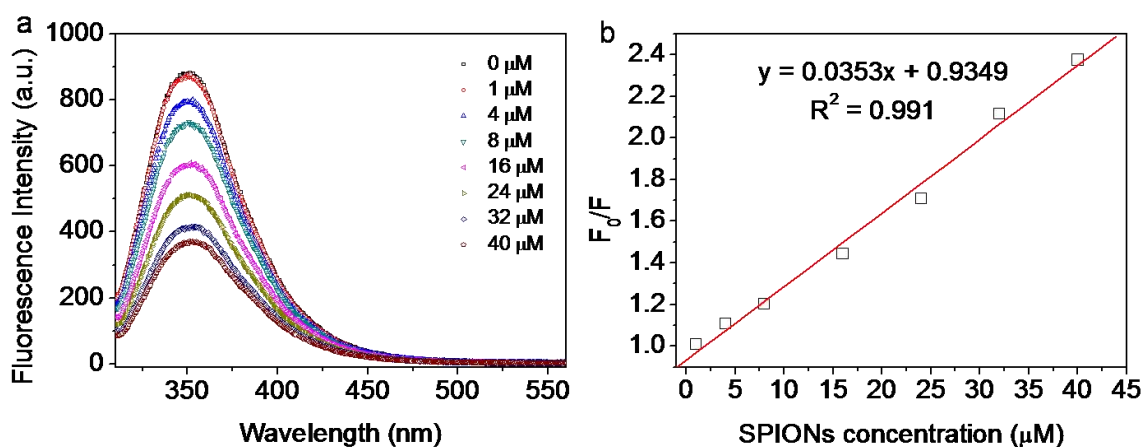


Figure 16. a) The fluorescence spectra of 4×10^{-6} M BSA with the increasing concentration of C-SPIONs at pH 7.4. b) Stern-Volmer plots for 4×10^{-6} M BSA in the presence of increasing concentrations of C-SPIONs pH 7.4.

The gradual decrease in fluorescence intensity of BSA indicates the quenching effect of C-SPIONs on Trp residues on BSA. The fluorescence quenching phenomenon can be described by the Stern–Volmer equation as described in the following equation⁶⁴:

$$\frac{F_0}{F} = 1 + K_q \tau_0 = 1 + K_{SV} [Q]$$

where F_0 and F are the maximum fluorescence intensities of BSA in the absence and presence of quencher, respectively. k_q is the quenching constant ($M^{-1} s^{-1}$) and τ_0 is the mean fluorescence lifetime of the fluorophore in the absence of quencher. The value of τ_0 for BSA is $10^{-8} s$ ⁶⁵. K_{SV} is the Stern–Volmer constant (M^{-1}), determining the quenching efficiency of quencher. Q is the concentration of a quencher. When we plotted F_0/F against $[Q]$, a linear curve was found (Fig. 16b), indicating the single type of quenching effect of C-SPIONs on BSA. From the curve, K_{sv} value of $2.7 \times 10^4 M^{-1}$ is determined. By Stern-Volmer equation, k_q is calculated to be $5.4 \times 10^{12} M^{-1} s^{-1}$. Quenching mechanism of C-SPIONs on BSA can be classified into two types: static and dynamic quenching effect which are determined from the quenching constant k_q . The static mechanism ($k_q > 2 \times 10^{10} M^{-1} s^{-1}$) indicates the formation of the protein-quencher complex due to the strong interaction of proteins with the quencher, whereas dynamic quenching ($k_q < 2 \times 10^{10} M^{-1} s^{-1}$) implies the weak interaction between proteins with quencher without stable complex formation⁶⁶. The quenching constant value of k_q ($5.4 \times 10^{12} M^{-1} s^{-1}$) obtained in our case is two orders of magnitude higher than $2 \times 10^{10} M^{-1} s^{-1}$, indicating the strong interaction between BSA and C-SPIONs with the formation of BSA-SPIONs complexes.

4.4.2.4 SYNCHRONOUS FLUORESCENCE SPECTROSCOPY

Synchronous fluorescence spectroscopy allows the excitation and the emission spectrum to be detected simultaneously, but keeping a constant value ($\Delta\lambda$) between the excitation and emission wavelength. Miller proposed that when $\Delta\lambda$ is set at 60 nm and 15 nm, the synchronous fluorescence spectra obtained thereby are especially used to trace Trp and Tyr residues, respectively⁵⁹. Fig. 17a shows that fluorescence intensity for $\Delta\lambda$ at 15 nm decreases gradually with increasing C-SPIONs concentration and the decrease rate followed an exponential function as shown in Fig. 17b. Synchronous fluorescence spectra for $\Delta\lambda = 60$ nm displays a similar trend, as can be seen in Fig 17c and 17d. It is noteworthy that synchronous fluorescence spectra of Trp residues is more sensitive to the BSA-SPIONs interaction, since the synchronous fluorescent intensity and the corresponding decrease in intensity were observed much higher than those of Tyr residues. Synchronous fluorescence measurements imply that binding of BSA onto SPIONs surface can also be through interacting with Tyr residues or residues at the vicinity of Tyr residues (as shown in Fig. 14c), leading to the slight unfolding of BSA.

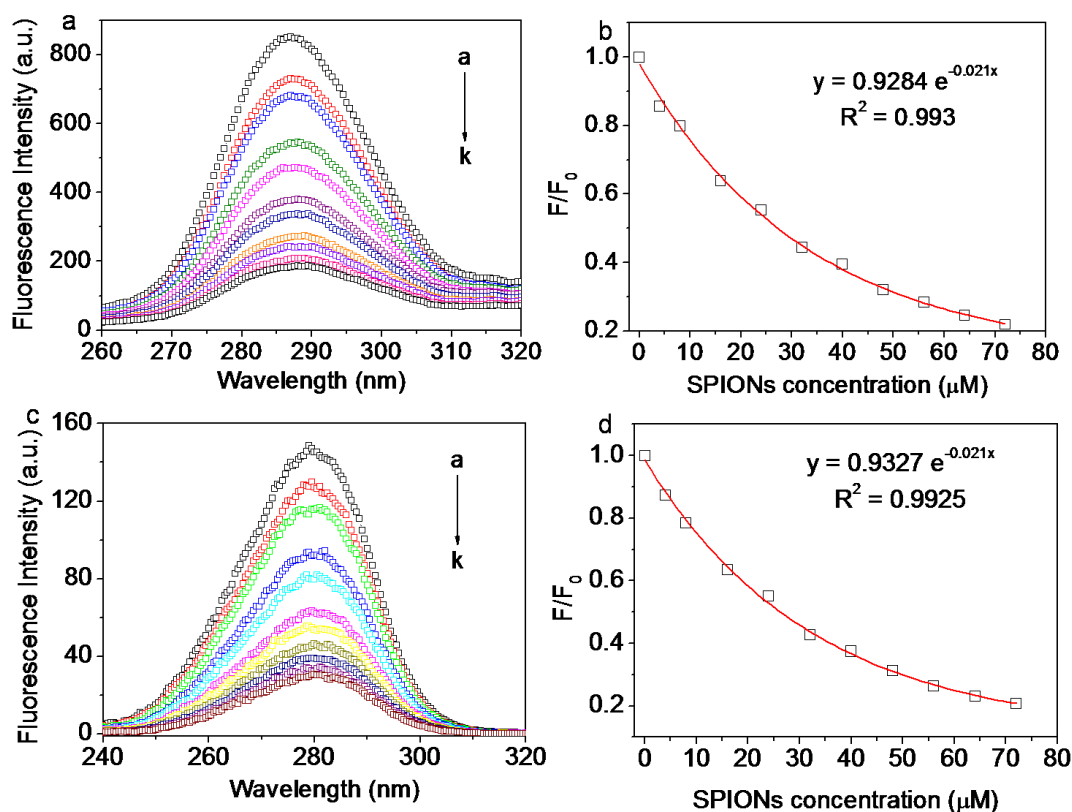


Figure 17. a) Synchronous fluorescence spectra of 4×10^{-6} M BSA with the increasing concentration of C-SPIONs at pH 7.4 for $\Delta\lambda = 15$ nm. C-SPIONs concentration is from 0 μM to 72 μM (curves a to k). b) Ratio of Synchronous fluorescent intensity (F/F_0) of 4×10^{-6} M BSA in the presence of increasing SPIONs concentrations for $\Delta\lambda = 15$ nm. c) Synchronous fluorescence spectra of 4×10^{-6} M BSA with the increasing concentration of C-SPIONs at pH 7.4 for $\Delta\lambda = 60$ nm. C-SPIONs concentration is from 0 μM to 72 μM (curves a to k). d) Ratio of Synchronous fluorescent intensity (F/F_0) of 4×10^{-6} M BSA in the presence of increasing SPIONs concentrations for $\Delta\lambda = 60$ nm.

In all, above spectroscopic analysis clearly indicates the slight unfolding of BSA upon interaction with C-SPIONs. Unfolding of BSA may occur in regions both close to the Trp residues and Tyr residues. In fact, during the protein adsorption process, in order to accommodate onto the surface of NPs in a most stable and compact way, proteins tend to adjust their orientation and conformation according to the size, shape, curvature, and surface compositions of the host NPs^{49,54,67,70}. Some previous work has reported the significant structure change of BSA upon interacting with SPIONs of different coating^{44,68}. However, structure change of BSA is not desirable as it can cause adverse effects on cellular responses^{69,70}. The significant structure change of protein may lead to the exposure of hidden epitopes or the formation of new structural epitopes. Such cryptic epitopes may in turn influence the following cellular signaling. Mortimer *et al.* showed that synthetic layered silicate NPs induced significant unfolding of adsorbed BSA, which resulted in exposure of a cryptic epitope that can be recognized by SR-AI and MARCO. This in turn promoted the clearance of the NPs from the circulation via the mononuclear phagocyte system⁷⁰. In our case, only slight unfolding of BSA structure was observed, suggesting a good biocompatibility of the prepared BSA-SPIONs.

4.5 THERMODYNAMICS OF PROTEIN ADSORPTION ON SPIONS

In general, heat production is associated with the protein adsorption process. By monitoring the heat release in the reaction system, information about the binding strength of protein with NPs can be revealed. In this section, the thermodynamics of protein adsorption on SPIONS' surface were analyzed by ITC. This technique allows us to do *in situ* investigation on the interaction of proteins with SPIONS in solution, providing direct information about the adsorption enthalpy changes and binding stoichiometry, the derived binding constant, entropy and free energy change. We have previously determined a strong interaction between BSA and SPIONS surface. Here, using ITC we can further quantify the strength of their interaction. Since FBS is an important component in cell media, the interaction of FBS with C-SPIONS and its competition with BSA on C-SPIONS' surface were also investigated here. On this purpose, we designed three experiments: i) titration of BSA to C-SPIONS dispersion to determine the affinity of BSA to C-SPIONS, ii) titration of FBS to C-SPIONS dispersion to determine the affinity of FBS to C-SPIONS and iii) titration of FBS to BSA-SPIONS dispersion to determine the competition between FBS and BSA adsorbing on C-SPIONS. All the obtained heat release profiles are fitted by using a model of one site binding and nonlinear least-squares fitting was performed to determine the thermodynamic parameters (Fig. 18 and Table 5).

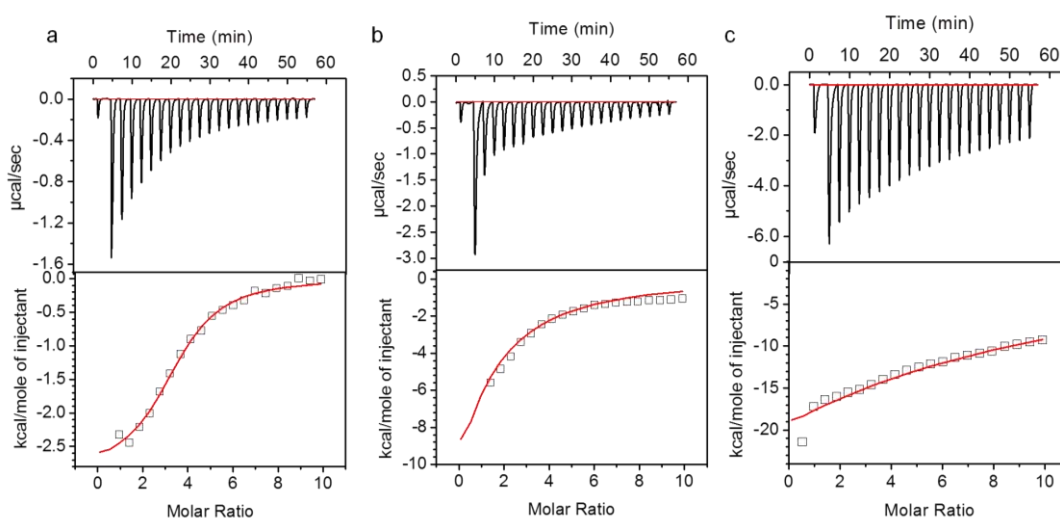


Figure 18. ITC data for the adsorption of BSA (a) and FBS (b) on C-SPIONS, and adsorption of FBS on BSA-SPIONS (c). Upper graphs represent the raw data obtained from the titrations and lower graphs represent the integrated heats of each peak with a corresponding fitting curve.

In all the three cases, an enthalpically favored interaction is observed since all the heat profiles are exothermic. Titration of BSA on C-SPIONS resulted in a high enthalpy change, which is an order of magnitude higher than that of FBS, as well as the binding constant. This indicates that BSA adsorbs to C-SPIONS' surface more strongly than FBS. Though BSA consists almost 55% of the whole FBS composition, lower enthalpy change and binding constant were found for FBS compared with BSA, probably due to the presence of other proteins in FBS with stronger affinity to C-SPIONS' surface than BSA. However, those proteins account only low percentage of the

whole proteins in FBS, their adsorption lead to the release of less heat. Moreover, the calculated stoichiometry (N) also indicates that the stronger interaction of BSA with C-SPIONs than FBS, as N observed for BSA is much higher (N is 3.4 and 0.48 for BSA and FBS, respectively).

The strong binding of BSA on C-SPIONs was further tested by titrating FBS to BSA-SPIONs dispersion. Though high enthalpy change (-1.445×10^6 KJ/mol) were produced, low binding constant is determined, indicating FBS proteins interact weakly with BSA-SPIONs. On the other hand, this implies that BSA interacts strongly with C-SPIONs, once adsorbed on C-SPIONs' surface, it can not be easily removed by FBS.

Table 5. Thermodynamic values of BSA-SPIONs interaction derived from ITC measurements.

Sample	Protein	$\Delta H(\text{KJ mol}^{-1})$	$K_a (10^5 \text{ M}^{-1})$	$\Delta S(\text{KJ mol}^{-1})$	N
C-SPIONs	BSA	-288	3.22	-15.5	3.44 ± 0.08
C-SPIONs	FBS	-36.4	0.36	-71.8	0.48 ± 1.46
BSA-SPIONs	FBS	-1445.4	0.035	-4.7	0.48 ± 3.66

4.6 CHAPTER CONCLUSION

The use of BSA to functionalize the SPIONs's surface showed great efficiency in enhancing the stability of both T-SPIONs and C-SPIONs in several biological media, while the addition of excess Na_3Cit was only suitable for stabilizing C-SPIONs. FTIR, Cryo-TEM and negative staining TEM reveal that BSA binds to T-SPIONs and C-SPIONs by interacting with TMAOH and citrate coating, forming a BSA monolayer with a thickness of about 3 nm on both systems. Likely, the BSA monolayer preserves the electrostatic repulsion force among the SPIONs while increasing the steric hindrance between SPIONs, preventing their aggregation in the biological media studied.

Study of BSA interaction with C-SPIONs further confirmed the formation of BSA monolayer on C-SPIONs surface with a preference "side on" adsorption manner. While the combination of several spectroscopic studies revealed a slight structure unfolding of BSA upon adsorption on C-SPIONs surface. Thermodynamics of BSA adsorption on SPIONs surface revealed that BSA has a much stronger affinity to SPIONs surface than FBS, FBS interact weakly with BSA-SPIONs.

4.7 ANNEX OF CHAPTER 4

In this part, detailed information about the steps for pH adjusted-BSA adsorption protocol for stabilizing SPIONs and Characterization of the obtained SPIONs were described.

4.7.1. MODIFIED pH ADJUSTED AND BSA ADSORPTION PROTOCOL

A modified pH adjusted and BSA adsorption protocol based on Guiot *et al.* was used¹. Briefly, synthesized C-SPIONs and T-SPIONs were diluted to 2 mg/mL SPIONs dispersions in MQ H₂O. BSA solutions with a concentration of 0.5 w/v %, 1 w/v %, 2 w/v %, 5 w/v %, 10 w/v % and 15 w/v % were also prepared in MQ H₂O. For C-SPIONs, the pH of C-SPIONs was first adjusted to 11 by adding 0.01 M NaOH, and then equal volumes of 2 mg/mL C-SPIONs dispersion and BSA solution were mixed rapidly and stirred on a vortex for 10 min. Finally, pH of the mixture was adjusted to 7.4 (physiological pH value) by adding 0.05 mM HNO₃ solution. As a result, 1 mg/mL BSA-C-SPIONs dispersion was obtained. The stability of the SPIONs dispersions after BSA addition was evaluated by dynamic light scattering (DLS) and Cryo transmission electron microscopy (Cryo-TEM).

For T-SPIONs, since the pH of T-SPIONs was already 11, we directly mixed equal volume of 2 mg/mL T-SPIONs dispersion and BSA solution and incubated for 10min, then pH of the mixture was adjusted to 7.4. As a result, 1 mg/mL BSA-T-SPIONs dispersion was obtained.

4.7.2. STABILITY OF THE OBTAINED BSA-T-SPIONs AND BSA-C-SPIONs DISPERSIONS IN BIOLOGICAL MEDIA.

50 µL of 1mg/mL BSA-T-SPIONs or BSA-C-SPIONs were added to 0.95 mL biological media, mixed and vortexed, then diluted BSA-C-SPIONs or BSA-T-SPIONs dispersions in biological media at a SPIONs concentration at 50µg/ml were obtained. Dynamic light scattering was used to monitor the stability of the prepared BSA-T-SPIONs and BSA-C-SPIONs dispersions in biological media during the period of 24h. It is noteworthy that the tested period of stability of BSA-T-SPIONs and BSA-C-SPIONs, as well as T-SPIONs and C-SPIONs in biological media was set at 24h, because *in vitro* toxicity assessment of NPs, in general, reports an incubation time of NPs with cells up to 24h.

4.7.3. CHARACTERIZATION

4.7.3.1. DLS MEASUREMENTS.

DLS measurements were performed to monitor the changes of SPIONs in the hydrodynamic diameter (D_h), polydispersity Index (PDI) and diffusion coefficient, which are all relative to the stability of SPIONs dispersions over time.

D_h of the C-SPIONs and T-SPIONs were determined by using a Zetasizer Nano ZS (Malvern) device with a He/Ne 633 nm laser at 25°C and at a SPIONs concentration of 50 µg/mL. For each sample, 3 independent measurements were performed with 15 scans for each measurement.

DLS measures the fluctuations of the intensity of the scattered lights caused by the random Brownian motion of NPs in solution. This fluctuation can be quantified through the autocorrelation function (ACF), $G(\tau)$ given by Eq. (1), where τ is the time difference between 2 measured signals. For monodisperse NPs, the correlation function can be expressed as Eq. (2), where A is the baseline of the correlation function, B is the intercept of the correlation function, Γ is the decay rate (the inverse of the correlation time). The relationship between Γ and translational diffusion coefficient D is shown by Eq. (3). q is determined by Eq. (4), where n is the refractive index of dispersant, λ_0 is the wavelength of the laser, θ is the scattering angle. From Eq. (3), translational diffusion coefficient D can be calculated. Once D is known, the hydrodynamic radius can be obtained through Stokes-Einstein equation, given by Eq. (5), where R_h is the hydrodynamic diameter, k is Boltzmann's constant, T is absolute temperature and η is viscosity of solvent.

The decay rate obtained by correlation function is related to a characteristic relaxation time, which provides information regarding to the dispersing state of NPs in solution. The characteristic relaxation time of well dispersed NPs is significantly faster than that of the aggregates. Since diffusion coefficient D is proportional to the reciprocal of the decay rate, it also could be used to describe changes in the dispersing state of NPs in solution along with time. Any detected decrease in diffusion coefficient D is related to the decreased stability of NPs dispersion, which can be also confirmed by the increasing Z-average sizes calculated through Stokes-Einstein equation

$$G(\tau) = \langle I(t) \cdot I(t+\tau) \rangle \quad (1)$$

$$G(\tau) = A[1 + B \exp(-2\Gamma\tau)] \quad (2)$$

$$\Gamma = \tau^{-1} = Dq^2 \quad (3)$$

$$q = (4\pi n / \lambda_0) \sin(\theta/2) \quad (4)$$

$$R_h = kT/6\pi\eta D \quad (5)$$

4.7.3.2. ZETA POTENTIAL MEASUREMENTS.

Zeta potential was carried out to determine the changes of SPIONs in electrophoretic mobility (EPM) and zeta potential (ζ) on a Zetasizer Nano ZS (Malvern) apparatus with a zeta potential analyzer software. SPIONs solutions were placed in a disposable plastic cuvette, followed by collecting experimental data automatically. For each measurement, 20 cycles were collected, and at least 3 independent measurements were performed for each sample.

4.7.3.3. ATTENUATED TOTAL REFLECTANCE FOURIER TRANSFORMED INFRARED SPECTRA MEASUREMENTS (ATR-FTIR).

ATR-FTIR was performed on a Spectrum RX1 FTIR Spectrometer (Perkin Elmer, USA), in the frequency range $4000-400 \text{ cm}^{-1}$ with a resolution of 4 cm^{-1} . All SPIONs samples were isolated from the solution by centrifugation, dried completely in the oven and placed on the crystal surface of the ATR-FTIR machine for measurements.

4.7.3.4. TRANSMISSION ELECTRON MICROSCOPE (TEM).

Size distribution, morphology and diffraction patterns of C-SPIONs and T-SPIONs were collected in JEOL JEM-1210 electron microscope at an operating voltage of 120 KV. TEM samples were prepared by placing one drop of the corresponding SPIONs dispersion on the copper grid for few seconds, blotting the copper grid with a filter paper and evaporate it completely at room temperature. Typically, about 200 to 300 different SPIONs were counted to depict the size distribution and the mean size of SPIONs.

4.7.3.5. CRYO-TRANSMISSION ELECTRON MICROSCOPE (Cryo-TEM).

Samples for Cryo-TEM were prepared according to the method described by Hondow². Briefly, 3 μL of 50 $\mu\text{g}/\text{mL}$ BSA-C-SPIONs (diluted 20 times in MQ H_2O) was placed on a glow discharge-treated carbon support film (R1.2/1.3 Quantifoil Micro Tools GmbH), blotted and plunge frozen in liquid nitrogen, then samples were subsequently transferred to a Gatan 626 cryo-holder stored in liquid nitrogen. Cryo-TEM measurement was performed on a JEOL 2011 electron microscope at a temperature of about $-170\text{ }^\circ\text{C}$ and 200 kv acceleration voltage.

4.7.3.6. NEGATIVE STAINING TRANSMISSION ELECTRON MICROSCOPE.

Adsorption of BSA on T-SPIONs and C-SPIONs were visualized by performing negative staining TEM³. Briefly, BSA-T-SPIONs or BSA-C-SPIONs were purified from the excess BSA solution by centrifugation at 10000 rcf for 3h and redispersed in MQ H_2O . Then one drop of the purified BSA-C-SPIONs was placed on a carbon-coated grid and then drained off with filter paper. Subsequently, 5 μL of 2% uranyl acetate was placed on the grid for 1 min before drained off. The grid was then placed in a 2011 JEOL electron microscope.

4.7.3.7. UV-Vis SPECTROSCOPY (UV-Vis)

UV-Vis extinction spectra of the samples were collected on a Cary-5000 UV-Vis spectrophotometer at room temperature. MQ water was used as the reference. To study the interaction of BSA with C-SPIONs, the BSA concentration was fixed at 4 μM , while the concentration of SPIONs ranged from 0 μM to 72 μM , 10 mM phosphate buffer (pH 7.4) was chose as the buffer. Each UV-Vis spectra was the average of three scans, 3 independent measurements were performed.

4.7.3.8. FLUORESCENT SPECTROSCOPY

Fluorescence measurements were performed on a fluorescence spectrophotometer (HITACHI F-7000, Japan) at 25 $^\circ\text{C}$, with the use of a 1.00 cm path length rectangular quartz cell. All the emission spectra were collected at the excitation wavelength of 295 nm using 10 nm/10 nm (excitation/emission) slit widths. Each spectrum presented was the average of at least three scans. the BSA concentration was fixed at 4 μM , while the concentration of SPIONs ranged from 0 μM to 72 μM , 10 mM phosphate buffer (pH 7.4) was chose as the buffer. Duplicate measurements were performed for each SPIONs concentration. Fluorescence backgrounds were corrected for blank buffer solutions in each measurement.

4.7.3.9. CIRCULAR DICHROISM (CD)

CD measurements were recorded on a Jasco J-810 spectropolarimeter (Easton, MD) with a 0.1 cm path length of cylindrical quartz cell at room temperature. The CD spectra were recorded from 190 to 260 nm, and each spectrum was an average of 3 scans. The concentration of BSA was fixed (4 μM), and the SPIONs concentration varied from 0 to 40 μM . 10 mM phosphate buffer (pH 7.4) was chosen as the buffer.

4.7.3.10. DIFFERENTIAL CENTRIFUGAL SEDIMENTATION (DCS)

DCS measurements were performed using a CPS 24000 disc centrifuge (CPS Instruments Inc., Stuart, Florida, USA). The instrument was operated at 24,000 rpm with a 14 mL sucrose gradient of 8-24% in water (average gradient density ρ_f between point of injection and detection the NPs of 1.055 g cm^{-3}). This was generated by injections of decreasing sucrose concentration, followed by a final addition of 0.5 mL dodecane as an evaporation barrier. A period of 30 min was allowed prior to measurement acquisition to facilitate thermal equilibrium. Measurements of 1 mg/mL concentrated samples were taken in duplicate, with calibration performed between each sample (100 μL injection volume). A refractive index of 2.4 and a density of 4.9 g/cm^3 were assumed for the SPION particles.

4.7.3.11. X-RAY PHOTOELECTRON SPECTROSCOPY (XPS)

X-ray Photoelectron Spectroscopy (XPS). Samples for XPS investigation were prepared by depositing drops of 11.6 mg/mL concentrated solution of NPs onto a 1 x 1 cm^2 polytetrafluoroethylene (PTFE)-wrapped silicon wafer. Aliquots of 5 μL were applied at a time and allowed to dry under vacuum in a desiccator before the addition of a further aliquot on top of each spot. This was repeated until uniform coverage of the surface was achieved.

XPS spectra were acquired using an Axis-Ultra XPS instrument (Kratos Analytical, Manchester, UK) with monochromatic Al $K\alpha$ X-rays (15 kV, 5 mA) in hybrid lens mode. Survey scans (single sweep) were acquired with a pass energy of 160 eV, step size 1000 meV, and a dwell time of 300 ms. Narrow scans were performed for the Fe 2p, C 1s, N 1s, O 1s, S 2p and F 1s regions with a pass energy of 40 eV, step size 100 meV and a dwell time of 500 ms. Two sweeps were acquired for each of the narrow scan regions except for iron, carbon and nitrogen, for which four sweeps were obtained. Charge neutralisation was employed to reduce charging of the samples, and balance settings were determined on an individual basis. XPS spectra were analysed using CasaXPS software (Version 2.3.16) and intensities were calibrated with the NPL's (National Physical Laboratory) own transmission function and average matrix relative sensitivity factors. Tougaard backgrounds were used for peak quantitation except for a minority of cases where linear background was used instead. The measurement of the thickness of the dry protein shell was performed by analysing XPS data as previously described^{47,48}.

4.7.3.12. ISOTHERMAL TITRATION CALORIMETRY (ITC)

Isothermal titration calorimetry measurement was performed on a VP-ITC calorimeter (Microcal Inc., Northampton, MA). BSA was dialyzed extensively against 10 mM sodium phosphate buffer, and C-SPIONs were dissolved in the last dialysate. A typical titration experiments involved 26 injections of the BSA solution (the titrant) (10 μ L aliquot per injection from a 0.5 mM stock solution) at 210 seconds intervals into the sample cell (volume 1.4359 mL) containing C-SPIONs (concentration, 8 μ M) During the experiment, the sample cell was stirred continuously at 1000 rpm. The heat of BSA dilution in the buffer alone was subtracted from the titration data for each experiment. The data were analyzed to determine the binding stoichiometry (N), affinity constant (K_a), and other thermodynamic parameters of the reaction using the coupled Origin software. The reported thermodynamic parameters were an average of duplicate experiments.

4.7.3.13. FLAME ADSORPTION SPECTROSCOPY

To determine the iron concentration of C-SPIONs, samples were sonicated for 10 min in an ultrasound bath. An aliquot of the sample was diluted with HCl (1%) and the iron content of the resulting solution was determined by flame absorption spectroscopy (air-acetylene) with a Perkin-Elmer 2100 spectrometer in a triplicate essay.

Table 1. Parameters extracted from DLS measurements, representing the stability of the prepared BSA-T-SPIONs dispersions at an evaluated time of 1h, 4h, 6h, and 24h.

Evaluated Time (h)	DLS				
	Dh (nm)	PDI	intensity distribution main peak (nm)	diffusion time (μ s)	Diffusion Coefficient ($\mu\text{m}^2/\text{s}$)
1	31 \pm 0.2	0.141	36 \pm 1	90.4	15.9
4	30 \pm 0.2	0.154	34 \pm 0.6	87.7	16.3
6	30 \pm 0.4	0.152	35 \pm 0.7	87.5	16.4
24	30 \pm 0.8	0.143	34 \pm 0.4	89.5	16.1

Table 2. Parameters extracted from DLS measurements, representing the stability of the prepared BSA-C-SPIONs dispersions at an evaluated time of 1h, 4h, 6h, and 24h.

Evaluated Time (h)	DLS				
	Dh (nm)	PDI	intensity distribution main peak (nm)	diffusion time (μ s)	Diffusion Coefficient ($\mu\text{m}^2/\text{s}$)
1	19 \pm 0.2	0.114	21 \pm 1	55.8	25.8
4	19 \pm 0.2	0.177	21 \pm 0.6	57.3	25.1
6	18 \pm 0.4	0.119	21 \pm 0.7	55.3	26
24	19 \pm 0.8	0.109	19 \pm 0.4	57.1	25.2

Table 3. Parameters extracted from DLS measurements, representing the stability of BSA-T-SPIONs dispersions in PBS at an evaluated time of 1h, 4h, 6h, and 24h.

Evaluated Time (h)	DLS				
	Dh (nm)	PDI	intensity distribution main peak (nm)	diffusion time (μ s)	Diffusion Coefficient ($\mu\text{m}^2/\text{s}$)
1	32 \pm 0.7	0.164	37 \pm 0.2	95.4	15.1
4	32 \pm 0.5	0.173	37 \pm 0.3	95	15.2
6	30 \pm 2	0.17	36 \pm 1	88.8	16.2
24	31 \pm 1	0.162	36 \pm 1	90.9	15.8

Table 4. Parameters extracted from DLS measurements, representing the stability of BSA-C-SPIONs dispersions in PBS at an evaluated time of 1h, 4h, 6h, and 24h.

Evaluated Time (h)	DLS				
	Dh (nm)	PDI	main peak by intensity (nm)	diffusion time (μ s)	Diffusion Coefficient ($\mu\text{m}^2/\text{s}$)
1	20 \pm 0.8	0.189	21 \pm 1	60	24
4	20 \pm 0.2	0.189	22 \pm 1	59.2	24.3
6	20 \pm 0.5	0.181	21 \pm 0.8	58.8	24.5
24	20 \pm 0.6	0.175	21 \pm 0.5	59.8	24.1

Table 5. Parameters extracted from DLS measurements, representing the stability of BSA-T-SPIONs dispersions in RPMI at an evaluated time of 1h, 4h, 6h, and 24h.

Evaluated Time (h)	DLS				
	Dh (nm)	PDI	main peak by intensity (nm)	diffusion time (μ s)	Diffusion Coefficient ($\mu\text{m}^2/\text{s}$)
1	24 \pm 1	0.273	34 \pm 1	72.8	19.8
4	40 \pm 0.3	0.271	47 \pm 0.3	118	18
6	59 \pm 0.5	0.267	69 \pm 0.5	173	13.4
24	100 \pm 0.1	0.275	136 \pm 0.1	292	4.92

Table 6. Parameters extracted from DLS measurements, representing the stability of BSA-T-SPIONs dispersions in DMEM at an evaluated time of 1h, 4h, 6h, and 24h.

Evaluated Time (h)	DLS				
	Dh (nm)	PDI	main peak by intensity (nm)	diffusion time (μ s)	Diffusion Coefficient ($\mu\text{m}^2/\text{s}$)
1	42 \pm 0.1	0.18	51 \pm 0.7	123	26
4	108 \pm 0.2	0.257	151 \pm 0.8	316	13.4
6	136 \pm 1	0.288	180 \pm 0.7	400	10.94
24	214 \pm 2	0.59	421 \pm 2	628	2.29

Table 7. Parameters extracted from DLS measurements, representing the stability of BSA-C-SPIONs dispersions in RPMI at an evaluated time of 1h, 4h, 6h, and 24h.

Evaluated Time (h)	DLS				
	Dh (nm)	PDI	main peak by intensity (nm)	diffusion time (μ s)	Diffusion Coefficient ($\mu\text{m}^2/\text{s}$)
1	19 \pm 1	0.214	19 \pm 1	56.2	25.6
4	18 \pm 0.3	0.199	20 \pm 0.3	54.3	26.5
6	18 \pm 0.5	0.23	18 \pm 0.5	53.9	26.7
24	18 \pm 0.1	0.183	21 \pm 0.1	56	25.7

Table 8. Parameters extracted from DLS measurements, representing the stability of BSA-C-SPIONs dispersions in DMEM at an evaluated time of 1h, 4h, 6h, and 24h.

Evaluated Time (h)	DLS				
	Dh (nm)	PDI	main peak by intensity (nm)	diffusion time (μ s)	Diffusion Coefficient ($\mu\text{m}^2/\text{s}$)
1	19 \pm 1	0.229	21 \pm 1	55.7	25.8
4	19 \pm 0.3	0.236	21 \pm 0.3	56.4	25.5
6	19 \pm 0.5	0.264	21 \pm 0.5	58	24.8
24	37 \pm 1	0.213	49 \pm 2	110	22.5

Table 9. Parameters extracted from DLS measurements, representing the stability of BSA-T-SPIONs dispersions in RPMI-FBS.

Evaluated Time (h)	DLS				
	Dh (nm)	PDI	main peak by intensity (nm)	diffusion time (μ s)	Diffusion Coefficient ($\mu\text{m}^2/\text{s}$)
1	31 \pm 0.2	0.363	40 \pm 0.5	99.8	15.5
4	32 \pm 0.1	0.36	42 \pm 0.6	110	15.1
6	32 \pm 0.2	0.349	40 \pm 1	145	14.6
24	42 \pm 0.6	0.285	57 \pm 0.7	163	11.4

Table 10. Parameters extracted from DLS measurements, representing the stability of BSA-T-SPIONs dispersions in DMEM-FBS at an evaluated time of 1h, 4h, 6h, and 24h.

Evaluated Time (h)	DLS				
	Dh (nm)	PDI	main peak by intensity (nm)	diffusion time (μ s)	Diffusion Coefficient ($\mu\text{m}^2/\text{s}$)
1	31 \pm 0.2	0.214	39 \pm 0.2	87.5	16.3
4	32 \pm 1	0.198	42 \pm 0.5	95	14.9
6	32 \pm 0.5	0.203	41 \pm 0.5	103	15.1
24	34 \pm 0.3	0.192	42 \pm 1	112	14.4

Table 11. Parameters extracted from DLS measurements, representing the stability of BSA-C-SPIONs dispersions in RPMI-FBS at an evaluated time of 1h, 4h, 6h, and 24h.

Evaluated Time (h)	DLS				
	Dh (nm)	PDI	main peak by intensity (nm)	diffusion time (μ s)	Diffusion Coefficient ($\mu\text{m}^2/\text{s}$)
1	30 \pm 1	0.302	45 \pm 1	16.1	89.3
4	31 \pm 0.3	0.286	46 \pm 0.3	15.4	93.5
6	32 \pm 0.5	0.292	49 \pm 0.5	15.1	95.2
24	35 \pm 1	0.303	53 \pm 2	13.7	105

Table 12. Parameters extracted from DLS measurements, representing the stability of BSA-C-SPIONs dispersions in DMEM-FBS at an evaluated time of 1h, 4h, 6h, and 24h.

Evaluated Time (h)	DLS				
	Dh (nm)	PDI	main peak by intensity (nm)	diffusion time (μ s)	Diffusion Coefficient ($\mu\text{m}^2/\text{s}$)
1	31 \pm 1	0.283	47 \pm 1	15.7	91.7
4	33 \pm 0.3	0.278	48 \pm 0.3	14.5	99
6	35 \pm 0.5	0.287	46 \pm 0.5	14	103
24	47 \pm 1	0.259	67 \pm 2	10.4	139

4.8. CHAPTER REFERENCES

- (1) Pratten, M. K.; Lloyd, J. B. *Pinocytosis and phagocytosis: the effect of size of a particulate substrate on its mode of capture by rat peritoneal macrophages cultured in vitro*. *Biochimica et Biophysica Acta (BBA) - General Subjects*, **1986**, 881, 307.
- (2) Sager, T. M.; Porter, D. W.; Robinson, V. A.; Lindsley, W. G.; Schwegler-Berry, D. E.; Castranova, V. *Improved method to disperse nanoparticles for in vitro and in vivo investigation of toxicity*. *Nanotoxicology*, **2007**, 1, 118.
- (3) Ji, Z.; Jin, X.; George, S.; Xia, T.; Meng, H.; Wang, X.; Suarez, E.; Zhang, H.; Hoek, E. M. V.; Godwin, H.; Nel, A. E.; Zink, J. I. *Dispersion and Stability Optimization of TiO₂ Nanoparticles in Cell Culture Media*. *Environmental Science & Technology*, **2010**, 44, 7309.
- (4) Metin, C.; Lake, L.; Miranda, C.; Nguyen, Q. *Stability of aqueous silica nanoparticle dispersions*. *J Nanopart Res*, **2011**, 13, 839.
- (5) Safi, M.; Sarrouj, H.; Sandre, O.; Mignet, N.; Berret, J. F. *Interactions between sub-10-nm iron and cerium oxide nanoparticles and 3T3 fibroblasts: the role of the coating and aggregation state*. *Nanotechnology*, **2010**, 21.
- (6) Safi, M.; Courtois, J.; Seigneuret, M.; Conjeaud, H.; Berret, J. F. *The effects of aggregation and protein corona on the cellular internalization of iron oxide nanoparticles*. *Biomaterials*, **2011**, 32, 9353.
- (7) Petri-Fink, A.; Steitz, B.; Finka, A.; Salaklang, J.; Hofmann, H. *Effect of cell media on polymer coated superparamagnetic iron oxide nanoparticles (SPIONs): Colloidal stability, cytotoxicity, and cellular uptake studies*. *European Journal of Pharmaceutics and Biopharmaceutics*, **2008**, 68, 129.
- (8) Butoescu, N.; Jordan, O.; Burdet, P.; Stadelmann, P.; Petri-Fink, A.; Hofmann, H.; Doelker, E. *Dexamethasone-containing biodegradable superparamagnetic microparticles for intra-articular administration: Physicochemical and magnetic properties, in vitro and in vivo drug release*. *European Journal of Pharmaceutics and Biopharmaceutics*, **2009**, 72, 529.
- (9) Kah, J. C. Y.; Chen, J.; Zubieta, A.; Hamad-Schifferli, K. *Exploiting the Protein Corona around Gold Nanorods for Loading and Triggered Release*. *ACS Nano*, **2012**, 6, 6730.
- (10) Carezza, E.; Barceló, V.; Morancho, A.; Montaner, J.; Rosell, A.; Roig, A. *Fast synthesis of water-dispersible SPIONs by microwave assisted route for safe labeling of endothelial progenitor cells*. *Acta biomaterialia*, **2014**.
- (11) Lee, P.; Knight, R.; Smit, J. M.; Wilschut, J.; Griffin, D. E. *A Single Mutation in the E2 Glycoprotein Important for Neurovirulence Influences Binding of Sindbis Virus to Neuroblastoma Cells*. *Journal of Virology*, **2002**, 76, 6302.
- (12) Euliss, L. E.; Grancharov, S. G.; O'Brien, S.; Deming, T. J.; Stucky, G. D.; Murray, C. B.; Held, G. A. *Cooperative Assembly of Magnetic Nanoparticles and Block Copolypeptides in Aqueous Media*. *Nano Letters*, **2003**, 3, 1489.
- (13) Nigam, S.; Barick, K. C.; Bahadur, D. *Development of citrate-stabilized Fe₃O₄ nanoparticles: Conjugation and release of doxorubicin for therapeutic applications*. *Journal of Magnetism and Magnetic Materials*, **2011**, 323, 237.
- (14) Eberbeck, D.; Kettering, M.; Bergemann, C.; Zirpel, P.; Hilger, I.; Trahms, L. *Quantification of the aggregation of magnetic nanoparticles with different polymeric coatings in cell culture medium*. *Journal of Physics D-Applied Physics*, **2010**, 43.
- (15) Wells, M. A.; Abid, A.; Kennedy, I. M.; Barakat, A. I. *Serum proteins prevent aggregation of Fe₂O₃ and ZnO nanoparticles*. *Nanotoxicology*, **2012**, 6, 837.
- (16) Allouni, Z. E.; Cimpan, M. R.; Høl, P. J.; Skodvin, T.; Gjerdet, N. R. *Agglomeration and sedimentation of TiO₂ nanoparticles in cell culture medium*. *Colloids and Surfaces B: Biointerfaces*, **2009**, 68, 83.

- (17) Geppert, M.; Petters, C.; Thiel, K.; Dringen, R. *The presence of serum alters the properties of iron oxide nanoparticles and lowers their accumulation by cultured brain astrocytes. J Nanopart Res*, **2012**, *15*, 1.
- (18) Casals, E.; Pfaller, T.; Duschl, A.; Oostingh, G. J.; Puntès, V. *Time Evolution of the Nanoparticle Protein Corona. ACS Nano*, **2010**, *4*, 3623.
- (19) Wiogo, H. T. R.; Lim, M.; Bulmus, V.; Gutiérrez, L.; Woodward, R. C.; Amal, R. *Insight into Serum Protein Interactions with Functionalized Magnetic Nanoparticles in Biological Media. Langmuir*, **2012**, *28*, 4346.
- (20) Corti, M.; Lascialfari, A.; Marinone, M.; Masotti, A.; Micotti, E.; Orsini, F.; Ortaggi, G.; Poletti, G.; Innocenti, C.; Sangregorio, C. *Magnetic and relaxometric properties of polyethylenimine-coated superparamagnetic MRI contrast agents. Journal of Magnetism and Magnetic Materials*, **2008**, *320*, e316.
- (21) Hoskins, C.; Wang, L.; Cheng, W.; Cuschieri, A. *Dilemmas in the reliable estimation of the in-vitro cell viability in magnetic nanoparticle engineering: which tests and what protocols? Nanoscale Research Letters*, **2012**, *7*, 77.
- (22) Kim, D. K.; Zhang, Y.; Kehr, J.; Klason, T.; Bjelke, B.; Muhammed, M. *Characterization and MRI study of surfactant-coated superparamagnetic nanoparticles administered into the rat brain. Journal of Magnetism and Magnetic Materials*, **2001**, *225*, 256.
- (23) Janes, K. A.; Calvo, P.; Alonso, M. J. *Polysaccharide colloidal particles as delivery systems for macromolecules. Advanced Drug Delivery Reviews*, **2001**, *47*, 83.
- (24) Liu, G.; Hong, R. Y.; Guo, L.; Li, Y. G.; Li, H. Z. *Preparation, characterization and MRI application of carboxymethyl dextran coated magnetic nanoparticles. Applied Surface Science*, **2011**, *257*, 6711.
- (25) Kircheis, R.; Wightman, L.; Wagner, E. *Design and gene delivery activity of modified polyethylenimines. Advanced Drug Delivery Reviews*, **2001**, *53*, 341.
- (26) Brewer, S. H.; Glomm, W. R.; Johnson, M. C.; Knag, M. K.; Franzen, S. *Probing BSA Binding to Citrate-Coated Gold Nanoparticles and Surfaces. Langmuir*, **2005**, *21*, 9303.
- (27) Dominguez-Medina, S.; Blankenburg, J.; Olson, J.; Landes, C. F.; Link, S. *Adsorption of a Protein Monolayer via Hydrophobic Interactions Prevents Nanoparticle Aggregation under Harsh Environmental Conditions. ACS Sustainable Chemistry & Engineering*, **2013**, *1*, 833.
- (28) Porter, D.; Sriram, K.; Wolfarth, M.; Jefferson, A.; Schwegler-Berry, D.; Andrew, M. E.; Castranova, V. *A biocompatible medium for nanoparticle dispersion. Nanotoxicology*, **2008**, *2*, 144.
- (29) Guiot, C.; Spalla, O. *Stabilization of TiO₂ Nanoparticles in Complex Medium through a pH Adjustment Protocol. Environmental Science & Technology*, **2012**, *47*, 1057.
- (30) Luciani, N.; Gazeau, F.; Wilhelm, C. *Reactivity of the monocyte/macrophage system to superparamagnetic anionic nanoparticles. Journal of Materials Chemistry*, **2009**, *19*, 6373.
- (31) Khullar, P.; Singh, V.; Mahal, A.; Dave, P. N.; Thakur, S.; Kaur, G.; Singh, J.; Singh Kamboj, S.; Singh Bakshi, M. *Bovine Serum Albumin Bioconjugated Gold Nanoparticles: Synthesis, Hemolysis, and Cytotoxicity toward Cancer Cell Lines. The Journal of Physical Chemistry C*, **2012**, *116*, 8834.
- (32) Nakata, S.; Kido, N.; Hayashi, M.; Hara, M.; Sasabe, H.; Sugawara, T.; Matsuda, T. *Chemisorption of proteins and their thiol derivatives onto gold surfaces: characterization based on electrochemical nonlinearity. Biophysical Chemistry*, **1996**, *62*, 63.
- (33) Moulin, A. M.; O'Shea, S. J.; Badley, R. A.; Doyle, P.; Welland, M. E. *Measuring Surface-Induced Conformational Changes in Proteins. Langmuir*, **1999**, *15*, 8776.
- (34) Walczyk, D.; Bombelli, F. B.; Monopoli, M. P.; Lynch, I.; Dawson, K. A. *What the Cell "Sees" in Bionanoscience. Journal of the American Chemical Society*, **2010**, *132*, 5761.

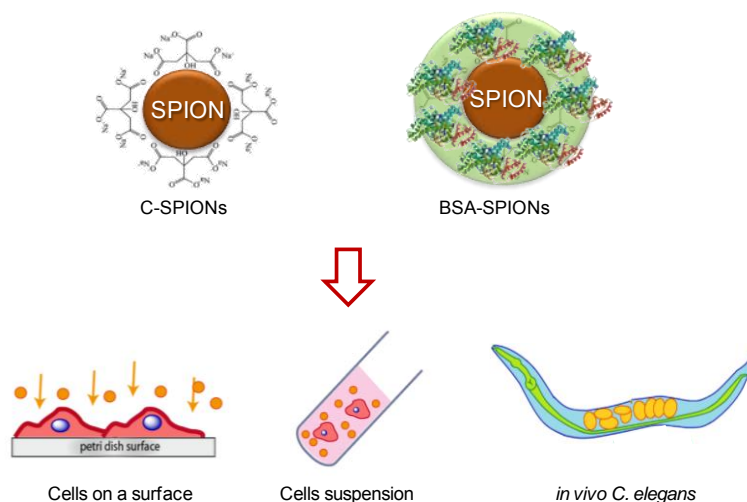
- (35) Freese, C.; Uboldi, C.; Gibson, M.; Unger, R.; Weksler, B.; Romero, I.; Couraud, P.-O.; Kirkpatrick, C. *Uptake and cytotoxicity of citrate-coated gold nanospheres: Comparative studies on human endothelial and epithelial cells. Particle and Fibre Toxicology*, **2012**, *9*, 23.
- (36) Uboldi, C.; Bonacchi, D.; Lorenzi, G.; Hermanns, M. I.; Pohl, C.; Baldi, G.; Unger, R.; Kirkpatrick, C. J. *Gold nanoparticles induce cytotoxicity in the alveolar type-II cell lines A549 and NCIH441. Particle and Fibre Toxicology*, **2009**, *6*, 18.
- (37) He, X. M.; Carter, D. C. *Atomic structure and chemistry of human serum albumin. Nature*, **1992**, *358*, 209.
- (38) Kohli, I.; Alam, S.; Patel, B.; Mukhopadhyay, A. *Interaction and diffusion of gold nanoparticles in bovine serum albumin solutions. Applied Physics Letters*, **2013**, *102*, 203705.
- (39) Natte, K.; Friedrich, J. F.; Wohlrab, S.; Lutzki, J.; von Klitzing, R.; Österle, W.; Orts-Gil, G. *Impact of polymer shell on the formation and time evolution of nanoparticle–protein corona. Colloids and Surfaces B: Biointerfaces*, **2013**, *104*, 213.
- (40) Sen, T.; Mandal, S.; Haldar, S.; Chattopadhyay, K.; Patra, A. *Interaction of Gold Nanoparticle with Human Serum Albumin (HSA) Protein Using Surface Energy Transfer. The Journal of Physical Chemistry C*, **2011**, *115*, 24037.
- (41) Ouasri, A.; Rhandour, A.; Dhamelincourt, M. C.; Dhamelincourt, P.; Mazzah, A. *Vibrational study of (CH₃)₄NSbCl₆ and [(CH₃)₄N]₂SiF₆. Spectrochimica Acta Part A: Molecular and Biomolecular Spectroscopy*, **2002**, *58*, 2779.
- (42) Andrade, Â. L.; Valente, M. A.; Ferreira, J. M. F.; Fabris, J. D. *Preparation of size-controlled nanoparticles of magnetite. Journal of Magnetism and Magnetic Materials*, **2012**, *324*, 1753.
- (43) Sasidharan, S.; Jayasree, A.; Fazal, S.; Koyakutty, M.; Nair, S. V.; Menon, D. *Ambient temperature synthesis of citrate stabilized and biofunctionalized, fluorescent calcium fluoride nanocrystals for targeted labeling of cancer cells. Biomaterials Science*, **2013**, *1*, 294.
- (44) Venerando, R.; Miotto, G.; Magro, M.; Dallan, M.; Baratella, D.; Bonaiuto, E.; Zboril, R.; Vianello, F. *Magnetic Nanoparticles with Covalently Bound Self-Assembled Protein Corona for Advanced Biomedical Applications. The Journal of Physical Chemistry C*, **2013**, *117*, 20320.
- (45) Bell, N. C.; Minelli, C.; Shard, A. G. *Quantitation of IgG protein adsorption to gold nanoparticles using particle size measurement. Analytical Methods*, **2013**, *5*, 4591.
- (46) Quillin, M. L.; Matthews, B. W. *Accurate calculation of the density of proteins. Acta Crystallographica Section D*, **2000**, *56*, 791.
- (47) Belsey, N. A.; Shard, A. G.; Minelli, C. *Analysis of protein coatings on gold nanoparticles by XPS and liquid-based particle sizing techniques. Biointerphases*, **2015**, *10*, 019012.
- (48) Shard, A. G. *A Straightforward Method For Interpreting XPS Data From Core–Shell Nanoparticles. The Journal of Physical Chemistry C*, **2012**, *116*, 16806.
- (49) Au, K. M.; Armes, S. P. *Heterocoagulation as a Facile Route To Prepare Stable Serum Albumin-Nanoparticle Conjugates for Biomedical Applications: Synthetic Protocols and Mechanistic Insights. ACS Nano*, **2012**, *6*, 8261.
- (50) Rocker, C.; Potzl, M.; Zhang, F.; Parak, W. J.; Nienhaus, G. U. *A quantitative fluorescence study of protein monolayer formation on colloidal nanoparticles. Nat Nano*, **2009**, *4*, 577.
- (51) Jedlovszky-Hajdú, A.; Bombelli, F. B.; Monopoli, M. P.; Tombácz, E.; Dawson, K. A. *Surface Coatings Shape the Protein Corona of SPIONs with Relevance to Their Application in Vivo. Langmuir*, **2012**, *28*, 14983.
- (52) Huang, R.; Carney, R. P.; Stellacci, F.; Lau, B. L. T. *Protein-nanoparticle interactions: the effects of surface compositional and structural heterogeneity are scale dependent. Nanoscale*, **2013**, *5*, 6928.

- (53) Maiorano, G.; Sabella, S.; Sorce, B.; Brunetti, V.; Malvindi, M. A.; Cingolani, R.; Pompa, P. P. *Effects of Cell Culture Media on the Dynamic Formation of Protein–Nanoparticle Complexes and Influence on the Cellular Response*. *ACS Nano*, **2010**, *4*, 7481.
- (54) Huang, R.; Carney, R. P.; Ikuma, K.; Stellacci, F.; Lau, B. L. T. *Effects of Surface Compositional and Structural Heterogeneity on Nanoparticle–Protein Interactions: Different Protein Configurations*. *ACS Nano*, **2014**, *8*, 5402.
- (55) Treuel, L.; Brandholt, S.; Maffre, P.; Wiegele, S.; Shang, L.; Nienhaus, G. U. *Impact of Protein Modification on the Protein Corona on Nanoparticles and Nanoparticle–Cell Interactions*. *ACS Nano*, **2014**, *8*, 503.
- (56) Zhong, J.; Song, L.; Meng, J.; Gao, B.; Chu, W.; Xu, H.; Luo, Y.; Guo, J.; Marcelli, A.; Xie, S.; Wu, Z. *Bio–nano interaction of proteins adsorbed on single-walled carbon nanotubes*. *Carbon*, **2009**, *47*, 967.
- (57) Sen, T.; Haldar, K. K.; Patra, A. *Au Nanoparticle-Based Surface Energy Transfer Probe for Conformational Changes of BSA Protein*. *The Journal of Physical Chemistry C*, **2008**, *112*, 17945.
- (58) Hai-Dong, W.; Catherine Hui, N.; Qiaoqin, Y.; Ildiko, B. *Study on protein conformation and adsorption behaviors in nanodiamond particle–protein complexes*. *Nanotechnology*, **2011**, *22*, 145703.
- (59) Paul, B. K.; Bhattacharjee, K.; Bose, S.; Guchhait, N. *A spectroscopic investigation on the interaction of a magnetic ferrofluid with a model plasma protein: effect on the conformation and activity of the protein*. *Physical Chemistry Chemical Physics*, **2012**, *14*, 15482.
- (60) Zhao, X.; Liu, R.; Chi, Z.; Teng, Y.; Qin, P. *New Insights into the Behavior of Bovine Serum Albumin Adsorbed onto Carbon Nanotubes: Comprehensive Spectroscopic Studies*. *The Journal of Physical Chemistry B*, **2010**, *114*, 5625.
- (61) Kanakis, C. D.; Tarantilis, P. A.; Polissiou, M. G.; Diamantoglou, S.; Tajmir-Riahi, H. A. *Antioxidant flavonoids bind human serum albumin*. *Journal of Molecular Structure*, **2006**, *798*, 69.
- (62) Albani, J. R. In *Structure and Dynamics of Macromolecules: Absorption and Fluorescence Studies*; Albani, J. R., Ed.; Elsevier Science: Amsterdam, 2004, p 141.
- (63) Chakraborti, S.; Joshi, P.; Chakravarty, D.; Shanker, V.; Ansari, Z. A.; Singh, S. P.; Chakrabarti, P. *Interaction of Polyethyleneimine-Functionalized ZnO Nanoparticles with Bovine Serum Albumin*. *Langmuir*, **2012**, *28*, 11142.
- (64) Shang, L.; Wang, Y.; Jiang, J.; Dong, S. *pH-Dependent Protein Conformational Changes in Albumin:Gold Nanoparticle Bioconjugates: A Spectroscopic Study*. *Langmuir*, **2007**, *23*, 2714.
- (65) Xiao, Q.; Huang, S.; Qi, Z.-D.; Zhou, B.; He, Z.-K.; Liu, Y. *Conformation, thermodynamics and stoichiometry of HSA adsorbed to colloidal CdSe/ZnS quantum dots*. *Biochimica et Biophysica Acta (BBA) - Proteins and Proteomics*, **2008**, *1784*, 1020.
- (66) Paul, B. K.; Guchhait, N. *A spectral deciphering of the binding interaction of an intramolecular charge transfer fluorescence probe with a cationic protein: thermodynamic analysis of the binding phenomenon combined with blind docking study*. *Photochemical & Photobiological Sciences*, **2011**, *10*, 980.
- (67) Deng, Z. J.; Liang, M.; Toth, I.; Monteiro, M. J.; Minchin, R. F. *Molecular Interaction of Poly(acrylic acid) Gold Nanoparticles with Human Fibrinogen*. *ACS Nano*, **2012**, *6*, 8962.
- (68) Liu, Y.; Ji, F.; Liu, R. *The interaction of bovine serum albumin with doxorubicin-loaded superparamagnetic iron oxide nanoparticles: spectroscopy and molecular modelling identification*. *Nanotoxicology*, **2013**, *7*, 97.
- (69) Ge, C.; Du, J.; Zhao, L.; Wang, L.; Liu, Y.; Li, D.; Yang, Y.; Zhou, R.; Zhao, Y.; Chai, Z.; Chen, C. *Binding of blood proteins to carbon nanotubes reduces cytotoxicity*. *Proceedings of the National Academy of Sciences*, **2011**, *108*, 16968.

(70) Mortimer, G. M.; Butcher, N. J.; Musumeci, A. W.; Deng, Z. J.; Martin, D. J.; Minchin, R. F. *Cryptic epitopes of albumin determine mononuclear phagocyte system clearance of nanomaterials*. *ACS nano*, **2014**, *8*, 3357.

CHAPTER 5

INTERACTION OF SUPERPARAMAGNETIC IRON OXIDE NANOPARTICLES WITH BIOLOGICAL ENTITIES



CHAPTER SUMMARY

In this chapter, we first investigated the degradation behavior of C-SPIONs and BSA-SPIONs in a solution mimicking cellular lysosomal environment (pH 4.6 in citrate buffer), in the presence or absence of 10% FBS. We observed that BSA-SPIONs displayed lower degradation rate than C-SPIONs and the presence of FBS further slowed down the degradation of SPIONs.

We then evaluated the effect of BSA coating on cellular responses, where adherent MDA MB 231 cell and suspension HL 60 cell were used as *in vitro* model cell lines. We show that both cell viability and cellular uptake were affected by the presence of the BSA coating, the effects depended on the type of cells evaluated. Furthermore, we extended our investigation on the effect of BSA coating in a 3D *in vivo* platform, the model organism *Caenorhabditis elegans* (*C. elegans*). We showed that the BSA coating has a protective role for the nematodes.

The work presented in this chapter was performed with other group members: Dr. Maria Milla and Laura Gonzalez-Moragas PhD student.

Chapter Index

	pag.
CHAPTER SUMMARY	133
5.1 EFFECT OF PROTEIN CORONA ON NANOPARTICLE-CELL INTERACTION	135
5.2 DEGRADATION OF C-SPIONs AND BSA-SPIONs IN BIOLOGICAL MEDIA	135
5.2.1 DEGRADATION KINETICS	136
5.2.2 SIZE EVOLUTION DURING THE DEGRADATION PROCESS	138
5.3 EFFECT OF PROTEIN CORONA ON NANOPARTICLE-CELL INTERACTION	139
5.3.1 CELL CULTURES	139
5.3.2 CELL VIABILITY: MTT ASSAYS	139
5.3.3 CELLULAR UPTAKE OF SPIONs: DETERMINATION OF IRON CONTENT IN CELLS	141
5.3.4 SPIONs LOCALIZATION WITHIN CELLS AFTER INTERNALIZATION	141
5.4 EVALUATION OF SPIONs ON 3D IN VIVO C-ELEGANS	143
5.5 CHAPTER CONCLUSION	146
5.6 ANNEX OF CHAPTER 5	147
5.7 CHAPTER REFERENCES	149

5.1 EFFECT OF PROTEIN CORONA ON NANOPARTICLE-CELL INTERACTION

It is well known that introducing nanoparticles (NPs) into biological environments results in the adsorption of different biomolecules on their surface, including proteins. The adsorbed proteins can modify their initial surface chemistry, provide them a distinct bio-identity in biological environments, hence mediate their interaction with biological entities¹. Cellular uptake of NPs and their fate in cellular compartments can be profoundly modified by the surface coating. Cellular uptake of NPs can be suppressed by the presence of protein corona.^{2,3} For instance, Lesniak *et al.* showed that after serum proteins adsorption, silica NPs displayed weaker interaction with the membrane of A549 cells, resulting in a lower uptake. Cellular uptake of silica NPs was also found significantly lowered compared to those without proteins⁴. Similar cellular responses have been also reported by Huhn *et al.*, where they found that the presence of proteins lowered the uptake of Au NPs by 3T3 fibroblasts³. Moreover, cellular uptake mechanism of NPs can be also modified in the presence of protein corona. Lunov *et al.* showed that macrophage uptake mechanism of polystyrene NPs changed from endocytosis to phagocytosis when they were coated with serum proteins⁵. Therefore, understanding the effect of protein adsorption on cellular responses to NPs is crucial for the improvement of NPs' applications in nanomedicine. In this chapter, we will evaluate how the presence of the BSA coating affects the degradation profile of SPIONs in mimic lysosomal environments, their interaction with two *in vitro* cell lines and an *in vivo* model *C. elegans*.

5.2 DEGRADATION OF C-SPIONs AND BSA-SPIONs IN BIOLOGICAL MEDIA

The understanding of the SPIONs' degradation in biological media prior to any application in nanomedicine is necessary. SPIONs degradation can release free ions, in particular in the form of Fe (II), and those ions are recognized as a source of potential toxic effects to cells producing hydroxyl radicals (OH⁻) and other reactive oxygen species (ROS)⁶. On the other hand, biomedical applications of SPIONs greatly rely on their magnetic properties⁷, and these magnetic properties are strongly size-dependent. Degradation causes changes in their size and subsequently influences their efficiency in biomedical applications. Therefore, degradation of C-SPIONs and BSA-SPIONs in the cellular environment was investigated.

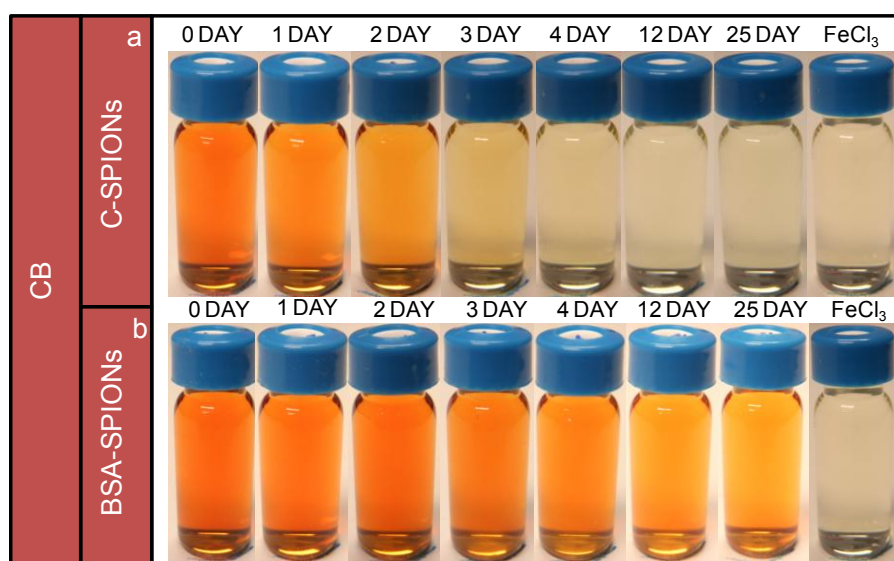
After uptake by cells, inorganic NPs are usually internalized into intracellular lysosomes (cellular organelles with acidic environment, which are considered as the intracellular digestive machinery) where they undergo degradation and further transformation⁸. Here, 20 mM citrate buffer (pH 4.6, referred as CB), mimicking the intracellular lysosome acidic environment (pH 4.6), was used to investigate the degradation kinetics of C-SPIONs and BSA-SPIONs⁹. The citrate buffer was prepared by mixing equal volumes of 10 mM citric acid and 10 mM sodium citrate monobasic solution. Appropriate amount of C-SPIONs and BSA-SPIONs were diluted in the prepared citrate buffer to get a final SPION concentration of 0.5 mg/mL. To mimic a more real intracellular lysosomal environment, citrate buffer with the addition of 10% FBS (referred as CB-FBS) were also used to study the degradation profile of C-SPIONs and BSA-SPIONs, since FBS is

an important and necessary component in a complete cellular medium. We assume that before being internalized in lysosomes, SPIONs have been already exposed to the FBS containing cellular media that leads to the FBS coating on their surface. The solutions were placed at room temperature for 30 days, and digital images were taken every day using a domestic camera. To monitor the size decrease and morphology change during the degradation process, small aliquots of the dispersions were collected every day and subjected to DLS and TEM measurements.

5.2.1 DEGRADATION KINETICS

During the degradation process, the brown color of the SPIONs dispersion changed gradually to yellow, and finally became transparent. FeCl_3 in CB was used as the reference (transparent). Digital images representing the degradation process of C-SPIONs and BSA-SPIONs in CB and in CB-FBS are shown in Fig. 1. The selected images show the different degradation behavior of SPIONs in different conditions. Qualitatively, SPIONs with BSA coating (BSA-SPIONs) degraded slower than C-SPIONs (comparing the changes in color of dispersions in Fig. 1a and 1b, Fig. 1c and 1d, respectively) both in CB and in CB-FBS, as the color of BSA-SPIONs changed more slowly. The presence of 10% FBS also slowed down the degradation of both SPIONs (comparing Fig. 1a and 1c, Fig. 1b and 1d separately), because changes in color were observed more slowly.

To further quantify the degradation behavior of SPIONs, the color intensity of the images was measured by using ImageJ software. Because all the images were carefully taken under exactly the same light exposure and placement, we assume that the intensity of the brown color of the SPIONs dispersions is proportional to the amount of SPIONs in solution. Hence, information about the degradation kinetics were then determined on the basis of the measured color intensity. The protocols are detailed in the annex of this chapter.



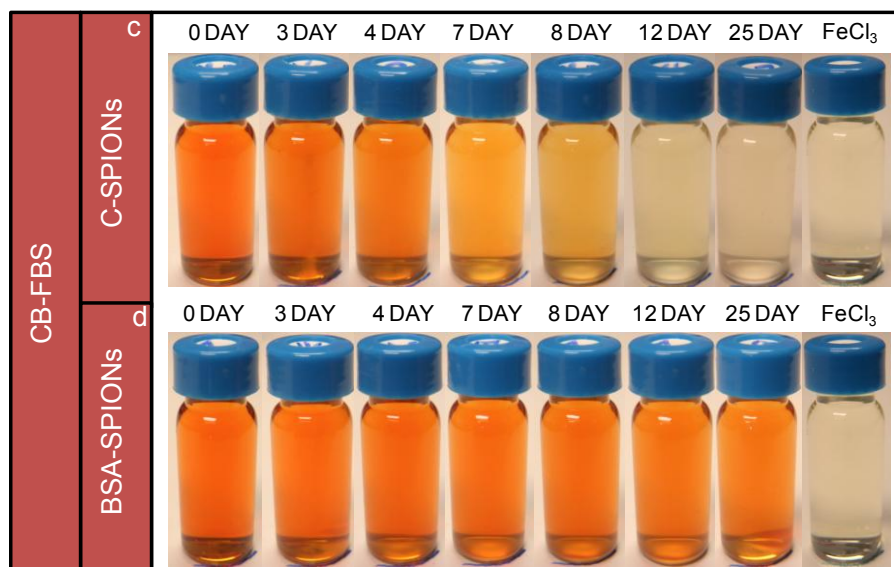


Figure 1. Digital images of the degradation process of C-SPIONs (a and c) and BSA-SPIONs (b and d) in CB and CB-FBS.

The degradation kinetics of C-SPIONs and BSA-SPIONs in both buffers are plotted as shown in Fig. 2. All the kinetics were fitted by a quadratic equation: $Y = Ax^2 + Bx + C$. The degradation rate was evaluated by comparing the coefficient A. Clearly, degradation rate follows the order: C-SPIONs in CB > C-SPIONs in CB-FBS > BSA-SPIONs in CB > BSA-SPIONs in CB-FBS (corresponds to coefficient A of 0.0315, -0.0076, -0.004 and 0). This indicates that kinetics of degradation of SPIONs in citrate buffer were affected by the presence of the BSA coating, as well as the FBS supplemented in CB.

In the case of C-SPIONs incubated in CB, SPIONs degraded in the initial 4 days, and almost complete degradation was observed at day 7 (Fig. 2a). The addition of FBS in CB decreased the degradation rate of C-SPIONs in CB, where a complete dissolution was found on day 15 (Fig. 2a). This could be due to the adsorption of FBS proteins on C-SPIONs surface, through which a protein corona is formed protecting the SPIONs. In contrast, BSA-SPIONs displayed a different degradation profile under the same conditions, in CB, BSA-SPIONs incubated only degraded slightly in the initial 7 days as the color intensity was found almost unchanged (Fig. 2b). BSA-SPIONs began to degrade after day 7, only 50% of the BSA-SPIONs were degraded after 30 days incubation. Remarkably, in the presence of FBS, only negligible degradation is found for BSA-SPIONs on day 30 (Fig. 2b).

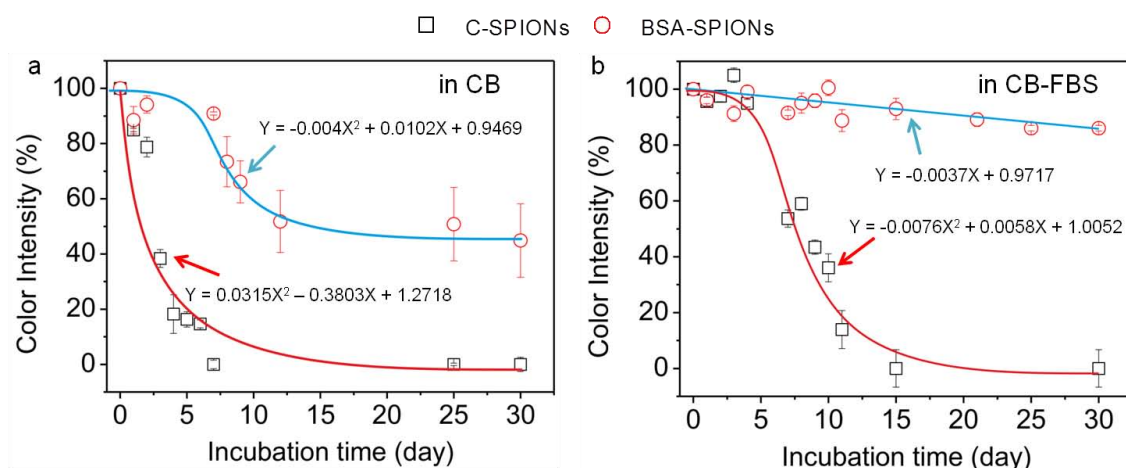


Figure 2. Degradation kinetics of C-SPIONs and BSA-SPIONs in CB (a) and CB-FBS (b).

Previous studies on degradation of SPIONs in solutions mimicking lysosomal environments also indicated a surface coating-dependent degradation kinetics⁹. Dextran coated SPIONs showed a complete degradation after 3 days incubation, while glucose coated SPIONs were not completely degraded even after 30 days incubation⁹. In our work, we showed that citrate coated SPIONs are more vulnerable to the acid conditions, while the presence of BSA coating significantly slow down the degradation rate of SPIONs in the same conditions. This is likely due to the strong affinity of BSA to C-SPIONs surface as suggested by ITC measurements (Chapter 4). The formed BSA monolayer protected the iron oxide core from being attacked and complexed by the citrate iron in the solution. Moreover, we also show that FBS in CB can lower the degradation kinetics of SPIONs, especially for BSA-SPIONs. We consider that both the BSA monolayer and the additional adsorbed FBS on SPIONs surface synergistically protected the SPIONs core from being complexed and chelated by the free citrate ions.

5.2.2 SIZE EVOLUTION DURING THE DEGRADATION PROCESS

The D_h of the SPIONs was also monitored during the degradation process (Fig. 3) by DLS. Consistent with previous results, D_h for C-SPIONs incubated in CB displayed a gradual decrease with time, which decreased from the initial 17 nm to less than 3 nm after 6 days incubation. It is noteworthy that after 6 days incubation of C-SPIONs in CB, small size (less than 3 nm) in the D_h distribution was not able to be detected, which we assigned to the complete degradation of C-SPIONs after day 6. However, for BSA-SPIONs incubated in CB, no apparent differences in D_h distributions was found over time, even after 30 days incubation, D_h maintained at around 25 nm. DLS results further indicate the protective role of the BSA coating on SPIONs in CB. Although 50% BSA-SPIONs were degraded, the rest ones maintained their initial intact structure.

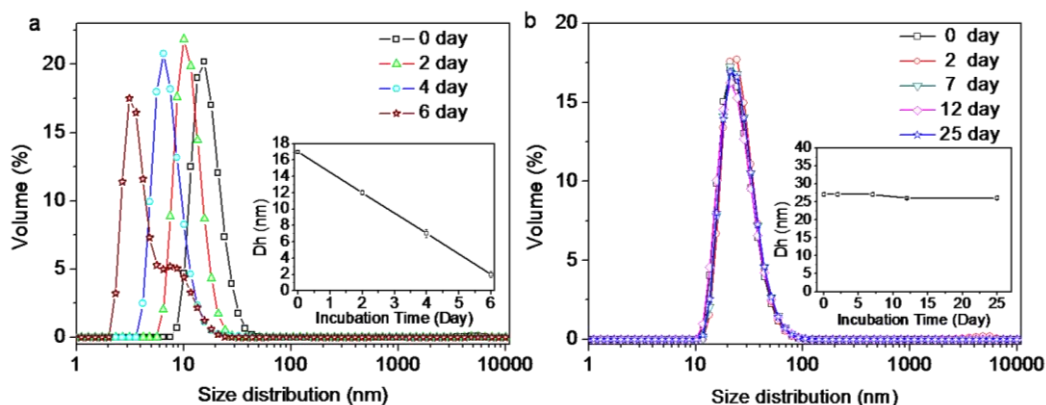


Figure 3. Hydrodynamic size evolution of C-SPIONs (a) and BSA-SPIONs (b) in CB (Inset are the Dh of C-SPIONs and BSA-SPIONs in different incubation intervals).

5.3 EFFECT OF THE PRESENCE OF BSA COATING ON SPIONs-CELL INTERACTION

In this part, biological effects of C-SPIONs and BSA-SPIONs were evaluated on *in vitro* cells. For this purpose, we chose two types of cell lines, MDA MB 231 adherent cells and HL 60 suspension cell. At the one hand, MDA MB 231 cells are a type of adherent cells which originated from human breast and are widely used in biological research to perform *in vitro* experiments. Also, NPs are usually intravenously injected, hence the use of blood cells are highly relevant to the clinical applications of NPs. Based on this consideration, HL 60 cells (originated from blood cells) are also chosen in our study. At the other hand, we have experience in culturing those two cell lines. The use of C-SPIONs and BSA-SPIONs, which are high stability in several biological media as reported in Chapter 4, allowed us to study their different behavior *in vitro* due to their different surface coating.

5.3.1 CELL CULTURES

MDA MB 231 cells were cultured at a concentration of approximately 1×10^6 cells/mL in a 96 well plate (0.2 mL per well), in complete medium (RPMI supplemented with 10% FBS and 6mM GlutaMax) and allowed to grow for 24h. HL 60 cells were cultured in complete medium (RPMI medium supplemented with 10% FBS, 6mM GlutaMax and 0.5mM sodium piruvate) at a concentration of 1×10^6 cells/mL in a 96 well-plate (0.1 mL per well). Both cell lines were obtained from American Type Culture Collection (ATCC, Manassas, VA), and grown in at 37 °C in 5% CO₂ until reaching 70% confluence.

5.3.2 CELL VIABILITY: MTT ASSAYS

EXPERIMENTS

For MDA MB 231 cell lines, after 24h growth with a confluence of 70%, the medium was replaced with fresh medium containing C-SPIONs or BSA-SPIONs, with a final SPIONs concentration of 40 µg/mL, 75 µg/mL, 100 µg/mL and 150 µg/mL. Cells and SPIONs were co-incubated for another 24h.

For HL 60 cell lines, after 24h growing with a confluence of 70%, another 0.1 mL fresh medium containing C-SPIONs or BSA-SPIONs, with concentrations doubled those for MDA MB 231 cell lines, was added to each well to reach a final volume of 200 μ l. The final SPIONs concentration in each well were also maintained at 40 μ g/mL, 75 μ g/mL, 100 μ g/mL and 150 μ g/mL. Cells were then allowed to co-incubate with SPIONs for another 24h.

Cell viability after SPIONs exposure was evaluated using MTT (Biomedica) assays. Briefly, appropriate amount of MTT reactive (10% of the sample volume in each well, 20 μ L) was added into each well, plates were incubated at 37°C for 2-5 hours and read in a micro plate reader (Victor3, Perkin Elmer) at 450 nm, and at 620 nm as reference.

CYTOTOXICITY ANALYSIS

First, evaluation of SPIONs' cytotoxicity on cells is of great importance before their practical use. Previous work in our group revealed that SPIONs with citrate coating caused negligible toxicity towards primary endothelial progenitor cells (OECs cell line) and neuron like cells (SH SY5Y cell line), for a concentration lower than 100 μ g/mL¹⁰. Hence, in this work, four concentrations of SPIONs, 40, 75, 100 and 150 μ g/mL, were chosen to evaluate the cytotoxicity of C-SPIONs and BSA-SPIONs on both cell lines. We also included SPIONs concentration at 150 μ g/mL in our study, because we want to examine whether the biocompatibility of SPIONs can be improved at high SPIONs concentration in the presence of BSA coating.

Fig. 4 shows the viability of MDA MB 231 cells and HL 60 cells upon exposure to C-SPIONs and BSA-SPIONs at different concentrations. Similar to the previous findings in our group¹⁰, C-SPIONs cause low toxicity to both cell lines. In all the cases, cell viability is higher than 80%, even at SPIONs concentration of 150 μ g/mL. Increase in C-SPIONs concentration leads to the decrease in cell viability of MDA MB 231 cell line ($p < 0.01$ when SPIONs concentration higher than 40 μ g/mL) and HL 60 cell line ($p < 0.05$ in all the concentrations). Exposure of BSA-SPIONs to adherent MDA MB 231 cell line lead to the decrease in cell viability, while an increase in cell viability was observed in HL 60 cell line. The differences in cell viability for MDA MB 231 cells at BSA-SPIONs concentrations of 40 and 100 μ g/mL are significant ($p < 0.05$ and $p < 0.01$, respectively). However the difference for HL 60 cells is not significant. This finding indicates that BSA coating can modify the interaction profile of SPIONs with cells in terms of cell viability in a cell-type dependent. For the adherent MDA MB 231 cell line, the presence of BSA coating caused adverse effects, while slight effect was observed in the case of HL 60 cell.

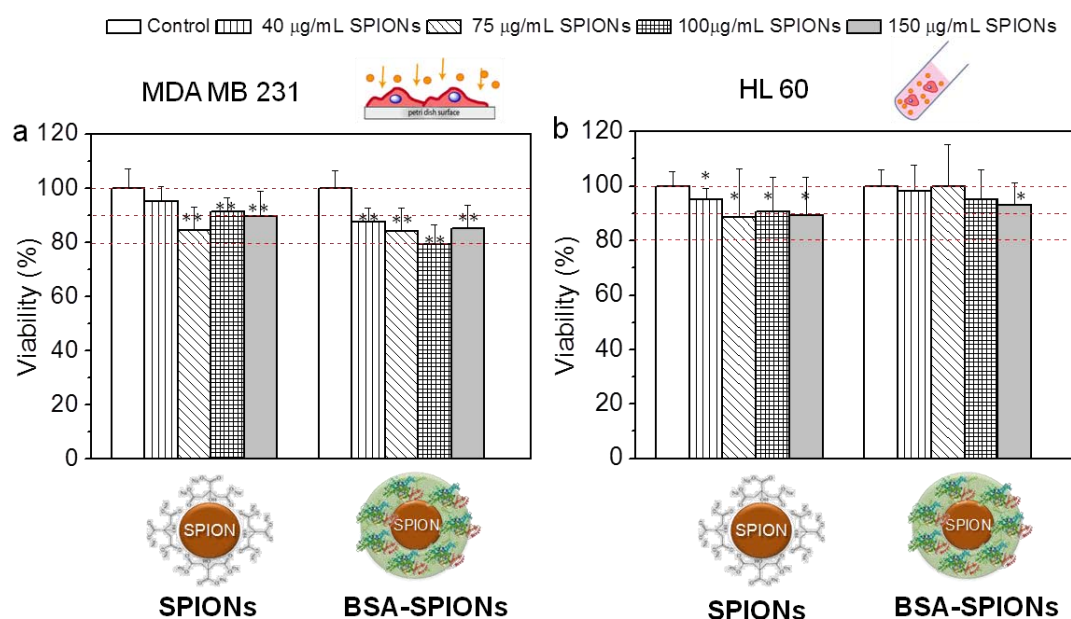


Figure 4. Effect of C-SPIONs and BSA-SPIONs on the viability of cells, adherent MDA MB 231 cell line (a) and suspension HL 60 cell line (b) treated with 0–150 µg/ml SPIONs. Seven replicates per concentration were performed. Error bars indicate standard error. $p < 0.05$ (*), $p < 0.01$ (**) and $p < 0.001$ (***).

5.3.3 CELLULAR UPTAKE OF SPIONs: DETERMINATION OF IRON CONTENT IN CELLS

Cellular uptake of C-SPIONs and BSA-SPIONs were further evaluated in both cell lines. We quantitatively determined the cellular uptake of C-SPIONs and BSA-SPIONs using a method established previously in our group, which is based on magnetometry measurements. Detailed protocol for the determination is given in the annex of this chapter. SPIONs uptake by cells after 24h incubation is summarized in Table 1. We chose the concentrations lower and higher than the safe SPIONs concentrations (100 µg/mL) as mentioned previously, 75 µg/mL and 150 µg/mL.

MDA MB 231 cells internalize SPIONs (C-SPIONs and BSA-SPIONs) more efficiently than HL 60 cells, iron content within MDA MB 231 cells doubles the amount of iron within HL 60 cells under the same conditions (Table 1). In general, for both cell lines, increasing SPIONs concentration results in higher SPION uptake. Remarkably, cellular uptake of SPIONs was largely affected by the presence of BSA coating in both cell lines, where a much lower uptake of BSA-SPIONs was observed compared with C-SPIONs (about 1-2 times less). This finding clearly shows that the presence of BSA coating modifies the interaction of SPIONs with cells, lowering their efficient internalization by cells. Decrease in cellular uptake of NPs with BSA coating was also reported by Ruge *et al.* in a recent study¹¹.

Table 1. SPIONs uptake by cells in different conditions after 24 h incubation.

Cell type	SPIONs type	SPIONs concentration incubated with cells ($\mu\text{g}/\text{mL}$)	SPIONs uptake by cells (pg/cell)
MDA MB 231	C-SPIONs	75	2.8
	C-SPIONs	150	3.9
	BSA-SPIONs	75	1.1
	BSA-SPIONs	150	1.2
HL 60	C-SPIONs	75	1.0
	C-SPIONs	150	1.5
	BSA-SPIONs	75	0.5
	BSA-SPIONs	150	0.9

5.3.4 SPIONs LOCALIZATION WITHIN CELLS AFTER INTERNALIZATION.

Adsorption of proteins on nanoparticles surface not only affects the cellular uptake of nanoparticles, but could also change the intercellular nanoparticle localization⁴. Therefore, the SPIONs localization within cells in the presence and absence of BSA coating was investigated by transmission electron microscopy (TEM). Here, we focused on the intracellular localization of C-SPIONs and BSA-SPIONs in MDA-231 cells. TEM observations were performed after 24h incubation of SPIONs and BSA-SPIONs with MDA 2D 231 cells, representative images are shown in Fig. 5. We found that both C-SPIONs and BSA-SPIONs accumulated in endosomes, indicating the presence of BSA coating on SPIONs surface did not change their distribution inside cells. However, we noted that for C-SPIONs, many aggregates were found near the cellular membrane of MDAMB 231 cells, even though several washing cycles were performed before the TEM sample preparation. Similar phenomenon was also observed when incubating silica nanoparticles with cells, where the authors assigned it to the strong interaction between silica nanoparticles and cell protrusions, which lead to the entanglements of silica nanoparticles around the cell surface⁴. As explained in Chapter 4 when investigating the stability of C-SPIONs in complete RPMI medium, we found that C-SPIONs maintained their colloidal stability after 24h incubation, without observation of aggregates. Therefore, the formation of the aggregates close to the cell membrane for C-SPIONs is not due to the instability of C-SPIONs in cell medium. We attribute it to the strong interaction of C-SPIONs with the membrane of MDA MB 231 cells, which resulted in their interpenetration within the cell membrane, as it is clearly seen in Fig. 5b-3. However, SPIONs clusters were not found at the cell surface for BSA-SPIONs incubated with MDA MB 231 cells, suggesting that the presence of BSA coating weakened SPIONs-cell membrane interaction. In fact, many proteins are associated with the cell membrane⁴. Those proteins probably have a high affinity to C-SPIONs and facilitate the attachment of NPs to the cell membrane. While they may have a low affinity to BSA-SPIONs and resulted the weak interaction between BSA-SPIONs and cell membrane. Previous ITC results (Chapter 4) also show that BSA-SPIONs interact weakly with other proteins in FBS. Moreover, TEM images show more NPs are internalized in endosome when cells incubated with C-SPIONs than that treated with

BSA-SPIONs. This is more evident at higher SPIONs concentration. Fig 5b-2 shows an endosome is fully loaded with C-SPIONs, while in the case of BSA-SPIONs, the endosome was only partially loaded.

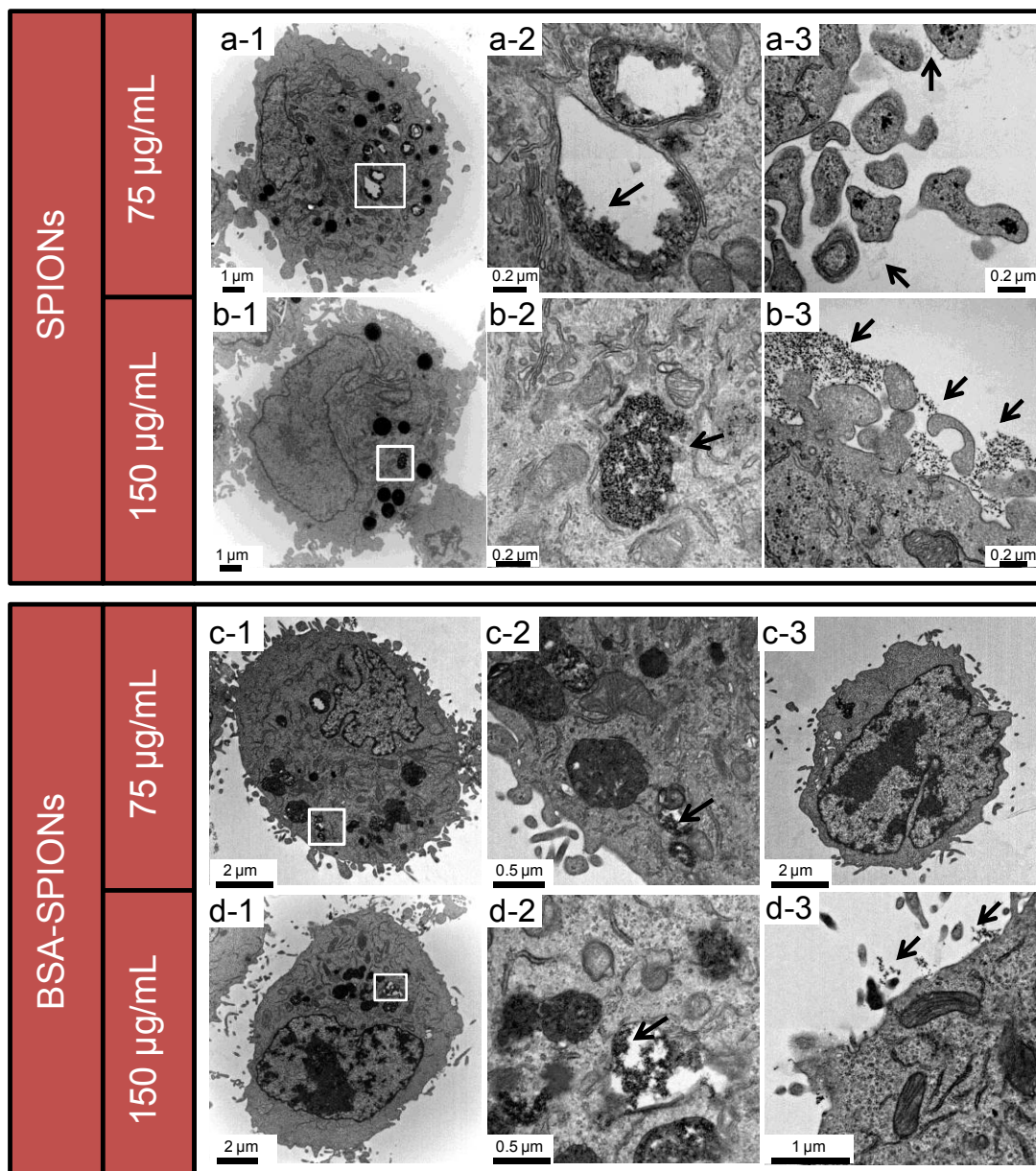


Figure 5. Localization of SPIONs and BSA-SPIONs after incubation with MDA MB 231 cells for 24 h in two SPIONs concentrations (75 µg/mL and 150 µg/mL), visualized by TEM measurements. Black arrows indicate the SPIONs.

It is well established that there are three possible ways for nanoparticles entering the cells, phagocytosis, macropinocytosis or endocytosis, depending on the surface chemistry of the nanoparticles and the type of the cells exposed¹². It has been reported by several recent work, the main pathway of cellular uptake of SPIONs is through endocytosis, and SPIONs' sedimentation in cell media promotes their cellular uptake^{10,13,14}. Even though Chapter 4 shows the high stability of C-SPIONs and BSA-SPIONs in the tested cellular media, with no evidence of aggregates formation after 24h incubation. A higher increase in D_h was observed for C-SPIONs than that of BSA-SPIONs after 24 h incubation with RPMI-FBS medium (20 nm and 5 nm

increase in D_h were observed for C-SPIONs and BSA-SPIONs, respectively). Therefore, we consider that C-SPIONs formed small FBS-C-SPIONs clusters (not aggregates, D_h size distribution shows a main peak at 70 nm) after 24 h incubation in RMPI-FBS medium, while BSA-SPIONs maintained their monodispersity in 24h (30 nm). The formation of small FBS-C-SPIONs clusters may explain the higher cellular uptake of C-SPIONs than that of monodisperse BSA-SPIONs, in a similar way as what been described by Hinderliter *et al*¹⁵.

In all, we consider that both the strong interaction of C-SPIONs with the cell membrane and the formation of small FBS-C-SPIONs clusters during the incubation process could determine the higher cellular uptake of C-SPIONs than BSA-SPIONs.

5.4 EVALUATION OF SPIONs ON 3D *IN VIVO* C. ELEGANS

In this section, we evaluated the effect of BSA coating in a 3D *in vivo* platform, *C. elegans*, for a better understanding of the nano-bio-interaction in a complex living system. *C. elegans*, due to its rapid-life cycle (3 days), short lifespan (2-3 weeks) as well as its small size and transparency¹⁶, has been widely used as a 3D *in vivo* model to study NPs uptake and distribution at the cellular, tissue and organism levels, and to study of the mechanisms of nanotoxicity^{17,18}. Fig. 6 shows the morphology and the life cycle of *C. elegans*.

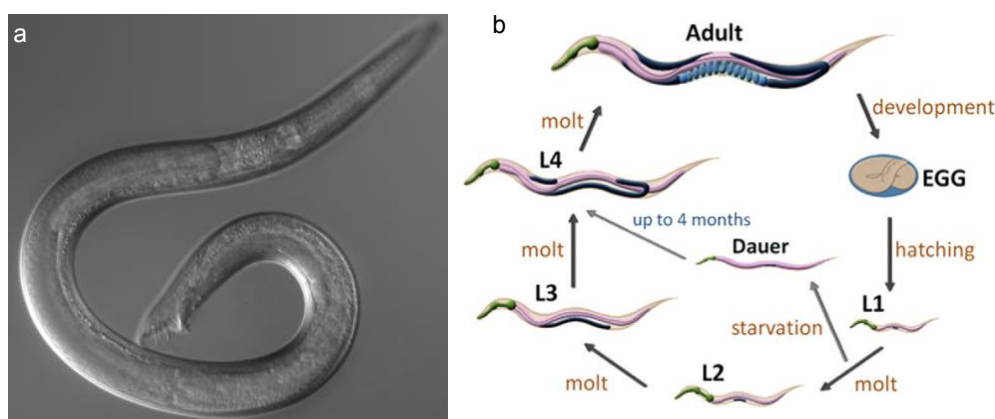


Figure 6. The morphology (a) and life cycle (b) of *C. elegans* L1 to L4 corresponds to larval stages¹⁹.

In this work, toxicity of SPIONs was evaluated on the basis of the survival rate of *C. elegans* upon exposure to C-SPIONs and BSA-SPIONs. Briefly, the adult and larval populations were treated separately with C-SPIONs and BSA-SPIONs in a final volume of 100 μ l in 96-well plates for 24h. The assay was performed in triplicate. The plates were tapped and the worms that moved were counted as alive. Each well contained between 9 ± 3 adult worms and 25 ± 8 larvae. The concentration range assayed was 0–500 μ g/ml. Survival of *C. elegans* after incubation with C-SPIONs and BSA-SPIONs is displayed in Fig. 7. The survival of adults for both types of SPIONs was higher than 70% in the range 100–400 μ g/ml, and decreased to 60% ($p < 0.05$) and 51% ($p < 0.01$) in the case of BSA-SPIONs and C-SPIONs, respectively, at 500 μ g/ml. In the case of larvae, survival was higher than 70% at all BSA-SPIONs concentrations, whereas the lethality of the C-

SPIONs increased rapidly at concentrations $>200 \mu\text{g/ml}$ ($p < 0.05$). The higher sensitivity of larvae to SPION treatment could indicate that the toxicological effects of SPIONs are stronger in the early stages of worms. Adult survival showed no differences in respect of the type of SPIONs, whereas statistical differences on larval survival were found at concentrations $>400 \mu\text{g/ml}$ ($p < 0.05$) depending on the treatment they received either C-SPIONs or BSA-SPIONs. The survival of *C. elegans* after 24h was fitted to linear regression equations, revealing a linear dose-response relationship of the short-term mortality over the range of concentration studied. The value of the slopes shows that the mortality increases quicker in the case of worms treated with C-SPIONs than in the case of treatment with BSA-SPIONs, although the differences are only statistically significant for larvae ($p < 0.01$).

In all, BSA-SPIONs showed a lower toxicity than C-SPIONs in a broader range of concentrations and highly distinctive at high concentrations ($500 \mu\text{g/ml}$). Larvae were strongly affected by C-SPIONs than adult worms; however BSA-SPIONs did not promote drastic toxicity even at high concentrations to adults or larvae, hence suggesting that the BSA coating layer has a protective role for the nematodes.

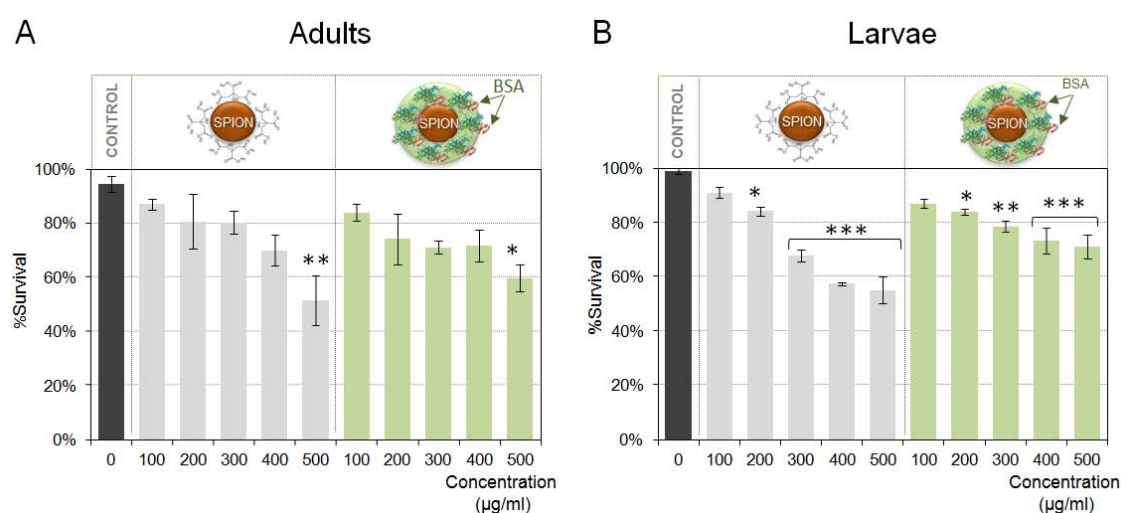


Figure 7. Effect of C-SPIONs and BSA-SPIONs on the survival of *C. elegans*. (A) Adult worms treated with 0–500 $\mu\text{g/ml}$ SPIONs. (B) Larvae treated with 0–500 $\mu\text{g/ml}$ SPIONs. Three replicates per concentration were performed. Error bars indicate standard error. $p < 0.05$ (*), $p < 0.01$ (**) and $p < 0.001$ (***).

5.5 CHAPTER CONCLUSIONS

In this chapter, degradation of C-SPIONs and BSA-SPIONs were investigated in pH 4.6 citrate buffer, mimicking the cellular lysosomal acidic environment. The presence of the BSA coating significantly lowered the degradation process of SPIONs in the acidic solution, due to the strong affinity of BSA on the C-SPIONs surface. Moreover, FBS also displayed a protective role, slowing down the degradation kinetics of SPIONs, especially for BSA-SPIONs. We considered that both the BSA monolayer and the additional adsorbed FBS on SPIONs surface synergistically protected the SPIONs from being attacked and complexed by the citrate ions in solution.

Furthermore, effects of the presence of BSA coating on SPIONs' interaction with different biological entities have been presented. For *in vitro* cells, BSA coating slightly decreased the cell viability of MDA MB 231 cells upon incubation with C-SPIONsm while BSA coating improved the biocompatibility of C-SPIONs to HL 60 cell line, as a slight increase in cell viability was found. Cellular uptake of SPIONs in both cell lines shows a significant decrease in the presence of the BSA coating. For *in vivo C. elegans*, a protective effect of BSA was observed, BSA-SPIONs were observed less toxic than C-SPIONs even at high concentrations to both adults and larvae.

5.6 ANNEX OF CHAPTER 5

5.6.1 DETERMINATION OF SPIONs CONTENT IN SOLUTION

First, all the images are converted to 256 shades (8-bit) of gray. In this scale, value 0 = pure black and 255 = pure white. The image of dispersion with less degraded SPIONs shows more black color than the one with more SPIONs degraded, because of the strong brown color of SPIONs. Then the mean gray intensity of each image was measured by selecting at least three different regions in each image. For an accurate determination of the color change during the degradation process, the mean gray intensity of FeCl_3 in citrate buffer was used as our reference ($\text{Int}_{(\text{FeCl}_3)}$), since it shows the similar color to that of the completely degraded SPIONs dispersion. The mean gray intensity of SPIONs dispersion at 0 Day was labeled as $\text{Int}_{100\%}$, those measured in the different intervals during the degradation process were referred as $\text{Int}_{(N)}$, finally the percentage of the SPIONs remain in the solution were calculated as

$$\text{SPIONs in solution}(\%) = \frac{\text{Int}_{(N)} - \text{Int}_{(0)}}{\text{Int}_{(\text{FeCl}_3)} - \text{Int}_{(0)}} \times 100\%$$

5.6.2 DETERMINATION OF IRON CONTENT IN CELLS

Briefly, after 24h incubation of cells with C-SPIONs and BSA-SPIONs, cell cultures were thoroughly washed 3 times with PBS, and counted. Cells were centrifuged and pellets obtained were dried overnight in polycarbonate capsules at 60°C and a 25-35 mmHg vacuum. Magnetization curve of samples was recorded on a superconductive quantum interference device (SQUID) measurement magnetometer (Quantum Design MPMS5XL). Magnetization curve of SPIONs at 5K was recorded as a function of applied magnetic field under 6 Tesla. At temperatures lower than the blocking temperature, superparamagnetic particles are blocked in a ferromagnetic state and display remnant magnetization at zero applied magnetic field. The uptake of the SPIONs can be evaluated by measuring the remnant magnetization value of treated cells ($M_{r \text{ cells}}$) after they were magnetized up to 6 Tesla. $M_{r \text{ cells}}$ was obtained by dividing the measured M_r value of cell sample by the counted cells number. To know the amount of iron per cell (Fe per cell), remnant magnetization value of the SPIONs ($M_{r \text{ SPIONs}}$) (emu/g Fe) was divided by the $M_{r \text{ cells}}$, calculation formulation was described below.

$$\text{Fe uptake (pg/cell)} = \frac{M_{r \text{ cells}} (\text{emu/cell})}{M_{r \text{ SPIONs}} (\text{emu/gFe}_2\text{O}_3)}$$

For example, magnetization curve for BSA-SPIONs and BSA-SPIONs internalized within MDA MB 231 cells at 5K were shown in Fig. 1, $M_{r \text{ BSA-SPIONs}}$ and $M_{r \text{ MDA MB231}}$ can be obtained from each hysteresis loop. By applying the above formulation, the amount of BSA-SPIONs internalized in the MDA MB 231 cells can be quantified.

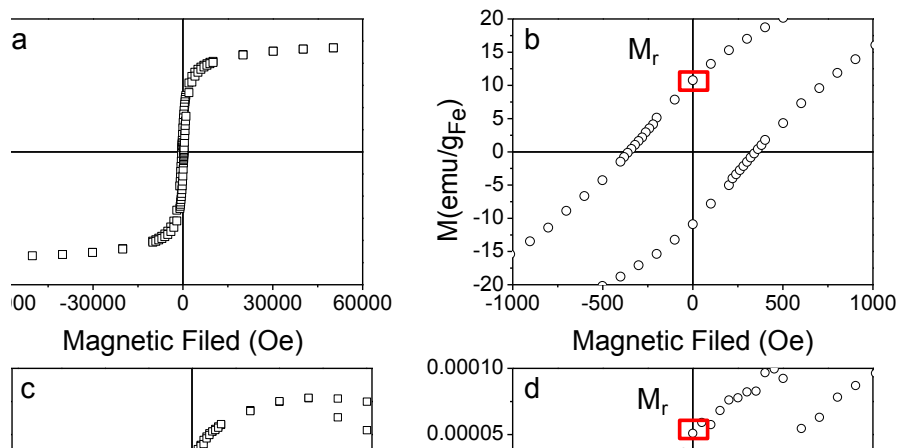


Figure 1. Magnetization curve for BSA-SPIONs (a, b) and BSA-SPIONs internalized within MDA MB 231 cells at 5K (c, d), in the applied magnetic field of 6 Tesla. b and d are enlarged hysteresis loop under small fields of a and b, separately.

5.6.3 INTERCELLULAR LOCALIZATION OF SPIONS-TEM SECTIONS

MDA MB 231 cells were seeded in a 96-well Petri Dish, grown and treated with 75 and 150 $\mu\text{g}\cdot\text{ml}^{-1}$ BSA-SPIONs. After 24h of incubation, cells were trypsinized, washed twice with PBS and collected by centrifugation (1400 rpm, 5 min). Supernatants were discarded and 2 ml of 2% glutaraldehyde (served as fixation solution) in cacodylate buffer was added to the pellet. Cells were incubated in the fixation solution at 4°C and further stained by using 1% OsO_4 . They were then dehydrated in an alcohol series and embedded in Epon resin. Ultrathin sections (70 μm) were transferred onto copper grids and analyzed by TEM, using a Jeol-JEM 1400 microscope operating at 200 kV.

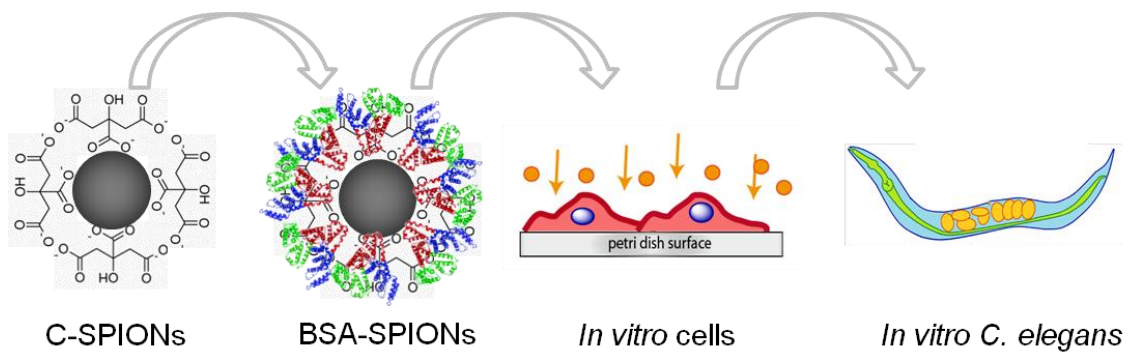
5.7 CHAPTER REFERENCES

- (1) Monopoli, M. P.; Aberg, C.; Salvati, A.; Dawson, K. A. *Biomolecular coronas provide the biological identity of nanosized materials*. *Nat Nano*, **2012**, *7*, 779.
- (2) Lesniak, A.; Fenaroli, F.; Monopoli, M.; Aberg, C.; Dawson, K.; Salvati, A. *Effects of the Presence or Absence of a Protein Corona on Silica Nanoparticle Uptake and Impact on Cells*. *ACS Nano*, **2012**, *6*, 5845
- (3) Hühn, D.; Kantner, K.; Geidel, C.; Brandholt, S.; De Cock, I.; Soenen, S. J. H.; Rivera_Gil, P.; Montenegro, J.-M.; Braeckmans, K.; Müllen, K.; Nienhaus, G. U.; Klapper, M.; Parak, W. J. *Polymer-Coated Nanoparticles Interacting with Proteins and Cells: Focusing on the Sign of the Net Charge*. *ACS Nano*, **2013**, *7*, 3253.
- (4) Lesniak, A.; Fenaroli, F.; Monopoli, M. P.; Åberg, C.; Dawson, K. A.; Salvati, A. *Effects of the Presence or Absence of a Protein Corona on Silica Nanoparticle Uptake and Impact on Cells*. *ACS Nano*, **2012**, *6*, 5845.
- (5) Lunov, O.; Syrovets, T.; Loos, C.; Beil, J.; Delacher, M.; Tron, K.; Nienhaus, G. U.; Musyanovych, A.; Mailänder, V.; Landfester, K.; Simmet, T. *Differential Uptake of Functionalized Polystyrene Nanoparticles by Human Macrophages and a Monocytic Cell Line*. *ACS Nano*, **2011**, *5*, 1657.
- (6) Winterbourn, C. C. *Toxicity of iron and hydrogen peroxide: the Fenton reaction*. *Toxicology Letters*, **1995**, *82–83*, 969.
- (7) Lu, A.-H.; Salabas, E. L.; Schüth, F. *Magnetic Nanoparticles: Synthesis, Protection, Functionalization, and Application*. *Angewandte Chemie International Edition*, **2007**, *46*, 1222.
- (8) Ohkuma, S.; Poole, B. *Fluorescence probe measurement of the intralysosomal pH in living cells and the perturbation of pH by various agents*. *Proceedings of the National Academy of Sciences*, **1978**, *75*, 3327.
- (9) Michael, L.; Florence, L.; Valentin-Adrian, M.; Marie-Geneviève, B.; François, G.; Claire, W.; Florence, G. *Degradability of superparamagnetic nanoparticles in a model of intracellular environment: follow-up of magnetic, structural and chemical properties*. *Nanotechnology*, **2010**, *21*, 395103.
- (10) Carezza, E.; Barceló, V.; Morancho, A.; Montaner, J.; Rosell, A.; Roig, A. *Rapid synthesis of water-dispersible superparamagnetic iron oxide nanoparticles by a microwave-assisted route for safe labeling of endothelial progenitor cells*. *Acta Biomaterialia*, **2014**, *10*, 3775.
- (11) Ruge, C. A.; Kirch, J.; Cañadas, O.; Schneider, M.; Perez-Gil, J.; Schaefer, U. F.; Casals, C.; Lehr, C.-M. *Uptake of nanoparticles by alveolar macrophages is triggered by surfactant protein A*. *Nanomedicine: Nanotechnology, Biology and Medicine*, **2011**, *7*, 690.
- (12) Saptarshi, S.; Duschl, A.; Lopata, A. *Interaction of nanoparticles with proteins: relation to bio-reactivity of the nanoparticle*. *Journal of Nanobiotechnology*, **2013**, *11*, 26.
- (13) Safi, M.; Courtois, J.; Seigneuret, M.; Conjeaud, H.; Berret, J. F. *The effects of aggregation and protein corona on the cellular internalization of iron oxide nanoparticles*. *Biomaterials*, **2011**, *32*, 9353.
- (14) Hirsch, V.; Kinnear, C.; Moniatte, M.; Rothen-Rutishauser, B.; Clift, M. J. D.; Fink, A. *Surface charge of polymer coated SPIONs influences the serum protein adsorption, colloidal stability and subsequent cell interaction in vitro*. *Nanoscale*, **2013**, *5*, 3723.
- (15) Hinderliter, P. M.; Minard, K. R.; Orr, G.; Chrisler, W. B.; Thrall, B. D.; Pounds, J. G.; Teeguarden, J. G. *ISDD: a computational model of particle sedimentation, diffusion and target cell dosimetry for in vitro toxicity studies*. *Particle and fibre toxicology*, **2010**, *7*, 36.
- (16) Wood, W. B. *The Nematode Caenorhabditis Elegans*; Cold Spring Harbor Laboratory, 1988.

- (17) Kim, S. W.; Nam, S.-H.; An, Y.-J. *Interaction of Silver Nanoparticles with Biological Surfaces of Caenorhabditis elegans*. *Ecotoxicology and Environmental Safety*, **2012**, *77*, 64.
- (18) Wu, Q.; Li, Y.; Li, Y.; Zhao, Y.; Ge, L.; Wang, H.; Wang, D. *Crucial role of the biological barrier at the primary targeted organs in controlling the translocation and toxicity of multi-walled carbon nanotubes in the nematode Caenorhabditis elegans*. *Nanoscale*, **2013**, *5*, 11166.
- (19) Gonzalez-Moragas, L.; Roig, A.; Laromaine, A. *C. elegans as a tool for in vivo nanoparticle assessment*. *Advances in Colloid and Interface Science*, **2015**, *219*, 10.

CHAPTER 6

CONCLUSIONS AND FUTURE WORK



CHAPTER SUMMARY

In this chapter, general conclusions and some suggestions for the future work to continue this PhD research topic are provided.

Chapter Index	
	pag.
CHAPTER SUMMARY	151
6.1GENERAL CONCLUSIONS	153
6.2 FUTURE WORK	156

6.1 GENERAL CONCLUSIONS

The main achievements accomplished during the PhD research are described in the following four paragraphs:

1- Microwave assisted synthesis method has been selected to synthesize SPIONs and I have confirmed that monodisperse SPIONs with high saturation magnetization can be fabricated in 15 min. Control of the size of SPIONs can be achieved by changing the microwave synthetic parameters, in particular reaction temperature and time. The obtained SPIONs were thoroughly characterized, and their stability in water was monitored. Furthermore, I have shown that surface coating of SPIONs by PVP, TMAOH or Na₃Cit rendered them to have high dispersibility and stability in water. PVP-SPIONs (5.6 ± 1 nm), which are monodisperse as colloids in water, displayed r_1 and r_2 relaxivity values of 1.57 and 54.23 mM⁻¹s⁻¹ at 7 tesla, respectively, indicating their potential use as T₁ contrast agent in magnetic resonance imaging.

I also demonstrated that synthesis of SPIONs can be scaled up using a multi-mode microwave apparatus. In our trials, the amount of SPIONs synthesized per batch increased from the milligram scale (around 20 mg by using the lab-scale device) to gram scale (about 3g by using the large scale microwave apparatus). The gram scale-up synthesis performed in the multi-mode microwave apparatus notably shortened the synthesis time and reduced the energy consumption compared to the lab-scale synthesis. Moreover, SPIONs produced in the large scale up synthesis maintained the spherical shape, monodispersity and the superparamagnetic properties as those synthesized in a lab-scale equipment.

Similarly, small Au nanoparticles with narrow size distribution and high stability in water were also synthesized by using one step microwave assisted method in 10 min. The optical properties of the Au nanoparticles can be moderately tuned by simply changing the amount of PVP used.

These results validate that microwave-assisted synthesis as a facile, fast and energetically favorable route for synthesizing SPIONs and Au nanoparticles with desirable physico-chemical properties. Moreover, the multi-mode MW apparatus provides the possibility for scaling up the synthesis of nanoparticles.

2- Regarding heterostructures, I also established a facile, fast and bio-friendly microwave-assisted polyol route to synthesize high yield of gold (Au) nanotriangles (NT) with their surface decorated with SPIONs. Significantly, the yield of Au NTs-SPIONs nanocomposites can be controlled by adjusting the amount of PVP used, while reaction time and temperature showed moderate effects on the yield of Au NTs-SPIONs. Moreover, the obtained Au NTs-SPIONs nanocomposites (60% shape yield) displayed a characteristic LSPR band in the NIR region of 800 nm and superparamagnetic properties at room temperature.

In summary, microwave assisted thermal decomposition route can also be extended to synthesize hybrid nanocomposites or heterostructures. In our case, PVP plays an important role in determining the morphology of Au nanocrystals.

3- Negatively charged SPIONs were further functionalized with BSA (the obtained SPIONs were labeled as BSA-SPIONs). BSA-SPIONs displayed high stability in several biological relevant media including PBS, cell media and complete cell media (supplemented with 10% FBS), in which no aggregations were observed after 24 h incubation.

Binding behaviors, structure changes and thermodynamics of BSA upon adsorption on C-SPIONs surface have been studied in detail. DLS, Zeta potential, FTIR and XPS measurements confirm the BSA adsorption on C-SPIONs surface. In particular, DLS measurement showed an increase of 7 nm in hydrodynamic diameter of C-SPIONs after BSA adsorption, DSC measurements confirmed the thickness of the BSA coating is about 3.3 nm. Negative staining TEM measurements provided visual evidence of BSA coating on C-SPIONs surface.

Changes in structure of BSA after adsorption have been studied by several spectroscopy techniques. UV-Vis measurements showed that UV-Vis adsorption at 220 nm and 280 nm shifted gradually with the increasing concentrations of C-SPIONs. CD measurements showed slight increase in ellipticity at wavelength of 208 nm and 222 nm. Both UV-Vis and CD measurements indicates the slight unfolding of BSA upon adsorption onto C-SPIONs' surface. Fluorescence spectroscopy showed that fluorescent intensity of BSA decreased gradually as SPIONs' concentration increased, and that the maximum emission band underwent a gradual slight red shift. The quenching mechanism of SPIONs on BSA has been determined to be static quenching, confirming the formation of BSA-SPIONs complex. A slight red shift observed in the synchronous fluorescent spectra of BSA indicated the slight unfolding of BSA occurred in regions close to the Trp residues. ITC measurements showed high affinity of BSA to C-SPIONs' surface, while FBS interacts weakly with BSA-SPIONs.

In conclusion, surface functionalization with BSA resulted in the improvement of SPIONs' stability in biologically relevant media. BSA has a strong affinity to C-SPIONs' surface, forming a BSA monolayer with a thickness of about 3.5 nm on the C-SPIONs surface after adsorption. C-SPIONs induced a slight unfolding of BSA in regions close to the Trp and Tyr residues.

4- Degradation studies of C-SPIONs and BSA-SPIONs performed in citrate buffer (20 mM, pH 4.6) in the presence or absence of 10% FBS show that BSA coating dramatically slowed down the degradation rate of SPIONs. The study on interaction of SPIONs and BSA-SPIONs with cells show that: i) BSA-SPIONs slightly decrease the cell viability of MDA MB 231 cells, while increased the cell viability of HL 60 cells, ii) the uptake of BSA-SPIONs in both cell lines was observed much lower than C-SPIONs and iii) both C-SPIONs and BSA-SPIONs are localized in lysosomes.

Moreover, by using a 3D *in vivo* platform, *C. elegans*, we found that BSA-SPIONs showed a lower toxicity than C-SPIONs in a broader range of concentrations.

In all, the BSA coating slow down the degradation of SPIONs in acidic environments. The presence of BSA coating slightly modified SPIONs' cytotoxicity and decrease SPIONs' uptake by *in vitro* cells. BSA coating layer also displayed a protective role for the nematodes.

Summarizing, this thesis contributed to i) expansion of the use of microwave assisted synthesis method in engineering hybrid inorganic nanocomposites; ii) a better understanding of complex interaction of SPIONs with biological entities including BSA, *in vitro* cells and *in vivo C. elegans*.

6.2 FUTURE WORK

On the basis of the work done in the PhD thesis, future experiments can be expanded in several directions:

- Regarding microwave synthesis of SPIONs, although we already showed that SPIONs' size can be tuned 2 nm larger by increasing reaction time and temperature, studies for further control of their size can be continued. For instance, introducing the seed-growth method in the microwave synthesis for producing larger SPIONs.
- In the case of Au NTs-SPIONs nanocomposites with 60% shape-yield of Au NTs, further purification of the product to obtain 100% Au NTs-SPIONs nanocomposites is a challenge but very necessary for further use of those materials in devices. Based on the different shapes of Au nanoparticles present in our system, the aqueous multiphase systems could be explored further purifying the Au NTs-SPIONs nanostructures.
- Moreover, based on the superparamagnetic properties and characteristic LSPR band in the NIR region (800 nm), the Au NTs-SPIONs nanocomposites should be evaluated in biomedical applications such as separation, sensing and hyperthermia.
- In this PhD work, BSA was used to functionalize the SPIONs to improve their stability in biological media and biocompatibility in biological environments. Considering that the final biomedical applications of the functionalized nanoparticles are targeted at human beings, human serum albumin (HSA) the most abundant protein in human blood serum) should be used to functionalize our SPIONs to make them more biocompatible to humans. The study on the interaction of SPIONs with HSA, and the effect of HSA coating on the behaviors of SPIONs in biological environments can also be further investigated.

CHAPTER 7

CURRICULUM VITAE OF THE AUTHOR

LIST OF PUBLICATIONS

Chapter Index	
	pag.
7.1 CURRICULUM VITAE OF THE AUTHOR	159
7.2 LIST OF PUBLICATIONS	163

CURRICULUM VITAE

PERSONAL INFORMATION

Name: Si-Ming Yu

Nationality: Chinese

Email: tayiyaes@gmail.com



EDUCATIONAL BACKGROUND

- PhD in Material Science 04/10/2012-04/09/2015
Institute of Material Science of Barcelona (ICMAB-CSIC), Autonomous University of Barcelona (UAB) Campus, Spain
Supervisor: Dr. Anna, Roig and Dr Anna, Laromaine
- Master in Engineering 01/09/2009-01/07/2012
Department of Light Industry and Food Science, South China University of Technology (SCUT), China
Supervisor: Prof. Shu-Juan Yu
- Bachelor in Engineering 01/09/2005-01/07/2009
Department of Food Science and Engineering, Jiangxi Agricultural University (JXAU), China

TECHNICAL EXPERIENCE

Nanotechnology: Synthesis of gold nanoparticles (Au NPs), iron oxide (SPIONs) and Au nanotriangles-SPIONs nanocomposites with tunable size and structure, and their surface functionalization for safe biomedical applications.

Immunoassay Technology: Preparation of fluorescent latex labeled immunochromatography test strip for rapid detection. Protein coupling technology (covalent binding with nanoparticles).

Food Science Technology: Extraction and purification of nature products (e.g. dihydromyricetin, flavone).

Characterization: Scanning electron microscopy (SEM), Electronic transmission microscopy (TEM), Cryo-TEM, HR-TEM, negative staining TEM, optical microscopy, dynamic light scattering (DLS), infrared spectroscopy (FTIR/ATR), differential centrifugal sedimentation (DCS), isothermal titration calorimetry (ITC), UV-Vis spectroscopy, fluorescent spectroscopy, high performance liquid chromatography (HPLC), X-ray diffraction (XRD), X-ray photoelectron spectroscopy (XPS), atomic flame spectrometry, superconducting quantum interference device (SQUID).

PROJECTS PARTICIPATED

1. "Advanced preparation techniques of nanoparticles and their biomedical and environmental assessment" (AdvancedNP). **MAT201235324** (01/2013-12/2015), Responsible Dr Anna Roig.
2. "Rational design of hybrids organic- inorganic interfaces: the next step towards advanced functional materials." **Cost Action MP1202** (2013-2016). Responsible Dr. Marie Helene Delville.
3. "Study on formation mechanism and reaction process control of maillard product HMF and 4-MeI". **National Natural Science Foundation** (01/2013-12/2016), Responsible Prof. Shu-Juan Yu.

PUBLICATIONS

IN PREPARATION

1. **S-M Yu**, M Milla, L Gonzalez, C Minelli, A Laromaine* and A Roig*. The role of BSA in nano-bio-interface: from its adsorption mechanism to its biological effects. In preparation, 2015.
2. M Milla, **S-M Yu**, A Laromaine* and A Roig*. Exposed cell surface influence cell toxicity, morphology and uptake upon SPIONs exposure. In preparation, 2015.

SUBMITTED

3. L Gonzalez, **S-M Yu**, E Carezza, A Laromaine* and A Roig*. Protective effects of BSA adsorption onto superparamagnetic iron oxide nanoparticles in the nematode *Caenorhabditis elegans*. Submitted, 2015.
4. M Borges, **S-M Yu**, A Laromaine, A Roig, D Ruiz-Molina* and F Novio*. Dual T1/T2 contrast agent for MRI based on coordination polymer-SPION hybrid nanomaterial. Submitted, 2015.

PUBLISHED

5. **S-M Yu**, A Laromaine* and A Roig*. Magnetic gold nanotriangles by polyol synthesis. *Nanoscale*, accepted, 2015. (IF 7.394)
6. L Gonzalez[‡], **S-M Yu**[‡], A Laromaine* and A Roig*. ([‡] **Equal contribution**). Scale up synthesis of iron oxide nanoparticles by microwave-assisted thermal decomposition. *Chemical Engineering Journal*, in press, 2015. (IF 4.321)
7. **S-M Yu**, A Laromaine* and A Roig*. Enhanced stability of superparamagnetic iron oxide nanoparticles in biological media using a pH adjusted-BSA adsorption protocol. *Journal of Nanoparticle Research*, 2014, 16: 2484. (IF 2.9)
8. Y-G Guan, S-L Wang, S-J Yu*, **S-M Yu** and Z-G Zhao. Changes in the initial stages of a glucose-proline Maillard reaction model system influences dairy product quality during thermal processing. *Journal of Dairy Science*, 2012, 95 (2): 590-601. (IF 2.55)
9. **S-M Yu**, Y-P Peng, S-J Yu* and H Lv. FTIR Analysis the Impact of Covalent Coupling on the Secondary Structure of Antibody Protein. *Spectroscopy and Spectral Analysis*, 2012, 32(3): 630-634. (IF 0.84)
10. **S-M Yu**, Y-P Peng, S-J Yu* and H Lv. Interaction between antibody protein and latex microspheres revealed by fluorescence spectroscopy. *Spectroscopy and Spectral Analysis*, 2012, 32 (8) 2166-2170. (IF 0.84)
11. **S-M Yu**, S-M Zhu, Shu-Juan Yu*, J-C Lin and M Xu. Effects of Coordination on the Crystallization Structure and the Anti-oxidation Activity of DMY (written in Chinese with English abstract). *Chinese Journal of Food Science*, 2011, 32: 34-37.

GRANTED PATENTS

1. S-J Yu*, **S-M Yu**, X-L Wu and Y-G Guan. Preparation of Immunochromatography test strip for quickly and quantitatively detecting hydroxymethylfurfural, **2014**. Priority number CN20111228315 20110810, publication number: CN 102384973 B, granted data: 10/09/2014.
2. S-J Yu*, **S-M Yu**, X-L Wu and Y-G Guan. Synthesis method of 5-hydroxymethylfurfural complete antigen, **2014**. Priority number CN20111228269 20110810, publication number: CN 102382189 B, granted data: 02/04/2014.
3. S-M Zhu*, **S-M Yu**, S-J Yu, Y-J Yang and Z-J Chen. Method for preparing inorganic potassium salt based on sugar making diethyl ether and dilute juice desalination, **2012**. Priority number CN20111228269 20110810, publication number: CN102319592 B, granted data: 05/12/2012.

CONFERENCES

1. Scientific Workshop on Hybrid Interfaces (COST Action 1202): Biomedical, Health and Bio-Related applications of Hybrid Materials.

8th - 9th, June, 2015, Barcelona, Spain.

Poster: “Bovine serum albumin functionalization enhances nanoparticles’ stability in biological environments and modifies their interaction with cells”. **S-M Yu**, M Milla, A Laromaine* and A Roig*.

2. Training school (COST Action 1202): Bottom-up Approaches of Hybrid Materials: Preparation and Design.

26th – 28th, May, 2015, Ljubljana, Slovenia.

Poster: “Microwave fast synthesis of inorganic hybrid nanocomposites: SPIONs decorated gold nanotriangles”. **S-M Yu**, A Laromaine* and A Roig*.

3. 1st Scientific Meeting of PhD students of Barcelona Nanotechnology Cluster.

20th – 21st, May, 2015, Barcelona, Spain.

Oral presentation: “The role of BSA in nano-bio-interface: from adsorption mechanism to its biological effects”. **S-M Yu**, M Milla, A Laromaine* and A Roig*.

4. 3rd International Workshop on NANOMEDICINE

27th November, 2014, Autonomous University of Barcelona (UAB), Bellaterra, Barcelona, Spain.

Poster: “The presence of a bovine serum albumin monolayer modifies the interaction of superparamagnetic iron oxide nanoparticles with cells”. **S-M Yu**, M Milla, A Laromaine* and A Roig*.

5. NANOSELECT ANNUAL MEETING

June 25th - 27th, 2014. Sant Feliu de Guíxols, Girona, Barcelona, Spain.

Oral presentation: “Enhanced stability of superparamagnetic iron oxide nanoparticles in biological media via BSA adsorption”. **S-M Yu**, A Laromaine* and A Roig*

6. 4th International Colloids Conference: Surface Design and Engineering

15th -18th June 2014, Madrid, Spain.

Poster: “Enhanced stability of superparamagnetic iron oxide nanoparticles in biological media using a pH adjusted-BSA adsorption protocol”. **S-M Yu**, A Laromaine* and A Roig*

7. Summer Training School: Magnetic particle based platforms and bioassays

30th June – 3rd July. Autonomous University of Barcelona (UAB), Barcelona, Spain.

8. International Doctoral School in Functional Material (IDS-FM): 4th Training School and Annual Meeting

16th-21st, March 2014, Spa, Belgium.

Oral presentation: **S-M Yu**, A Laromaine* and A Roig*

9. 2nd International Workshop on NANOMEDICINE

10th October, 2013, Autonomous University of Barcelona (UAB), Bellaterra, Barcelona, Spain.

Poster: “Characterization of nanoparticle-protein interaction by dynamic light scattering”. **S-M Yu**, A Laromaine* and A Roig*

10. International Magnetic Nanocontainers for Combined Hyperthermia and Controlled Drug Release Workshop.

20th-22nd, February, 2013, Barcelona, Spain.

HONORS AND AWARDS:

10/2012-10/2015 China Scholarship Council (CSC) Scholarship

05/2012-06/2012 Award in the 2nd Academic Paper contest of South China University of Technology

09/2011-07/2012 First-Class Scholarship of South China University of Technology

09/2008-07/2009 First-Class National Scholarship

09/2005-07/2006 First-Class Scholarship of Jiangxi Agricultural University

LANGUAGES

English: Advanced-Level 6(Common European Framework of Reference for Language-**Level C1**)

Spanish: Basic (Common European Framework of Reference for Language-**Level A2**)

Cantonese: Fluent, Chinese: Mother Language

Enhanced stability of superparamagnetic iron oxide nanoparticles in biological media using a pH adjusted-BSA adsorption protocol

Si-Ming Yu · Anna Laromaine · Anna Roig

Received: 3 February 2014 / Accepted: 23 May 2014
© Springer Science+Business Media Dordrecht 2014

Abstract Superparamagnetic iron oxide nanoparticles (SPIONs) are widely used for biological applications due to their unique properties compared to their bulk counterparts, simplified SPIONs stabilization protocols applicable for a wide spectra of biological media remains a challenging issue. In this work, SPIONs with different surface coatings, tetramethylammonium hydroxide-coated SPIONs (T-SPIONs), and citrate-coated SPIONs (C-SPIONs) were synthesized by a facile, rapid and cost effective microwave-assisted method. C-SPIONs show robust stability in biological media of phosphate buffered saline and Roswell Park Memorial Institute Medium, while destabilize in DMEM. T-SPIONs were found to aggregate rapidly and significantly in all tested media. Then, a modified pH adjusted-BSA adsorption protocol and an addition of

excess trisodium citrate dihydrate (Na₃Cit) were used to enhance their stability in the media. The BSA adsorption protocol showed great efficiency in stabilizing the dispersed state of both SPIONs in the tested media, while the addition of excess Na₃Cit showed limited effect, and it was only applicable for C-SPIONs. The formed BSA layer on SPIONs could be imaged by negative staining TEM, and revealed by Cryo-TEM, FTIR, DLS, and the zeta potential measurements. Results indicated that BSA forms a monolayer of a thickness of about 3 ± 1 nm and BSA interacts with C-SPIONs and T-SPIONs through their coating, rather than by replacing them. This synthetic method and stabilization protocol offer a general methodology to obtain SPIONs with a variety of surfactants, stable in different biological media in few minutes.

Keywords Microwave synthesis · Iron oxide nanoparticles · Biological media · Stability · Bovine serum albumin · Citrate

Electronic supplementary material The online version of this article (doi:10.1007/s11051-014-2484-1) contains supplementary material, which is available to authorized users.

S.-M. Yu · A. Laromaine (✉) · A. Roig (✉)
Institut de Ciència de Materials de Barcelona (ICMAB-CSIC), Campus de la UAB, 08193 Bellaterra, Barcelona, Spain

e-mail: alaromaine@icmab.es
URL: <http://www.icmab.es/nn>

A. Roig
e-mail: roig@icmab.es
URL: <http://www.icmab.es/nn>

Abbreviations

BSA	Bovine serum albumin
BSA- T-SPIONs	T-SPIONs after BSA adsorption
BSA- C-SPIONs	C-SPIONs after BSA adsorption
C-SPIONs	Superparamagnetic iron oxide nanoparticles coated with Na ₃ Cit
DMEM	Dulbecco's modified Eagle's medium
DMEM- Na ₃ Cit	DMEM with 10 mM Na ₃ Cit

DMEM-FBS	DMEM with 10 % FBS
DMEM-FBS- Na ₃ Cit	DMEM with 10 % FBS and 10 mM Na ₃ Cit
FBS	Fetal bovine serum
Na ₃ Cit	Trisodium citrate dihydrate
PBS	Phosphate-buffered saline
PBS- Na ₃ Cit	PBS with 10 mM Na ₃ Cit
RPMI	Roswell Park Memorial Institute Medium
RPMI- Na ₃ Cit	RPMI with 10 mM Na ₃ Cit
RPMI-FBS	RPMI with 10 % FBS
RPMI-FBS- Na ₃ Cit	RPMI with 10 % FBS and 10 mM Na ₃ Cit
SPIONs	Superparamagnetic iron oxide nanoparticles
TMAOH	Tetramethylammonium hydroxide
T-SPIONs	Superparamagnetic iron oxide nanoparticles coated with TMAOH

Introduction

In recent years, the rapid development of modern nanotechnology emerged various nanoparticles (NPs) for biomedical applications. Among these NPs, superparamagnetic iron oxide NPs (SPIONs) are extensively investigated. Besides the properties of ultra-small size and high surface area to volume ratio, their unique magnetic properties, particular surface reactivity, and excellent biocompatibility have paved the way for SPIONs to be effectively applied in biomedicine. Some of their biomedical applications are drug and gene delivery, hyperthermia therapy, magnetic resonance imaging, and cell separation (Grief and Richardson 2005; McBain et al. 2008; Hergt and Dutz 2007; Carenza et al. 2014a; Gupta and Gupta 2005; Pamme and Wilhelm 2006; Levy et al. 2011; Di Corato et al. 2009; Figuerola et al. 2008; Corti et al. 2008b).

To date, many methods have been developed to synthesize SPIONs, including co-precipitation (Wei et al. 2011), thermal decomposition (Sun and Zeng 2002), microemulsion (Deng et al. 2003), and microwave-assisted synthesis (Baghbanzadeh et al. 2011). Co-precipitation method is generally easy and affords high yields, but the reported SPIONs are rather

polydisperse and their crystallinity is poor (Lu et al. 2007). Although both polydispersity and crystallinity can be improved by thermal decomposition, SPIONs synthesized by this method are usually hydrophobic and sometimes with a toxic surface coating which hampers their applications in bio-related fields. The yield in microemulsion method is the lowest compared to other methods, and also it requires large amount of solvents, which indicates it is a poor efficient method (Lu et al. 2007). Recently, microwave-assisted synthesis has gathered the interest of many researchers due to its rather simple synthetic process, homogeneity of the temperature, and high yields within short time. Moreover, SPIONs synthesized by this method usually show a high saturation magnetization value and low surface reactivity. (Pascu et al. 2012).

Biomedical applications of SPIONs, or NPs in general, involve inevitably the contact with biological fluids, which are media with high ionic strength and/or various biomolecules. One main issue that researchers face is the stability of NPs in those complex biological media. Due to the interaction with the biological media, NPs tend to destabilize and undergo to aggregation processes, leading to the significant increase in their hydrodynamic size, as well as changes in NPs surface properties in terms of shape, surface area, and charge. (Pratten and Lloyd 1986; Sager et al. 2007; Ji et al. 2010; Metin et al. 2011; Safi et al. 2010). Recent studies also evidenced that some biological responses greatly depend on the behavior of NPs in the biological media; the change in NPs hydrodynamic size probably influence their final bio-distribution and trigger desirable or deleterious biological responses. (Safi et al. 2010, 2011; Petri-Fink et al. 2008; Butoescu et al. 2009; Kah et al. 2012; Carenza et al. 2014b). Moreover, the aggregation and sedimentation in biological conditions could possibly affect the in vitro and in vivo toxicity assessments of NPs, and introduce problems of irreproducibility, difficulty interpreting the toxicity results, inaccurate determination of the dose for potential treatments, and the reduced diagnostic efficiency (Petri-Fink et al. 2008; Butoescu et al. 2009). For these reasons, improving the stability of NPs in biologically relevant environments and establishing generalized protocols are of great importance and a major challenge.

In the last decades, many efforts were made to ensure stable NPs dispersions for in vitro or in vivo applications. A common used strategy to stabilize

them is the functionalization of their surface using polymers or surfactants. Polyethylenimine (PEI), for example, as reported in many researches, is a well-known polymer that stabilizes efficiently NPs (Corti et al. 2008a; Hoskins et al. 2012), as well as polyethylene glycol (PEG), chitosan, dextran, citrate are other examples. (Kim et al. 2001; Janes et al. 2001; Liu et al. 2011; Safi et al. 2011). The choice of surfactant undoubtedly needs to be carefully evaluated to avoid any potential toxicity to cells and interference in the interpretation of NPs cytotoxicity. (Ji et al. 2010; Kircheis et al. 2001). Moreover, in many cases, functionalization of NPs is not sufficient for their biological application purpose; the resulting NPs are stable in biological relevant media only for few hours. Wiogo et al. (2012) showed that although the surface of SPIONs was modified by polymethacrylic acid, polyethylenimine, and branched oligoethylenimine, they aggregated and precipitated in biological media, despite the highly positively or highly negatively charged surface of the SPIONs.

Bovine serum albumin (BSA) is the most abundant protein in serum and one of the most important components in biological culture media. It has been reported as an efficient stabilizing agent to keep the dispersing state of several types of NPs in biological media, including gold NPs (Brewer et al. 2005; Dominguez-Medina et al. 2013), carbon nanotube (Porter et al. 2008), and titanium dioxide (Ji et al. 2010). Recently, a pH adjustment protocol was proposed by Guiot (Guiot and Spalla 2012) to stabilize TiO₂-NPs with different surface coatings in biological media, where the pH of TiO₂-NPs was first adjusted before adsorption of bovine serum albumin. As a result, the protocol showed robust ability in stabilizing TiO₂-NPs in LB media (Lysogeny broth media, which is primarily used for the growth of bacteria). Meanwhile, other works demonstrated that addition of excess trisodium citrate (Na₃Cit), one of the widely used additive in food and drug industry, into biological media could also stabilize SPIONs dispersions (Euliss et al. 2003; Luciani et al. 2009). These findings provide novel ways of further enhancing the dispersion stability of SPIONs in complex biological media.

In the present work, water-dispersable tetramethylammonium hydroxide (TMAOH)-coated SPIONs (T-SPIONs) and citrate-coated SPIONs (C-SPIONs) were synthesized in a facile, rapid, cost-effective, and energetically favorable manner using microwave-

assisted method (MW). To the best of our knowledge, C-SPIONs were the first time synthesized by this method. The obtained T-SPIONs and C-SPIONs were stabilized by adding BSA on their surface, which significantly enhanced their stability, with no aggregation phenomenon detected in 24 h. Such stabilization protocol offers a fast and facile general methodology to obtain stable SPIONs in different biological media.

Materials and methods

Materials

Iron (III) acetylacetonate (Fe(acac)₃, ≥97.0 %), tetramethylammonium hydroxide (TMAOH, 25 wt% in H₂O), trisodium citrate dihydrate (Na₃Cit), bovine serum albumin (BSA, ≥98 %), and phosphate-buffered saline (PBS, 1×) were purchased from Sigma-Aldrich. Roswell Park Memorial Institute medium (RPMI), Dulbecco's Modified Eagle's Medium (DMEM), and fetal bovine serum (FBS) were obtained from Invitrogen. Benzyl alcohol was obtained from Scharlau. Acetone was bought from Panreac. If not stated otherwise, all materials were used as received.

Microwave (MW)-assisted synthesis of SPIONs

MW-assisted method was used to synthesize pristine SPIONs in a CEM Discover reactor (Explorer 12-Hybrid) at a frequency of 2.45 GHz and 300 W. The synthesis process is slightly modified from Pascu et al. (2012). Briefly, 0.35 mmol Fe(acac)₃ was dissolved completely in 4.5 mL anhydrous benzyl alcohol in a special MW-tube and vortexed for 30 s. Reaction tubes were transferred to the microwave reactor; the heating ramp was 5 min at 60 °C and 10 min reaction at 180 °C, and further cooled down to 50 °C in 3 min using compressed nitrogen.

Synthesis of T-SPIONs

20 μL 25 wt% TMAOH was added to each MW-tube and sonicated for 1 min. Then the solution of SPIONs is divided into 2 equal parts in 50 ml centrifugal tubes. Each tube was filled with acetone and centrifuged at 6,000 rpm for 30 min. After removing the supernatant, 20 μL 25 wt% TMAOH was added to each tube

and sonicated for 1 min; SPIONs were then washed and centrifuged three times. Collected SPIONs pellets were dried completely in a 60 °C oven overnight and redispersed in 2 mL MQ H₂O containing 10 µL 25 wt% TMAOH; pH of the obtained T- SPIONs colloidal dispersion was about 11.

Synthesis of C-SPIONs

150 µL 10 wt% Na₃Cit was added to each reaction MW-tube and sonicated for 1 min. Then, the solution of SPIONs is divided into 2 equal parts in separate 50 mL centrifugal tubes. Each centrifugal tube was filled up to 50 mL with acetone to wash the SPIONs, and the tubes were then subjected to centrifugation at 6,000 rpm for 30 min. After removing the supernatant, 150 µL 10 wt% Na₃Cit was added to each centrifugal tube and sonicated for 1 min. SPIONs were washed and centrifuged again under the same conditions. Collected SPIONs pellets were dried completely in a 60 °C oven overnight, and redispersed in 2 mL MQ H₂O; pH of the obtained C- SPIONs colloidal dispersion was about 8.3.

Modified pH adjusted and BSA adsorption protocol

A modified pH adjusted and BSA adsorption protocol based on Guiot et al. was used (Guiot and Spalla 2012). Briefly, synthesized C-SPIONs and T-SPIONs were diluted to 2 mg/mL SPIONs dispersions in MQ H₂O. BSA solutions with a concentration of 0.5, 1, 2, 5, 10, and 15 % (w/v) were also prepared in MQ H₂O. For C-SPIONs, the pH of C-SPIONs was first adjusted to 11 by adding 0.01 M NaOH, and then equal volumes of 2 mg/mL C-SPIONs dispersion and BSA solution were mixed rapidly and stirred on a vortex for 10 min. Finally, pH of the mixture was adjusted to 7.4 (physiological pH value) by adding 0.05 mM HNO₃ solution. As a result, 1 mg/mL BSA-C-SPIONs dispersion was obtained. The stability of the SPIONs dispersions after BSA addition was evaluated by dynamic light scattering (DLS) and Cryo transmission electron microscopy (Cryo-TEM).

For T-SPIONs, since the pH of T-SPIONs was already 11, we directly mixed equal volume of 2 mg/mL T-SPIONs dispersion and BSA solution and incubated for 10 min, and then pH of the mixture was adjusted to 7.4. As a result, 1 mg/mL BSA-T-SPIONs dispersion was obtained.

Stability of the obtained BSA-T-SPIONs and BSA-C-SPIONs dispersions in biological media

50 µL of 1 mg/mL BSA-T-SPIONs or BSA-C-SPIONs was added to 0.95 mL biological media, mixed and vortexed, and then diluted BSA-C-SPIONs or BSA-T-SPIONs dispersions in biological media at a SPIONs concentration of 50 µg/mL. Dynamic light scattering was used to monitor the stability of the prepared BSA-T-SPIONs and BSA-C-SPIONs dispersions in biological media during 24 h. It is noteworthy that the tested period of stability of BSA-T-SPIONs and BSA-C-SPIONs, as well as T-SPIONs and C-SPIONs in biological media was set at 24 h, because in vitro toxicity assessment of NPs, in general, reports an incubation time of NPs with cells up to 24 h (Soenen et al. 2011).

Characterization

DLS measurements

DLS measurements were performed to monitor the changes of SPIONs in the hydrodynamic diameter (Dh), polydispersity Index (PDI), and diffusion coefficient, which are all relevant to the stability of SPIONs dispersions over time.

Dh of the C-SPIONs and T-SPIONs was determined by using a Zetasizer Nano ZS (Malvern) device with a He/Ne 633 nm laser at 25 °C and at a SPIONs concentration of 50 µg/mL. For each sample, three independent measurements were performed with 15 scans for each measurement.

Zeta potential measurements

Zeta potential was carried out to determine the changes of SPIONs in electrophoretic mobility (EPM) and zeta potential (ζ) on a Zetasizer Nano ZS (Malvern) apparatus with a zeta potential analyzer software. SPIONs solutions were placed in a disposable plastic cuvette, followed by collecting experimental data automatically. For each measurement, 20 cycles were collected, and at least 3 independent measurements were performed for each sample.

Attenuated total reflectance Fourier transformed infrared spectra measurements (ATR-FTIR)

ATR-FTIR was performed on a Spectrum RX1 FTIR Spectrometer (Perkin Elmer, USA), in the frequency range 4,000–400 cm^{-1} with a resolution of 4 cm^{-1} . All SPIONs samples were isolated from the solution by centrifugation, dried completely in the oven, and placed on the crystal surface of the ATR-FTIR machine for measurements.

TEM

Size distribution, morphology, and diffraction patterns of C-SPIONs and T-SPIONs were collected in JEOL JEM-1210 electron microscope at an operating voltage of 120 kV. TEM samples were prepared by placing one drop of the corresponding SPIONs dispersion on the copper grid for few seconds, blotting the copper grid with a filter paper and evaporate it completely at room temperature. Typically, about 200–300 different SPIONs were counted to depict the size distribution and the mean size of SPIONs.

Cryo-TEM

Samples for Cryo-TEM were prepared according to the method described by Hondow. (Hondow et al. 2012). Briefly, 3 μL of 50 $\mu\text{g}/\text{mL}$ BSA-C-SPIONs (diluted 20 times in MQ H_2O) was placed on a glow discharge-treated carbon support film (R1.2/1.3 Quantifoil Micro Tools GmbH), blotted and plunge frozen in liquid nitrogen, and then samples were subsequently transferred to a Gatan 626 cryo-holder stored in liquid nitrogen. Cryo-TEM measurement was performed on a JEOL 2011 electron microscope at a temperature of about -170°C and 200 kV acceleration voltage.

Negative staining TEM

Adsorption of BSA on T-SPIONs and C-SPIONs was visualized by performing negative staining TEM. (Ye et al. 2006) Briefly, BSA-T-SPIONs or BSA-C-SPIONs were purified from the excess BSA solution by centrifugation at 10,000 rcf for 3 h and redispersed in MQ H_2O . (Casals et al. 2010) Then one drop of the purified BSA-C-SPIONs was placed on a carbon-coated grid and then drained off with filter paper. Subsequently, 5 μL of 2 % uranyl acetate was placed

on the grid for 1 min before drained off. The grid was then placed in a 2011 JEOL electron microscope.

Results and discussion

Synthesis and characterization of C-SPIONs and T-SPIONs

In the present work, C-SPIONs were synthesized for the first time by a facile, rapid, cost effective, and energetically favorable microwave-assisted method, modifying the previously reported for T-SPIONs (Pascu et al. 2012). In this method, bare SPIONs were first synthesized in benzyl alcohol by a single-step microwave heating method, followed by coating the SPIONs surface with citrate and TMAOH ligands, respectively.

Figure 1a shows representative TEM images of the as-synthesized spherical T-SPIONs and C-SPIONs. Particle size histograms of T-SPIONs and C-SPIONs (Fig. 1b) indicate the high monodispersity of both SPIONs, with an identical SPIONs core of 6 ± 1 nm. Selected area electron diffraction (Fig. 1c) reveals the crystallinity of both SPIONs. The electron diffraction rings correspond to (220), (311), (400), (422), (511), and (440) planes, and they indicate the inverse spinel structure (magnetite, maghemite) of C-SPIONs and T-SPIONs. DLS intensity-weighted size distributions further evidenced the monodispersity of SPIONs (Fig. 1d), with D_h of about 26 ± 1 nm for T-SPIONs and 14 ± 1 nm for C-SPIONs. Zeta potential values for T-SPIONs and C-SPIONs are -54 and -36 mV, respectively (see Supporting Information Tables S1, S2), indicating both T-SPIONs and C-SPIONs are charged negative.

FTIR spectrum of T-SPIONs and C-SPIONs presents adsorption bands at $620\text{--}635$ cm^{-1} , respectively (Fig. 2A-c, B-c); these bands are attributed to the Fe–O stretching vibration, evidencing the existence of magnetite (Namduri and Nasrazadani 2008). Typical band for TMAOH at 944 cm^{-1} (Fig 2A-a), characteristic of the asymmetric methyl deformation mode of C–N on TMAOH (Ouasri et al. 2002), was found to shift to 975 cm^{-1} (Fig. 2A-c), indicating the existence of TMAOH on T-SPIONs. Peaks at $1,570\text{--}1,450$ cm^{-1} (Fig. 2B-a) are characteristic of the RCO_2 symmetric and asymmetric stretches (Sasidharan et al. 2013), though both peaks show a slight shift from $1,579$ to $1,415$ cm^{-1} (Fig 2B-c), respectively, suggesting citrate ligand is present on the SPIONs surface.

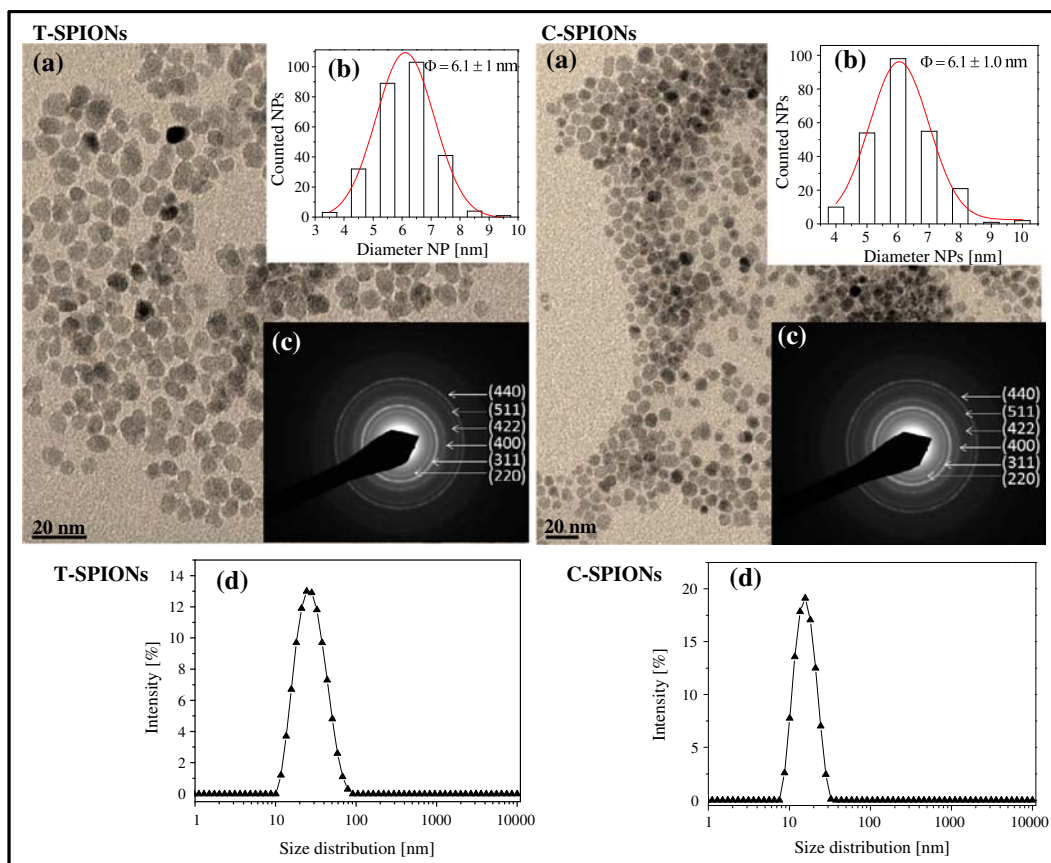


Fig. 1 **a** TEM images, **b** particle size histogram, **c** electron diffraction, and **d** DLS intensity-weighted size distribution of T-SPIONs and C-SPIONs

Stability of T-SPIONs and C-SPIONs in biological media

In the present investigation, stability of T-SPIONs and C-SPIONs was assessed in biologically relevant media, PBS, RPMI, and DMEM, at a SPIONs concentration of 50 $\mu\text{g}/\text{mL}$. We chose PBS, RPMI,

and DMEM since they are media extensively used in *in vitro* toxicity and stability assays of SPIONs and differ significantly in their ionic strength and salt content like Ca^{2+} and Mg^{2+} . The salt content in terms of Ca^{2+} concentration, for example, follows the order of $\text{PBS} < \text{RPMI} < \text{DMEM}$, with a value of 0, 0.4, and 1.8, respectively (Lee et al. 2002).

Fig. 2 **A** FTIR spectrum of *a* TMAOH, *b* BSA, *c* T-SPIONs, and *d* BSA-T-SPIONs; **B** FTIR spectrum of *a* Na_3Cit , *b* BSA, *c* C-SPIONs, and *d* BSA-C-SPIONs

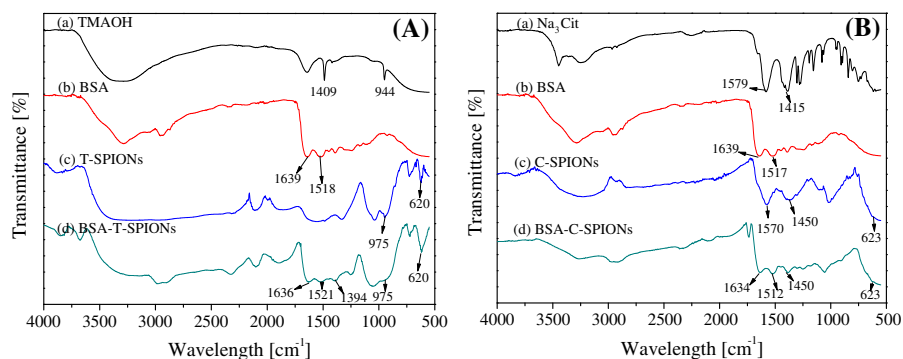


Figure 3 shows the Dh evolution of T-SPIONs and C-SPIONs in H₂O and in different biological media as a function of time. Both SPIONs show good stability in H₂O since Dh does not change up to 3 months (data not shown); this is attributed to the highly negative-charged surface of both SPIONs. When incubated in biologically relevant media, however, T-SPIONs destabilized and precipitated rapidly (Fig. 3a). In all the cases, a similar behavior is observed. Dh of T-SPIONs in RPMI, for instance, goes up sharply from 25 nm to about 2,800 nm in 2 min, and subsequently T-SPIONs precipitated. Moreover, the addition of 10 % FBS to RPMI and DMEM media could not prevent the sedimentation of T-SPIONs, as Dh of T-SPIONs in RPMI-FBS and DMEM-FBS shows an increase within 10 min. Consistent with the dramatic increase in Dh, significant decrease in diffusion coefficient, obvious increase in zeta potential (ζ), and electrophoretic mobility (EPM) were also detected (Supporting Information Table S1), confirming the destabilization of T-SPIONs in these media. On the other hand, C-SPIONs displayed a different aggregation behavior in these biological media. C-SPIONs show excellent stability in PBS and RPMI, as Dh remains unchanged up to 24 h (Fig. 3b). C-SPIONs in DMEM, unfortunately, just show a transient stability. Dh unchanged in the first initial 1 h, although increased rapidly to about 250 nm in the following 1 h, and reached up to 2,800 nm in 4 h. In RPMI-FBS and DMEM-FBS, Dh of C-SPIONs shows a slight increase in the initial 30 min and remains flat in the later time, also suggesting the good stability of C-SPIONs in the serum containing media; the slight increase in both cases could be interpreted as the adsorption of serum proteins on the surface of C-SPIONs. Changes in diffusion coefficient, zeta potential (ζ), and EPM (Supporting Information Table S2) further confirm these findings.

From the above results, we can see clearly that C-SPIONs show better stability than T-SPIONs in biological media, then it could be concluded that surface coating greatly influences the stability of SPIONs in these media. Although both T-SPIONs and C-SPIONs show highly negative-charged surface, the adsorption mechanism of TMAOH and citrate ligands on SPIONs surface is quite different. For T-SPIONs, TMAOH cations adsorb onto SPIONs surface through electrostatic interaction and this results in an electrostatic double layer which provides stability for

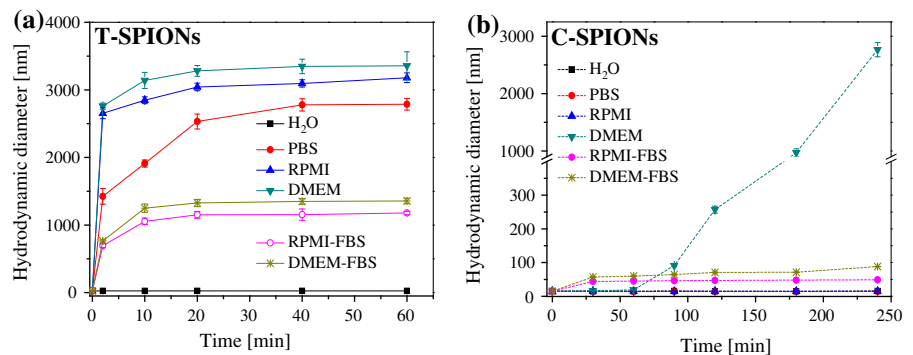
SPIONs in aqueous solution (Euliss et al. 2003). However, this electrostatic double layer can be easily disassembled by the species in biological media like salts and biomolecules. As for C-SPIONs, the three carboxylate groups of citrate ligand have strong coordination affinity to Fe(III) ions; some of the carboxylate groups strongly coordinate to SPIONs surface; the rest carboxylate groups extend into the water, providing a more robust coating and higher stability to SPIONs in H₂O and even in some complex media like PBS and RPMI (Nigam et al. 2011).

The stability and aggregation behavior of SPIONs in biological media were reported to be not only dependent on the SPIONs surface coating, but also on the nature of the surrounding media (Petri-Fink et al. 2008; Eberbeck et al. 2010). Some research reported that NPs aggregate and sediment immediately when exposed to biological media (Wells et al. 2012; Allouni et al. 2009; Geppert et al. 2012), where high ionic strength was considered an important factor to cause the NPs aggregation. When NPs are in contact with these media, surface charges on their surface were suppressed by the high ionic strength of salts presented in these media, decreasing the electrostatic repulsion significantly and subsequently precipitating the NPs (Casals et al. 2010; Wiogo et al. 2012). In particular, Safi M. and coworkers found that the divalent calcium and magnesium cations presenting in the cell media significantly reduce the stability of the C-SPIONs through the complex reaction with the citrate ligands (Safi et al. 2011). Similar significant aggregation phenomenon happened to our synthesized T-SPIONs in biological media and C-SPIONs in DMEM, despite the highly negatively charged surface of both T-SPIONs and C-SPIONs. This suggests that the surface coating of C-SPIONs and T-SPIONs is not enough to maintain their stability when exposed to biologically relevant media with high salts content, which could in turn limit their biological applications. Thus, improvement of the stability of SPIONs in biologically relevant media is of significant importance.

Stabilization of T-SPIONs and C-SPIONs in biological media with a pH adjusted and BSA adsorption protocol

To improve further the stability of T-SPIONs in biological media and C-SPIONs in DMEM, we

Fig. 3 Stability of **a** T-SPIONs and **b** C-SPIONs in H₂O, PBS, RPMI-FBS, and DMEM-FBS in terms of Dh as a function of time



adsorbed BSA to the SPIONs. The adsorption of BSA on NPs surface could offer higher stability and biocompatibility rather than using strategies as poly (methyl methacrylate) (PMMA), PEI, or other organic layers (Khullar et al. 2012; Dominguez-Medina et al. 2013). In particular, a modified pH adjusted and BSA adsorption protocol based on that proposed by Guiot (Guiot and Spalla 2012) was used in this work to modify the T-SPIONs and C-SPIONs.

The protocol presented by Guiot et al. (Guiot and Spalla 2012) was in fact based on the colloidal stability theory, in particular the DLVO theory, which indicates electrostatic repulsion force, rather than Van der Waals attraction force is responsible for the colloidal stability of NPs dispersions. In other words, once the electrostatic repulsion increased, the stability of the NPs dispersions improved. Following this principle, we first adjusted the pH of SPIONs at 11 where SPIONs and BSA exhibit a net charge of identical sign, and then we added BSA to the SPIONs dispersion. BSA with a negative net charge at pH 11 can still be attached to the negative charge NPs due to the intrinsic amphiphilic character of the protein as reported previously. (Brewer et al. 2005; Wiogo et al. 2012) The addition of enough BSA in the SPIONs solutions allows the coverage of the SPIONs while maintaining its stability. The BSA coverage avoids the aggregation of the SPIONs solutions once we change the solutions to physiological pH. (Dominguez-Medina et al. 2013)

The pH of the synthesized C-SPIONs was first adjusted to 11 by adding 0.1 M NaOH (pH of synthesized T-SPIONs was already 11). At pH 11, the zeta potential measurement of BSA and C-SPIONs decreased from -22 mV (pH 7.4) to -28 and -36 mV (pH 8.3) to -42 mV, respectively. Then,

SPIONs dispersions were incubated with BSA solution for 10 min, and then pH of the mixture was adjusted to the physiological value of 7.4. BSA-T-SPIONs and BSA-C-SPIONs dispersions prepared are extremely stable due to the electrostatic repulsion among them and the BSA coverage on the SPIONs surface.

50 μ L of the obtained BSA-T-SPIONs and BSA-C-SPIONs (1 mg/mL) was diluted 20 times in water to a final concentration of 50 μ g/mL, and their stability was monitored by DLS over 24 h. DLS intensity-weighted size distributions (Supporting Information Fig. S1a, 4a), Dh, diffusion coefficient, and diffusion time remain unchanged over 24 h (Supporting Information Tables S3, S4), implying high stability of the prepared BSA-T-SPIONs and BSA-C-SPIONs dispersions over time. In the DLS measurement, there is no peak observed at 8 nm, from the excess of BSA, confirming that the 20 times dilution decreases the BSA content in the samples. Different literature suggest the existence of two layers contributing to the stabilization of NPs with BSA: the hard protein corona, strongly interacting with the NPs surface and the soft protein corona, BSA molecules loosely bounded to the BSA-NPs. (Casals et al. 2010). Therefore, the dilution of our samples and the excess of the BSA could contribute to the stabilization of the NPs. Cryo-TEM is a potential technology that provides a representative view of the real dispersing state of NPs in solution, therefore, Cryo-TEM measurements were also performed to reveal the stability of the obtained BSA-C-SPIONs, as it is shown in Fig. 4b. BSA-C-SPIONs exist in the solution as small aggregates but well separated from each other, suggesting the well dispersing state of BSA-C-SPIONs in solution even after 24 h incubation; this might due to the

Fig. 4 **a** DLS intensity-weighted size distributions of C-SPIONs (control) and the prepared BSA-C-SPIONs at an evaluated time of 1, 4, 6, and 24 h in water; **b** Cryo-TEM image of the prepared BSA-C-SPIONs after 24 h preparation

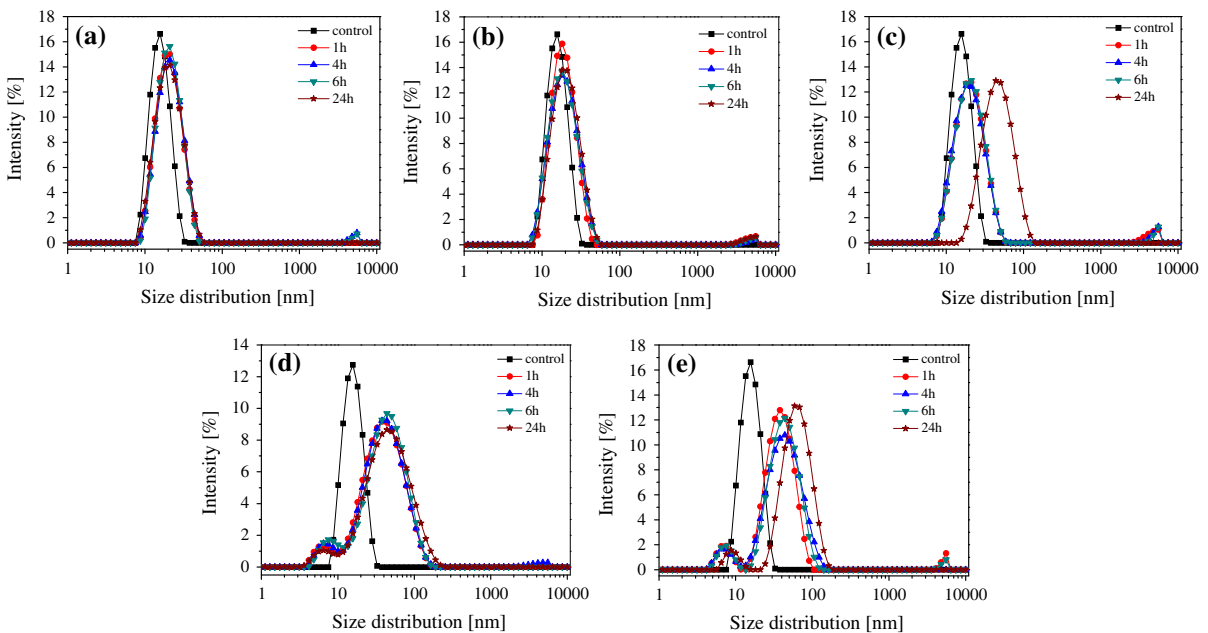
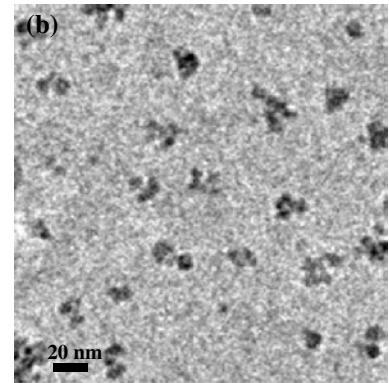
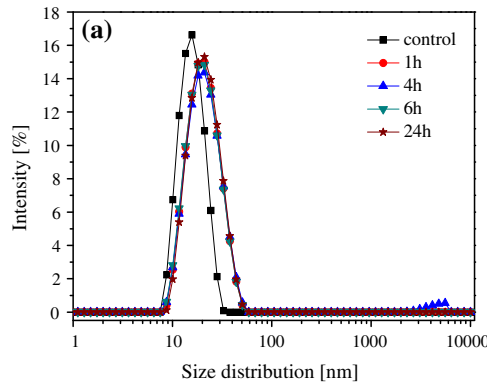


Fig. 5 DLS intensity-weighted size distributions of C-SPIONs (control) and BSA-C-SPIONs **a** PBS; **b** RPMI; **c** DMEM; **d** RPMI-FBS; and **e** DMEM-FBS at an evaluated time of 1, 4, 6, and 24 h

electrostatic repulsion provided by their negative-charged surfaces.

To test the practical effect of our protocol, we evaluated the stability of BSA-T-SPIONs and BSA-C-SPIONs in PBS, RPMI, and DMEM. First, they were diluted 20 times to a final BSA-SPIONs concentration at 50 µg/mL with the appropriate media, and we monitored their aggregation evolution using DLS over 24 h. BSA-T-SPIONs and BSA-C-SPIONs are well dispersed and stable in PBS, without any increase in Dh observed over the tested period, as well as the diffusion coefficients and diffusion times (Fig. 5a,

Supporting Information Figs. S1b, S2a; Tables S5, S6).

Stability of BSA-T-SPIONs and BSA-C-SPIONs 50 µg/mL solutions in RPMI and DMEM, which have higher salt content compared to PBS, was tested. Intensity-weighted size distributions of BSA-T-SPIONs in RPMI and DMEM show a gradual shift toward larger size as incubation time increased; Dh increases from 24 nm to 100 nm in RPMI over 24 h and to 220 nm in RPMI (Supporting Information Fig. S1c, d). The increase in Dh is also confirmed by the decreased diffusion coefficient and the increased diffusion time

(Supporting Information Tables S7, S8). Although BSA-T-SPIONs increased in size in RPMI and DMEM, the present size is still desirable for in vitro toxicity studies when compared to the rapid and significant aggregation behavior of the synthesized T-SPIONs in the same media. Moreover, no sedimentation appeared in 24 h for BSA-T-SPIONs in both media (Supporting Information Fig. S2a).

As expected, BSA-C-SPIONs remain extremely stable in RPMI and DMEM even after 24 h incubation. Intensity-weighted size distributions of BSA-C-SPIONs in RPMI as a function of time superimposed to each other (Fig. 5b), diffusion coefficient and diffusion time also kept unchanged (Supporting Information Table S9), indicating the identical distribution of the BSA-C-SPIONs in 24 h. Dh of BSA-C-SPIONs in DMEM only increased few nanometers (Fig. 5c), whereas synthesized C-SPIONs show dramatic aggregation, implying the robustness of the pH adjusted and BSA adsorption protocol. Slight changes in diffusion coefficient and diffusion time are found for BSA-C-SPIONs in DMEM, confirming the excellent stability. (Supporting Information Table S10)

Media for cell culture are always supplemented with serum proteins; therefore, we further tested the stability of BSA-T-SPIONs and BSA-C-SPIONs under serum conditions, RPMI-FBS and DMEM-FBS, respectively. In all these cases, DLS intensity-weighted size distributions as a function of time exhibit minor shifts in Dh, as well as slight changes in diffusion coefficient and diffusion time, which clearly precludes the possibility of aggregation or sedimentation of BSA-T-SPIONs and BSA-C-SPIONs in these media (Fig. 5d, e; Supporting Information Figs. S1e, f, S2a; Tables S11, S12, S13, S14).

In the present investigation, we also found that to endow SPIONs dispersions with sufficient stability in the biological media, the necessary concentration of BSA in the protocol varied significantly (Table 1). For both SPIONs, the necessary concentration of BSA followed the order of in DMEM > RPMI > PBS > RPMI-FBS and DMEM-FBS. We attribute this to the different compositions of these tested media. As mentioned before, the salt content in terms of Ca^{2+} concentration follows the order of PBS < RPMI < DMEM (Mg^{2+} concentration also follows the same order), and it is the divalent calcium and magnesium cations in biological media that are reported to mainly cause the SPIONs aggregation though interacting with the surface coating on the

Table 1 The necessary concentration of BSA needed for T-SPIONs and C-SPIONs in different media by using the pH adjusted and BSA adsorption protocol

SPIONs	Concentration of BSA needed (%) (w/v)				
	PBS	RPMI	DMEM	RPMI-FBS	DMEM-FBS
T-SPIONs	2	10	15	1	1
C-SPIONs	1	2	5	0.5	0.5

SPIONs surface. BSA added to the SPIONs dispersions could complex with these divalent cations, protecting the SPIONs surface by screening these divalent cations from interacting directly with the SPIONs surface, thus keeping the SPIONs stable in the tested media. Hence, in biological media with higher concentration of divalent cations, it is expected that the amount of BSA needed should be also higher. For this reason, the amount of BSA needed is the highest in DMEM, followed by RPMI and PBS. Furthermore, Ji et al. (2010) found that compositions in FBS, like globulin and transferrin, exhibit a synergistic effect on stabilizing the NPs dispersions with BSA. Therefore, in RPMI-FBS and DMEM-FBS, FBS itself served as the additional stable reagent in addition to BSA, thus the necessary concentration of BSA is the least compared to those media in the absence of 10 % FBS. The amount of FBS is clearly detected in the DLS intensity-weighted size distributions in Fig. 5d, e.

Moreover, we observed that in all the tested media, the necessary concentration of BSA needed for C-SPIONs is always lower than that for T-SPIONs. We relate this to the different surface coatings of C-SPIONs and T-SPIONs. As it was concluded before, citrate ligands exhibit stronger ability of resisting against high salt and high ionic strength than TMAOH. Previous studies also revealed nonspecific binding of BSA to self-assembled monolayers following the order of hydrophobic $>\text{COO}^- > \text{NH}_3^+ > \text{OH}^- > \text{ethylene glycol}$ (Nakata et al. 1996; Moulin et al. 1999), which indicates BSA has a preference and a higher affinity for binding to SPIONs surface with citrate ligands (with three COO^- groups per molecule) than those with TMAOH coating (with one OH^- per molecule). As a result, more BSA is envisaged to bind more effectively on C-SPIONs than on T-SPIONs under the same BSA concentration. For those reasons, using less BSA we could get the same or even better stability of C-SPIONs in biological media than T-SPIONs.

Stabilization of C-SPIONs and T-SPIONs in biological media by adding excess Na_3Cit

As a comparison, addition of excess Na_3Cit to enhance the stability of the T-SPIONs and C-SPIONs in biological media was also used, because some researches indicated its enhancing effects (Euliss et al. 2003; Luciani et al. 2009). Briefly, a solution of 50 $\mu\text{g}/\text{mL}$ SPIONs in biological media and with a 10 mM Na_3Cit were prepared and their stability was monitored by DLS over 24 h. Results show that adding 10 mM excess Na_3Cit could not prevent the aggregation of T-SPIONs in all the tested media, T-SPIONs destabilized and precipitated in 1 h (Supporting Information Fig S2b). While stability of C-SPIONs was maintained in 24 h by adding 10 mM excess Na_3Cit in DMEM as well as in the other media (Fig. 6). Dh does not show any increase in PBS- Na_3Cit within 24 h, only slight increase in RPMI- Na_3Cit and DMEM- Na_3Cit was found. In RPMI-FBS- Na_3Cit and DMEM-FBS- Na_3Cit , Dh increase to about 35 nm in the initial 1 h, and kept unchanged in the following 24 h. The increase in Dh during the beginning 1 h is due to the formation of protein corona on C-SPIONs surface, demonstrated by Walczyk (Walczyk et al. 2010) who described that protein corona on NPs surface formed in a relatively stable manner over a period of one hour.

In summary, the modified pH adjusted and BSA adsorption protocol shows excellent prospect in preparing extremely stable SPIONs dispersions in several biologically relevant media, which are desirable for reliable *in vitro* and *in vivo* toxicity assessments.

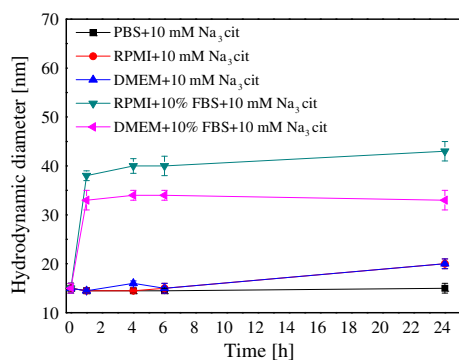


Fig. 6 The changes in hydrodynamic size of C-SPIONs in PBS- Na_3Cit , RPMI- Na_3Cit , DMEM- Na_3Cit , RPMI-FBS- Na_3Cit , and DMEM-FBS- Na_3Cit at an evaluated time of 24 h

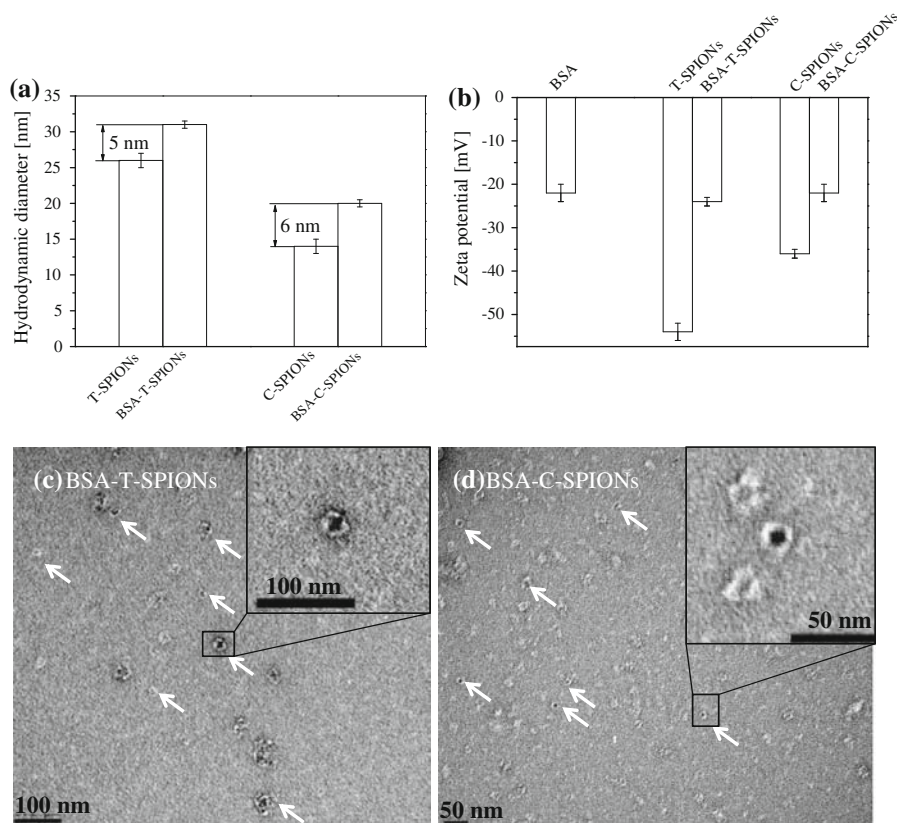
Although the addition of excess Na_3Cit could prevent C-SPIONs from aggregation in DMEM and other media, the stabilization effect is limited. Moreover, high concentration of Na_3Cit in biological media is reported to produce risky effects to the growth of the cells (Freese et al. 2012; Uboldi et al. 2009). Therefore, the modified BSA adsorption and pH adjusted protocol seems a general and more suitable method to improve the stability of SPIONs in biological media.

Characterization of BSA layer on C-SPIONs and T-SPIONs

We further characterized the binding mechanism of the BSA layer on T-SPIONs and C-SPIONs surface and the interaction mechanism of SPIONs and BSA. Figure 7a shows the changes in Dh of T-SPIONs and C-SPIONs before and after performing the pH adjusted BSA adsorption protocol. Diluted BSA-T-SPIONs show 5 nm increase in Dh and 6 nm for diluted BSA-C-SPIONs. The dimension of BSA is reported to be $(8 \times 8 \times 8 \times 3.4 \text{ nm})$ as a triangular equilateral prism (He and Carter 1992); the increase of Dh for both SPIONs after using the protocol just corresponds to the shorter dimension of BSA, and therefore, we conclude that a BSA monolayer was formed on both SPIONs surface in the form of triangular base. The result obtained here is in agreement with previous findings using BSA as a model protein and Au NPs as model NPs (Dominguez-Medina et al. 2013; Kohli et al. 2013). To provide clearer evidence of the formed BSA monolayer on SPIONs surface, we present negative staining TEM data for the purified BSA-T-SPIONs and BSA-C-SPIONs in water. Representative negative staining TEM images (Fig. 7c, d) show clear evidence of this BSA monolayer, which completely covers the both SPIONs surface. Moreover, after measuring the thickness of these images, an increase in diameter of $6 \pm 1 \text{ nm}$ was computed, which is consistent with the data obtained by DLS, suggesting a BSA monolayer with thickness about 3 nm was formed on T-SPIONs and C-SPIONs surface.

The formation of protein corona on SPIONs surface will likely change their zeta potential and the isoelectric point (IEP) (Natte et al. 2013), thus the change in zeta potential of C-SPIONs and T-SPIONs before and after performing the protocol should also evidence the BSA adsorption on their surface. The zeta potential value of

Fig. 7 **a** Hydrodynamic size and **b** zeta potential of T-SPIONs, BSA-T-SPIONs, C-SPIONs, and BSA-C-SPIONs; negative staining TEM images of **c** BSA-T-SPIONs and **d** BSA-C-SPIONs



T-SPIONs and C-SPIONs (-54 and -42 mV, respectively) increased to -24 and -22 mV for BSA-T-SPIONs and BSA-C-SPIONs, respectively (Fig. 7b).

Recent studies on the interaction of Au NPs and BSA revealed two possible mechanisms: (1) strong binding of BSA to Au NPs due to the electrostatic attraction between positive residues of BSA and negative-charged surface coating on Au NPs surface (Sen et al. 2011) and (2) the surface coating on Au NPs is removed by BSA upon absorption, amino acids on BSA, in particular cysteine, bind directly to the Au NPs surface (Brewer et al. 2005). To the best of our knowledge, the interaction mechanism of BSA and SPIONs is still poorly understood. FTIR confirmed the BSA coverage on T-SPIONs and C-SPIONs surfaces. BSA-T-SPIONs and BSA-C-SPIONs were separated from the excess BSA solution by centrifugation at 10,000 rcf for 3 h (under which condition excess BSA have been proved not to be centrifuged down (Casals et al. 2010)), dried completely and then FTIR spectra were collected. Spectra of BSA-T-SPIONs and BSA-C-SPIONs show clearly two adsorption bands at

wavelength around $1,635$ and $1,515$ cm^{-1} (Figs. 2A-d, B-d), which are characteristic of amide I and amide II bonds of proteins, further confirming the formation of BSA layer on the surface of BSA-T-SPIONs and BSA-C-SPIONs. Moreover, FTIR spectrum could help us reveal the binding mechanism of BSA onto SPIONs surface. FTIR spectrum of BSA-T-SPIONs (Fig. 2A-d) shows an adsorption band at 975 cm^{-1} ; this band is assigned to the asymmetric methyl deformation mode C-N on TMAOH (Ouasri et al. 2002), though with 30 nm shift from 944 cm^{-1} . Another band also appears at $1,394$ cm^{-1} (Fig. 2A-d), characteristic of the asymmetric methyl deformation mode of $-(\text{CH}_3)$ on TMAOH (Andrade et al. 2012). These results indicate that TMAOH ligands still exist on BSA-T-SPIONs, implying that the binding of BSA to T-SPIONs surface is through interactions with the TMAOH layer, instead of replacing it. The FTIR spectrum of BSA-C-SPIONs presents an absorption band at $1,450$ cm^{-1} (shifts from $1,415$ cm^{-1} Fig. 2B-d), characteristic of asymmetric stretches of RCO_2 of Na_3Cit (Sasidharan et al.

2013), suggesting the existence of citrate ligands on BSA-C-SPIONs. The disappearance of absorption bands at $1,579\text{ cm}^{-1}$ of Na_3Cit and band shift from $1,415$ to $1,450\text{ cm}^{-1}$ imply strong interaction of citrate group with BSA.

Therefore, we concluded that interaction between BSA and surface coating of SPIONs results in the formation of BSA monolayer on SPIONs. The additional BSA monolayer maintains the electrostatic repulsion force and the steric hindrance between each SPIONs and hence protecting them from aggregating in biological media.

Conclusion

The present work provides a facile, rapid, and cost effective microwave-assisted method to synthesize C-SPIONs with robust stability in biological media for the first time. Although with an identical SPION core, the distinct behavior of T-SPIONs and C-SPIONs in biological media implies that surface coating of SPIONs plays a very important role in determining their stability.

The use of BSA showed great efficiency in enhancing the stability of both T-SPIONs and C-SPIONs in several biological media, while the addition of excess Na_3Cit was only suitable for C-SPIONs. The necessary BSA concentration to provide sufficient stability to both SPIONs in biological media depended on the nature of the tested media, as well as the surface coating of SPIONs. FTIR, Cryo-TEM, and negative staining TEM reveal that BSA binds to T-SPIONs and C-SPIONs by interacting with TMAOH and citrate coating, forming a BSA monolayer with a thickness of about $3 \pm 1\text{ nm}$ on both SPIONs. Likely, the additional BSA monolayer preserves the electrostatic repulsion force among the SPIONs while increasing the steric hindrance between SPIONs, preventing their aggregation in biological media.

This work provides a reference for preparing stable SPIONs dispersion used for biological applications, which could lead to the development of reliable in vitro SPIONs toxicity assessments and accurate evaluation of SPIONs dosage needed for in vivo treatment.

Acknowledgments The research leading to these results has received funding from the People Program (Marie Curie Actions) of the European Union's Seventh Framework

Program (FP7/2007-2013) under REA grant agreement n° 303630 and cofunded by the European Social Fund. Authors acknowledge the funding from Spanish Ministry of Economy MAT 2012-35324, COST Action MP1202 and Ramon y Cajal grant RYC-2010-06082 (AL), China Scholarship Council fellowship (SMY, 201206150053).

References

- Allouni ZE, Cimpan MR, Høl PJ, Skodvin T, Gjerdet NR (2009) Agglomeration and sedimentation of TiO_2 nanoparticles in cell culture medium. *Colloid Surf B* 68(1):83–87. doi:10.1016/j.colsurfb.2008.09.014
- Andrade ÂL, Valente MA, Ferreira JMF, Fabris JD (2012) Preparation of size-controlled nanoparticles of magnetite. *J Magn Magn Mater* 324(10):1753–1757. doi:10.1016/j.jmmm.2011.12.033
- Baghbanzadeh M, Carbone L, Cozzoli PD, Kappe CO (2011) Microwave-assisted synthesis of colloidal inorganic nanocrystals. *Angew Chem Int Edit* 50(48):11312–11359. doi:10.1002/anie.201101274
- Brewer SH, Glomm WR, Johnson MC, Knag MK, Franzen S (2005) Probing BSA binding to citrate-coated gold nanoparticles and surfaces. *Langmuir* 21(20):9303–9307. doi:10.1021/la050588t
- Butoescu N, Jordan O, Burdet P, Stadelmann P, Petri-Fink A, Hofmann H, Doelker E (2009) Dexamethasone-containing biodegradable superparamagnetic microparticles for intra-articular administration: physicochemical and magnetic properties, in vitro and in vivo drug release. *Eur J Pharm Biopharm* 72(3):529–538. doi:10.1016/j.ejpb.2009.03.003
- Carenza E, Barceló V, Moráncho A, Levander L, Boada C, Laromaine A, Roig A, Montaner J, Rosell A (2014a) In vitro angiogenic performance and in vivo brain targeting of magnetized endothelial progenitor cells for neurorepair therapies. *Nanomed Nanotechnol* 10(1):225–234. doi:10.1016/j.nano.2013.06.005
- Carenza E, Barceló V, Moráncho A, Montaner J, Rosell A, Roig A (2014b) Rapid synthesis of water-dispersible SPIONs by microwave assisted route for safe labeling of endothelial progenitor cells. *Acta Biomater*. doi:10.1016/j.actbio.2014.04.010
- Casals E, Pfaller T, Duschl A, Oostingh GJ, Puntès V (2010) Time evolution of the nanoparticle protein corona. *ACS Nano* 4(7):3623–3632. doi:10.1021/nn901372t
- Corti M, Lascialfari A, Marinone M, Masotti A, Micotti E, Orsini F, Ortaggi G, Poletti G, Innocenti C, Sangregorio C (2008a) Magnetic and relaxometric properties of poly-ethylenimine-coated superparamagnetic MRI contrast agents. *J Magn Magn Mater* 320(14):e316–e319. doi:10.1016/j.jmmm.2008.02.115
- Corti M, Lascialfari A, Micotti E, Castellano A, Donativi M, Quarta A, Cozzoli PD, Manna L, Pellegrino T, Sangregorio C (2008b) Magnetic properties of novel superparamagnetic MRI contrast agents based on colloidal nanocrystals. *J Magn Magn Mater* 320(14):e320–e323. doi:10.1016/j.jmmm.2008.02.064

- Deng Y, Wang L, Yang W, Fu S, Elaissari A (2003) Preparation of magnetic polymeric particles via inverse microemulsion polymerization process. *J Magn Magn Mater* 257(1): 69–78. doi:10.1016/S0304-8853(02)00987-3
- Di Corato R, Piacenza P, Musarò M, Buonsanti R, Cozzoli PD, Zambianchi M, Barbarella G, Cingolani R, Manna L, Pellegrino T (2009) Magnetic-fluorescent colloidal nanobeads: preparation and exploitation in cell separation experiments. *Macromol Biosci* 9(10):952–958. doi:10.1002/mabi.200900154
- Dominguez-Medina S, Blankenburg J, Olson J, Landes CF, Link S (2013) Adsorption of a protein monolayer via hydrophobic interactions prevents nanoparticle aggregation under harsh environmental conditions. *ACS Sustain Chem Eng* 1(7):833–842. doi:10.1021/sc400042h
- Eberbeck D, Kettering M, Bergemann C, Zirpel P, Hilger I, Trahms L (2010) Quantification of the aggregation of magnetic nanoparticles with different polymeric coatings in cell culture medium. *J Phys D Appl Phys* 43(40):1–9. doi:10.1088/0022-3727/43/40/405002
- Euliss LE, Grancharov SG, O'Brien S, Deming TJ, Stucky GD, Murray CB, Held GA (2003) Cooperative Assembly of Magnetic Nanoparticles and Block Copolypeptides in Aqueous Media. *Nano Lett* 3(11):1489–1493. doi:10.1021/nl034472y
- Figuerola A, Fiore A, Di Corato R, Falqui A, Giannini C, Miccotti E, Lascialfari A, Corti M, Cingolani R, Pellegrino T, Cozzoli PD, Manna L (2008) One-pot synthesis and characterization of size-controlled bimagnetic FePt–iron oxide heterodimer nanocrystals. *J Am Chem Soc* 130(4): 1477–1487. doi:10.1021/ja078034v
- Freese C, Uboldi C, Gibson M, Unger R, Weksler B, Romero I, Couraud P-O, Kirkpatrick C (2012) Uptake and cytotoxicity of citrate-coated gold nanospheres: comparative studies on human endothelial and epithelial cells. *Part Fibre Toxicol* 9(1):23. doi:10.1186/1743-8977-9-23
- Geppert M, Petters C, Thiel K, Dringen R (2012) The presence of serum alters the properties of iron oxide nanoparticles and lowers their accumulation by cultured brain astrocytes. *J Nanopart Res* 15(1):1–15. doi:10.1007/s11051-012-1349-8
- Grief AD, Richardson G (2005) Mathematical modelling of magnetically targeted drug delivery. *J Magn Magn Mater* 293(1):455–463. doi:10.1016/j.jmmm.2005.02.040
- Guiot C, Spalla O (2012) Stabilization of TiO₂ nanoparticles in complex medium through a pH adjustment protocol. *Environ Sci Technol* 47(2):1057–1064. doi:10.1021/es3040736
- Gupta AK, Gupta M (2005) Synthesis and surface engineering of iron oxide nanoparticles for biomedical applications. *Biomaterials* 26(18):3995–4021. doi:10.1016/j.biomaterials.2004.10.012
- He XM, Carter DC (1992) Atomic structure and chemistry of human serum albumin. *Nature* 358(6383):209–215. doi:10.1038/358209a0
- Hergt R, Dutz S (2007) Magnetic particle hyperthermia—biophysical limitations of a visionary tumour therapy. *J Magn Magn Mater* 311(1):187–192. doi:10.1016/j.jmmm.2006.10.1156
- Hondow N, Brydson R, Wang P, Holton M, Brown MR, Rees P, Summers H, Brown A (2012) Quantitative characterization of nanoparticle agglomeration within biological media. *J Nanopart Res* 14(7):1–15. doi:10.1007/s11051-012-0977-3
- Hoskins C, Wang L, Cheng W, Cuschieri A (2012) Dilemmas in the reliable estimation of the in vitro cell viability in magnetic nanoparticle engineering: which tests and what protocols? *Nanoscale Res Lett* 7(1):77. doi:10.1186/1556-276X-7-77
- Janes KA, Calvo P, Alonso MJ (2001) Polysaccharide colloidal particles as delivery systems for macromolecules. *Adv Drug Deliver Rev* 47(1):83–97. doi:10.1016/S0169-409X(00)00123-X
- Ji Z, Jin X, George S, Xia T, Meng H, Wang X, Suarez E, Zhang H, Hoek EMV, Godwin H, Nel AE, Zink JI (2010) Dispersion and stability optimization of TiO₂ nanoparticles in cell culture media. *Environ Sci Technol* 44(19):7309–7314. doi:10.1021/es100417s
- Kah JCY, Chen J, Zubieta A, Hamad-Schifferli K (2012) Exploiting the protein corona around gold nanorods for loading and triggered release. *ACS Nano* 6(8):6730–6740. doi:10.1021/nm301389c
- Khullar P, Singh V, Mahal A, Dave PN, Thakur S, Kaur G, Singh J, Singh Kamboj S, Singh Bakshi M (2012) Bovine serum albumin bioconjugated gold nanoparticles: synthesis, hemolysis, and cytotoxicity toward cancer cell lines. *J Phys Chem C* 116(15):8834–8843. doi:10.1021/jp300585d
- Kim DK, Zhang Y, Kehr J, Klason T, Bjelke B, Muhammed M (2001) Characterization and MRI study of surfactant-coated superparamagnetic nanoparticles administered into the rat brain. *J Magn Magn Mater* 225(1–2):256–261. doi:10.1016/S0304-8853(00)01255-5
- Kirchies R, Wightman L, Wagner E (2001) Design and gene delivery activity of modified polyethylenimines. *Adv Drug Deliv Rev* 53(3):341–358. doi:10.1016/S0169-409X(01)00202-2
- Kohli I, Alam S, Patel B, Mukhopadhyay A (2013) Interaction and diffusion of gold nanoparticles in bovine serum albumin solutions. *Appl Phys Lett* 102(20):203705–203705-203704. doi:10.1063/1.4807672
- Lee P, Knight R, Smit JM, Wilschut J, Griffin DE (2002) A single mutation in the E2 glycoprotein important for neurovirulence influences binding of sindbis virus to neuroblastoma cells. *J Virol* 76(12):6302–6310. doi:10.1128/jvi.76.12.6302-6311-2002
- Levy M, Quarta A, Espinosa A, Figuerola A, Wilhelm C, García-Hernández M, Genovese A, Falqui A, Alloyeau D, Buonsanti R, Cozzoli PD, García MA, Gazeau F, Pellegrino T (2011) Correlating magneto-structural properties to hyperthermia performance of highly monodisperse iron oxide nanoparticles prepared by a seeded-growth route. *Chem Mater* 23(18):4170–4180. doi:10.1021/cm201078f
- Liu G, Hong RY, Guo L, Li YG, Li HZ (2011) Preparation, characterization and MRI application of carboxymethyl dextran coated magnetic nanoparticles. *Appl Surf Sci* 257(15):6711–6717. doi:10.1016/j.apsusc.2011.02.110
- Lu A-H, Salabas EL, Schüth F (2007) Magnetic nanoparticles: synthesis, protection, functionalization, and application. *Angew Chem Int Ed* 46(8):1222–1244. doi:10.1002/anie.200602866
- Luciani N, Gazeau F, Wilhelm C (2009) Reactivity of the monocyte/macrophage system to superparamagnetic

- anionic nanoparticles. *J Mater Chem* 19(35):6373–6380. doi:[10.1039/B903306H](https://doi.org/10.1039/B903306H)
- McBain SC, Griesenbach U, Xenariou S, Keramane A, Batich CD, Alton EFWF, Dobson J (2008) Magnetic nanoparticles as gene delivery agents: enhanced transfection in the presence of oscillating magnet arrays. *Nanotechnology* 19(40):405102. doi:[10.1088/0957-4484/19/40/405102](https://doi.org/10.1088/0957-4484/19/40/405102)
- Metin C, Lake L, Miranda C, Nguyen Q (2011) Stability of aqueous silica nanoparticle dispersions. *J Nanopart Res* 13(2):839–850. doi:[10.1007/s11051-010-0085-1](https://doi.org/10.1007/s11051-010-0085-1)
- Moulin AM, O'Shea SJ, Badley RA, Doyle P, Welland ME (1999) Measuring surface-induced conformational changes in proteins. *Langmuir* 15(26):8776–8779. doi:[10.1021/la990416u](https://doi.org/10.1021/la990416u)
- Nakata S, Kido N, Hayashi M, Hara M, Sasabe H, Sugawara T, Matsuda T (1996) Chemisorption of proteins and their thiol derivatives onto gold surfaces: characterization based on electrochemical nonlinearity. *Biophys Chem* 62(1–3): 63–72. doi:[10.1016/S0301-4622\(96\)02208-9](https://doi.org/10.1016/S0301-4622(96)02208-9)
- Namduri H, Nasrazadani S (2008) Quantitative analysis of iron oxides using Fourier transform infrared spectrophotometry. *Corros Sci* 50(9):2493–2497. doi:[10.1016/j.corsci.2008.06.034](https://doi.org/10.1016/j.corsci.2008.06.034)
- Natte K, Friedrich JF, Wohrlab S, Lutzki J, von Klitzing R, Österle W, Orts-Gil G (2013) Impact of polymer shell on the formation and time evolution of nanoparticle–protein corona. *Colloid Surf B* 104:213–220. doi:[10.1016/j.colsurfb.2012.11.019](https://doi.org/10.1016/j.colsurfb.2012.11.019)
- Nigam S, Barick KC, Bahadur D (2011) Development of citrate-stabilized Fe₃O₄ nanoparticles: conjugation and release of doxorubicin for therapeutic applications. *J Magn Mater* 323(2):237–243. doi:[10.1016/j.jmmm.2010.09.009](https://doi.org/10.1016/j.jmmm.2010.09.009)
- Ouasri A, Rhandour A, Dhamelincourt MC, Dhamelincourt P, Mazzah A (2002) Vibrational study of (CH₃)₄NSbCl₆ and [(CH₃)₄N]₂SiF₆. *Spectrochim Acta A* 58(12):2779–2788. doi:[10.1016/S1386-1425\(02\)00019-7](https://doi.org/10.1016/S1386-1425(02)00019-7)
- Pamme N, Wilhelm C (2006) Continuous sorting of magnetic cells via on-chip free-flow magnetophoresis. *Lab Chip* 6(8):974–980. doi:[10.1039/B604542A](https://doi.org/10.1039/B604542A)
- Pascu O, Carezza E, Gich M, Estradé S, Peiró F, Herranz G, Roig A (2012) Surface reactivity of iron oxide nanoparticles by microwave-assisted synthesis; comparison with the thermal decomposition route. *J Phys Chem C* 116(28):15108–15116. doi:[10.1021/jp303204d](https://doi.org/10.1021/jp303204d)
- Petri-Fink A, Steitz B, Finka A, Salaklang J, Hofmann H (2008) Effect of cell media on polymer coated superparamagnetic iron oxide nanoparticles (SPIONs): Colloidal stability, cytotoxicity, and cellular uptake studies. *Eur J Pharm Biopharm* 68(1):129–137. doi:[10.1016/j.ejpb.2007.02.024](https://doi.org/10.1016/j.ejpb.2007.02.024)
- Porter D, Sriram K, Wolfarth M, Jefferson A, Schwegler-Berry D, Andrew ME, Castranova V (2008) A biocompatible medium for nanoparticle dispersion. *Nanotoxicology* 2(3):144–154. doi:[10.1080/17435390802318349](https://doi.org/10.1080/17435390802318349)
- Pratten MK, Lloyd JB (1986) Pinocytosis and phagocytosis: the effect of size of a particulate substrate on its mode of capture by rat peritoneal macrophages cultured in vitro. *BBA-Gen Subjects* 881(3):307–313. doi:[10.1016/0304-4165\(86\)90020-6](https://doi.org/10.1016/0304-4165(86)90020-6)
- Safi M, Sarrouj H, Sandre O, Mignet N, Berret JF (2010) Interactions between sub-10-nm iron and cerium oxide nanoparticles and 3T3 fibroblasts: the role of the coating and aggregation state. *Biomaterials* 21(14):145103. doi:[10.1088/0957-4484/21/14/145103](https://doi.org/10.1088/0957-4484/21/14/145103)
- Safi M, Courtois J, Seigneuret M, Conjeaud H, Berret JF (2011) The effects of aggregation and protein corona on the cellular internalization of iron oxide nanoparticles. *Biomaterials* 32(35):9353–9363. doi:[10.1016/j.biomaterials.2011.08.048](https://doi.org/10.1016/j.biomaterials.2011.08.048)
- Sager TM, Porter DW, Robinson VA, Lindsley WG, Schwegler-Berry DE, Castranova V (2007) Improved method to disperse nanoparticles for in vitro and in vivo investigation of toxicity. *Nanotoxicology* 1(2):118–129. doi:[10.1080/17435390701381596](https://doi.org/10.1080/17435390701381596)
- Sasidharan S, Jayasree A, Fazal S, Koyakutty M, Nair SV, Menon D (2013) Ambient temperature synthesis of citrate stabilized and biofunctionalized, fluorescent calcium fluoride nanocrystals for targeted labeling of cancer cells. *Biomater Sci* 1(3):294–305. doi:[10.1039/C2BM00127F](https://doi.org/10.1039/C2BM00127F)
- Sen T, Mandal S, Haldar S, Chattopadhyay K, Patra A (2011) Interaction of gold nanoparticle with human serum albumin (HSA) protein using surface energy transfer. *J Phys Chem C* 115(49):24037–24044. doi:[10.1021/jp207374g](https://doi.org/10.1021/jp207374g)
- Soenen SJH, Himmelreich U, Nuytten N, De Cuyper M (2011) Cytotoxic effects of iron oxide nanoparticles and implications for safety in cell labelling. *Biomaterials* 32(1):195–205. doi:[10.1016/j.biomaterials.2010.08.075](https://doi.org/10.1016/j.biomaterials.2010.08.075)
- Sun S, Zeng H (2002) Size-controlled synthesis of magnetite nanoparticles. *J Am Chem Soc* 124(28):8204–8205. doi:[10.1021/ja026501x](https://doi.org/10.1021/ja026501x)
- Uboldi C, Bonacchi D, Lorenzi G, Hermanns MI, Pohl C, Baldi G, Unger R, Kirkpatrick CJ (2009) Gold nanoparticles induce cytotoxicity in the alveolar type-II cell lines A549 and NCIH441. *Part Fibre Toxicol* 6(1):18. doi:[10.1186/1743-8977-6-18](https://doi.org/10.1186/1743-8977-6-18)
- Walczyk D, Bombelli FB, Monopoli MP, Lynch I, Dawson KA (2010) What the cell “Sees” in bionanoscience. *J Am Chem Soc* 132(16):5761–5768. doi:[10.1021/ja910675v](https://doi.org/10.1021/ja910675v)
- Wei X, Wei Z, Zhang L, Liu Y, He D (2011) Highly water-soluble nanocrystal powders of magnetite and maghemite coated with gluconic acid: Preparation, structure characterization, and surface coordination. *J Colloid Interf Sci* 354(1):76–81. doi:[10.1016/j.jcis.2010.10.049](https://doi.org/10.1016/j.jcis.2010.10.049)
- Wells MA, Abid A, Kennedy IM, Barakat AI (2012) Serum proteins prevent aggregation of Fe₂O₃ and ZnO nanoparticles. *Nanotoxicology* 6(8):837–846. doi:[10.3109/17435390.2011.625131](https://doi.org/10.3109/17435390.2011.625131)
- Wiogo HTR, Lim M, Bulmus V, Gutiérrez L, Woodward RC, Amal R (2012) Insight into serum protein interactions with functionalized magnetic nanoparticles in biological media. *Langmuir* 28(9):4346–4356. doi:[10.1021/la204740t](https://doi.org/10.1021/la204740t)
- Ye A, Flanagan J, Singh H (2006) Formation of stable nanoparticles via electrostatic complexation between sodium caseinate and gum arabic. *Biopolymers* 82(2):121–133. doi:[10.1002/bip.20465](https://doi.org/10.1002/bip.20465)